UNCLASSIFIED

AD NUMBER

ADB266523

NEW LIMITATION CHANGE

TO

Approved for public release, distribution unlimited

FROM

Distribution authorized to U.S. Gov't. agencies only; Proprietary Info.; Sep 2000. Other requests shall be referred to U.S. Army Medical Research and Materiel Command, 504 Scott St., Fort Detrick, MD 21702-5012.

AUTHORITY

U.S. Army Medical Research and Materiel Command and Fort Detrick ltr., dtd October 17, 2001.

THIS PAGE IS UNCLASSIFIED

AD_____

Award Number: DAMD17-96-C-6061

TITLE: 3-D Ultrasound Vascularity Assessment for Breast Cancer Diagnosis

PRINCIPAL INVESTIGATOR: Paul L. Carson, Ph.D.

CONTRACTING ORGANIZATION: The University of Michigan
Ann Arbor, Michigan 48109-1274

REPORT DATE: September 2000

TYPE OF REPORT: Final

PREPARED FOR: U.S. Army Medical Research and Materiel Command
Fort Detrick, Maryland 21702-5012

DISTRIBUTION STATEMENT: Distribution authorized to U.S. Government agencies only (proprietary information, Sep 00). Other requests for this document shall be referred to U.S. Army Medical Research and Materiel Command, 504 Scott Street, Fort Detrick, Maryland 21702-5012.

The views, opinions and/or findings contained in this report are those of the author(s) and should not be construed as an official Department of the Army position, policy or decision unless so designated by other documentation.

20010518 039

NOTICE

USING GOVERNMENT DRAWINGS, SPECIFICATIONS, OR OTHER DATA INCLUDED IN THIS DOCUMENT FOR ANY PURPOSE OTHER THAN GOVERNMENT PROCUREMENT DOES NOT IN ANY WAY OBLIGATE THE U.S. GOVERNMENT. THE FACT THAT THE GOVERNMENT FORMULATED OR SUPPLIED THE DRAWINGS, SPECIFICATIONS, OR OTHER DATA DOES NOT LICENSE THE HOLDER OR ANY OTHER PERSON OR CORPORATION; OR CONVEY ANY RIGHTS OR PERMISSION TO MANUFACTURE, USE, OR SELL ANY PATENTED INVENTION THAT MAY RELATE TO THEM.

LIMITED RIGHTS LEGEND

Award Number: DAMD17-96-C-6061
Organization: The University of Michigan
Location of Limited Rights Data (Pages):

Those portions of the technical data contained in this report marked as limited rights data shall not, without the written permission of the above contractor, be (a) released or disclosed outside the government, (b) used by the Government for manufacture or, in the case of computer software documentation, for preparing the same or similar computer software, or (c) used by a party other than the Government, except that the Government may release or disclose technical data to persons outside the Government, or permit the use of technical data by such persons, if (i) such release, disclosure, or use is necessary for emergency repair or overhaul or (ii) is a release or disclosure of technical data (other than detailed manufacturing or process data) to, or use of such data by, a foreign government that is in the interest of the Government and is required for evaluational or informational purposes, provided in either case that such release, disclosure or use is made subject to a prohibition that the person to whom the data is released or disclosed may not further use, release or disclose such data, and the contractor or subcontractor or subcontractor asserting the restriction is notified of such release, disclosure or use. This legend, together with the indications of the portions of this data which are subject to such limitations, shall be included on any reproduction hereof which includes any part of the portions subject to such limitations.

THIS TECHNICAL REPORT HAS BEEN REVIEWED AND IS APPROVED FOR PUBLICATION.

Anusingha Charan Mishra
04/30/01

REPORT DOCUMENTATION PAGE

Form Approved
OMB No. 074-0188

Public reporting burden for this collection of information is estimated to average 1 hour per response, including the time for reviewing instructions, searching existing data sources, gathering and maintaining the data needed, and completing and reviewing this collection of information. Send comments regarding this burden estimate or any other aspect of this collection of information, including suggestions for reducing this burden to Washington Headquarters Services, Directorate for Information Operations and Reports, 1215 Jefferson Davis Highway, Suite 1204, Arlington, VA 22202-4302, and to the Office of Management and Budget, Paperwork Reduction Project (0704-0188), Washington, DC 20503

1. AGENCY USE ONLY (Leave blank)	2. REPORT DATE	3. REPORT TYPE AND DATES COVERED
	September 2000	Final (1 Sep 96 - 31 Aug 00)

4. TITLE AND SUBTITLE
3-D Ultrasound Vascularity Assessment for Breast Cancer Diagnosis

5. FUNDING NUMBERS
DAMD17-96-C-6061

6. AUTHOR(S)
Paul L. Carson, Ph.D.

7. PERFORMING ORGANIZATION NAME(S) AND ADDRESS(ES)
The University of Michigan
Ann Arbor, Michigan 48109-1274

E-MAIL:
pcarson@umich.edu

8. PERFORMING ORGANIZATION REPORT NUMBER

9. SPONSORING / MONITORING AGENCY NAME(S) AND ADDRESS(ES)
U.S. Army Medical Research and Materiel Command
Fort Detrick, Maryland 21702-5012

10. SPONSORING / MONITORING AGENCY REPORT NUMBER

11. SUPPLEMENTARY NOTES

12a. DISTRIBUTION / AVAILABILITY STATEMENT
DISTRIBUTION STATEMENT: Distribution authorized to U.S. Government agencies only (proprietary information, Sep 00). Other requests for this document shall be referred to U.S. Army Medical Research and Materiel Command, 504 Scott Street, Fort Detrick, Maryland 21702-5012.

12b. DISTRIBUTION CODE

13. ABSTRACT ***(Maximum 200 Words)***

Several developments were undertaken to improve ultrasound imaging for breast cancer diagnosis and management. Techniques to align and reshape 3-D ultrasound image volumes were explored using MIAMI Fuse™ software to display 3-D studies of the breast to make subtle image features and changes over time more easily detected, evaluated and quantified. Applications studied included: 1) creation of composites from volumes acquired from differing viewpoints; 2) combination of multiple, slightly-overlapping 3-D image volumes to allow display of large-scale breast architecture as well as large masses and their change.

Measurement of scan head motion based on the rate of changes in images resulted in initial commercial implementation of simple 3D imaging in real time. Software was also developed to enable researchers to better study mapping of lactic ducts in 3D ultrasound. Further, this project also contributed to a larger clinical study of quantitative vascularity as a discriminator between benign and malignant breast masses. Recently, an ultrasound breast vascularity measure was found to be as good as subjective evaluation of nonvascular structures, and the combination of the vascularity and gray scale measures were very promising.

14. SUBJECT TERMS	15. NUMBER OF PAGES
Breast Cancer	172
	16. PRICE CODE

17. SECURITY CLASSIFICATION OF REPORT	18. SECURITY CLASSIFICATION OF THIS PAGE	19. SECURITY CLASSIFICATION OF ABSTRACT	20. LIMITATION OF ABSTRACT
Unclassified	Unclassified	Unclassified	Unlimited

Table of Contents

I. Cover.....

II. SF 298..... 2

III. Table of Contents..... 3

IV. Introduction..... 4

V. Body..... 4

A. Clinical Trials and Vascularity Measures.....4
1. Clinical Trials of ~30 subjects .....
2. Trials data analysis and write-up .....

B. Compound and Sequential Imaging.....5
1. Develop automated image registration by mutual information .....
2. Process ultrasound images to evaluate/demonstrate compound and sequential imaging therewith .....

C. Image-based Registration of Slice Position [IBaR].....6
1. Real time speckle decorrelation for image plane positioning.....

D. Digital ductography development and analysis.....6

E. Figures.....7

VI. CONCLUSIONS 9

Key Research Accomplishments.....9

Reportable Outcomes.....9

Conclusions.....12

Clinical Trials .....

Compound and Sequential Imaging.....

Image-based Slice Positioning [IBaR] .....

Digital Ductography Development and Analysis.....

VII. REFERENCES 13

VIII. APPENDICES 14

IV.INTRODUCTION

The research to be conducted over the four year period of this contract centers around four areas 1) expansion of clinical trials capabilities performed under an ongoing NIH grant and their continuation after those trials are completed; 2) image registration using the mutual information cost function for evaluation/demonstration of image compounding and sequential examinations; 3) approaches to real time image-based slice positioning; 4) imaging and delineation of lactic ducts in 3D and preliminary evaluation of their diagnostic potential. The following list of tasks was given in the funded scope of work.

Table 1. Tasks for Grant Period
Clinical Trials
Validation/improvement of vascularity measures
Clinical Trials
Trials data analysis and write-up
Compound and Sequential Imaging
Develop automated image registration by max. information
Process ultrasound images to evaluate/demonstrate compound and sequential* imaging therewith
Image-based Slice Positioning [IBAR]
Real time speckle decorrelation for image plane positioning
Digital ductography development
Ductographic analysis of selected clinical trial cases

*Auto registration of breast images from multiple exams

The following series of deliverables and associated materials are provided below in this final report and in the appendices. Included are a listing of papers, abstracts and manuscripts, published and submitted.

Item A: Final report on clinical trials conducted and analyzed.
Item B: Final report on image processing for auto-registration in sequential and compound imaging.
Item C: Final report on real-time implementation of image-based registration IBaR.
Item D Final report on ductography techniques and illustrative results.

V. BODY

Significant goals were met in the four areas of emphasis of this grant as listed below.

A. Clinical Trials and Vascularity Measures

1. Clinical Trials of ~30 subjects (Deliverable Item 1)

We have studied 51 subjects (2 African American, 49 White), using the latest apparatus including the 1.5 D matrix array scanhead for discrimination of benign and malignant breast masses and evaluation of 3D compound imaging. Of these, 10 were for a second or later exam of a serial study averaging 2.67 studies per subject to evaluate our techniques for displaying and quantifying change in the breast. 4 were normals. This was in addition to 133 subjects studied with the same techniques on an NIH grant RO1 CA 55076, which terminated earlier. Both sets of patient data were combined for several publications and presentations described below.

2. Trials data analysis and write-up

This contract contributed to publications, References/Appendices [1-4] and abstracts (1-4, 6,7) on methods used in the clinical trials, as well as publications ([5-7], one manuscript to be submitted [8] and five abstracts (9, 10,13, 14, 16, 17,19, 23, 25) on results obtained in part from patients studied with this grant. Two patient groups were studied. The initial 38 were primarily studied through an NIH grant. The second 40 were done in part with this Army contract. Linear discriminant analysis on the first group (18 benign (mean age 46), 20 malignant (mean age 56)) resulted in 100% accuracy (A_z) for a three variable index of our vascularity measure (SWD), Age, and a subjective gray scale (GS) Index. Applying the exact

same discriminator to the second group of subjects provided and accuracy of 97%, as shown in Figure 1, along with ROC curves for other combinations of variables.

B. Compound and Sequential Imaging by Image Volume Registration (Deliverable Item 2)

Because of our exciting advances with the automatic registration of two or more 3D image sets for assessment of sequential and compound imaging, we continued to emphasize this goal during the entire project period. The surprising high resolution and improvement in detectability of low contrast regions and connective tissue layers with compound imaging are revealed in Figure 2.

1. Develop automated image registration by mutual information

The software modified here for use with ultrasound, MIAMI Fuse, continues to be refined and its utility for application to diagnostic ultrasound extended. The first demonstrated 3D coregistrations of ultrasound image sets were published in [1] and in abstracts (7,9,10). In year 04, a new method, involving elements of MIAMI Fuse plus registration of subvolumes of the imaged breast volume, was developed to speed image volume registration with many control points [9], (20). This allowed comparison of results from the new method and those from the "entire volume" registration method of MIAMI Fuse for estimation of errors and relative registration times. Extensive error analyses are published [9,10] and in abstracts (18,20, 21,24,26).

2. Process ultrasound images to evaluate/demonstrate compound and sequential* imaging therewith

1. The software has been modified and the registration is now being applied on patient examples for demonstration of each of several uses, including: 1) Combining views from multiple angles (compounding) [9,10,12], Abstracts (11,12,16,18-22,24); 2) highlighting and quantifying changes in essentially normal breasts as a prelude to improved detection of preclinical disease, Abstracts/Website (6,7,9,10,18,22,24); 3) tracking changes for patients undergoing chemotherapy and antiangiogenesis therapy [1,4,11] and Abstracts (6,7,9,10,16,18,22,24); 4) combining 3D data sets from various ultrasound imaging modes to properly register the unique information provided by each (References/Appendices 7), (Abstracts 6,7,9,10,18); 5) expanding the field of view by combining several partially-overlapping 3D scans to see the full volume of medium to large lesions and reasonable amounts of surrounding vascular morphology and to show a reasonable volume of the breast for tracking difficult areas of the breast in follow up studies [4], Abstracts (6,7,10,18). The advantages of being able to slice synchronously through spatially-registered ultrasound data separated in time are difficult to convey on paper. However, a demonstration movie on our public website (22), gives some indication of the ease of comparing side-by-side registered volumes as well as the difficulty of comparing volumetric 3D breast data displayed at the slightly different locations and orientations of acquisition.

Description	Accuracy (mm)	Duration (min/set)
5x5x5 subvols.	0.17	5.3
4x4x4 subvols., regular	0.27	4.9
4x4x4 subvols., fast	0.33	1.1
3x3x3 control points, global optimization	0.81	53.8

Table 1. Average registration times and accuracy per data set (13MB). Mean simulated warp: 2.0 mm, Std dev of noise distribution: 15 of 255 gray levels. Accuracy ≡ mean of remaining deformation after registering the warped volume to the original volume.

2. Comparison of errors in image sets obtained of the same volume, from five different directions were obtained by manual identification of homologous points, and comparison of subvolume and global registration. As presented in [10], registration errors obtained in four *in vivo* scans after two different registrations with reference scan #1 yielded a mean registration error of .024 mm. A quite different approach was recently employed to validate and compare the global and subvolume (SURE) registration methods [9], available at http://www.ultrasound.med.umich.edu/proceedings/). To simulate sequential scans, a random, nonlinear deformation was applied using the inverse of the subvolume registration method, but at higher spatial frequencies (e.g., 6x6x6 subvolumes) than used in the subsequent registration. Both spatially correlated and uncorrelated noise was added to 20 *in*

vivo breast image volumes to simulate speckle changes in multiview imaging. Registration using SURE reduced the average displacements of 2.0 mm in the artificially deformed volumes to 0.27 mm, respectively (Table 1). Registration times were below 5 min on a 500 MHz CPU. The greatest registration errors were in deeper areas where there were no echoes on which to register. Between the SURE method in row 3 and the global registration method in row 4, the accuracy and registration time improved by factors of 2.5 and 50, respectively. Rows 1 and 4 show improvements of factors of 5 and 10, respectively. This more accurate and faster technique (for ultrasound to ultrasound registrations) will be used for the routine registrations in Project 3.

C. *Image-based Registration of Slice Position [IBaR]*

1. **Real time speckle decorrelation for image plane positioning** (Deliverable Item 3)

As part of our research on this topic, we have continued to work with one company and interact with another, both of which have implemented crude real time versions of our IBaR technology [13,14], (9,12). One has implemented software which uses the image decorrelation to estimate the average scan rate over the entire 3D sweep and applies that average rate to assign the image slice spacings. The other does not yet apply the true decorrelation calculation on the clinically-released systems. To accurately estimate elevational movement, the frame rates must be high enough such that consecutive images are not completely decorrelated.

D. *Digital ductography development and analysis (Deliverable Item 4)*

Software tools were developed to help the user manually find, map and review ductal structures in the volume of B mode ultrasound data. Initially, the user identifies the relative location of the nipple to the data volume. The user then searches the volume by rotating a plane about the nipple. When a duct-like structure is seen, the user draws a line along the duct. The software then enables him/her to rotate the search plane around this line to verify if it is a duct, find the portions of it not in the initial search plane, and identify visible lobules feeding it. During this process, the user can mark any feature as part of the ductal tree, ultimately creating a 3D mapping of ductal structures within the volume (3,5,6).

These graphical analysis tools have proven useful for visual definition of ducts in a few selected cases such as (Figure 4). The main future work will be in development of more automated duct segmentation, which has not been undertaken extensively due to the major emphasis we have placed on the compound imaging and the variable compression of the ducts caused by our hand scanning.

We have developed, in conjunction with CIRS, Inc., a phantom that can be used for many purposes, including testing of detection and delineation of short lengths of ducts. This CIRS Model 44 cylindrical plug phantom is shown in Figure 3. It contains 45, high contrast stubby cylinders within the imaging range of the M12 scanhead planned for this study. These are in known locations relative to each other for tests of spatial registration accuracy in multiple view compounding, as well as for the ductographic detection.

E. Figures

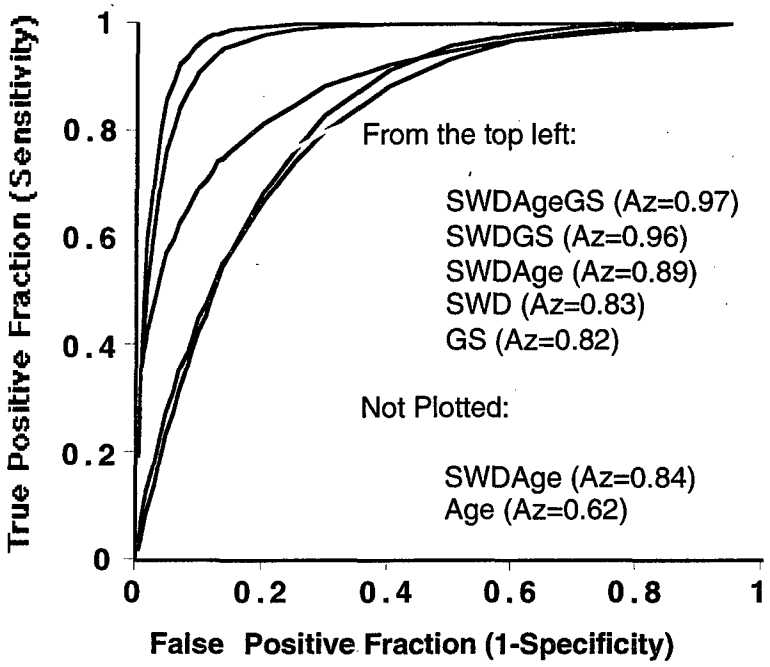

Figure 1. *Performance of various discrimination indices on a second, test set, of 40 subjects, as demonstrated by maximum likelihood binormal estimates of ROC curves. Speed-weighted pixel density (SWD), average grayscale rating (GS), and patient age were blindly applied to the multivariable classifiers derived from the initial patient population (n=38). The high performance (Az=0.97) of the SWD-Age-GS again exceeded all other indices and demonstrated statistically significant improvement over all single variable indices.*

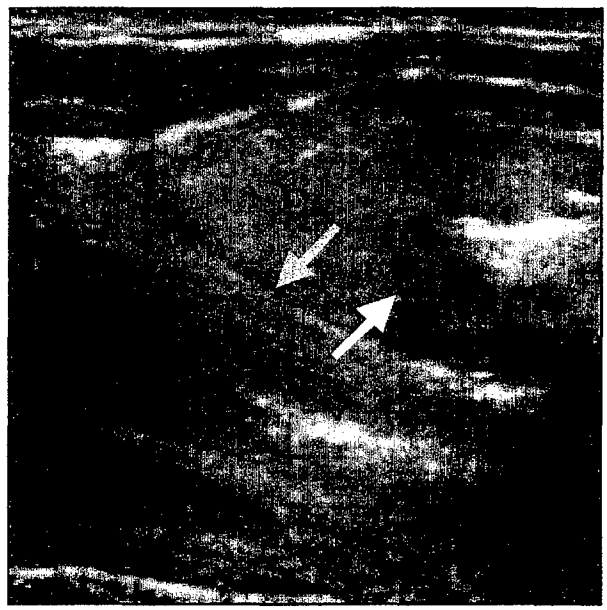

Figure 2. *(a) Uncompounded image of a breast from reference, 0° scan. Statistical analysis showed an almost ideal $\propto\sqrt{N}$ increase in SNR and CNR (contrast-to-noise ratio) for N views compounded vs. this reference view. Note the overall reduction in granularity and the better delineation of connective tissues (gray arrow) in (b).*

(b) Same image area compounded from 5 scans at 0°, 6.4°, 12.8°, -5.1°, and –10.2°, registered using 11 control point warping transformations. Most importantly, note the slightly hypoechoic, lobulated inhomogeneities surrounding the left end of the hyperechoic structure on the central right. The white arrow denotes one such lobulation with a thin, echogenic rim that is not visible on any of the constituent single views.

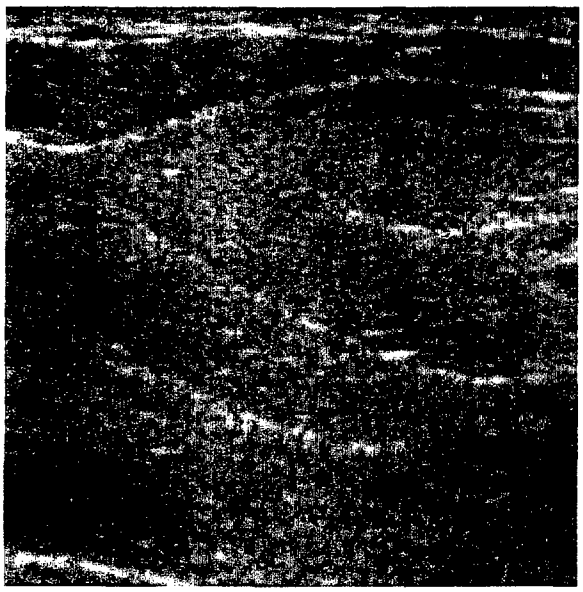

(c) Uncompounded image of a breast from reference, 0°, scan, 2.4 mm (8 slices) superior to image (a). Structures noted in (d) are not seen as well here.

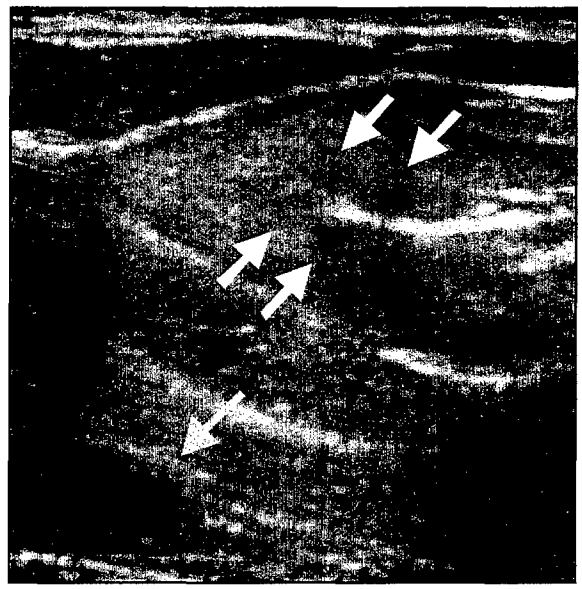

(d) Same image plane as (c) but from the same compounded image set as (b). Again note the slightly hypoechoic, lobulated inhomogeneities surrounding the left end of the hyperechoic structure on the central right (e.g., white arrows), corresponding to those at the white arrow in (b). Note also the improved delineation of the dark rib in the lower left (gray arrow) and the tissue striations extending to the right of it.

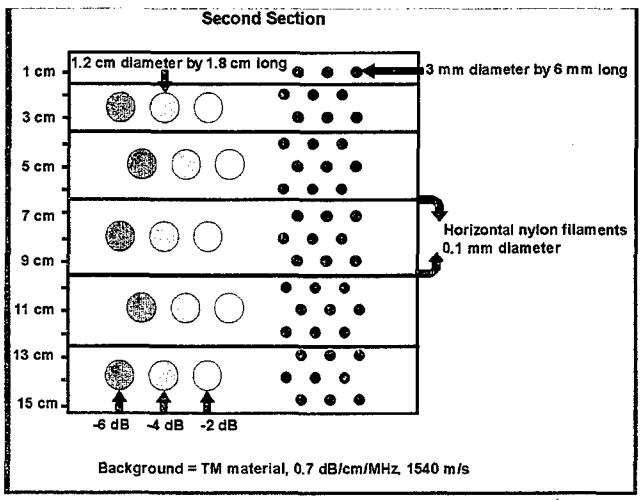

Figure 3. *Diagram of our existing CIRS Model 44 cylindrical plug phantom, which we developed jointly with CIRS. Within the 5.5 cm range useable for the GE M12 scanhead, the front side shown contains 15 3 x 6 mm cylindrical plugs and the back side of the phantom, parallel to this side, contains 15, 1.5 mm x 2.4 mm long, and 15, 3 mm x 3 mm, cylindrical plugs of high contrast, ~-12 dB re the background material. This yields a total of 45 plugs with easily localized centers. Specific attenuation of the background material on the back side is 0.5 dB cm^{-1} MHz^{-1}. This phantom will provide excellent measures of the change in resolution (contrast of the small plugs) and increase of contrast to noise ratio on the large, low contrast cylinders.*

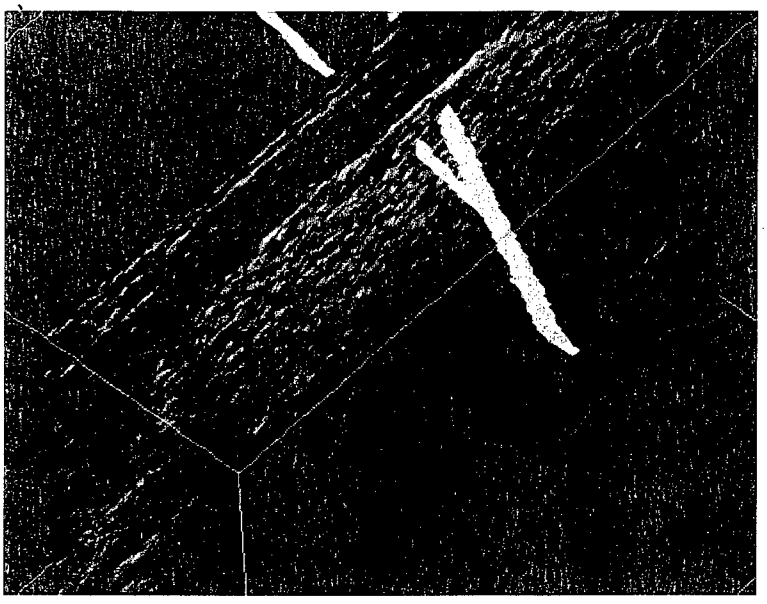

Figure 4. *Ductal tree of a lactating breast is shown in green 3D, superimposed on one of the gray scale slices in the volume. The Dark layer in the gray scale slice, arrow, might be thought of as a duct, but careful panning through the slices shows it to be a surface, rather than a tube. Duct identification software reduces the duct delineation time to approximately 1/4 that with conventional 3D tools.*

VI. CONCLUSIONS

KEY RESEARCH ACCOMPLISHMENTS:

- Advanced 3D ultrasound image acquisition and display as well as quantification of breast lesion vascularity.
- Helped demonstrate the increased sensitivity and specificity of ultrasound color flow imaging for discrimination of benign and malignant breast masses
- Used 3D registration for combining images from different look directions to provide a compound image volume of (often) improved information content
- Developed subvolume registration of imaged breast volumes to speed their registration with high spatial frequencies.
- Used 3D registration for comparing images obtained at different times for following changes in the breast
- Extended our image-based slice positioning to allow tracking of scanhead position to the extent that a simplified form has been implemented commercially in real time.
- Developed graphical analysis tools that proved useful for visual definition of ducts in a few selected cases.

REPORTABLE OUTCOMES:

All listed publications are included as Appendices.

* = supported primarily by another grant

** = supported solely** or primarily** by this contract

No asterisk = indirect result of developed techniques

Manuscripts, Published Journal Articles and Proceedings

1. *Meyer CR, Boes JL, Kim B, Bland PH, LeCarpentier GL, Fowlkes JB, Roubidoux MA, Carson PL, Semiautomatic Registration of Volumetric Ultrasound Scans, Ultrasound Med. Biol., 25/3, 339-347, 1999.
2. *Rubin JM, Bude RO, Fowlkes JB, Spratt RS, Carson PL, Adler RS (1997), Normalizing Fractional Moving Blood Volume Estimates with Power Doppler US: Defining a Stable Intravascular Point with the Cumulative Power Distribution Function, Radiology, 205, 757-765.
3. *Fenn RC, Fowlkes JB, Moskalik A, Zhang Y., Roubidoux MA, Carson PL (1997) A hand-controlled, 3-D ultrasound guide and measurement system, in Acoustical Imaging, S. Lees, ed., Plenum Press, N.Y. ISBN 0306457687 TC, v. 23, 237-242.

4. ** Krüker JF, LeCarpentier GL, Meyer CR, Fowlkes JB, Roubidoux MA, Carson PL, 3D Image Registration for Multimode, Extended Field of View, and Sequential Ultrasound Imaging, RSNA EJ, http://ej.rsna.org/ej3/0098-99.fin/index.html .
5. *Carson PL, Fowlkes JB, Roubidoux MA, Moskalik AP, Govil A, Normolle D, LeCarpentier G, Nattakom S, Rubin JM (1998), 3D Doppler Image Signal Quantification of Breast Masses, Ultrasound Med. Biol., 24:6, 945-952, 1998.
6. *LeCarpentier, G.L., Tridandapani, P.B., Fowlkes, J. B., Roubidoux, M. A., Moskalik, A.P. and Carson, P. L. Utility of 3D ultrasound in the discrimination and detection of breast cancer, RSNA EJ, 1999, http://ej.rsna.org/ej3/0103-99.fin/titlepage.html .
7. *Bhatti PT, LeCarpentier GL, Roubidoux MA, Fowlkes JB, Helvie MA, Carson P.L., Discrimination of Sonographic Breast Lesions Using Frequency Shift Color Doppler Imaging in Combination with Age, and Gray Scale Criteria, accepted with minor revisions.
8. *LeCarpentier GL, Roubidoux MA, Fowlkes JB, Krücker JF, Helvie MA, Thorson NJ, Engle KD, Carson P.L., Assessment of 3D Doppler Ultrasound Indices in the Classification of Suspicious Breast Lesions Using an Independent Test Population and a 4-Fold Cross Validation Scheme, in preparation.
9. **Krücker JF, LeCarpentier GL, Carson PL, Meyer CR, Rapid Image Registration for 3D Ultrasound Compounding, Proceedings, 2000 IEEE International Ultrasonics Symposium, San Juan, in Press.
10. ** Krücker JF, Meyer CR, LeCarpentier GL, Fowlkes JB, Carson PL, 3D Spatial Compounding of Ultrasound Images Using Image-Based, Nonrigid Registration, Ultrasound Med. Biol., accepted.
11. Brewer, DJ, Dick, RD, Grover, DK, LeClaire, V, Tseng, M, Wicha, M, Pienta, K, Redman, BG, Jahan, T, Sondak, VK, Strawderman, M, LeCarpentier, GL, Merajver, SD, Treatment of metastatic cancer with tetrathiomolybdate, an anti-copper, antiangiogenic agent: I. phase I. study, Clin. Cancer Res., 6, 1-10, 2000.
12. ** Krücker JF, Meyer CR, Tuthill TA, LeCarpentier GL, Fowlkes JB, Carson PL. 3D compounding of B-scan ultrasound images. Joint Meeting: 137th Meeting of the Acoustical Society of America and 2nd Convention of the European Acoustics Association, Berlin, 15-19 March, 1999, Collected Papers (CD), ISBN 3-9804568-5-4, # 4ABB_3, 1999, 4pp.
13. *Chen J-F, Fowlkes JB, Carson PL, Rubin JM: Determination of Scan-Plane Motion Using Speckle Decorrelation. Theoretical Consideration and Initial Test, Internat. J. Imaging Systems and Technology, 8, 38-44, 1997.
14. **Tuthill TA, Krücker JF, Fowlkes JB, Carson PL (1998) Automated 3-D US Frame Positioning Computed from Elevational Speckle Decorrelation, Radiology, 209, 575-582.
15. Kremkau FW, Merritt CRB, Carson PL, Needleman L, Nelson TR, Pretorius DH, Rubin JM (1997), Future Directions in Diagnostic Ultrasound, Radiology, 209, 305-311 (review only, no acknowledgement, portions are from this grant work).

Published Abstracts and Presentations

1. Fenn RC, Fowlkes JB, Roubidoux MA, Moskalik A, **Carson PL** (1997) A Miniature Position-Encoding System for Flexible, Hand-Controlled, 3D Ultrasound, (Procs., AIUM 41st Annual Conv., Mar. 17-20) J. Ultras. in Med., 16:S1, S 11.
2. **Carson PL** (1997) 3D Ultrasound Imaging: Vascular quantification and patterns, ductography, transmission tomography (And session chair/organizer). Symposium of Federal Multi-Agency Consortium on Imaging Technologies to Improve Women's Health, May 1-2, 1997, Washington, D.C.
3. Fenn RC, Fowlkes JB, Moskalik A, Zhang Y., Roubidoux MA, **Carson PL** (1997) A hand-controlled, 3-D ultrasound guide and measurement system, 23rd Internat Symp. on Acoustical Imaging, April 13-16, Boston.
4. **Carson PL**, Fowlkes JB, Roubidoux MA, Moskalik AP, LeCarpentier GL, Helvie M (1997) Basic Advances in 3D Ultrasound Imaging of the Breast Including Vascularity Analysis and Ductography, U.S. Army Breast Cancer Research Program., Oct. 31-Nov 4. Chicago, Poster and Platform Presentation, Proceedings, I, 221-222.

5. LeCarpentier GL, Moskalik AP, Roubidoux MA, **Carson PL** (1997) 3D Tracking and Display of Mammary Ducts. RSNA, Nov 26-Dec. 1, Chicago, Radiology, 205 (P), 491.
6. LeCarpentier GL, Moskalik AP, Meyer CR, Bland PH, Roubidoux MA, **Carson PL** (1997) Breast and Prostate 3D Color Flow Ultrasound Quantification and Image Fusion. RSNA, Nov 26-Dec. 1, Chicago, InfoRad Exhibit, Radiology, 205 (P), 740.
7. **Carson PL**, (1998) 3D Ultrasound, Image Registration, UCT: Key Problems and Opportunities, Working Group on Novel Breast Ultrasound Technology, Amer. Col. Radiol., Jan. 19, 1998, Reston, VA, presentation and 3 pg. report.
8. Tuthill GA, Fowlkes JB, Krücker JF, Rubin JM, **Carson** PL (1998) Elevational B-Scan Registration Using Frame-to-Frame Speckle Decorrelation, (Procs., AIUM 42nd Annual Conv., Mar. 22-25) J. Ultras. in Med., 17:S1, S96.
9. Meyer CR, LeCarpentier GL, Roubidoux MA, Boes JL, Fowlkes JB, Kim B, Bland PH, **Carson PL** (1998) Automated Coregistration of Three-Dimensional Ultrasound Volumes by Mutual Information: Sequential Examples of Breast Masses, (Procs., AIUM 42nd Annual Conv., Mar. 22-25) J. Ultras. in Med., 17:S1, S87.
10. **Carson PL** (1998) Technological Advances. In: Plenary Session--Breast Ultrasound, Pathways to the Future, (Program and Abstracts, AIUM 42nd Annual Conv., Mar. 22-25) p.13. 268
11. Krücker JF, Tuthill TA, LeCarpentier GL, Fowlkes JB, **Carson PL**, Image Based Calculation of Elevational B-Scan Separation, Presentation at 135th Meeting of the Acoustical Society of America, Seattle, WA, June 22-26, 1998.
12. Krücker JF, Meyer CR, Tuthill TA, LeCarpentier GL, Fowlkes JB, **Carson PL**. 3D compounding of B-scan ultrasound images. Presentation at 137th Meeting of the Acoustical Society of America, Berlin, 15-19 March, 1999, Abstract # 4ABB_3, J. Acoust. Soc. Amer., 105/2 Pt. 2, 1208, 1999.
13. Tridandapani PB, LeCarpentier GL, Roubidoux MA, Helvie MA, Fowlkes JB, **Carson PL**. Enhanced Discrimination Breast Cancer Using Doppler Ultrasound Imaging, (Procs., AIUM 43rd Annual Conv., Mar. 14-17) J. Ultras. in Med., 18 S: 30, 1999.
14. LeCarpentier, G. L., Bhatti, P.T., Roubidoux, M.A., Fowlkes, J.B., Helvie, M.A., Carson, P.L. Characterization of Benign Versus Malignant Breast Lesions Using Quantitative Measures of Color Doppler Ultrasound Imaging. Visualizing the Future of Biology and Medicine, Bethesda, MD, NIH, June 25-6, 1999, http://www.capconcorp.com/grants/becon/meeting99/poster.htm.
15. Krücker JF, Meyer CR, LeCarpentier GL, Fowlkes JB, Carson PL, Volume registration for 3D compounding of ultrasound images, RSNA, Nov 28-Dec. 3, Chicago, Radiology, 213 (P), 101, 1999.
16. LeCarpentier GL, Roubidoux, MA, Krücker JF, Carson PL, Fowlkes, JB, Preliminary observations on correlations of volume and vascularity measurement of breast cancer during neoadjuvant chemotherapy, (Procs., AIUM 44th Annual Conv., Apr. 2-5, San Francisco) J. Ultras. In Med., 19, S18, 2000.
17. LeCarpentier GL, Bhatti PT, Roubidoux MA, Fowlkes JB, Helvie MA, Thorson N, Carson PL, 3D color Doppler imaging and grayscale assessment in discriminating benign versus malignant breast lesions, (Procs., AIUM 44th Annual Conv., Apr. 2-5, San Francisco) J. Ultras. In Med., 19 S85, 2000.
18. Krücker JF, Meyer CR, Fowlkes JB, Carson PL, Applications of Image Registration in 3-Dimensional Ultrasound Imaging, Young Investigator Spring Symposium, Great Lakes Chapter, AAPM and HPS, May 3, Ann Arbor, 2000, 5 pp. in book of presentations.
19. LeCarpentier GL, Roubidoux MA, Bhatti PT, Fowlkes JB, Thorson NJ, Engle KD, Carson PL, A Prospective Study of a Frequency Shift Color Doppler Ultrasound Index in the Determination of Benign Versus Malignant Breast Lesions, (Procs., World Congress on Medical Physics and Biomedical Engineering, Session TH-B305-2, 9:20 am, July 23-28, Chicago, 2000.
20. Krücker JF, LeCarpentier GL, Carson PL, Meyer CR, Rapid Image Registration for 3D Ultrasound Compounding, 2000 IEEE International Ultrasonics Symposium, Oct. 22-25, San Juan, Book of Abstracts, 134.
21. Movies on our public website **http://www.ultrasound.med.umich.edu**/previews/
22. LeCarpentier GL, Roubidoux MA, Bhatti PT, Fowlkes JB, Thorson NJ, Engle KD, Carson PL, A Prospective Study of a Frequency Shift Color Doppler Ultrasound Index in the Determination of

Benign Versus Malignant Breast Lesions, (Procs., World Congress on Medical Physics and Biomedical Engineering, Session TH-B305-2, 9:20 am, July 23-28, Chicago, 2000.

23. Carson PL, Krücker J, LeCarpentier G, Roubidoux M, Fowlkes JB, 3D Registration of Serial and Compound Breast Ultrasound, British Med. Ultras. Soc. Meeting, Dec. 4-7, Eastbourne, UK, Book of Abstracts, 2000, p. 11.

24. LeCarpentier GL*, Roubidoux MA, Fowlkes JB, Kruecker JF, Thorson NJ, Engle KD, Carson PL, Validation and Assessment of 3D Doppler Ultrasound Indices in the Classification of Suspicious Breast Lesions, (Procs., AIUM 45th Annual Conv., Mar. 10-14, Orlando) J. Ultras. In Med., 20, 2001.

25. Krücker JF, LeCarpentier GL, Carson PL, Meyer CR, Subvolume... Registration for 3D Ultrasound Compounding, (Procs., AIUM 45th Annual Conv., Mar. 10-14, Orlando) J. Ultras. In Med., 20, 2001.

Funding Applied for Based In Part on Work Supported in part by This Award

Army Idea Grant USAMRMC (G LeCarpentier) (3/1/2001-2/29/2004)
$286,872 total direct

Title: Characterization of Breast Masses Using a New Method of Ultrasound Contrast Agent Imaging in 3D Mapping of Vascular Anomalies.

The purpose of the proposed work is to develop an innovative dual-transducer method to control the destruction and imaging of ultrasound contrast during 3D ultrasound scanning of suspicious breast masses.

NIH BRG Proposal (PI: P. Carson) 7/01/2001-6/30/2005 **Confidential Material**
$500,000

Title: Digital X-ray-Ray and Ultrasound Breast Imaging

The major goal of this project is to develop and assess a 3D ultrasound system in relation to digital mammography for breast cancer diagnosis.

Project 3 of 1P01 CA887634-01 (Meyer, C.R.) 7/01/01-6/30/06
NIH/NCI $1,842,115

Title: Automatic 3D Registration for Enhanced Cancer Management

The general theme of the P01 application is to apply 3D registration technique to a variety of clinical cancer management problems in a preclinical setting to demonstrate potential benefits over existing methods. Project 3 concentrates on registering interval 3D color flow and gray scale ultrasound exams for the quantitatively following patients on chemotherapy.

CONCLUSIONS

Considerable innovative work to improve and evaluate ultrasound imaging of breast cancer has been accomplished with primary or secondary support from this contract. Several of these advances are receiving national attention (References 15-20).

Clinical Trials

The 3D color flow quantification and other advances described above should increase the sensitivity and specificity of ultrasound imaging for discrimination of benign and malignant masses. They should

also improve tracking of changes during treatment or even detection of masses by highlighting of subtle changes in follow-up studies. Data analysis and write-up of earlier trials has been completed and contributions were made to advance 3D image acquisition, display and quantification.

Compound and Sequential Imaging

3D registration was studied for combining images from different look directions. Registration accuracy (related to obtainable resolution was documented. More complete delineation of many low contrast and specular gray scale structures was demonstrated in many cases. Fig. 2 reveals the success of techniques. The registration is also useful for following changes in the patient in serial examinations. Both, but particularly the latter, can revolutionize medical imaging and interpretation. The former is approaching the quality necessary to allow compound scanning (imaging the same tissues from different viewing angles) in at least some cases and combining dedicated high resolution, (multifocal) gray scale images with f-CDI and/or p-CDI scans. These combinations will reduce speckle and electronic noise, while revealing more of the structure seen only at a few of the image look directions. The types of serial exams that might be followed include tracking of tumor size and vascularity for early indications of response to treatment, as well as serial follow-up or even screening exams to reveal abnormal growth .

Image-based Slice Positioning [IBaR]

The possibility of practical implementation has been demonstrated commercially, albeit in a reduced form from what we have published (References 7 and 9). We believe it will be practical to make high quality 3D scans, that are either linear or sector, but possibly not both. The ability to make accurate distance measurements will probably be limited to fairly short distances and to areas around relatively uniform tissues.

Digital ductography development

The functional part of the breast is the glandular tissue which is found in 15-20 lobes which radiate out from the nipple. Each lobe is drained by its central duct which exits from the nipple. Almost all breast cancer occurs in the glandular tissue, and a significant proportion is intraductal. Therefore, being able to find and map the ducts might greatly increase the efficacy of B mode ultrasound for breast cancer screening and diagnosis. Display of the ductal tree in 3D, while panning through the gray scale images should be a significant aid to orientation and anatomy. At the least it will facilitate registration of serial volume image sets of the breast.

VI. REFERENCES

1. **Meyer CR, Boes JL, Kim B, Bland PH, LeCarpentier GL, Fowlkes JB, Roubidoux MA, Carson PL, Semiautomatic Registration of Volumetric Ultrasound Scans, Ultrasound Med. Biol., 25/3, 339-347, 1999.
2. *Rubin JM, Bude RO, Fowlkes JB, Spratt RS, Carson PL, Adler RS (1997), Normalizing Fractional Moving Blood Volume Estimates with Power Doppler US: Defining a Stable Intravascular Point with the Cumulative Power Distribution Function, Radiology, 205, 757-765.
3. *Fenn RC, Fowlkes JB, Moskalik A, Zhang Y., Roubidoux MA, Carson PL (1997) A hand-controlled, 3-D ultrasound guide and measurement system, in Acoustical Imaging, S. Lees, ed., Plenum Press, N.Y. ISBN 0306457687 TC, v. 23, 237-242.
4. ** Krüker JF, LeCarpentier GL, Meyer CR, Fowlkes JB, Roubidoux MA, Carson PL, 3D Image Registration for Multimode, Extended Field of View, and Sequential Ultrasound Imaging, RSNA EJ, http://ej.rsna.org/ej3/0098-99.fin/index.html .
5. *Carson PL, Fowlkes JB, Roubidoux MA, Moskalik AP, Govil A, Normolle D, LeCarpentier G, Nattakom S, Rubin JM (1998), 3D Doppler Image Signal Quantification of Breast Masses, Ultrasound Med. Biol., 24:6, 945-952, 1998.

6. *LeCarpentier, G.L., Tridandapani, P.B., Fowlkes, J. B., Roubidoux, M. A., Moskalik, A.P. and Carson, P. L. Utility of 3D ultrasound in the discrimination and detection of breast cancer, RSNA EJ, 1999, http://ej.rsna.org/ej3/0103-99.fin/titlepage.html .
7. Bhatti PT, Roubidoux MA, LeCarpentier GL, Fowlkes JB, Helvie MA, Carson P.L., Discrimination of Sonographic Breast Lesions Using Frequency Shift Color Doppler Imaging in Combination with Age, and Gray Scale Criteria, accepted with minor revisions.
8. *LeCarpentier GL, Roubidoux MA, Fowlkes JB, Krücker JF, Helvie MA, Thorson NJ, Engle KD, Carson P.L., Assessment of 3D Doppler Ultrasound Indices in the Classification of Suspicious Breast Lesions Using an Independent Test Population and a 4-Fold Cross Validation Scheme, in preparation.
9. **Krücker JF, LeCarpentier GL, Carson PL, Meyer CR, Rapid Image Registration for 3D Ultrasound Compounding, Proceedings, 2000 IEEE International Ultrasonics Symposium, San Juan, in Press.
10. ** Krücker JF, Meyer CR, LeCarpentier GL, Fowlkes JB, Carson PL, 3D Spatial Compounding of Ultrasound Images Using Image-Based, Nonrigid Registration, Ultrasound Med. Biol., accepted.
11. *Brewer, DJ, Dick, RD, Grover, DK, LeClaire, V, Tseng, M, Wicha, M, Pienta, K, Redman, BG, Jahan, T, Sondak, VK, Strawderman, M, LeCarpentier, GL, Merajver, SD, Treatment of metastatic cancer with tetrathiomolybdate, an anti-copper, antiangiogenic agent: I. phase I. study, Clin. Cancer Res., 6, 1-10, 2000.
12. ** Krücker JF, Meyer CR, Tuthill TA, LeCarpentier GL, Fowlkes JB, Carson PL. 3D compounding of B-scan ultrasound images. Joint Meeting: 137th Meeting of the Acoustical Society of America and 2nd Convention of the European Acoustics Association, Berlin, 15-19 March, 1999, Collected Papers (CD), ISBN 3-9804568-5-4, # 4ABB_3, 1999, 4pp.
13. *Chen J-F, Fowlkes JB, Carson PL, Rubin JM: Determination of Scan-Plane Motion Using Speckle Decorrelation. Theoretical Consideration and Initial Test, Internat. J. Imaging Systems and Technology, 8, 38-44, 1997.
14. **Tuthill TA, Krücker JF, Fowlkes JB, Carson PL (1998) Automated 3-D US Frame Positioning Computed from Elevational Speckle Decorrelation, Radiology, 209, 575-582.
15. Kremkau FW, Merritt CRB, Carson PL, Needleman L, Nelson TR, Pretorius DH, Rubin JM (1997), Future Directions in Diagnostic Ultrasound, Radiology, 209, 305-311 (review only, no acknowledgement, portions are from this grant work).
16. ** Carson PL (primary author), (1999) Technological needs for improvement of ultrasound in detection of preclinical breast disease in high risk women. Draft report for Working Group on Novel Breast Ultrasound Technology, Amer. Col. Radiol., 3 pp. Not included, still confidential, no copyright release.
17. Merritt, C. R. (1999). "Future directions in breast ultrasonography." Sem. in Breast Disease **2**: 89-96.
18. Fine-tuning Breast Ultrasound. RT Image, 2000. 13(28): p. 10-11.
19. Rowell, N., 3-D ultrasound makes breast cancer detection easier. Biophotonics International, Nov. 2000: p. 32-3.
20. Ward, J.A., Breast cancer: spotting the "hungry animals". Advance for Radiologic Science Professionals, 2000.

VII. APPENDICES

Appendices are those publications listed above as Manuscripts, Published Journal Articles and Proceedings , under Reportable Outcomes.

ELSEVIER

Ultrasound in Med. & Biol., Vol. 25, No. 3, pp. 339–347, 199
Copyright © 1999 World Federation for Ultrasound in Medicine & Biology
Printed in the USA. All rights reserved
0301-5629/99/$–see front matter

PII S0301-5629(98)00148-3

● *Original Contribution*

SEMIAUTOMATIC REGISTRATION OF VOLUMETRIC ULTRASOUND SCANS

CHARLES R. MEYER, JENNIFER L. BOES, BOKLYE KIM, PEYTON H. BLAND, GERALD L. LECARPENTIER, J. BRIAN FOWLKES, MARILYN A. ROUBIDOUX, and PAUL L. CARSON

Department of Radiology, University of Michigan Medical School, Ann Arbor, MI

(*Received* 5 *May* 1998; *in final form* 7 *September* 1998)

Abstract —We demonstrate the ability to register easily and accurately volumetric ultrasound scans without significant data preprocessing or user intervention. Two volumetric ultrasound breast scan data sets were acquired from two different patients with breast cancer. Volumetric scan data were acquired by manually sweeping a linear array transducer mounted on a linear slider with a position encoder. The volumetric data set pairs consisted of color flow and/or power mode Doppler data sets acquired serially on the same patients. A previously described semiautomatic registration method based on maximizing mutual information was used to determine the transform between data sets. The results suggest that, even for the deformable breast, three-dimensional full affine transforms can be sufficient to obtain clinically useful registrations; warping may be necessary for increased registration accuracy. In conclusion, mutual information-based automatic registration as implemented on modern workstations is capable of yielding clinically useful registrations in times <35 min.
© 1999 World Federation for Ultrasound in Medicine & Biology.

Key Words: **Ultrasound, Mutual information, Registration, Volumetric, affine, Thin plate spline warping.**

INTRODUCTION

There are potentially many reasons why ultrasound examinations might benefit from registration. Images from different transducer positions are at least partially, if not fully, uncorrelated, and summing them can significantly improve the contrast-to-speckle noise ratio. Doppler color flow acquisitions suffer from undetected flow where the flow is parallel to the transducer's face. Volumes collected from different viewing directions may detect such missing flow vectors, and registration across acquisitions can assist in computing flow velocity vectors that are consistent across different views. Perhaps the most important reason to register ultrasound data sets is to assist the comparison of serial examinations performed on the same patient. Presenting two-dimensional images from different serial examinations with the same orientation and partial volumes may help the clinician more easily to distinguish what has changed. To the extent that echogenicities from different examinations can be approximately equalized, registered serial examinations can be subtracted to emphasize changes. Such differential approaches could be especially important when serially monitoring patient response to chemotherapy or radiation therapy.

Although such automatic registration methods for ultrasound data sets may be desirable, there are preliminary reasons for caution in expecting automatic methods to function well. Such reasons include the ubiquitous speckle noise and attenuation artifacts such as "comet tails" of either shadowing or enhancement. Attenuation artifacts that present differently in each of the data sets depending on transducer orientation may compromise chances of successful registration for any automatic method. An additional source of inconsistent features comes from strong coherent echoes that are observed from structures large with respect to wavelength when observed in an orientation normal to the reflecting surface. Thus, coherent echoes as well as shadows in different data sets are often sources of inconsistent geometry when the data sets were acquired using different transducer orientations. Refraction, i.e., ray bending, may yield additional inconsistencies.

Address correspondence to: Charles R. Meyer, Department of Radiology, University of Michigan Medical School, Ann Arbor, MI 48109-0553, USA. E-mail: cmeyer@umich.edu

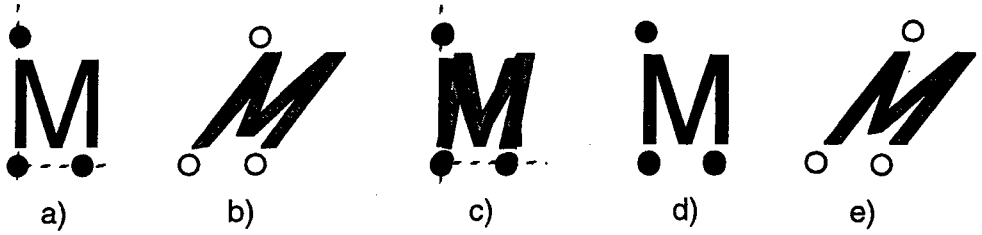

Fig. 1. A simplified two-dimensional example of the registration process is illustrated. (a, b) Two "multimodal" images in which the user has poorly chosen approximate homologous points. (c) Geometric registration that maps the corresponding markers onto each other after the user's initialization, but before automatic optimization begins. After initialization, although the markers are perfectly aligned, the images are still misregistered. (d) Resulting final registration obtained by the optimizer's driving the locations of the homologous points in (b) to minimize the cost function, −I, *i.e.*, maximizing I. (e) Note that the position of the upper marker in (b) has been moved by the optimization process to a new position. (Reproduced with permission from Oxford University Press from Medical Image Analysis 1997;3:195–206.)

The following paragraphs describe the use of a semiautomatic registration technique that appears to be capable of registering ultrasound data sets based on the preliminary information presented herein. The term "semi" qualifies the description of the otherwise totally automatic method because the initial pose between the two data sets must be set by the user. At present, the authors are unaware of any semi- or fully automatic registration algorithms that have been applied successfully to ultrasound data volumes. A recent review of registration techniques in general can be seen in Maintz and Viergever (1998).

METHODS

Volumetric ultrasound data were acquired using a 9-MHz linear array clamped to a linear slide and position encoder on a hand-held frame (Fenn et al. 1997). The transducer manually was swept across the tissue of interest in a direction normal to the linear array's scanning plane. Accuracy of beam position measurement relative to the scan frame was 0.1 mm in the focal plane of the transducer. Data volumes on a uniform Cartesian grid were created by trilinear interpolation between acquired images from known positions.

Pairs of such ultrasonic volumes were registered using a method that requires an initial rough guess of the orientation between the two data sets. As can be seen later in the Results section for the random void phantom, the initial orientation may be far from accurate, but will still within the capture range of the algorithm and result in an accurate registration. The initial, approximate orientation is computed by having the user position a minimum of three corresponding point pairs in each data volume. One of the data sets is chosen by the user as the reference data set, and the other data set, which will be geometrically transformed onto the reference, is referred to as the homologous set. Points in both sets are deposited by clicking the computer's mouse as the cursor is positioned manually over similar-looking, three features. Then, under automatic control of the optimizer, the first three points in just the homologous data set are moved to recompute different geometric orientations of the homologous data set with respect to the reference data set. The points in the homologous data set are referred to as control points, because the geometric orientation between the two data sets is changed to satisfy the homology defined by the control points. The automatic optimizer repeatedly perturbs the loci of the control points in the homologous data set, such that the resulting mutual information, as computed for all voxels in the reference volume and all corresponding voxels in the homologous volume, is maximized to yield the final computed registration model between the two data sets (Collignon et al. 1995; Meyer et al. 1997; Studholme et al. 1997; Viola and Wells 1995; Wells et al. 1996). Figures 1, 2, and 3 help visualize the interplay among the control points, the computation of mutual information, and the recursive optimizer algorithm.

The entropy of a data set is defined as its average information content, whereas joint entropy is the average information of two ordered data sets. The joint entropy H(a,b) of two data sets, a and b, is related to mutual information of both, I(a,b), by the following classic relationship:

$$H(a,b) = H(a) + H(b) - I(a,b) \qquad (1)$$

where H(a) and H(b) are the individual entropies of data sets a and b, respectively (Papoulis 1984). As can be seen in the classic relationship, mutual information I(a,b) is the amount by which the sum of the individual data set entropies must be reduced to account for correlations that

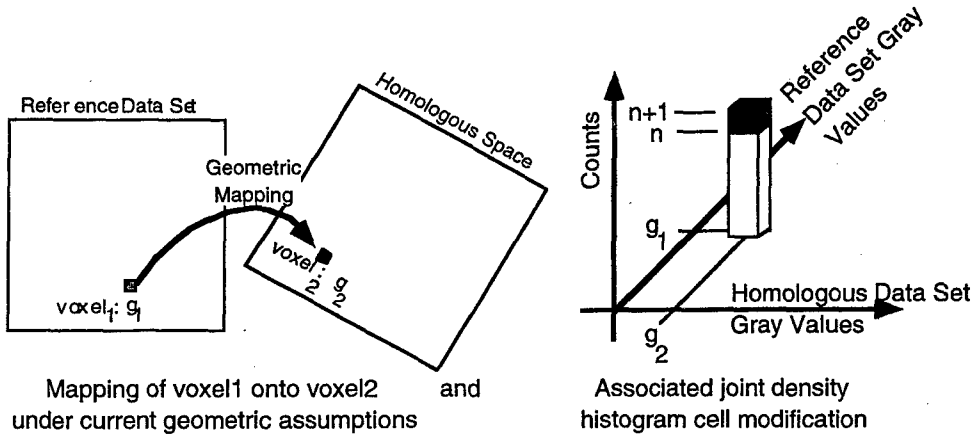

Fig. 2. Two-dimensional joint histogram constructed by raster scanning through all voxels in the reference image set and incrementing bin counts corresponding to the gray-scale values from geometrically mapped voxel pairs under an assumed geometric transformation, which changes with each iteration of the optimizer. (Reproduced with permission from Oxford University Press from Medical Image Analysis 1997;3:195–206.)

exist between the two individual data sets (H and I are non-negative). The previous expression defining mutual information in relation to entropies reduces to the following equation for mutual information in terms of the more fundamental probability density functions for data sets a and b:

$$I(a,b) = \int\int da\, db\, p(a,b) \log(p(a,b)/p(a)p(b)). \quad (2)$$

The initial geometric transform model optimized via moving the initial three control points is the simple, rotate–translate (six degrees of freedom) transform. In a subsequent optimization, the parameters for a full affine (linear, 12 degrees of freedom) transform are estimated via four control points (the three previous plus one new control point positioned automatically into the homologous data set using the previously optimized rotate–translate transform). Finally, if desired, repeated thin plate spline (TPS) warpings are computed using five or more control points as necessary, where the previous full affine optimum transform is used to instantiate the additional control points. In this manner, the mutual information is optimized at each stage of increasing geometric model complexity, while requiring the user only roughly to estimate approximate geometric homology for the three initial points. The additional control points beyond the first three, which eventually are mapped into the homologous data set, initially are placed in the reference

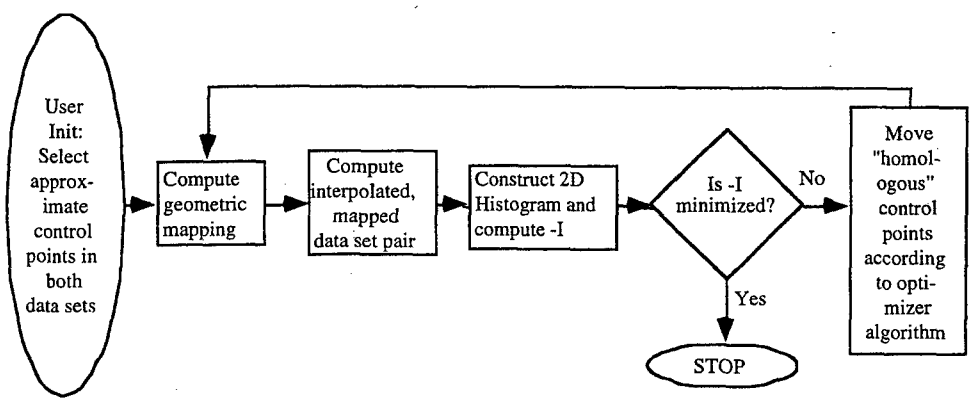

Fig. 3. Functional flow chart of the automatic registration algorithm for one optimization cycle. The process is repeated using the previously computed optimized control point positions as the new starting vector, until the incremental change in mutual information between cycles falls below a user set threshold, typically 0.0002 bits. (Reproduced with permission from Oxford University Press from Medical Image Analysis 1997;3:195–206.)

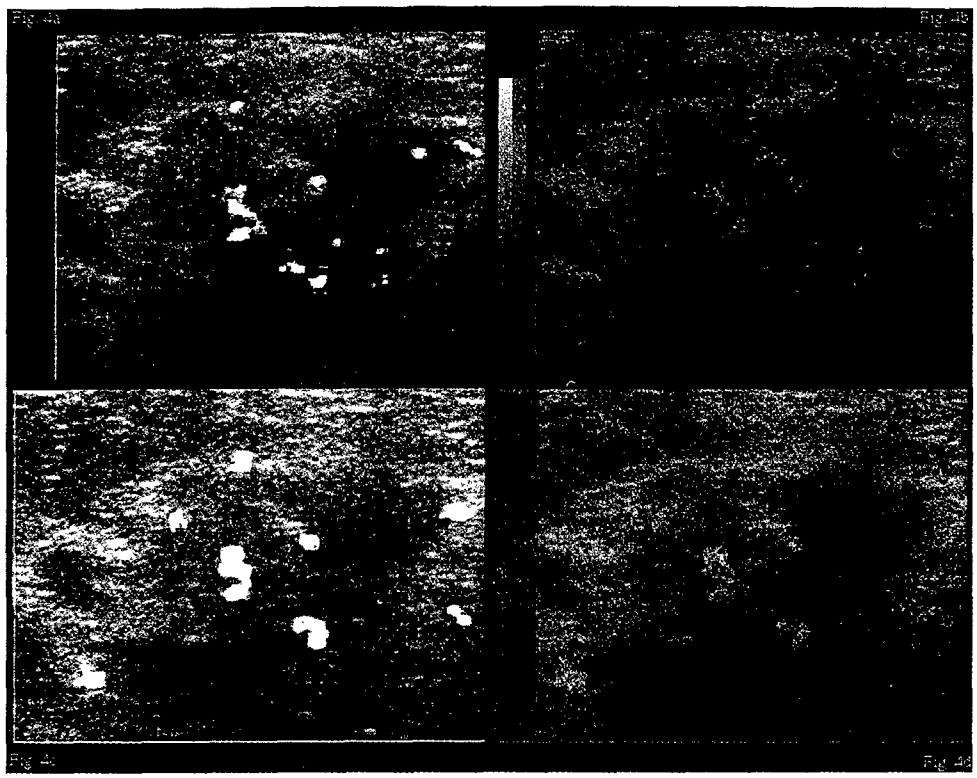

Fig. 4. (a) Image from the red channel of a color flow volume breast examination. (b) Pseudocolored image of (a). Lowest echogenicities are represented by dark blue, intermediate echogenicities by green, and highest echogenicities by bright red hues. Color mapping relationship is explicitly demonstrated in the attached gray-scale and color bars. (c) Power mode data corresponds to same loci as the color flow slice of a following registration. (d) Composite image constructed using "screen door" transparency, where adjacent pixels alternate between the color and gray-scale sources of (b) and (c).

data set by the user, without identification of corresponding positions in the homologous data set.

Uniformly sampled data volume sizes are approximately 400 × 350 × 55–100 voxels depending on the manual acquisition; voxel volumes are typically 80 × 80 × 200 μm^3. The registrations computed herein use decimated reference data sets to speed computation. During the initial use of the rotate-translate model, only every fourth voxel in the three major coordinate directions is used in the reference data sets. Each optimization cycle stops when the controller requests control point movements of less than some user chosen criterion, selected here as 0.1 mm, in each coordinate direction. The optimizer is the standard Nelder simplex algorithm, often referred to as "amoeba" (Press et al. 1988). Optimization cycles are repeated until the mutual information increment in the last cycle is less than or equal to another user chosen criterion, selected here and for almost all other modality pairings as 0.0002. After computing the optimal forward transform, which maps the homologous data set onto the reference, the high-resolution mapping of every voxel of the reference data set onto the homologous is computed once, using the inverse transform.

RESULTS

The first registered volumetric data set pair shown in Fig. 4 consists of color flow and power mode Doppler data sets acquired serially during the same patient examination visit. A three-dimensional, nine control point (27 degrees of freedom) thin plate spline warping was computed in 31 min of CPU time on a 200-MHz DEC Alpha workstation, model 3000/500x, using a total of 1552 iterations (where each iteration consists of calculating the geometric transformation, reconstruction of the mapped homologous gray-scale volume, joint histogram, and resulting mutual information) . The red channel of each data set pair was used to compute the geometric mapping. Although radiologists commonly avoid the use of pseudocolored images, such composite images assist in visualizing the results of registration. Display of the registered data sets as shown in Fig. 4d enhances visual differentiation of the individual image sources and facilitates the visual assessment of registration accuracy at all locations in a single image.

Figure 5 allows the reader to assess the accuracy of the volumetric registration over a large volume of sup-

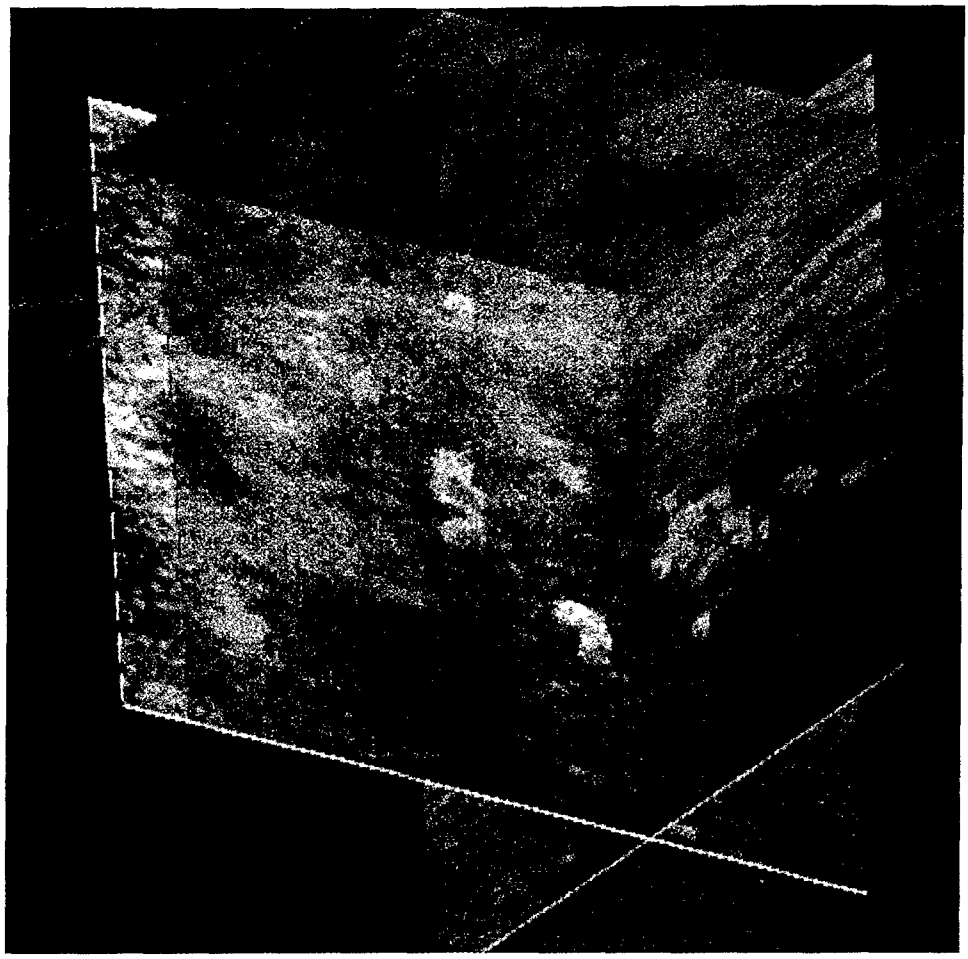

Fig. 5. View of the registered color flow and power mode volumes visualized on three orthogonal, intersecting cut planes using a color composite rendering method that approximates the screen door transparency shown in Fig. 4d. The observer's viewpoint presented here is one of looking back at the transducer from a distal position deep within the breast (top of the image is still patient's anterior). The cut plane whose orientation is nearly perpendicular to the viewer is the same image as that shown in Fig. 4d, where the underlying gray-scale image represents one of the (high resolution) acquisition planes of the color flow data volume. The intersecting cut plane across the top of the volume renders the registration at a constant, shallow depth below the transducer (C-mode), and the remaining cut plane right of center renders a slice of the registered volume below the line traversed by a single transducer element during the manual sweep of the transducer. The color bars that define the pseudocolor conversion for the reference scan is visible on the reader's left.

port. The color composite display computes the relative color contribution to each voxel, based on a linear combination of the intensities of the voxels of the two registered input volumes. The orthogonal cut plane method of display was chosen because of its clarity, intuition, freedom from confusing intervening structures, and the ability simultaneously to display spatially diverse, three-dimensional locations.

Figure 6a demonstrates the effects of the computed geometric warping, by applying the same warping to a rectilinear grid occupying the power mode volume. Figures 6b–6d show views of the deformation from the right, front, and top, respectively. Note that the major component of the geometric transform is a simple affine transformation, as best seen in Fig. 6d, where the volume has been sheered to the left as a function of distance away from the observer, *i.e.*, transducer position. Upon closer inspection, a nonlinear warp can be observed in the front central section of the volume, the same region occupied by the lesion, indicating that, during the second scan, the lesion moved differently than the surrounding tissue.

The second pair of registered volumetric data sets presented here consists of two power mode Doppler data sets acquired on the same patient and separated by 45 d during chemotherapy for locally advanced infiltrating ductal carcinoma. In contrast to the previous case, the registration model's complexity was capped at the level of the full affine (linear, 12 degrees of freedom) trans-

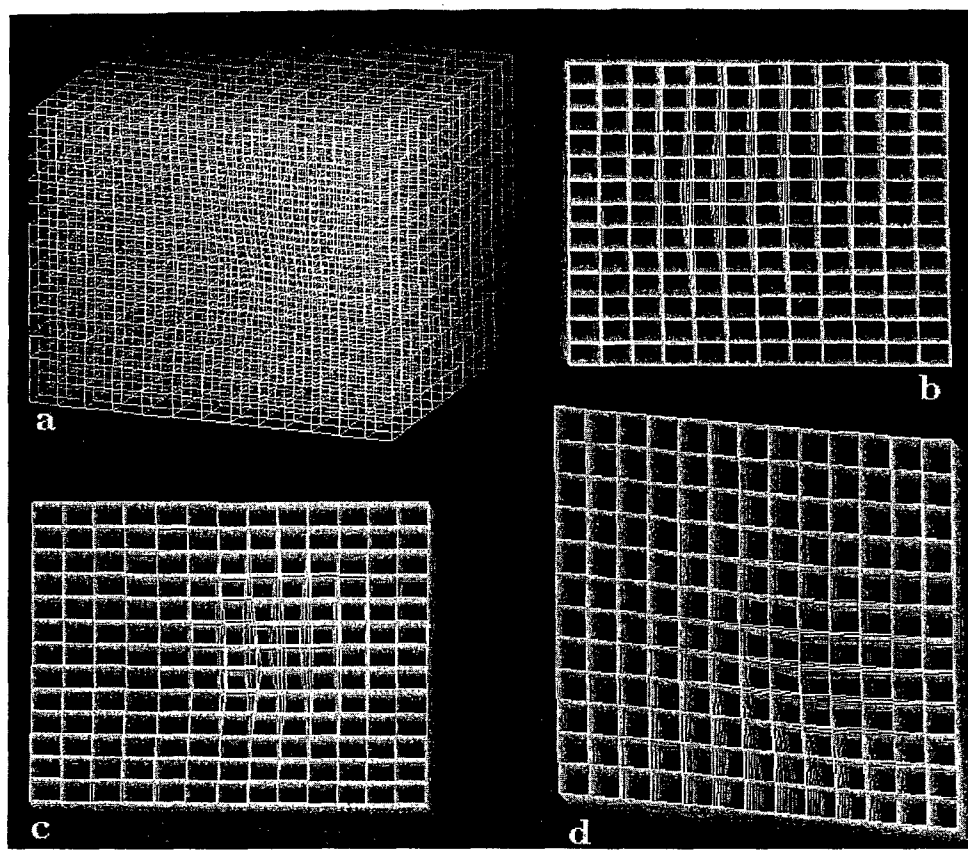

Fig. 6. (a) Computed geometric warp of the power mode volume is demonstrated by applying the same warp to a rectilinear grid occupying the initially undistorted power mode volume. (b, c, d) Views of the warped deformation from the right, front, and top of the scanned volume, respectively.

form due to the resulting excellent overall accuracy, as determined visually. Computing this transform from the initial rough estimate required 909 total iterations over the period of 11.3 min. As in the previous case, the red channel of each pair was used for computing the geometric mapping and display of results. Figure 7a shows three orthogonal cut planes through the registered data set volumes, as visualized from a position above the transducer looking deeper into the scanned volume. Note the shear (most appreciated on the plane nearly perpendicular to the viewer) required to register the data sets. Figure 7b is a single slice of the more recent data set, and Fig. 7c shows the data from the earlier scan corresponding to the geometry of the slice shown in Fig. 7b obtained after volumetric registration. Because the two cases were performed with nearly equivalent depth-gain compensation, equalization of the echogenicities of both scans was trivially achieved using linear gray-scale contrast adjustment. Figure 7d demonstrates the signed difference between the two scans, where the yellow hue represents differences of positive sign, the blue hue represents differences of negative sign, and the intensity for each hue is proportional to the magnitude of the difference. Although some bright, horizontal, linear, coherent structures clearly are represented in the difference image, a lower contrast echogenic structure also is visualized (arrow), *i.e.*, present in the earlier data set but missing in the later volume.

In addition to the two breast data sets presented herein, we include results from scanning a commercially available, random void phantom in two different orientations. The phantom is made by Computerized Imaging Reference Systems, Inc. (Norfolk, VA, USA) and consists of two slabs of randomly placed spherical voids surrounded by a random scattering medium having an attenuation of 0.5 dB cm^{-1} MHz^{-1}. One slab consists of 5-mm diameter voids, and the other consists of 3-mm diameter voids. The two slabs are separated by a voidless slab consisting of the same random scattering medium used to surround the voids in the other slabs. Scattering from the voids averages 14 dB down from the surrounding random scattering medium. Nylon fibers run parallel to the slabs at depth ranges of 2 and 6 cm.

One volumetric scan acquisition was made by manually translating the transducer parallel to the sides of the phantom and, thus, parallel to the wall of spherical voids

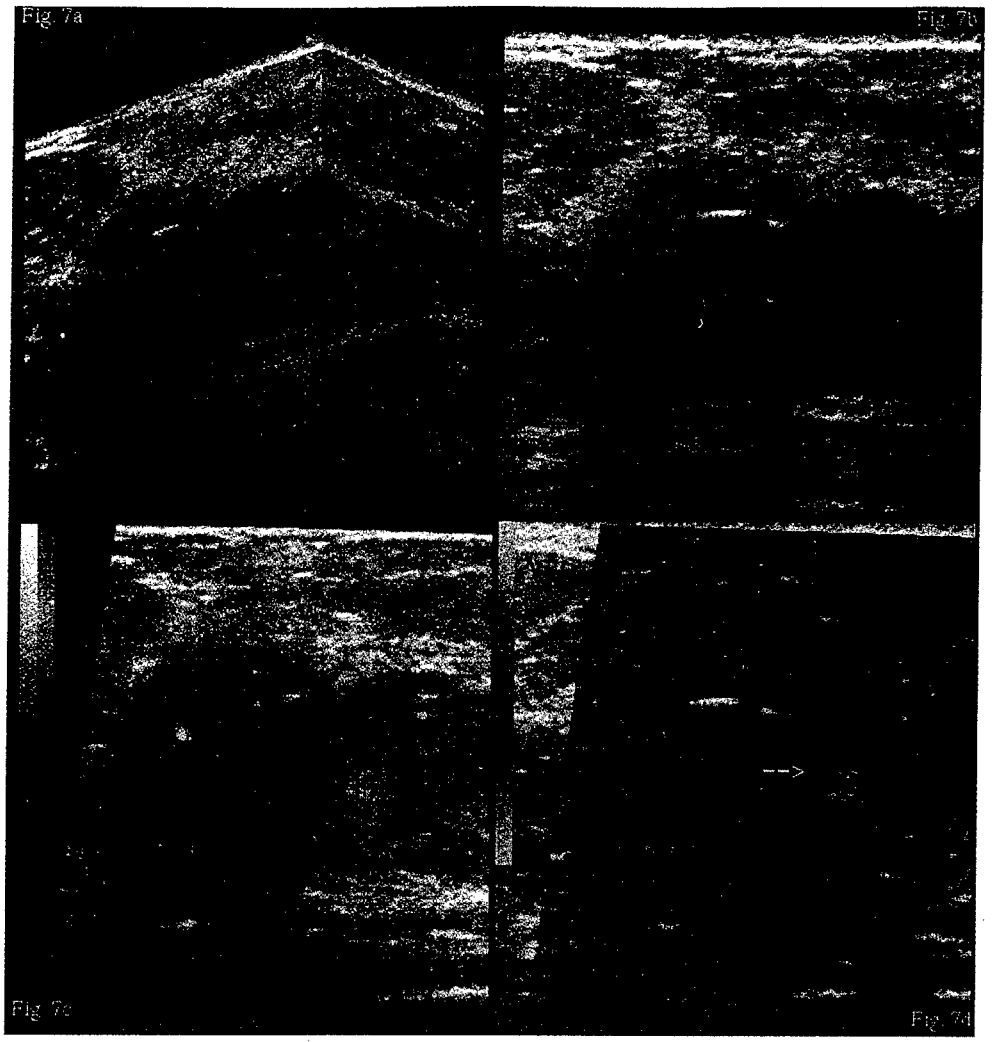

Fig. 7. (a) Orthogonal cut planes through the registered power mode data set volumes from serial examinations visualized from a position above the transducer looking deeper into the scanned volume. The pseudocolored volume was acquired 45 d earlier than the gray-scale volume. (b) Single slice of the more recently acquired data set. (c) Data from the earlier scan corresponding to the geometry of slice (b) after volumetric registration has been implemented; (c) also is visible as the pseudocolored component in (a). (d) Signed difference between (b) and (c), where the two hues represent differences of opposite sign, whereas intensity of each hue is proportional to the magnitude of the difference. In the color bar, a difference of +127 is represented by bright yellow, a difference of zero is black (center of bar), and a difference of −128 is bright blue.

with the transducer held approximately perpendicular to the phantom's surface. The second scan was taken by reorienting the translation path 45° to the initial position using a draftsman's triangle. Thus, in the second scan, the transducer remained approximately perpendicular to the phantom's surface, whereas the path of the translated transducer crossed the wall of voids diagonally. The initial poor placement of the starting markers was intentional, to demonstrate to the reader how severe misregistration of features appears (Fig. 8a) using the display technique shown in Figs. 4 and 5, where blended pseudocolor and gray-scale scans demonstrate the large capture range of the automatic registration algorithm. Note that the bright gray-scale line in the homologous data volume represents the same nylon fiber in the phantom as the red pseudocolor line in the reference volume. The angular misregistration is readily apparent between the two data sets. Note that the voids appear to be filled with higher level scattering, due to the misregistration of the two data volumes.

The results of the final registration are presented in Fig. 8b. The linear nylon fiber in the homologous data set has been superimposed with the red pseudocolored reference data volume fiber. The linear fiber superimposi-

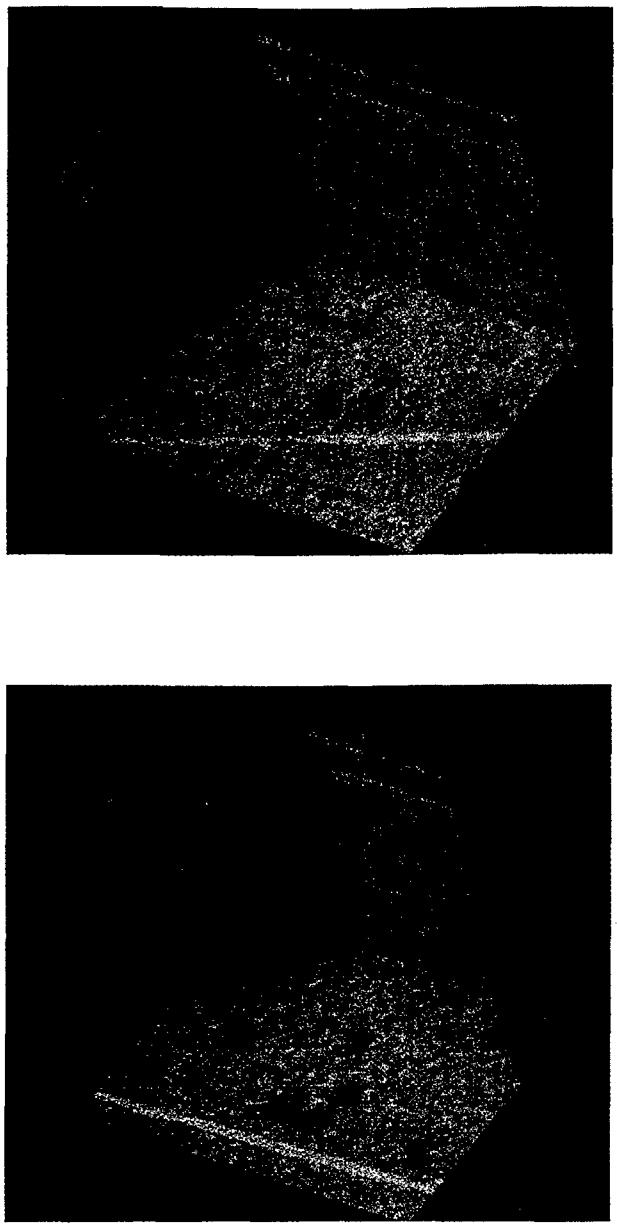

Fig. 8. (a) Initial pose of the 45° diagonal scan of void phantom in gray scale with 0° reference scan in pseudocolor is displayed on three orthogonal planes through data volume. Note the filled appearance of the voids as well as the lack of alignment of the linear nylon fiber in this initially misregistered pose. The reference data set is shown in pseudocolor, with the same color conversion relationship used previously. (b) The same display of reference data set shown in (a) after automatic registration of the volumetric 45° scan with the reference 0° scan. Note that, after registration, the voids have more contrast, because they are not inappropriately filled with misregistered scatterers, and the nylon fiber in the 45° scan is nearly collinear with its position in the reference volume.

tion is nearly perfect to the viewer's right, whereas a slight misregistration can be observed to the viewer's left, as a partial separation of both bright gray and red. This slightly visible error correlates well with the computed angles of $-1.0°$, $-45.4°$, and $-0.5°$ for θ_x, θ_y, and θ_z, respectively, of the rotate-translate approximation to the computed full affine geometric transformation matrix; we would expect 0°, 45.0°, and 0° for a perfect result. The mutual information of the initial pose was 0.064 bits, which was optimized to 0.229 bits in 17 cycles of 1025 total iterations under the rotate-translate geometry model, and finished at 0.383 bits after 16 additional cycles consisting of a total of 1869 iterations, using the full affine geometry model. It is worth noting that simple low-pass filtering of the two data sets significantly speeds the convergence of the registration algorithm, by reducing the grand total of all iterations to 1200, which require total compute times <9 min on a 433-MHz DEC Personal Alpha workstation.

DISCUSSION

Volumetric registration was computed in all cases using a full affine transform as the first endpoint. If the resultant registration was judged by visual inspection to be flawed in local regions, a higher degree of freedom geometry model, *i.e.*, warping, was computed. Thus, the thin plate spline warping of the data set associated with Figs. 1 and 2 was implemented using both a number, *i.e.*, nine, and placement of control points that resulted in a better global solution. The improved accuracy of the registration resulting from warping was determined both visually and quantitatively by the increase in the final, optimized mutual information, *i.e.*, a significant 27% increase in I was observed from 0.805 for the full affine solution to 0.827 for the nine point TPS solution. The presence of a small mass with different elastic modulus than the surrounding tissue is suggested by observing the nonlinear warping depicted in Fig. 3, because the computed tissue deformation indicates a local rotation. This rotation could have been in response to the overall deformation caused by the pressure of the transducer on the skin in the process of scanning.

For the case of the void phantom, although the error associated with θ_y was $<0.5°$ from the expected value of 45°, the error of 1° in θ_x can be explained by our inability accurately to mount the transducer perpendicular to the plane of the manual translation baffle. Any deviation away from 90° in the angle subtended by the rotation of the autoscanning plane of the transducer into that of the manual scanning baffle, *i.e.*, θ_x, will require compensation by both θ_x and θ_z, depending on the rotation imposed on θ_y. Additional registration accuracies using phantom data from computed tomography, magnetic resonance imaging, and positron emission tomography, are available in Meyer et al. (1997). Although no preprocessing was necessary for the phantom data to obtain accurate registrations, a >50% decrease in registration

time was obtained by low-pass filtering the input data sets before registration. Such behavior should be expected, because low-pass filtering increases the long range correlations in the data sets and smoothes the resulting cost function, such that convergence can be obtained without entrapment by many local maxima.

Because bright, linear structures in the scanned volume occur when the transmitted beam is perpendicular to an echogenic surface, a lack of overlapping alignment of such linear structures is expected, due to the variation in transducer angles used to acquire the different volumes. Conversely, good registration of less intense, incoherent backscattering structures is expected and should be used as an independent visual evaluation tool for qualitatively judging the accuracy of the registration.

The robust behavior of the previously developed mutual information for automatic multimodality image fusion (MIAMI Fuse) registration algorithm (Meyer et al. 1997) for these pairs of same-modality, *i.e.*, ultrasound, data sets was a pleasant surprise. No preprocessing of the data sets, such as speckle reduction, was necessary, and the resulting registrations were of excellent quality and were obtained in relatively short times. Even the demanding task of warping using nine control points, *i.e.*, 27 degrees of freedom, yielded accurate, repeatable registrations, a feat even the authors initially considered as unlikely.

Acknowledgements—This work was supported in part by DHHS PHS NIH grants 2R01CA59412-04, 1R01CA55076, and U.S. Army Contract No. DAMD17-96-C-6061. Assistance in acquiring the scanning data provided by Theresa Tuthill and Stanley Samuel is gratefully acknowledged as well.

REFERENCES

Collignon A, Maes F, Delaere D, et al. Automated multimodality image registration using information theory. In: Viergever MA, ed. Computational imaging and vision, vol. 3. Ile de Berder: Kluwer Academic Publishers, 1995:263–274.

Fenn R, Fowlkes J, Moskalik A, et al. A hand-controlled, 3-D ultrasound guide and measurement system. In: Lees S, ed. Acoustical imaging, vol. 22. New York: Plenum Press, 1997;237–242.

Maintz J, Viergever M. A survey of medical image registration. Med Image Anal 1998;2:1–36.

Meyer CR, Boes JL, Kim B, et al. Demonstration of accuracy and clinical versatility of mutual information for automatic multimodality image fusion using affine and thin plate spline warped geometric deformations. Med Image Anal 1997;3:195–206.

Papoulis A. Probability, random variables, and stochastic processes. New York: McGraw-Hill, Inc., 1984.

Press WH, Flannery BP, Teukolsky SA, Vetterling WT. Numerical recipes in C: The art of scientific computing. Cambridge: Cambridge University Press, 1988.

Studholme C, Hill DLG, Hawkes DJ. Automated 3D registration of MR and PET brain images of the head by multiresolution optimization of voxel similarity measures. Med Phys 1997;24:25–35.

Viola P, Wells WM. Alignment by maximization of mutual information. 5th Int'l. Conf. on Computer Vision, vol. 95CH35744, IEEE, MIT, 1995:16–23.

Wells W, Viola P, Atsumi H, Hakajima S, Kikinis R. Multimodal volume registration by maximization of mutual information. Med Image Anal 1996;1:35–51.

Jonathan M. Rubin, MD, PhD • Ronald O. Bude, MD • J. Brian Fowlkes, PhD
R. Steven Spratt, PhD • Paul L. Carson, PhD • Ronald S. Adler, PhD, MD

Normalizing Fractional Moving Blood Volume Estimates with Power Doppler US: Defining a Stable Intravascular Point with the Cumulative Power Distribution Function[1]

PURPOSE: To normalize the power Doppler ultrasound (US) signal to the expected signal from 100% blood in the calculation of a fractional moving blood volume estimate.

MATERIALS AND METHODS: To locate the signal from flowing blood with a consistent backscatter coefficient, the authors estimated the knee of the cumulative Doppler power distribution function. They used a flow-tube phantom to test the use of this knee to locate a radial position that would fall into a region of high shear stress and minimal rouleaux formation. They also studied how well the method normalized fractional moving blood volume estimates of the right renal cortex in a volunteer when simulating different body habitus and in a group of six healthy volunteers to estimate variability.

RESULTS: Over five flow velocities and over undersaturated to severely oversaturated receiver gains, the calculated flow-tube area was a mean 89% ± 7 (± standard deviation) of a standard. In humans, the technique normalized the fractional moving blood volume estimates over an 8-dB receiver gain variation; the mean ± standard deviation of fractional moving blood volume estimates for the six volunteers was 37.6% ± 3.6.

CONCLUSION: Vascularity estimates with power Doppler US are feasible with a normalization scheme based on the cumulative Doppler power distribution function.

ALTHOUGH of substantial interest, ultrasound (US) Doppler vascularity measurements have been used on a variable basis in several organ systems (1–4). They have generally, but not exclusively, been based on the counting of color pixels in standard color Doppler US scans and have been used clinically most frequently to assess tumor vascularity in the breast and prostate (5–13). The choice of these organs is informative, because it reveals one of the greatest shortcomings of US vascularity assessments: their depth dependence. In all of the examples in which quantitation has been used, either the target is superficial or the transducer has been positioned very closely to the area of interest. This is because vascularity is assessed by counting the number of color pixels in a given region, and anything that alters color pixel count will affect a vascularity assessment. Unfortunately, the density of blood vessels, the quantity one wishes to measure, is only one of the factors that influences the color pixel count. Major contributors to this measurement are attenuation, aperture size, or any other property that alters the strength of the backscattered echoes. Given identical tissue samples, their vascularity at US will change the deeper in the body they are located. The closer a tissue is to the transducer, the more vascular it will appear. For example, flow in ovaries may be very hard to detect transabdominally and yet very easily seen transvaginally. The vascularity detection improvement is due primarily to a reduced attenuation path in the latter, which yields some combination of higher signal and which allows the use of higher frequency transducers (14). Because of this very definite attenuation effect, vascularity measurements with US are tricky to make and interpret.

A potential solution to this problem does exist. If one can identify an object of known vascularity or blood volume, one can use the Doppler power in that object to normalize the values in the surrounding tissue (15–17). If the tissues of interest are near enough to the known object, the fraction of the Doppler power in the surrounding tissue relative to the standard can be used as a vascularity estimate. This process effectively compensates for any attenuation or transducer beam profile effects. Because blood vessels contain 100% blood, objects of known vascularity exist throughout the body and could be used to normalize vascularity measurements. We will call such measurements fractional moving blood volume estimates (17).

There is one problem, however, that has to be overcome before this method can be applied. The problem arises because the backscattered signal from blood is variable owing mostly to the degree of rouleaux formation (18–22). The reason for this is that rouleaux

Index terms: Blood, flow dynamics, 9*.12983[2] • Blood vessels, US, 9*.12983 • Ultrasound (US), power Doppler studies, 9*.12983 • Ultrasound (US), technology, 9*.12983

Radiology 1997; 205:757–765

[1] From the Department of Radiology, University of Michigan Hospitals, 1500 E Medical Center Dr, Ann Arbor, MI 48109 (J.M.R., R.O.B., J.B.F., P.L.C., R.S.A.); and Diasonics, Santa Clara, Calif (R.S.S.).
Received May 19, 1997; revision requested July 8; revision received August 12; accepted August 13. Supported in part by a grant from Diasonics, U.S. Public Health Service grant RO1CA55076 from the National Cancer Institute, and the U.S. Army Medical Research Materiel Command contract DAMD17-94-J-4144. **Address reprint requests to** J.M.R.

[2] 9* indicates vascular system, location unspecified.

© RSNA, 1997

effectively increases the size of the scattering units in blood. Clumps of red blood cells will backscatter more ultrasound energy than will individual cells, which makes areas of vessels with more rouleaux have stronger Doppler signals than those with less. This effect is most pronounced when comparing the Doppler power in the center of large blood vessels with the Doppler power in the edges. There is typically much more signal amplitude in the center of the vessels owing to increased rouleaux formation (23). The higher shear rate and shear stress near the vessel wall apply more force to separate rouleaux clumps of red cells. The magnitude of the shear rate, which is directly proportional to the shear stress, depends on the velocity profile (24). For a parabolic flow profile, the shear rate and, thus, the shear stress are directly proportional to the radius (20). Hence, for a 1-cm-diameter vessel, the shear rate at the wall will be 10 times that 0.5 mm from the center of the vessel. For near plug flow, the shear rate at the wall can be arbitrarily high. Because of this variation in the appearance of blood flow, one cannot just identify a blood vessel, obtain a normalization value, and calculate a fractional moving blood volume estimate at a given depth. A more sophisticated technique is required.

It is known that smaller vessels have greater shear than do larger vessels for a given mean velocity (25). Because we would like to normalize vascularity by the power that corresponds to 100% blood in tissue, where the blood vessels are small, a value outside the region of high rouleaux would be appropriate. Because of a condition of no slippage at the wall or boundary, there is no flow immediately adjacent to the wall of a vessel. Hence, the "correct" normalizing value lies somewhere between the high value in the center of a vessel and the zero value at the wall.

To perform a fractional moving blood volume estimate, we first calculate a cumulative Doppler power distribution function over the region of interest (see below). We then identify the knee of the cumulative Doppler power distribution function. This knee is used in an algorithm to define a boundary point within highly vascular areas in which we will search for a normalization value. The knee of this distribution is a reasonable choice for segmenting a population into two groups, which is similar to what is done in segmenting populations in receiver operating characteristic analysis (26,27). Once the normalization value is measured, we use that value to determine the fractional moving blood volume estimate in tissue.

We performed this study to normalize the power Doppler US signal to the expected signal from 100% blood in the calculation of a fractional moving blood volume estimate. We used this technique to compensate for depth, attenuation, receiver gain, and machine variability. Ultimately, we believe that the results strongly suggest that this technique could be generally used to assess vascularity in tissues.

MATERIALS AND METHODS

Definition

The cumulative Doppler power distribution function is the integral of the histogram of the Doppler powers within a region of interest (28). It is defined in a discrete sense as

$$N(p) = \sum_{i=0}^{i=p} n(i),$$

where $n(i)$ is the number of pixels with the ith power value and $N(p)$ is the total number of pixels with power values less than or equal to p; that is, $i \leq p$. Because this is an integral of the histogram, the cumulative Doppler power distribution function has some nice random noise–suppressing properties that make it an interesting candidate for finding a normalization value. In a cumulative distribution, fluctuations are referenced to the entire display range, whereas with a standard histogram, being the derivative of the cumulative distribution, fluctuations are seen relative to locally changing values for which any variation is a much larger percentage.

Phantom Studies

We designed a flow-tube experiment to evaluate the boundary-detection properties of the cumulative Doppler power distribution function. The tube consisted of an elongated balloon of 5.5 mm in diameter in a fluid bath. The balloon was draped across a sound-absorbing pad to suppress reverberations. Flow in the balloon was generated by using a pulsatile pump (Harvard Apparatus, South Natick, Mass) with a 70% duty cycle and 50 strokes per minute. Before reaching the balloon, the fluid passed through a long segment of compliant gum rubber tubing that made the flow nonpulsatile. Degassed water that contained corn starch particles (0.5 g per liter of water) as scatterers was run through the balloon. To simulate real flow-containing tissue, we put cross-linked dextran beads (Sephadex particles; Sigma Chemical, St Louis, Mo; 20–80 μm diameter at concentrations of 0.0373–0.2372 g/L, depending on the background Doppler power level) into the bath outside the balloon. By stirring the bath, we could introduce a Doppler shift in the medium and generate Doppler power in the background similar to the effect of tissue that contains flowing blood. The quantities of cross-linked dextran beads and corn starch were selected so that the tube always visually had more power than the water bath at each flow setting, thus simulating a vessel surrounded by flowing blood within perfused tissue. We made three measurements at each flow rate investigated (Table 1). These three measurements were made with low gain to simulate a weak signal deep in tissue, optimal gain (see below) to simulate tissue that was superficial enough or vascular enough to supply sufficient signal, and high gain in which the signal in the tube was saturated to simulate bad technique or the presence of contrast agents.

Table 1
Raw Data from the 15 Flow Experiments

Run	Mean Flow Velocity (cm/sec)	Pulse Repetition Frequency (Hz)	Receiver Gain Setting (dB)	Fractional Area*
1	17	1,250	79	0.849
2	17	1,250	86	0.972
3	17	1,250	92	0.875
4	35	2,250	80	0.941
5	35	2,250	85	0.893
6	35	2,250	90	1.03
7	51	2,750	84	0.894
8	51	2,750	89	0.889
9	51	2,750	94	0.93
10	60	3,500	84	0.704
11	60	3,500	89	0.917
12	60	3,500	94	0.885
13	79	4,500	84	0.903
14	79	4,500	89	0.897
15	79	4,500	94	0.886

* Fractional area is the area of the tube calculated by using the knee of the cumulative distribution over the image divided by the area subjectively determined by tracing the outline of the tube.

To define the gain settings for the flow-tube measurements in testing the cumulative Doppler power distribution function algorithm, we had to define what low gain, optimal gain, and high gain would be. We used VST US scanners (Diasonics, Santa Clara, Calif) to make the measurements. We used a 10-MHz linear-array transducer (Diasonics) with a 6.0-MHz Doppler frequency. The angle of the scanhead to the tube was 22° to generate a Doppler angle. We measured signal strength and saturation level by assigning a green-tag value to Doppler power measurements. Each green-tag step defined by the manufacturer corresponded to 0.4 dB. We set the saturation level such that the highest green-tagged pixels in the flow tube were within three click steps of the highest decibel level, 24 dB. This corresponded to having the highest pixel values in the flow tube be no more than 23.2 dB on the 24-dB scale, which represents the

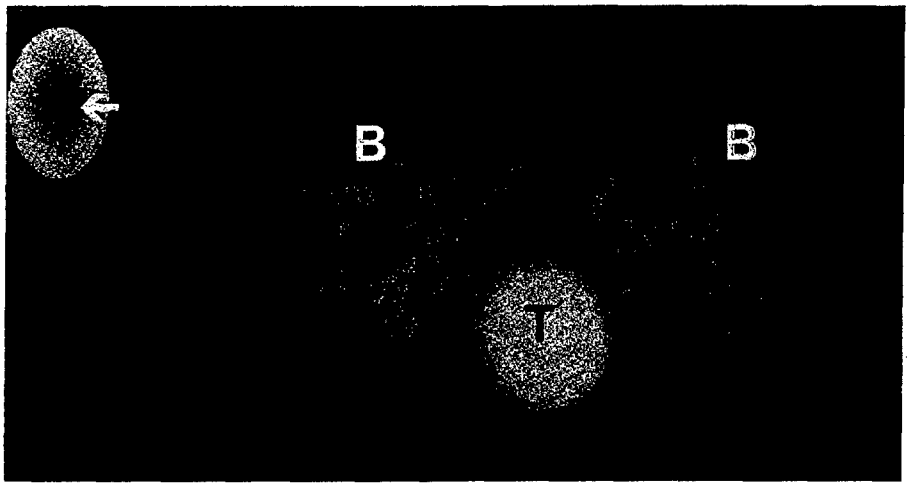

Figure 1. Cross-sectional US image of corn-starch–containing flow tube (*T*) in a water bath (*B*) that contains cross-linked dextran beads. The water bath was manually stirred to generate a Doppler signal, represented in yellow, and simulated viable, blood-perfused tissue. The tube, which represents a blood vessel, corresponds to 100% blood and, hence, has more Doppler power than the water bath, which simulates less vascular tissue. This is demonstrated as a tube brighter than the water bath in power mode. The outer margin of the blue outline of the flow tube marks the boundary of the tube, as calculated by using the automated boundary detector. The blue line is actually thicker than the true boundary threshold for purposes of display. The blue pixels equal the set of all pixels in the image, such that threshold ≤ pixel value ≤ threshold + 0.9 dB. Note that there are regions in the water bath that also either are surrounded by blue or are blue. These correspond to potential areas of 100% blood in tissue. The black area behind the tube and water bath is the top of the sound-absorbing rubber pad. Also note that there is a blue ring in the color wheel in the upper left-hand corner (arrow). The area of the wheel that is located between the blue ring and the outer edge represents the portion of the entire power dynamic range that is assigned to 100% blood in this particular trial.

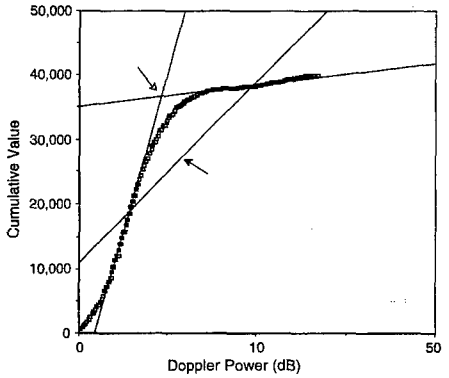

Figure 2. Cumulative distribution for one of the phantom flow experiments. The plot shows the three best-fit lines used in the two-tangent technique. The global best-fit line (solid arrow) intersects the distribution at two points. A tangent line is defined at each intersection point, and the intersection of the tangents (open arrow) defines the position of the knee. This technique clearly underestimates the position of the knee. This particular plot was for one of the undersaturated experiments, which is why it does not extend to 24 dB.

dynamic range of the power-mode signal. When the Doppler gain was set such that the pixels with the highest power in the image fell into this range, the settings were considered optimally saturated. We then set the saturation limit in a range that was clearly undersaturated (5–7 dB), below the optimally saturated setting, and finally set a range in which the Doppler power in the tube was clearly oversaturated (5–7 dB above optimal saturation). A representative image from each flow run was stored digitally to the hard disk on the scanner and transferred to an image analysis program (AVS; Advanced Visual Systems, Waltham, Mass) for analysis.

The boundary of 100% blood as seen with the ultrasound beam in the flow tube was identified by using a cumulative distribution based on the entire data set and was compared to an observer-traced perimeter of the tube, which was considered the standard of reference (Fig 1). To define the region over which the cumulative distribution was taken, an observer first traced the entire area of the stored image of the tube and the water bath, with the exclusion of the sound-absorbing rubber pad. The pad was excluded because, having no "flow," it would bias the measurement by introducing a structure that was much different from the paradigm of interest, that is, blood vessels and background tissue with flow. A cumulative distribution was calculated on the basis of the power values within this enclosed region. The knee or point of maximum curvature of the distribution was then subjectively selected on the cumulative distribution curve for each flow measurement. We used the visual estimate of the knee of the distribution for this calculation because it was deemed to be the best estimator of that point. To compensate for variability, we selected a range of about ±1 dB about the selected threshold and calculated the areas within these limits. Of course, this method of detecting the threshold would not work in practice; therefore, we developed techniques for automating the location of the knee (see below). For this part of the study, however, it was thought that our best estimate of the knee, the visual estimate, was the most appropriate to use.

An observer then traced the tube as a standard of reference for comparison with the cumulative distribution-selected boundary. The tube was traced three times at each flow setting, the area calculated with each traced perimeter, and a mean area calculated for the tube. The mean areas for the cumulative distribution–detected region and for the manually traced region were then compared.

Automated Distribution Determination

To implement a fractional blood volume measurement in vivo and to make more objective measurements, we wanted to use automation to calculate the position of the knee of the distribution. We used two techniques, each of which was initiated in the same way. A best-fit line was first plotted through the distribution by using a standard least-squares technique. For the first technique, the points of intersection of the line with the distribution were located, and tangent lines parallel to the cumulative distribution curve were drawn at the points of intersection. The intersection of these two tangent lines defined the knee of the cumulative distribution. The points of intersection were determined by taking the difference between the cumulative distribution value and the calculated estimate, which was accomplished by using the best-fit line for each successive power value. For those points at which the sign of the difference changes, there must be an intersection between the best-fit line and the distribution between that point and its neighbor, either one of which could be defined as the intersection for the purposes defined here. The tangent lines were empirically defined over 21 point regions, the intersection point ± 10 points (Fig 2). (Further details are in the Appendix.)

The second method begins as the first, with fitting of the cumulative distribution with a best-fit straight line. The distribution is then rotated about the best-fit line so that the line falls onto the abscissa. On the basis of the shape of the cumulative distribution, this function should have a negative curvature and there should therefore be a global maximum. A global maximum could then easily be identified and corresponded to the knee. To account for noise about the global maximum, a region of ±10 points around this initially identified global maximum was selected and fitted with a second-order polynomial. The power value that corresponds to the peak of this polynomial could also represent the knee of the distribution. Although not identical, this technique is similar to other methods in which second-order polynomials are used to search for maxima (29).

The tangent method and then the curve-fitting method, that is, the initial rotated peak and then the second-order polynomi-

al–fitted peak, were then each compared to the subjective standard of reference for finding the knees of the cumulative distributions for the tube-flow data by taking a mean absolute difference between the measurements.

Human Studies

The human studies were divided into two phases. The first consisted of the acquisition of multiple scans in one healthy volunteer at different gain settings to simulate different body habitus, while the second consisted of the acquisition of multiple scans in six healthy volunteers to investigate variability.

In the first phase, the right kidney of a single healthy male volunteer (age, 49 years; weight, 76 kg; height, 173 cm) was scanned on five different occasions. The studies were performed by using a 3.5-MHz curved linear scanhead with a pulse repetition frequency of 1,000, a color Doppler frequency of 2.5 MHz, and an ensemble length of 10. The receiver gain was successively increased from 102 dB to 112 dB in 2-dB steps. Over this range, the images clearly progressed from highly undersaturated to highly oversaturated. This manifested as a lack of flow detection at the 102-dB setting and as a very bright ballooned color display at the 112-dB setting. Again, this range was used to simulate scanning a deep structure without the use of contrast agents. The typical optimal setting for power Doppler, that is, when the noise floor just begins to break through the uniform color background (29), was at about 105–107 dB . During each sampling, the kidney was scanned longitudinally at each gain setting by using a region of interest defined by the machine's color box that included as much of the near-field cortex of the kidney as possible and at least half of the renal sinus. Because of the curvilinear shape of the color box implemented with this probe, some liver and perinephric fat were also included in the region of interest. The image of the cortex chosen for analysis at any given scanning setting was the one that subjectively had the most visible blood flow. The first cumulative distribution was taken over the entire color box, and the knee of the distribution was automatically calculated with both the tangent and the curve-fitting techniques described above. A green tag was assigned to all power values equal to or greater than the value identified as the knee of the distribution. The technique that helped identify a knee that resulted in assigning the greatest fraction of the color dynamic range to potentially 100% blood, that is, that resulted in green tagging of the most pixels, was then used in the next stage of the algorithm.

A second cumulative distribution was then taken over only those points selected in the first run. The knee of this second distribution was then identified by using the two techniques described above, and the value that assigned the largest fraction of the dynamic range to green was again used as the normalization value. This value became the normalization value for the fractional moving blood volume estimation, or, equivalently, the lowest Doppler power that corresponded to 100% blood. This process is demonstrated in Figure 3.

A region of cortex in which the fractional moving blood volume was to be estimated was then traced within the color box by using the machine's tracker ball. Other than the selection of the size and location of the color box itself, this was the only portion of the examination in which there was operator interaction. A fractional moving blood volume estimate was calculated from this region. The means and standard deviations of the selected initial green-tag level were plotted as a function of receiver gain to show the effect of attenuation and, potentially, body habitus on the normalization level. Further, a mean value and a standard deviation of the fractional moving blood volume estimate as a function of receiver gain were plotted over the five measurements.

The second phase comprised examinations of six healthy volunteers (one man, five women; mean age ± standard deviation, 34 years ± 6 years; age range, 27–41 years; mean weight, 78 kg ± 22; weight range, 57–116 kg; mean height, 173 cm ± 11; height range, 160–188 cm) by one examiner (J.M.R.). Each volunteer underwent scanning on 3 different days without preparation, for purposes of practicality. The volunteers were examined by using the same machines described above, with optimization of the setting for power Doppler in the usual manner, that is, the gain was increased sequentially until the noise floor just broke through the uniform background (30). Once the receiver gain was set, the same process for determining the fractional moving blood volume estimate in the single volunteer was used. The means and standard deviations for the fractional moving blood volume estimates for each of the volunteers were plotted.

RESULTS

Flow Experiment

The experimental flow runs are given in Table 1. The area of the tube detected by using the knee of the cumulative distribution was 89% ± 7 of the subjective boundary. It must be said that at the highly saturated settings, the difference between the boundary and the background scatterers in the medium was hard to see, and the knee of the distribution was often thought to be a better marker of the boundary than the standard of reference. Furthermore, it is obvious that there was blooming of the flow tube with increasing gain, which made the detected boundary move outward. This corresponded to a larger tube area for any given velocity (Table 1) and is to be expected with higher levels of saturation. This would manifest in vivo as enlargement of blood vessels with increasing gain.

We then compared the different knee-detecting techniques to see how well they identified the knee compared with the subjectively chosen location (Table 2). It is clear that the tangent method underestimates the subjectively designated position of the knee, thereby assigning more power values to 100% blood. The mean absolute difference between the two tangents and the knee was 0.91 dB. The second-order polynomial–fitting technique more closely approximated the subjectively selected knee: 0.33 dB for the peak value and 0.30 dB for the second-order polynomial–fitted peak.

Human Studies

The segmentation values of vascular structures from the less vascular background were plotted as a function of receiver gain (Fig 4). The plot shows a monotonic decline in the normalization level as a function of receiver gain. The slope is significantly different from zero (95% confidence interval: −0.996, −0.694). This result is what would be expected if the knee of the cumulative distribution were compensating for overlying attenuation and depth of the organ, that is, body habitus. The weaker the flow signal in general, the greater the portion of the dynamic range that may be assigned to 100% blood. Furthermore, despite this change in normalization level with gain, the ultimate fractional moving blood volume estimate is largely independent of receiver gain (Fig 5). This is based on taking a linear regression and determining the slope over the 8-dB highest dynamic range measurements, 104–112 dB, which is 0.00624 (95% confidence interval: −0.00067, 0.01315). Thus, zero is included in the 95% confidence limits. The addition of the lowest dynamic range measurement, 102 dB, produces a significant positive trend in the data, with a slope of 0.00798 (95% confidence interval: 0.00198, 0.01400). Finally, scans obtained in the six volunteers show the means ± standard deviations of the fractional moving blood volume estimates one might expect with this technique (Fig 6). The standard deviation for any single individual can be up to ±0.1. This corresponds to approximately a 30% variation relative to the mean value. However, the mean of the means ± the standard deviation of the means for the six volunteers' fractional moving blood volume estimates is 37.6% ± 3.6.

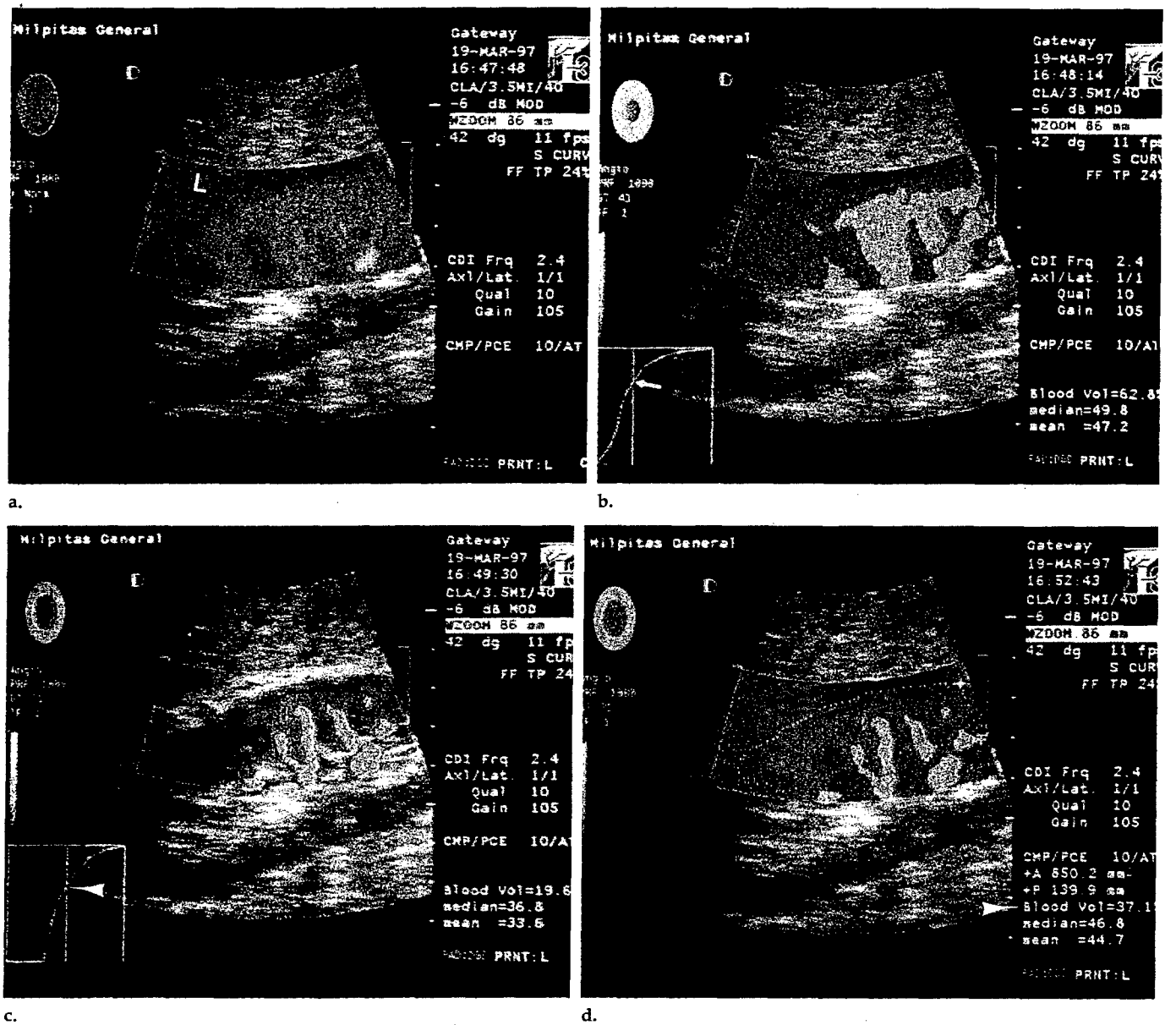

Figure 3. **(a)** Longitudinal US image of the renal cortex with near-field hilar vessels in a 49-year-old volunteer. The brighter the orange, the higher the Doppler power. Blue represents the noise floor or the lowest Doppler power displayed. Notice the large blue area in the near field, which corresponds to liver (*L*). **(b)** Same longitudinal US image as **a** after the first cumulative distribution has been taken over the entire color box in **a.** The green-tagged pixels correspond to those that could represent 100% blood on the basis of the knee of the cumulative distribution plot for the region of interest, shown in the lower left-hand corner. This curve is typical of the initial in vivo distributions in this study. The calculated position of the knee is marked with an arrow. All pixels with power values equal to or greater than the knee are green. (The highlighted pixels adjacent to the green-tagged regions are artifacts of photography and are not included in the green-tagged region.) **(c)** Same longitudinal US image as **b** after the second cumulative distribution has been taken over only those pixels labeled green in **b.** A second group of pixels, a subset of those in **b,** is labeled green and represents the final pixels determined to contain 100% blood. They were selected on the basis of the cumulative distribution plot, shown in the lower left-hand corner. The calculated position of the knee (arrowhead) corresponds to the lowest Doppler power that represents 100% blood; hence, this value is used to normalize all the tissue values in the image. Note that the second distribution demonstrates a much truer vascular geometry because it has segmented high-shear-rate from low-shear-rate blood flow within large vessels. Small vessels in tissue will not show up owing to high shear and partial volume averaging with tissue, that is, a fractional moving blood volume estimate of less than 100%. (The highlighted pixels adjacent to the green-tagged regions are artifacts of photography and are not included in the green-tagged region.) **(d)** Same longitudinal US image as **c** with the region of the cortex to be measured enclosed by the dotted line. The fractional moving blood volume estimate was calculated over that entire region and is normalized by the value selected in **c.** The fractional moving blood volume estimate in this case was 37.1% (arrowhead). (Again, the highlighted pixels adjacent to the green-tagged regions are artifacts of photography and are not included in the green-tagged region.)

DISCUSSION

The ultimate aim of many flow imaging techniques is to image vascularity or perfusion, and US is no exception. The opportunity for US to display vascularity has never been better. With contrast agents on the horizon and power Doppler, it is now possible for US to directly display the amount of moving blood in tissue, because, unlike standard mean-frequency color Doppler, the power in the Doppler signal is a reflection of the vascular blood volume of the tissue sample (20–22,31). Furthermore, power Doppler has the potential to overcome a major limitation of US vascularity measurements. By normalizing power Doppler signals in tissue against a blood vessel that is in or

near a region being evaluated, it is possible to compensate for the distance between the transducer and the region of interest, the attenuation coefficient of the overlying tissue, and the available imaging aperture, among other things (32).

The problem with this strategy is that the amplitude of the Doppler shift signal is highly dependent on rouleaux formation (18–22), which makes it impossible to merely select any point within a large vessel for normalization. However, by selecting a normalization value from the region of high shear near the vessel wall, the effects of rouleaux can presumably be minimized. This creates a situation that approximates that in small vessels in tissue where the shear is high and rouleaux is low (25).

Hence, a normalization technique must allow detection of blood vessels and identification of a position in the vessels to use for normalizing. The flow phantom study shows that the cumulative distribution can find blood vessels. In fact, it can optimally find them to within about 0.3 dB relative to the observer. In the clinical portion of the study, we typically used the tangent estimate, the poorer of the two estimating techniques, because it tended to overestimate the number of pixels that may contain 100% blood and thus increased the number of points included in the distribution. However, even by using an optimal technique such as the subjective method in the flow phantom, regions still are selected in the "hypovascular" tissue bath that were identified as flow-containing (Fig 1). Findings in the right kidneys studied were similar. This is not surprising and would be expected, at least in the first distribution, given the presence of small blood vessels inside tissue, which are analogous to the random high signals in the water bath.

We used a continuous-flow phantom, even though flow in vivo can clearly be pulsatile. We decided to do this because power Doppler is generally highly frame averaged in vivo. This has the effect of averaging out the pulsatility in the sampling. Hence, the nonpulsatile phantom would in some sense be an estimate of what happens in this first approximation. Yet, pulsatility will change the velocity distribution in a vessel, which will change the power distribution on the basis of the shear rate effects, as described above. This may require further study.

After determining the knee of the first distribution, we used a second distribution to find the normalization value in vivo. The reason for this is that, as in the flow phantom, the first distribution essentially located the wall or the neighborhood just outside of the walls of blood vessels that would be used for normalization. We needed to find a value inside the vessels to use as a standard in normalization. Thus, the second distribution over only the vessels accomplished this.

If we had not included a second distribution, we would have had the problem of distinguishing an organ of normal vascularity that is located deep in the body from a superficial organ with low vascularity. The reason for this is that the first distribution only basically locates the walls of large vessels, as shown above. It will find the walls whether an organ is deep and normal or superficial and hypovascular. Because we use an approximation of the knee as the threshold and this knee is defined relative to the parenchymal, hypovascular tissue, dividing this threshold into the tissue value will give a similar ratio in both cases. The distinction between a deep organ and a superficial one does not lie in the vessel boundaries but is in the Doppler power of the blood. For identical vessels, the more superficial, the more power the blood will have. This requires that a second distribution be taken over the vessels themselves to actually find a normalization value representative of the blood in the vessels. This value is a function of the vessel depth. We could have just identified the vessels manually or by using some other technique and performed a distribution over the vessels only. Then we would have needed only one distribution. The first distribution lets us automate the method.

There obviously have to be at least two points of negative curvature to find two knees in our process, and it makes sense that there should be at least two. The first knee separates the hypovascular parenchyma from the blood vessels, and the second knee separates the high-rouleaux central portions of blood vessels from the high-shear margins of the vessels. There will always be more points in the first distribution, because it includes the vessels and the hypovascular tissue, and, given a large enough region of interest, the first knee will dominate and will be the one selected with our method. Once the vessels have been segmented out, the method detects the second knee. If the number of points included in this second distribution is small, it may limit the ability to accurately detect a knee in some circumstances. We did not encounter this problem in this study; however, this may require a change in strategy when very small regions are being measured. This effect can be seen in Figure 3b and 3c: The knee is well defined in Figure 3b but is not as well defined, although present, in Figure 3c.

It is clear in this study that we have not determined where that precise site in the vessel is or what the true normalization value should be. However, we have done the next best thing; that is, we have identified a method that compensates for the rouleaux and at-

Table 2
Comparison of Methods for Locating the Knee Position of the Cumulative Distribution for the Flow-Tube Experiments

Run	Subjective Knee Position (dB)	Knee Position		
		Two-Tangent Model (dB)	Rotated Curve Peak (dB)	Second-Order Polynomial Fitted Peak (dB)
1	6.09	4.69	5.53	5.44
2	9.09	8.06	8.72	8.53
3	10.31	9.19	9.94	9.94
4	5.16	4.41	5.44	5.25
5	7.50	6.38	7.50	7.13
6	9.09	7.50	9.19	8.91
7	6.47	5.81	6.19	6.28
8	8.72	9.28	9.47	9.38
9	9.00	7.78	8.91	8.72
10	8.72	8.34	8.25	8.16
11	7.78	7.03	8.34	7.88
12	9.66	9.28	9.47	9.47
13	5.72	5.16	5.81	5.72
14	6.75	5.91	6.94	6.75
15	9.84	8.63	9.19	9.56

Note.—The subjective knee position is the standard of reference.

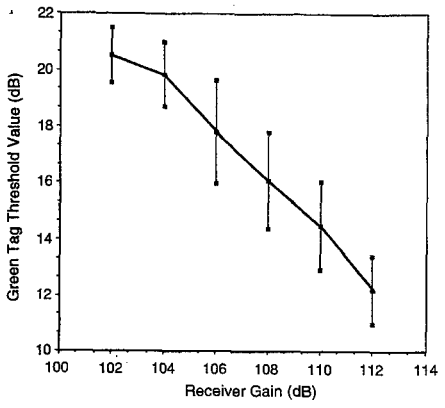

4.

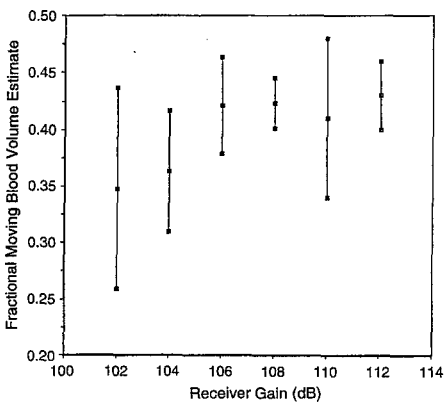

5.

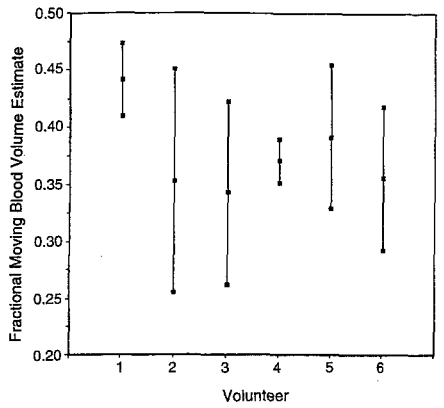

6.

Figures 4–6. **(4)** Green-tag threshold for the first cumulative distribution as a function of the receiver gain. These values represent the threshold for those pixels that may contain 100% blood. Only those pixels with higher power values than the threshold will be considered as possibly containing 100% blood in the algorithm used. The points are bounded above and below by ±1 standard deviation. Notice that the slope is negative, which means that the lower the gain, which corresponds to weak signal or large amounts of attenuation, the more dynamic the range that may be assigned to blood. **(5)** Fractional moving blood volume estimates as a function of receiver gain in the single volunteer. The points represent means ± 1 standard deviation. **(6)** Fractional moving blood volume estimates in the six volunteers. The points represent means ± 1 standard deviation.

tenuation problem in a general way. First, we have shown that the plot of the initial normalization value with receiver gain showed a continuous compensation for different amounts of signal by setting the normalization value to different fractions of the usable color dynamic range (Fig 4). This change in normalization compensated for the varying amounts of backscattered signal received at the different receiver gains, which corresponded to increasing amounts of attenuation, increasing depth, decreasing amounts of available transducer aperture, or a combination of these. The slope of the regression line through the data defined in Figure 4 shows a clear trend, with a 95% confidence interval that did not intersect zero. Thus, there was a distinct and significant decrease in the proportion of the color dynamic range that was assigned to 100% blood as the signal strengthened, or, conversely, the weaker the signal, the more of the dynamic range that was assigned to 100% blood.

This result makes sense if one considers that, if there were no detectable flow, flowing blood would look like everything else, and the entire dynamic range would look as if it contained 100% blood. The same problem would also occur in highly oversaturated images, where the gain is so high that everything, including noise, is enhanced to look like blood. This would have created a jump at the high receiver gain end of the curve if we had gone high enough. However, at that point, everything would be saturated and it would be impossible to distinguish blood vessels from less vascular surrounding tissue. This is unlikely to happen in practice because the user would immediately recognize it and turn the gain down, as occurs in blooming with contrast agents (33,34). However, the differential blooming effect of power Doppler is an advantage here, where, unlike in mean frequency color US, the display increase corresponds to the amount of signal present. Hence, vessels will still look brighter than background tissue, even with blooming (33,34), and our results suggest that as long as tissue can be distinguished from large blood vessels, the fractional moving blood volume estimate method could work in principle.

Second, once depth dependence of the transducer beam profile and attenuation are compensated for, the measurement of the same tissue region should be identical if the normalization method is working. Figure 5 shows this to largely be the case. The slope of the regression line through the data that describe the fractional moving blood volume estimates for gain settings of 104–112 dB was not different from zero to within 95% confidence (35). Hence, when there was sufficient signal to detect, the method compensated for the attenuation and transducer effects, as one would hope. However, when the data included the 102-dB values, there was a significant trend. In addition, the variability in the 102-dB measurement was higher than that in any of the others. The implication here is that when there is very little flow to detect, the method undercompensates and results become more variable. This suggests that when the signal is weak and is harder to detect, the method tends to locate a normalization value within the high-rouleaux portion of the flow stream and would, in a sense, overcompensate for the lost signal in the cortex, where the rouleaux effects are small. This would give a low estimate because the method would be comparing high-rouleaux areas in vessels to low-rouleaux areas in tissue. At some attenuation level, the Doppler signal will be too weak to measure, and any normalization technique will fail. One compensating fact is that when the signal gets very weak, it is still possible to compare the measurement to itself (17). Hence, the normalization from day to day may make it possible to evaluate relative flow changes in the same organ, even if the attenuation is high.

Finally, the evaluation of the volunteers without preparation estimated the potential variability in the method under scanning conditions. Clearly, one would like a technique with little or no variability at all; yet, in some cases the standard deviation in the measurements was up to 10%, which produced a variability relative to the local mean of approximately 30% from day to day, even when the signal was optimized. In these studies, there was no control for hydration, time of day, or fasting; all of which could have influenced the variability. Furthermore, given the single-volunteer studies, where the variance was smaller, it may be reasonable to presume that the variability is the true variation in the blood flow to the renal cortex. It is clear to anyone who does US that there are regions of the cortex with more flow than others; so, when performing scanning in the same per-

son on different days it is possible to obtain different results.

Will such variability preclude using this test? We do not think so. First, the mean values are very close among all the individuals, which suggests that a mean value may be usable in any given case. Thus, taking the mean of several measurements may give very reasonable results. This is exactly what is done presently with all resistive index measurements. Second, there can be equally wide variability among results of other parametric tests, such as resistive indices, pulsatility indices, acceleration, and acceleration times (36–38). Each of these has found use in the medical community. Finally, there are ways to improve the collection on the horizon, that is, three-dimensional imaging (16). This method would be perfectly integrated into a three-dimensional acquisition system. The segmentation would be used in the same way, but the sampling would be more robust. Given the large set of flows that would be sampled in the cortex in three dimensions, the flow variation in an organ would likely decrease.

Besides the limitations described above, there are others. As mentioned above, we have not defined the absolute fractional blood volume in the kidney. Although the mean values obtained are within or close to the published normal levels in the kidney (39–41), we do not know if those numbers measured here are in fact absolute fractional blood volume estimates. This may be true, but it will likely have little effect on the clinical application of such a measure as this. There are plenty of "indices" that relate to physiologic parameters of interest but may not directly measure them, such as the resistive index (42,43). Also, there are clearly flows that will not be included in this measurement. Capillary flow, for instance, is too slow to measure by using present Doppler techniques. Thus, these vessels will not be included in any vascularity estimate derived with our method. Of course, capillaries will not contribute to any US color Doppler vascularity measure, in neither mean-frequency color-flow nor power mode. In addition, vascularity assessments by using color Doppler techniques cannot be easily normalized, unlike ours. Hence, we believe that our method should surpass these.

In conclusion, we have defined a method for normalizing the power Doppler fractional moving blood volume estimate by using properties of the cumulative Doppler power distribution. The technique is almost completely nonsubjective and could easily be automated. The method works in phantom studies to find blood vessel boundaries, can be normalized for depth, gives constant measurements for the same flow situation largely independently of body habitus, and gives reasonable mean fractional moving blood volume estimates in healthy volunteers with a variability similar to that of other functional parametric indices. Further studies in pathologic cases are needed to define its usefulness.

APPENDIX

Quantitatively, the definition of the intersection points and tangent lines looks like this: $P'(x) = Ax + B$, which is the form of the best-fit line for a given distribution, where $P'(x)$ is the estimated cumulative value for a given x, the Doppler power, and A and B are constants. If $P(x)$ is the true distribution of the data, then $P(x) - P'(x)$ will be zero at the points of intersection of the true distribution and the best-fit line. Because this is real data, we cannot rely on the actual points of intersection being in the data set. Hence, one can identify the point in the data set closest to the intersection as being the one where there is a sign change. For example, an intersection would lie immediately between points x_i and $x_i + 1$ if $P(x_i) - P'(x_i) < 0$ and $P(x_i + 1) - P'(x_i + 1) > 0$. As a first approximation, one could choose either x_i or $x_i + 1$ as the intersection. Because we are interested only in a set of points centered at either x_i or $x_i + 1$ to define a tangent, it does not really matter which point we pick. Choosing either one of these points at each intersection, we empirically selected a 21-point region of interest centered about each selected point, for example, $x_i \pm 10$ points, and fitted a line through each group of 21 points. We selected a 21-point region because that worked well empirically. This local, fitted line is the local tangent.

The final complication is that it is possible that there could be more than two intersections of the global best-fit line with the distribution. To get around this possibility, we progressively identified each point of intersection of the best-fit line with the cumulative distribution by moving from the origin toward increasing abscissa values, that is, Doppler power. We then selected the first pair of tangent lines in which the difference between their slopes was negative, that is, in which their slopes were decreasing or the curvature was negative. For example, if T is a tangent line and i is a set of abscissa values of intersection points that range sequentially from 1 to n, then $T(i)$ is the line tangent to the cumulative distribution at i. If slope $T(i)$ is the slope of tangent line $T(i)$ and if $T(i)$ and $T(i + 1)$ are the first pair of tangent lines encountered when moving toward the right from the origin whose difference in slopes is negative (slope $T(i + 1)$ − slope $T(i) < 0$), then the intersection of $T(i)$ and $T(i + 1)$ is the chosen point for the knee. ■

References

1. Tanaka S, Kitamura T, Fujita M, et al. Color Doppler flow imaging of liver tumors. AJR 1990; 154:509–514.
2. Shiamato K, Sadayuke S, Ishigaki T, et al. Intratumoral blood flow: evaluation with color Doppler echography. Radiology 1987; 165:683–685.
3. Bourne T, Campbell S, Steer C, et al. Transvaginal colour flow imaging: a possible new screening technique for ovarian cancer. Br Med J 1989; 299:1367–1370.
4. Luker GD, Siegel MJ. Pediatric testicular tumors: evaluation with gray-scale and color Doppler US. Radiology 1994; 191:561–564.
5. Adler DD, Carson PL, Rubin JM, Quinn-Reid D. Doppler US color flow imaging in the study of breast cancer: preliminary findings. Ultrasound Med Biol 1990; 16: 553–559.
6. Sohn CH, Stolz W, Grischke EM, et al. Die dopplersonographische untersuchung von mammatumoren mit hilfe der farbdopplersonographie, der duplex sonographie und des CW-Dopplers. Zentralbl Gynakol 1992; 114:249–253. [German]
7. Dixon JM, Walsh J, Paterson D, Chetty U. Colour Doppler ultrasonography studies of benign and malignant breast lesions. Br J Surg 1992; 79:259–260.
8. Cosgrove DO, Bamber JC, Davey JB, McKinna JA, Sinnett HD. Color Doppler signals from breast tumors: work in progress. Radiology 1990; 176:175–180.
9. Cosgrove DO, Kedar RP, Bamber JC, et al. Breast diseases: color Doppler US in differential diagnosis. Radiology 1993; 189:99–104.
10. Kedar RP, Cosgrove DO, Bamber JC, Bell DS. Automated quantification of color Doppler signals: a preliminary study in breast tumors. Radiology 1995; 197:39–43.
11. Rifkin MD, Sudakoff GS, Alexander AA. Prostate: techniques, results, and potential applications of color Doppler US scanning. Radiology 1993; 186:509–513.
12. Newman JS, Bree RL, Rubin JM. Prostate cancer: diagnosis with color Doppler sonography with histologic correlation of each biopsy site. Radiology 1995; 195:86–90.
13. Carson PL, Moskalik AP, Govil A, et al. The 3D and 2D color flow display of breast masses. Ultrasound Med Biol 1997; 23: 837–849.
14. Shung KK, Sigelmann RA, Reid JM. Scattering of ultrasound by blood. IEEE Trans Biomed Eng 1976; 23:460–467.
15. Hottenger CF, Meindl JD. Blood flow measurement using the attenuation-compensated flowmeter. Ultrason Imaging 1979; 1:1–15.
16. Carson PL, Li X, Pallister J, Moskalik A, Rubin JM, Fowlkes JB. Approximate quantification of detected fractional blood volume in the breast by 3D color flow and Doppler signal amplitude imaging. In: Levy M, McAvoy BR, eds. 1993 ultrasonics symposium proceedings. Institute for Electrical and Electronics Engineers catalog no. 93CH3301-9. Piscataway, NJ: Institute for Electrical and Electronics Engineers, 1993; 1023–1026.
17. Rubin JM, Adler RS, Fowlkes JB, et al. Fractional moving blood volume: estimation with power Doppler US. Radiology 1995; 197:183–190.
18. Sigel B, Machi JJ, Beitler JC, Justin JR. Red cell aggregation as a cause of blood-flow echogenicity. Radiology 1983; 148:799–802.
19. Machi JJ, Sigel B, Beitler JC, Coelho JCU,

Justin JR. Relation of in vivo blood flow to ultrasound echogenicity. JCU 1983; 11:3–10.
20. Shung KK, Cloutier G, Lim CC. The effects of hematocrit, shear rate, and turbulence on ultrasound Doppler spectrum from blood. IEEE Trans Biomed Eng 1992; 39:462–469.
21. Shung KK. In vitro experiment results on ultrasonic scattering in biological tissues. In: Shung KK, Thieme GA, eds. Ultrasonic scattering in biological tissues. Boca Raton, Fla: CRC Press, 1993; 291–312.
22. Shung KK, Kuo IY, Cloutier G. Ultrasound scattering properties of blood. In: Roelandt J, Gussenhoven EJ, Bom N, eds. Intravascular ultrasound. Dordrecht, the Netherlands: Kluwer Academic, 1993; 119–139.
23. Yuan YW, Shung KK. Ultrasonic backscatter from flowing whole blood. I. Dependence on shear rate and hematocrit. J Acoust Soc Am 1988; 84:52–58.
24. Feynman RP, Leighton RB, Sands M. The Feynman lectures on physics. Vol 2. Reading, Mass: Addison-Wesley, 1964; 41–2.
25. Whitmore RL. The flow fluids. In: Whitmore RL, ed. Rheology of the circulation. Oxford, England: Pergamon, 1968; 37–46.
26. Metz CE. Basic principles of ROC analysis. Semin Nucl Med 1978; 8:283–298.
27. Halperin EJ, Albert M, Krieger AM, Metz CE, Maidment AD. Comparison of receiver operating characteristic curves on the basis of optimal operating points. Acad Radiol 1996; 3:245–253.
28. Papoulis A. Probability, random variables, and stochastic processes. New York, NY: McGraw-Hill, 1965; 92–94.
29. Press WH, Flannery BP, Teukolsky SA, Vetterling WT. Numerical recipes in C: the art of scientific computing. Cambridge, England: Cambridge University Press, 1988; 299–302.
30. Rubin JM, Bude RO, Carson PL, Bree RL, Adler RS. Power Doppler US: a potentially useful alternative to mean frequency-based color Doppler US. Radiology 1994; 190:853–856.
31. Meyerowitz CB, Fleischer AC, Pickens DR, et al. Quantification of tumor vascularity and flow with amplitude color Doppler sonography in an experimental model: preliminary results. J Ultrasound Med 1996; 15:827–834.
32. Goldstein A. Physics of ultrasound. In: Rumack CM, Wilson SR, Charboneau JW, eds. Diagnostic ultrasound. St. Louis, Mo: Mosby–Year Book, 1991; 2–18.
33. Murphy KJ, Bude RO, Dickinson LD, Rubin JM. Use of intravenous contrast in transcranial sonography: preliminary observations. Acad Radiol 1997; 4:577–582.
34. Burns PN. Harmonic imaging with ultrasound contrast agents. Clin Radiol 1996; 51(suppl):50–55.
35. Metz CE. Quantification of failure to demonstrate statistical significance: the usefulness of confidence intervals. Invest Radiol 1993; 28:59–63.
36. Kliewer MA, Tupler RH, Carroll BA, et al. Renal artery stenosis: analysis of Doppler waveform parameters and tardus-parvus pattern. Radiology 1993; 189:779–787.
37. Keogan MT, Kliewer MA, Hertzberg BS, DeLong DM, Tupler RH, Carroll BA. Renal resistive indexes: variability in Doppler US measurement in a healthy population. Radiology 1996; 199:165–169.
38. Paulson EK, Kliewer MA, Frederick MG, Keogan MT, Delong DM, Nelson RC. Hepatic artery: variability in measurement of resistive index and systolic acceleration time in healthy volunteers. Radiology 1996; 200:725–729.
39. Selkurt EE. The renal circulation. In: Hamilton WF, Dow P, eds. Handbook of physiology, circulation. Vol 2, section 2. Washington, DC: American Physiological Society, 1963:1471.
40. Ladefoged J, Pedersen F. Renal blood flow, circulation times and vascular volume in normal man measured by the intraarterial injection: external counting technique. Acta Physiol Scand 1967; 69:220–229.
41. Wiencek JG, Feinstein SB, Walker R, Aronson S. Pitfalls in quantitative contrast echocardiography: the steps to quantitation of perfusion. J Am Soc Echocardiogr 1993; 6:395–416.
42. Bude RO, Rubin JM, Platt JF, Fechner KP, Adler RS. Pulsus tardus: its cause and potential limitations in detection of arterial stenosis. Radiology 1994; 190:779–784.
43. Halpern EJ, Deane CR, Needleman L, Merton DA, East SA. Normal renal artery spectral Doppler waveform: a closer look. Radiology 1995; 196:667–673.

A HAND-CONTROLLED, 3D ULTRASOUND GUIDE AND MEASUREMENT SYSTEM

Ralph C. Fenn, J. Brian Fowlkes, Aaron P. Moskalik
Yong Zhang, Marilyn A. Roubidoux, Paul L. Carson

Department of Radiology
University of Michigan Medical Center
Ann Arbor, Michigan 48109-0553

INTRODUCTION

Summary

Three dimensional (3D) ultrasound images provide superior visualization of anatomical features than two dimensional (2D) power mode or frequency shift color Doppler B-scan ultrasound images. However, 3D data sets require transducer position measurements that can be problematic. One previously investigated approach completely automates transducer positioning and measurements with one dimensional motorized stages. Other system types permit full six degree-of-freedom (DOF) manual transducer manipulation while measuring all six axes. In contrast this work explores the middle ground of measuring the two degrees of freedom most important for free-hand scanning while fixing the remaining axes for minimized complexity.

The device designed, fabricated, and tested allows linear motion perpendicular to the scan plane and along the beam axis, as well as rotation about an axis parallel to the array. The measurement system is designed to minimize size, weight, and cost while maximizing accuracy and ease of operator use. The resulting design weighs 500g in its heaviest configuration and is 150 mm long, 64 mm high, and 70 mm wide. It is capable of 0.1 mm accuracy in the focal plane. Three dimensional data with continually varying translational and rotary speeds was interpolated in 3D by image processing software to minimize distortion in standard Cartesian coordinates. Phantom images show little distortion due to the measuring system or data processing algorithm. This inexpensive, compact, and lightweight system interferes minimally with clinician free-hand scanning and enhances 3D image collection and generation capabilities in the clinical setting.

Three Dimensional Data Acquisition

The goal of three dimensional ultrasound imaging has been pursued by a number of research laboratories. Conventional 2D ultrasound images are inherently limited in their ability to display 3D human anatomy and their diagnostic usefulness is thus reduced. A number of laboratories have investigated various methods of attaining the critical transducer position measurements to create 3D data sets. A common feature of many of these imaging systems is

Acoustical Imaging, Vol. 23
Edited by Lees and Ferrari, Plenum Press, New York, 1997

computer controlled, motor-driven linear ultrasound transducer motion (Pretorius et al., 1992, Picot et al., 1993, Moskalik et al., 1995, Tong et al., 1996, and Hernandez et al., 1996). These designs give precise control of the ultrasound transducer position, usually with one degree-of-freedom. However these motorized systems frustrate the clinician's desire for the flexibility of conventional hand-controlled ultrasound examinations. Free-hand control facilitates localizing a specific region of interest (ROI), especially when examining organs of convex or concave external shape such as the shoulder, the uterus, and the liver near the ribs.

In contrast, other studies have provided complete freedom of motion for manual examinations while measuring the positions of each of the 6 axes of motion, both translation and rotation (Detmer et al., 1994, Kelly et al., 1994, Nelson and Pretorius, 1995, and Hughes et al., 1996). Such systems are often less accurate and may be complex, large, and more costly. The approach of the present work uses an intermediate approach with manual transducer control only in the degrees-of-freedom that are most helpful, while avoiding complete 6 DOF freedom of motion that increases complexity and cost. The current design measures 2 DOF and can be easily retrofitted for measurement of the third axis, which is a second translation axis.

METHODS

Instrumentation System Overview

The 3D ultrasound data acquisition system is comprised of three major parts. First is the ultrasound imaging system. The scanning data presented was gathered by a General Electric Logiq 700 MR machine with a 739L transducer but the design is equally applicable to other machine types. Second is the personal computer which handles data acquisition and storage. The current experiments collect position data at the same fixed, 4 Hz rate as the production of ultrasound B-scan images. In future experiments, the personal computer will store B-scans at desired spatial increments through signals to the cardiac gating feature of the ultrasound machine. For color flow studies of maximum sensitivity, cardiac signals will trigger ultrasound image storage and simultaneous position measurements by the personal computer. The third major component, and the focus here, is the mechanical transducer guiding system and its translation and rotation sensors. Postprocessing for 3D image construction is performed on a Digital Equipment Corporation Alpha workstation.

System Design of the Guide and Measurement System

The overall goal of allowing natural, free-hand transducer motion in 2 DOF while measuring translation and rotation drove the design of the measurement system. This goal requires a compact device that allows natural grasp of the transducer grip. The device must not provide too much friction or require movement of significant mass. It should provide range of motion greater than required for screening examinations. The device must have low overall mass to maximize patient comfort. The accuracy and linearity must be high so that these factors contribute little additional distortion to the 3D image. Finally it should be inexpensive. These factors all influenced the design described below.

Figure 1 shows the design developed by this program that provides transducer guidance and measurement. The design uses a "series" design where multiple DOF are created by selecting a base motion type and installing the other DOF on the now moving base stage. In the device described here the base stage provides translation. This is advantageous because of the large stroke required. The alternative of mounting the translation stage on the rotary axis would be very clumsy because of the large radius of the resulting rotating mass. For this reason the rotation stage is mounted on the translation carriage. Finally a second translation stage is mounted on the rotating shaft to provide the third DOF. The first two DOF are measured however the third is not but could be instrumented using straightforward methods. This third DOF can be locked, or left free when positional accuracy is not critical, e.g. while following rough surface contours.

The major components shown in Figure 1 are described below beginning with those components nearest the patient. At the base is a stabilizing platform made of acrylic sheet with a window for transducer array access to the skin. The material is clear for ease of positioning, has low thermal conductivity for patient comfort, and is easily cleanable.

Mounted horizontally on the base plate is a Thompson Series 10 miniature linear

bearing. This bearing provides motion of the transducer in the z axis which is defined to be perpendicular to the long dimension of the ultrasound array (x axis).

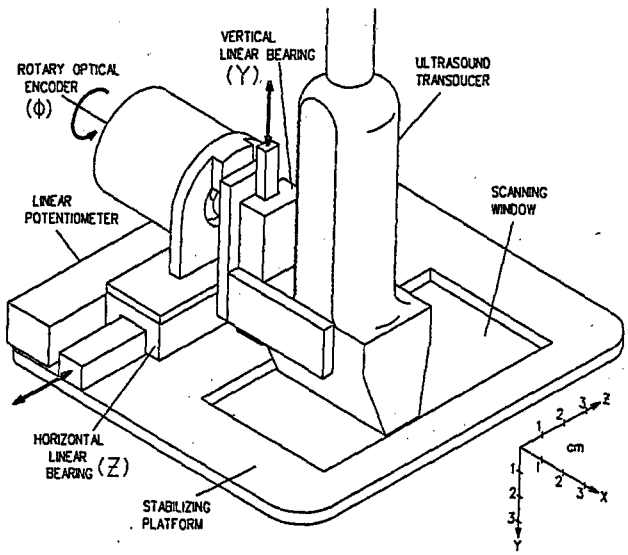

Figure 1. The ultrasound transducer guide and measurement system (drawing by Ben Moskalik).

Low friction is provided by the light rather than heavy preload on the bearings, and by the use of low friction bearing seals. Preload is required to minimize backlash, particularly in the roll axis. Waterproof grease such as petroleum jelly excludes gel and cleaning water from the bearing interior while being nontoxic to the patient.

Parallel to the linear bearing and also mounted on the base plate is a precision linear potentiometer. This off-the-shelf Duncan Electronics 400 Series potentiometer uses a high linearity conductive plastic film and has dual, parallel wipers to reduce noise. This potentiometer measures the translation of the ultrasound array by providing a voltage output when a reference voltage is applied to the resistive element. The friction and damping of the wiper is adjustable by removal of plastic inserts. The wiper access slot has rubber seals that face the side to avoid gel and water intrusion. This sensor has the advantage of providing an analog output which simplifies development of interfaces to various laboratory instruments during system development and experiments. Minimal distortion of the interpolated three dimension model of the tissues requires low position noise and high accuracy. These important potentiometer parameters were measured with results presented at the end of this section.

The capacity to rotate the transducer array around an axis parallel to the array (x axis) is provided by a rotary optical encoder mounted onto the linear bearing carriage. This optical encoder integrates the functions of a rotary bearing and rotary sensor. If separate components were used instead and connected by a belt, for example, backlash and calibration errors would be much larger. The RIS15 encoder from BEI Encoder Systems Division is used and has 2,000 lines on the disk, thus supplying 8,000 counts per turn using quadrature electronics. This disk resolution supplies angle precision of 0.045 degrees or linear precision of 0.075 mm at 50 mm below the skin. The internal encoder bearings provide 22N (5 lbf) load capability which is sufficient to support the transducer and normal operator hand forces. An analog output is provided for simplicity of interface thus avoiding software intensive serial communication.

A major goal of this effort is miniaturization of the measurement system. The resulting design weighs 650g including the ultrasound transducer. This mass is divided into stationary parts weighing 190 g, which includes the base plate, potentiometer, and linear bearing rail. The moving parts weigh 460 g which includes a typical 140 g ultrasound transducer, an optical encoder weighing 170 g, a vertical linear bearing weighing 30 g, and various brackets.

The length of the package along the translation (z) axis is 153 mm, and the width (x

axis) is 142 mm parallel to the transducer array. The height (y axis) without a ultrasound transducer installed is 64 mm to the top of the optical encoder body. The device fits into a rectangular prism of 1400 cc. In the configuration illustrated the translational range is 70 mm which is easily expandable.

Translation Sensor Linearity and Noise Measurements

Poor linearity and contact noise are traditional weaknesses of potentiometers. The potentiometer was selected for the final design because of the advantages of size and weight over competing linear optical encoders, but only after complete testing of linearity and noise.

Linearity was measured by translating the potentiometer wiper with a lead screw and measuring the potentiometer wiper voltage with a constant voltage applied to the resistive element. The voltage was read by a 12 bit analog-to-digital-converter (ADC) board that was also used for the phantom and clinical data presented in the Results Section. This experimental protocol tests the linearity of the ADC as well as the potentiometer. The error of the digital position measurement was calculated from the best linear model of the data using a least mean square algorithm. The worst cumulative error is 0.47 mm or 0.68 percent. By avoiding the first 2 mm of the 69 mm stroke the nonlinear error can be limited to 0.35 percent. It is important to note that the maximum nonlinear error between successive 0.5 mm slices is limited to 0.16 mm or 32 percent of the slice spacing. This implies that the greatest distortion using this potentiometer would be one third of a space between scan planes. Further improvement in linearity is available in high linearity (0.1%) potentiometers available from the manufacturer.

The electrical noise of the translational sensing system was also measured during a typical slew maneuver of 1 mm per second. Resistance changes as the wipers slid across the conductive film were determined as well as noise from the cabling and ADC circuitry. Figure 2 shows the calculated position during slewing. The primary feature of the plot is the series of steps due to the quantization size of the 12 bit ADC circuit. The resistor output voltage is 10 V for a 100 mm range. This is processed by a 12 bit ADC having 4096 steps and an input range which is also 10 V. The result is quantization steps of 2.4 mV, or 0.024 mm, for the stated position and voltage ranges. Figure 2 shows that this quantization noise dominates the calculated transducer position. Potentiometer noise is small relative to the ADC quantization error and is insignificant for this application.

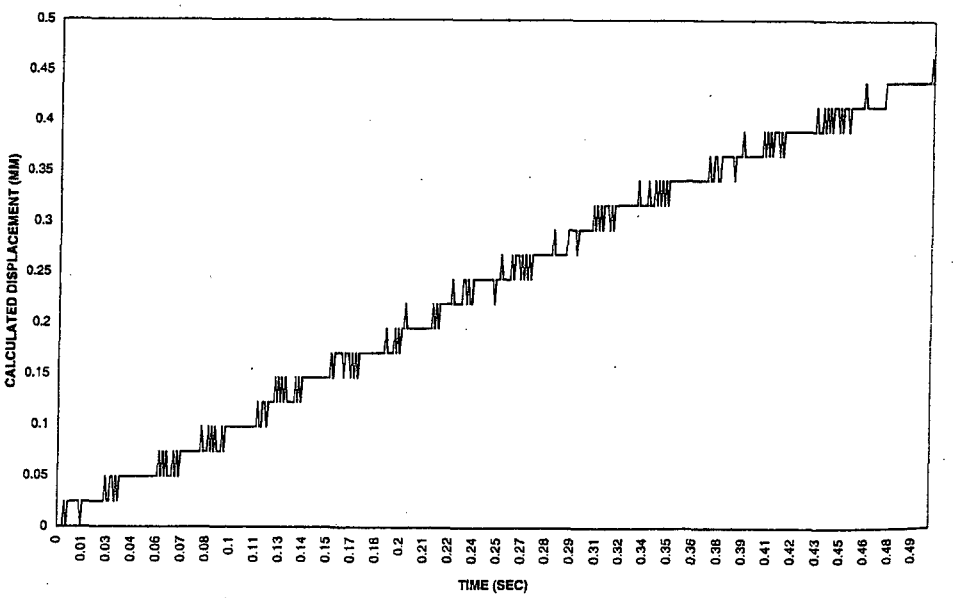

Figure 2. Electrical noise during slewing of the plastic film linear sensor.

RESULTS

The goal of the program is construction of a measurement system that provides linear and rotary position of the ultrasound transducer. The ultimate goal for this data is the construction of 3D data sets where any 2D image section can be presented to the viewer without significant distortion. Real-time measurements avoid the need for evenly spaced B-scans because the 3D image processing software can accomodate the varying slice spacing. Trilinear interpolation is used to assign weighted fractions of the raw image data into the desired 3 D grid. A raw 3D data set was created from scans of a filament phantom. A single B-scan was used as a reference image and a similar section of the interpolated 3D data was evaluated for distortion.

The first step in this evaluation was creation of a reference 2D B-scan image of the phantom. The B-scan was taken perpendicular to the phantom filaments for finest detail and minimal sensitivity to precise transducer alignment. This 2D image is shown in Figure 3.

A 3D data set was created from a set of B-scans taken *parallel* to the phantom filaments, i.e., perpendicular to the reference 2D scan. Motion was allowed in both translation and

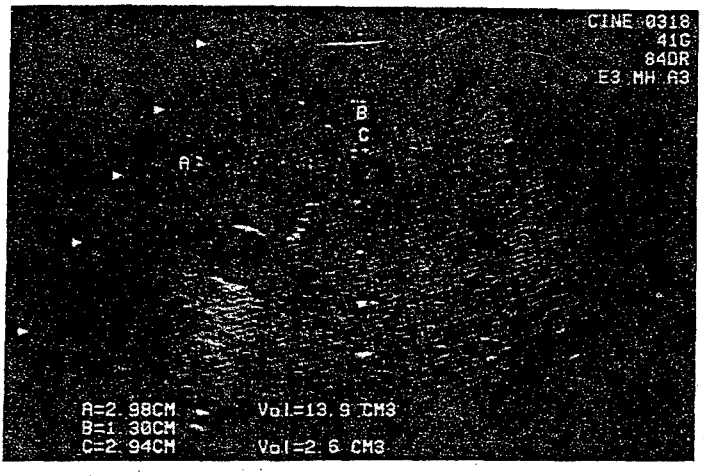

Figure 3. Reference B-scan perpendicular to the phantom filaments.

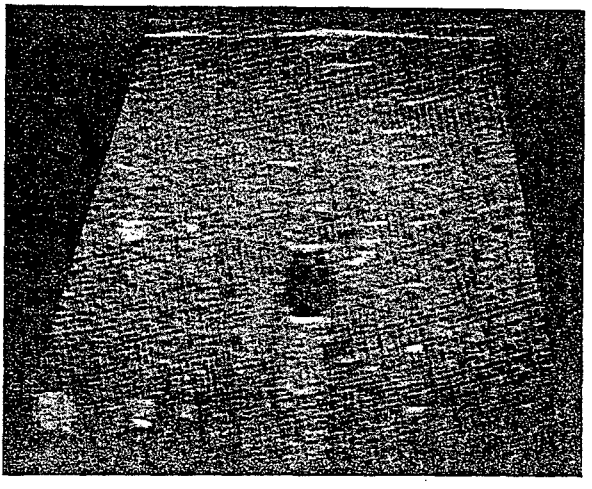

Figure 4. An image from the 3D data set after interpolation for rotation and uneven spacing.

rotation. Figure 4 shows an image reconstructed from the 3D data set after interpolation based on the measurement system. Data from each scan plane was placed into the nearest Cartesian-grid vertices using trilinear interpolation. The figure shows how the features from Figure 3 are presented with an acceptable level of distortion. Note that the lateral boundaries the image are not parallel and thus accurately reflect the degree of rotation employed during the 3D data collection.

Figure 4 shows some degradation in image quality due to reduced resolution. This effect results from the different precision of beam focusing between the in-plane and out-of-plane directions. Electronic focusing within the B-scan plane provides better focusing, and also high depth of field through changes in focus depth. In the elevational, or out-of-plane direction used by the 3D software to reconstruct objects perpendicular to the constituent B-scans, single array elements provide poorer focusing. The resulting 3D image is smeared in the translation direction because of the large elevational beam width. The 3D image shown is provides the most severe conditions for comparison of B-scan and 3D data.

CONCLUSIONS

This work has developed a small, low cost ultrasound transducer position measuring system that minimally affects the clinician's preferred technique during ultrasound examinations. Manual examination is facilitated by permitting varying speeds of translation while still producing low distortion 3D image sets. Patient comfort is maximized by the device's light weight while its small size permits access to a range of body regions comparable to the ultrasound transducer alone. Measurement of the two axes critical to image acquisition flexibility is provided while motion in other axes is prohibited, thus simplifying measurement, data acquisition, and image processing.

ACKNOWLEDGMENTS

General Electric Medical Systems and Corporate Research Laboratory were particularly helpful with development of rapid acquisition and transfer of digital image data. This work was supported in part by PHS grant R01 CA55076 from the National Cancer Institute and contract No. DAMD 17-96-C-6061 from the Army Medical Research and Development Command.

REFERENCES

Detmer, P.R., Bashein, G., Hodges, T., Beach, K.W., Filer, E.P., Burns, D.H., and Strandness, D.E., 1994, 3D ultrasonic image feature localization based on magnetic scanhead tracking: In vitro calibration and validation, *Ultrasound Med. and Bio.* 20:923.

Hernandez, A., Basset, O., Dautraix, I., and Magnin, I., 1996, Acquisition and stereoscopic visualization of three-dimensional ultrasonic breast data, *IEEE Trans. Ultrasonics,Ferro. and Freq. Ctl.* 43:576.

Hughes, S.W., D'Arcy, T.J., Maxwell, D.J., Chiu, W., Milner, A., Saunders, J.E., and Sheppard, R.J., 1996, Volume estimation from multiplanar 2D ultrasound images using a remote electromagnetic position and orientation sensor, *Ultrasound in Medicine.* 22:561.

Kelly, I.A.G., Gardener, J.E., Brett, A.D., Richards, R., and Lees, W.R., 1994, Three dimensional US of the fetus, *Radiology* 192:253.

Moskalik, P.L., Carson, P.L., Meyer, C.R., Fowlkes, J.B., Rubin, J.M., and Roubidoux, M.A., 1995, Registration of three-dimensional compound ultrasound scans of the breast for refraction and motion correction, *Ultrasound in Med. And Biol.* 21:769.

Nelson, T.R. and Pretorius, D.H., 1995, Visualization of the fetal thoracic skeleton with three-dimensional sonography, *AJR.* 164:1485.

Picot, P.A., Rickey, D.W., Mitchell, R., Rankin, R., and Fenster, A., 1993, Three dimensional colour doppler imaging, *Ultrasound in Med. and Bio.* 19:95.

Pretorius, D.H., Nelson, T.R., and Jaffe, J.S., 1992, 3-dimensional sonographic analysis based on color flow doppler and gray scale image data, *Ultrasound Med.* 11:225.

Appendix A4

Back to Contents | Send Letter

Examples of 3D Image Registration for Multimode, Extended Field of View, and Sequential US Imaging

Jochen F. Krücker, Dipl-Phys, Gerald L. LeCarpentier, PhD, Charles R. Meyer, PhD, Marilyn A. Roubidoux, MD, J. Brian Fowlkes, PhD, Paul L. Carson, PhD

Department of Radiology
University of Michigan Medical Center
Ann Arbor, Mich, USA

Correspondence:
Paul L. Carson, PhD
University of Michigan Medical Center
Department of Radiology
Kresge III, R3315
200 Zina Pitcher Place
Ann Arbor, MI 48109-0553
Voice: (734) 763-5884
Fax: (734) 764-8541

Acknowledgment: This work was supported in part by PHS grant R01CA55076 from the National Cancer Institute and by the U.S. Army Medical and Material Command under DAMD17-96-C-6061.

Received February 4, 1999; revision requested March 29; revision received and posted May 4.

©RSNA, 1999

Index terms :

- Breast, US, 00.12987, 00.12989
- Images, display
- Images, processing
- Ultrasound (US), experimental
- Ultrasound (US), technology
- Ultrasound (US), three-dimensional

[Abstract]

Back to Contents | To Article | Next Abstract

Send Letter

Examples of 3D Image Registration for Multimode, Extended Field of View, and Sequential US Imaging

Jochen F. Krücker, Gerald L. LeCarpentier, Charles R. Meyer, Marilyn A. Roubidoux, J. Brian Fowlkes, Paul L. Carson

Abstract

Several potential uses of image registration and new display techniques in three-dimensional ultrasound (US) imaging are demonstrated in three examples, representing several types of applications: First, the gray-scale information of a color Doppler flow image set was coregistered with a high-resolution gray-scale image set covering the same region of interest. The high accuracy achieved in this registration suggests that this technique can create improved images from combined US modes. Second, several parallel, partly overlapping gray-scale scans of a female breast with several lesions were coregistered and combined into one larger volume. Only in this extended field of view could the lesions be viewed simultaneously and their relative sizes and positions be appreciated, suggesting the potential of better detection of changes in breast regions being followed up for potential cancer. Third, the image registration was applied to a series of US breast studies for cancer therapy assessment. Despite considerable tumor shrinkage occurring between the two scans, obtained several weeks apart, the coregistration mapped the dominant features in the region of interest and thus facilitated tracking of changes over time, both with direct comparison and with displays that highlighted changes. The quality of the semiautomatic coregistrations achieved and the significance of the applications demonstrated here indicate that image registration may become a valuable tool in improving diagnosis with US imaging.

Introduction

Image registration or coregistration, the alignment of two or more two-dimensional (2D) or three-dimensional (3D) images of an object, has been applied to medical imaging for more than 10 years. One major application of medical image registration is fusion of morphologic images such as magnetic resonance (MR) images and computed tomographic (CT) images with functional studies such as positron emission tomographic (PET) and single photon emission computed tomographic (SPECT) studies (1-7). Other applications of coregistration include motion detection (8,9), subtraction imaging (10,11), and treatment planning (12,13). A comprehensive review of different approaches and techniques in medical image matching can be found in reference 14.

Until recently, ultrasound (US) image registration has not been successful, partly because of the small 2D field of view (FOV) and possibly because of the large tissue motion and deformation that make it difficult to obtain consistent image pairs for coregistration with conventional manual scanning.

With the advent of 3D sonography in research (15,16) and, more recently, in commercially available US scanners, volumetric US data have become available and can, in principle, be registered like 3D data sets from other imaging modalities. However, the speckle noise and image artifacts usually present in US images and the strong angular dependency of the apparent brightness of specular reflectors challenge the robustness of registration algorithms.

Apparently the first successful coregistration of 3D US scans in a phantom and in the breast, with registration software that required user definition of homologous points, lines, and planes in the data sets, has been reported (17). Semiautomatic coregistration of US scans was achieved recently (18,19) with software based on the mutual information of two data sets. The same software was used in this study to demonstrate three examples of potential applications of coregistration in US breast imaging. The display possibilities in this electronic medium, especially the movie features, should allow better visualization of registration quality and assessment of errors than would print journals.

The gray-scale image obtained along with the color information in Doppler US modes usually has poor spatial resolution compared with the high resolution obtainable in the gray-scale-only mode. After registration of a 3D Doppler mode data set with a gray-scale set, the color information can be superimposed on a high-resolution gray-scale background, thus extracting the best of both imaging modes. Potentially, this allows more accurate diagnosis and higher sensitivity in lesion detection by displaying flow information along with a high-quality gray-scale image.

The small FOV usually covered by a high-resolution scan head may be insufficient for full use of the capabilities of 3D US in detecting and tracking changes in breast regions being screened or followed up for possible lesions or response to treatment. Often the FOV is also too small to allow full use of the advantages of 3D in displaying morphologic distortions of normal tissue and flow surrounding the mass and differences between the possible mass and a statistically robust sampling of surrounding tissue. To create a complete or more complete image of the breast, the small volume covered by a single scan can be extended by repeatedly scanning the breast in parallel, partially overlapping sweeps that can then be combined by using coregistration of the overlap. Compared to a commercially available 2D extended FOV approach (20,21), our extended volume imaging (EVI) allows much faster acquisition of 3D volumes and can be used as a postprocessing scheme after the individual scans have been obtained.

In US screening of the breast, some malignant changes are manifest as changes in echogenicity, texture, and morphology. Early detection of these changes can improve survival rates (22). Changes in the size or shape of a structure can also aid in detection of a malignancy or give important feedback in serial US studies for the assessment of response to cancer therapy. Coregistration of 3D US studies can facilitate the temporal tracking of changes by coregistering the suspect regions of interest imaged at different times, thus allowing direct comparison of the "before" and "after" texture and morphology.

[Previous: Abstract] [Next: Materials and Methods]

[Title Page | Abstract | Introduction | Materials and Methods]
[Results | Discussion | References]

Materials and Methods

A LOGIQ 700 US scanner (GE Medical Systems, Milwaukee, Wis) with a 12-MHz, 1.5-dimensional matrix linear array probe was used to obtain 3D data sets of the breast. The probe was mounted in a holder that restricted it to a linear motion in the elevational direction (perpendicular to the image plane), while electronically encoding the linear position of the probe in that direction. A more detailed description of the data acquisition scheme can be found in reference 23.

The holder was placed on the breast and the transducer slowly moved by hand over the region of interest. The high-resolution gray-scale (GS) and frequency-shift (f-CDI) and power-mode (p-CDI) color Doppler images obtained were then interpolated and resampled with a uniform elevational spacing of approximately 0.4 mm by using the position data stored along with the images. Display and registration of the data sets were performed with AVS/5 and AVS/Express (Advanced Visual Systems, Waltham, Mass).

The 3D image registration software MIAMI Fuse was originally developed for fusion of data sets from multiple imaging modalities, including various combinations of MR imaging, CT, PET, and SPECT.

To define the approximate relative positions of the two data sets to be coregistered, three control points must be defined in each set. This is usually done by assuming that the images were obtained in the same location and in the same orientation and requires limited user interaction. The algorithm then repeatedly performs geometric transformations, rigid or full affine, on one of the two sets and maps it onto the second set until the best fit between the two sets is found. The mutual information (24,25) of the data sets is used as a cost function to determine the quality of a fit. With more control points, warping transformations can be performed, but that was not done in the present study. For a more detailed description of the algorithm and evaluation of its performance with PET and CT, PET and MR imaging, and SPECT and CT multimodal data sets, see reference 26. More details on the application of this image registration software to 3D US data sets are given in reference 19.

The registration software was used here to demonstrate registration of 3D US scans of the breast for three different applications. For each application, one typical case is displayed to demonstrate its potential value in US diagnostic imaging. All patient data were acquired after informed consent was obtained.

1. The first application is the fusion of color information from Doppler imaging modalities with gray-scale information from a high-resolution gray-scale scan of the same volume. For this purpose, the right breast of a 40-year-old woman was scanned in f-CDI mode and, several minutes later, in high-resolution gray-scale mode, with average elevational frame spacings of 0.43 mm and 0.47 mm, respectively. The gray-scale information of the two scans was then coregistered and displayed in various ways to evaluate the quality of the match.

2. Extended volume imaging is the second application demonstrated in this study. Three parallel, high-resolution gray-scale scans were obtained in the left breast of a 65-year-old woman with a diagnosis of a 60-mm-diameter invasive ductal carcinoma. The relative position and alignment of the scans is shown schematically in Figure 1. Starting with a scan in the center of the region of interest (B ; average elevational frame spacing, 0.32 mm), the 4-cm-wide aperture of the transducer was then shifted 1-3 cm medially (A ; frame spacing, 0.29 mm) and laterally (C ; frame spacing, 0.37 mm), respectively, before the second and third scans. Thus, 3D data sets with 25%-75% overlap (AB , BC) were obtained. Volume registration was then performed on the overlapping regions to find the necessary transformations and exact relative positions of the data sets, mapping scan A and C into the reference frame given by scan B .

Note that our hardware does not encode the lateral position of the transducer, and that image-based methods, such as our volume registration method, are preferable to hardware-encoded positioning, since the image may be distorted by tissue motion or refraction artifacts. These distortions would not be detected by an external position encoder and could therefore result in discontinuities in the extended image.

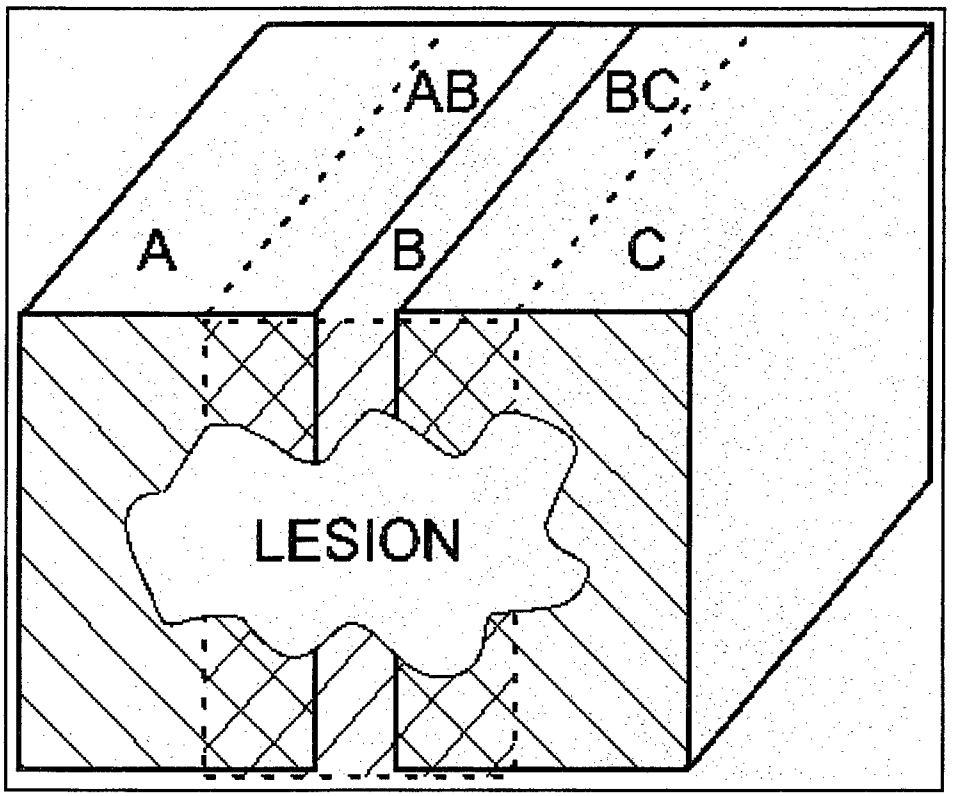

Figure 1. The diagram shows the relative positions of three individual scans *A* , *B* , and *C* , combined into one extended 3D FOV. The three scans are approximately parallel and overlap at least 25% to achieve sufficient accuracy in the coregistration. Scan *B* serves as a reference, while the overlap *AB* is used to align scan *A* relative to *B* ; similarly, *BC* is used to align *C* relative to *B* .

3. The third application presented in this article is the registration of US scans obtained several weeks apart in the course of a serial study. For this application, the same subject was scanned as for the extended volume imaging. The central lesion in the left breast of the same woman as in the second application was scanned four times, 8 days before and 29, 55, and 78 days after the first of four cycles of CAF (cytoxin, adriamycin, flourouracil) chemotherapy. The second scan served as a reference relative to which the first, third, and fourth scans were coregistered. Although visual inspection of the scans showed significant changes in the lesion, the coregistrations were done without prior cropping or any other preprocessing of the image sets. While this inherently increases the inaccuracy of the coregistration, it does serve to demonstrate the feasibility of using US image registration for evaluation of serial studies without substantial user interaction.

In each application, the quality of the coregistration was evaluated by displaying the registered image sets side by side and manually defining pairs of corresponding feature landmarks in the two sets. The mean of the distances between point pairs defining common landmarks was then used as an estimate of the alignment errors after registration. More objective and user-independent measures of accuracy are currently under research and are addressed in the Discussion section.

[Previous: Introduction] [Next: Results]

[Title Page | Abstract | Introduction | Materials and Methods]
[Results | Discussion | References]

Results

Application 1: Multimodal US Imaging

Figures 2 and 3 show the results of registering a 3D f-CDI volume with a high-resolution gray-scale volume. The two image volumes were acquired sequentially during a single patient visit. The 40-year-old woman had a diagnosis of right infiltrative ductal carcinoma. Note the 13-mm-diameter spiculated mass (arrow) in both Figures 2b and 3.

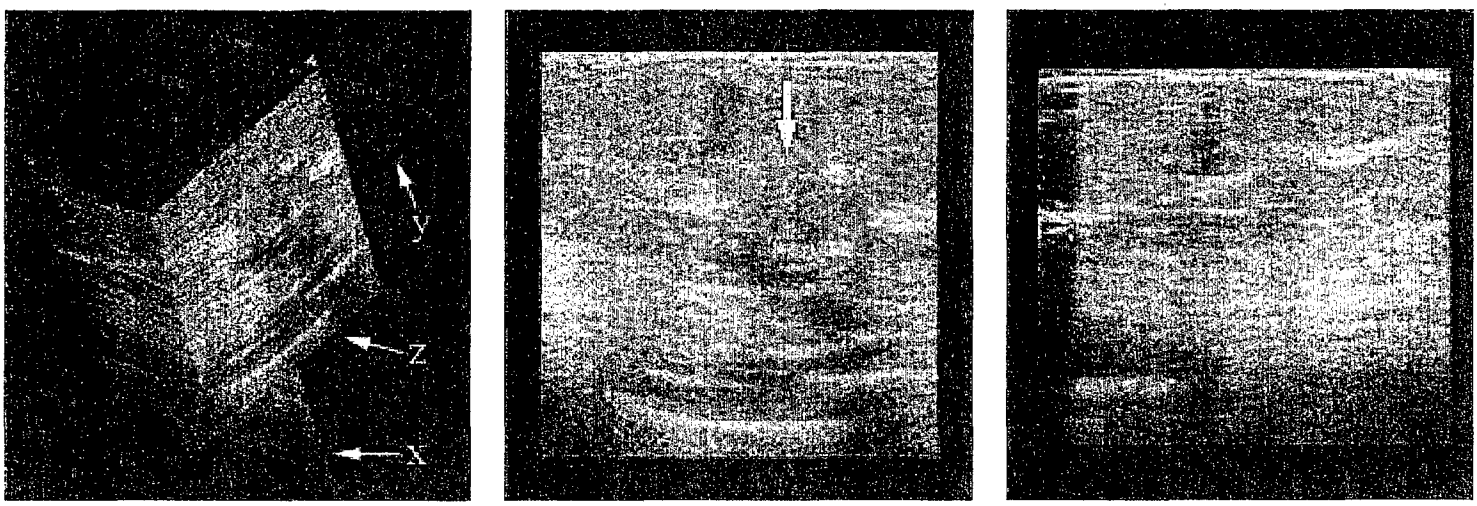

a. **b.** **c.**

Figure 2. Composite representation of an f-CDI volume coregistered with a high-resolution gray-scale volume. The high-resolution gray-scale images are pseudocolorized from blue (weak echo) to red (strong echo) and superimposed onto the gray scale of the f-CDI set. Note the overlap of features in all three images, with reds and yellows overlapping the lighter features. The scans were performed minutes apart. Click on each image for a larger version. **(a)** Three orthogonal planes of the 3D coregistered volume. The labels indicate our naming scheme for the three planes. **(b)** Axial-lateral (z) scan plane. The arrow indicates the 13-mm-diameter spiculated mass. **(c)** Axial-elevational (x) transverse plane. Click here for a Quicktime movie (444 kB) that scans through the entire volume and contains the frames shown in **a-c.** For a high-quality version of the same movie (1.2 MB), click here.

In Figure 3, the particular scan plane shown in Figure 2b is presented in a different way. In this case, the coregistered planes are not combined into a composite view. Rather, a diagonal line separates the gray-scale image from the f-CDI (upper left) from the high-resolution gray-scale image (lower right). The viewer is then able to see the alignment of various features at the diagonal boundary for comparison. Note that the sharp borders of the spiculated mass (arrow) clearly visible in Figure 3b are barely discernible on the gray-scale image from the f-CDI (Fig 3a). In a Quicktime "wiper" movie (348 kB), the viewer can appreciate both the accuracy of the registration and the sharpness of the high-resolution gray scale over that of the f-CDI view by sweeping the border back and forth over the suspicious region.

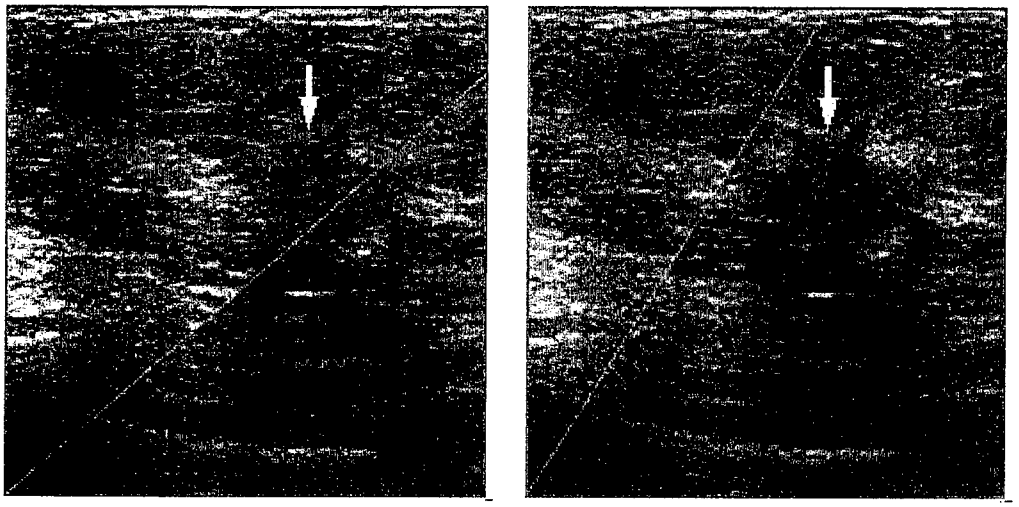

a. **b.**

Figure 3. Lateral-axial scan plane shown in Figure 2b. In both images, to the left of the diagonal line is the gray-scale image from the f-CDI, while to the right is the high-resolution multifocal gray-scale image. Click on each image for a larger version. **(a)** In this view, more of the lower-resolution image is shown. Note the alignment of various structures at the diagonal image boundary. **(b)** In this view, more of the high-resolution gray-scale image is shown. Note the detectability of the spiculated mass (arrow) just to the right of the diagonal line in the upper portion of the image. In **a,** this structure is barely discernible. Click here for a Quicktime "wiper" movie (348 kB) containing the frames shown in **a** and **b.**

Even if the mapping of the two image sets displayed above appears to be accurate, close inspection of the data reveals a small remaining error in the alignment of discernible landmarks. The main causes of error appear to be the following:

1. Local tissue motion and deformation caused by respiratory motion and compression of superficial tissue by the transducer itself. These local deformations can be corrected only in part by the global geometric transformation applied here to register the two data sets.
2. Noise in the image sets or any other inherent differences between the sets to be registered, introduced by using different imaging modes or modalities (here: gray-scale and f-CDI US).
3. Changes in the view direction, which cause changes in the apparent brightness of specular reflectors, since the echo received from specular reflectors depends strongly on the angle of incidence of the ultrasound pulse. Even if very apparent to the eye, this may actually be only a minor cause of misalignment, since the volume covered by specular reflectors is small compared to the total volume, and thus the mutual information associated with it contributes little to the maximization of the total mutual information.

The quality of the registration was evaluated by a single observer, as described above. The mean alignment error obtained, based on 13 manually defined common landmarks, was 1.1 mm. It should be noted that this value depends on the position and distribution of the selected points throughout the volume and is somewhat subjective. The peak alignment error estimate was 2.9 mm on the left side of the image near the chest wall, the movability of which is unrelated to the transducer pressure applied.

Application 2: Extended Volume Imaging

Figure 4 displays the extended 3D FOV of an invasive ductal carcinoma scanned in a 65- year-old woman. The orientation and relative position of the three scans used to form this extended volume was described in Figure 1. In this particular example, the central (*B*) and medial (*A*) scans overlapped about 75%, the central and lateral (*C*) scans overlapped 25%, resulting in a total width of the extended field of about 7.9 cm. In Figure 4, the boundaries between the displays of the coregistered scans at 0.3 and 0.6 of the total width of the extended volume, marked by arrows in the 2D view of Figure 4, are hardly noticeable. Note that no averaging or other processing (other than slight image compression for online display) was used at the boundaries to smooth out the transition. The display changes abruptly from scan *A* to *B* and from *B* to *C* , which makes the continuous appearance of the extended view even more remarkable.

A Quicktime movie (548 kB) can be displayed for appreciation of the quality of the composite view throughout the volume.

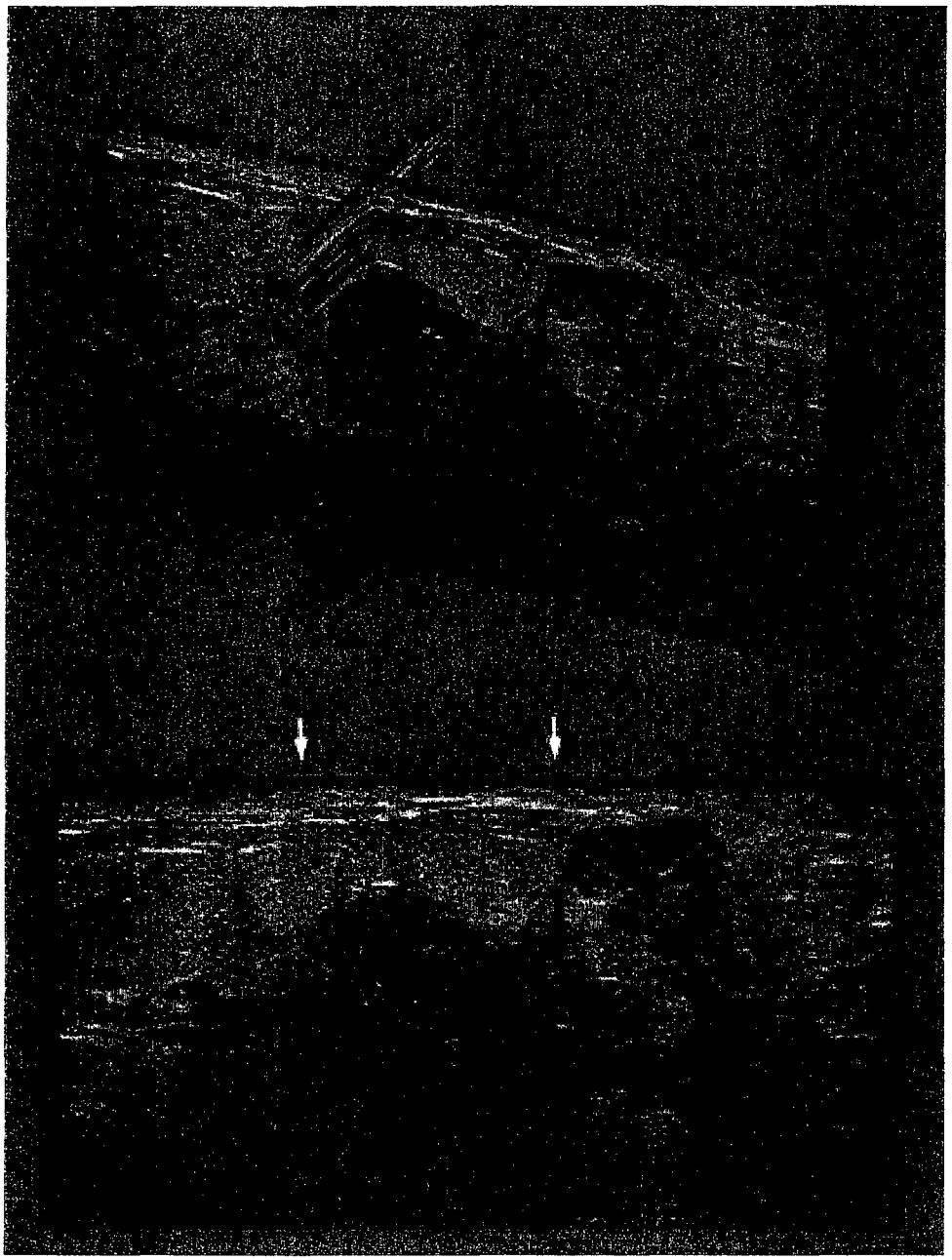

Figure 4. (Top) 3D view of a volume combined from three parallel, partly overlapping scans in a 65-year-old woman with invasive ductal carcinoma. (Bottom) 2D view of the axial-lateral plane displayed in the volume above. The width of this extended view is 7.9 cm. The boundaries between the original scans at about one third and two thirds of the width of the composite image (arrows) are hardly noticeable. Click here for a Quicktime movie (548 kB) displaying an elevational sweep through the extended volume. For a high-quality version (1.3 MB) of the same movie, click here.

In this example, commercially available high-resolution transducers with aperture widths of typically 4 cm could have fully displayed only one of the masses at a time. This limitation may make the visualization and evaluation of the entire structure with US more difficult. In the extended view, the three distinct masses are displayed simultaneously in their relative positions, as determined

with coregistration in the overlapping regions. This allows immediate perception of the entire region of interest and reveals more of the overall anatomy and the anatomic relationships. The large FOV should also reduce the danger of missing important details at the edges and facilitate measurements within the extended volume.

The remaining misalignment of the registered scans in the overlapping regions, based again on visual inspection of identifiable structures and measurement of their apparent shift, was estimated to be a mean of 0.8 mm (1.5 mm peak) in the 75% overlap region and 1.4 mm (3.1 mm peak) in the 25% overlap region.

Application 3: Sequential 3D Imaging

Figure 5 is an example of a coregistration of sequential scans of a breast lesion in a patient undergoing CAF chemotherapy. The 65-year-old woman had a palpable 2.5-cm-diameter mass and later had a diagnosis of left invasive ductal carcinoma with a focal mucinous carcinoma component. The two scans displayed here were acquired 8 days before and 29 days after the start of the chemotherapy. Two more scans obtained and coregistered 55 and 78 days, respectively, after the start of the therapy yielded similar registration results and are not displayed here. Although the size and shape of the lesion changed considerably between the first two scans, the registration procedure aligned the lesions well and allows better comparison and visualization of changes than without registration.

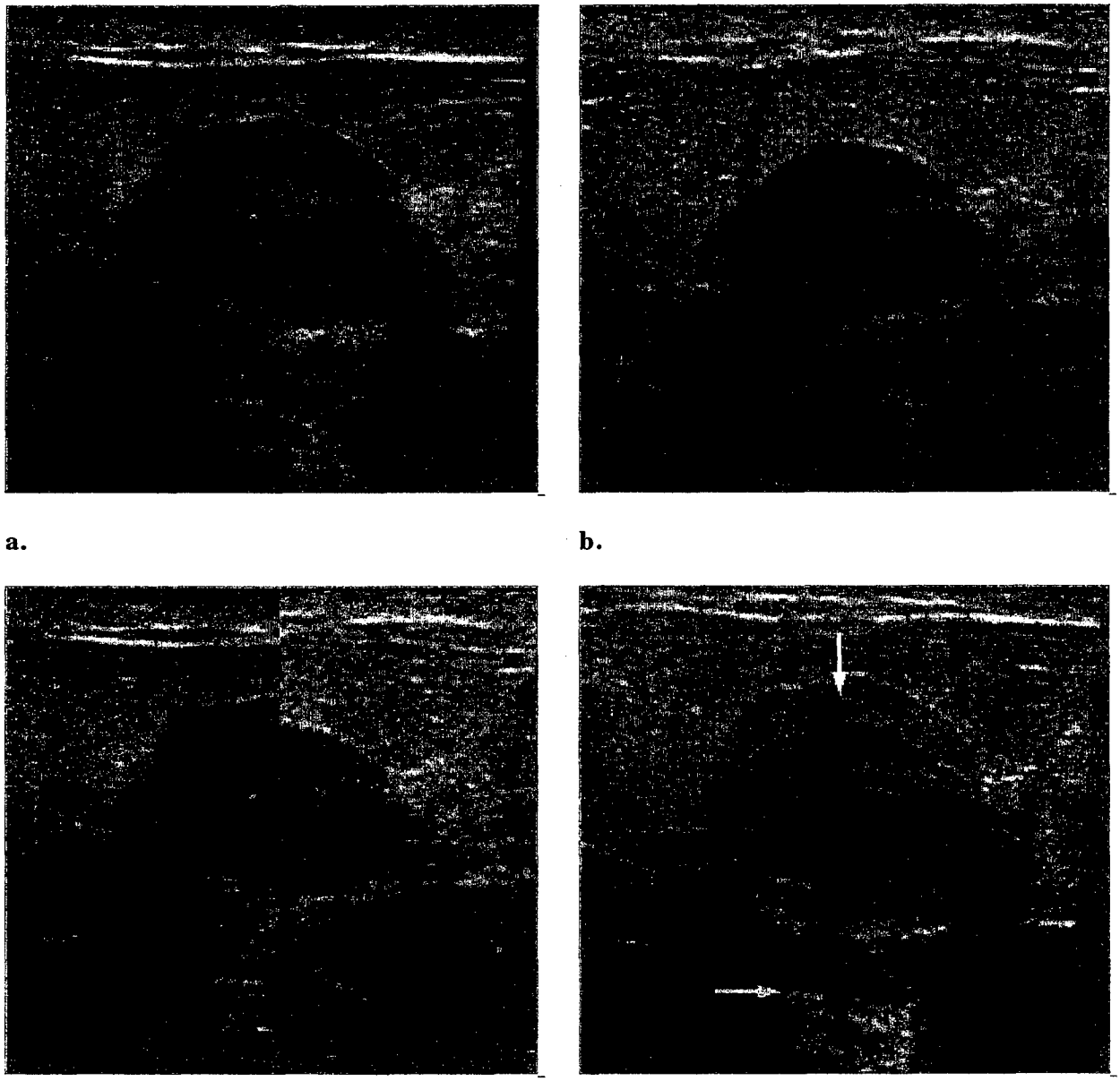

a. **b.**

c. **d.**

Figure 5. Coregistration of two sequential scans of a breast lesion in a patient undergoing chemotherapy.

(**a**) Central B-scan frame of the first scan, obtained 1 week before the start of therapy, coregistered and transformed to map onto the second scan. (**b**) Corresponding frame of the second scan, obtained 5 weeks later. (**c**) Combined view of the same frame in the first (left) and second scan (right). Click here for a Quicktime "wiper" movie (304 kB) showing the temporal changes throughout the frame obtained by moving the border between the scans from left to right. (**d**) Pseudo-color image of the differences between the two scans, showing increased echogenicity (blue) where the mass shrank (white arrow) and decreased echogenicity (yellow) below the mass (gray arrow). Click here for a movie (292 kB) showing the differences throughout the scanned volume.

Figure 5a and 5b show corresponding frames from the center of the first and second scans, respectively, after coregistration of the volumes. In this case, the first scan was transformed by using a full affine transformation to map onto the second one. In a serial study with scans obtained manually and several weeks apart, small changes in view direction or positioning of the transducer are unavoidable even if the sonographer tries to carefully reproduce the FOV of a previous scan. These variations can make direct comparison of two serial scans more difficult. However, if the two scans have enough common information, the registration software can detect these changes and transform one set accordingly. Hence, the slight rotation of the image in Figure 5a can be understood as a correction to a small change in view direction between the two scans.

Figure 5c shows a combined view of the frames displayed in Figure 5a (left half) and 5b (right half of the image), and reveals the change in size and other characteristics of the lesion. Also seen is a small error in aligning the specular reflectors at the top of the images, assuming the same tissue planes are producing the specular reflections in the two scans. This near-field error is most likely the result of a local deformation of the tissue by the pressure of the transducer against the skin. The estimation of the average misregistration in this serial study is difficult and prone to error because of the additional effect of drug-induced changes over time. These changes cannot be unambiguously distinguished from the other causes of registration error discussed above. However, estimation of the average error by identification of corresponding landmarks in the two registered data sets well outside the tumor volume, resulted in a mean error of 1.4 mm (peak, 2.2 mm).

For better visual evaluation of the registration quality and change in tumor size, a Quicktime movie (304 kB) can be viewed. In the movie, the border between the two scans as displayed in Figure 5c can be moved from left to right, thus revealing more of the first or the second scan.

In Figure 5d, the change in tumor size is highlighted by using a pseudo-color display. By simultaneously feeding the gray-scale values of the coregistered first scan into the red and green channels of an RGB (red, green, blue) display and the gray-scale values of the second scan into the blue channel of the same display, a difference image is created with a color map from yellow (echogenicity of first scan greater) through gray (echogenicities identical) to blue (echogenicity of second scan greater). The saturation of the colors is proportional to the difference in gray-scale value; in other words, the larger the difference, the stronger the color. The shrinkage of the hypoechoic mass causes an increase in echogenicity on the mass periphery in the second scan compared to the first. This difference is clearly visible as a blue rim (white arrow) surrounding the proximal half of the mass in Figure 5d. The distal part of the mass shows no such blue rim and therefore appears to be unchanged. This may be explained by the surrounding anatomy, which can cause asymmetric tissue deformation and displacement around the shrinking mass.

The other prominent feature in this figure is the yellow area immediately below the tumor (gray arrow), indicating an area of decreased echogenicity. This decrease could be explained by a mostly blood-filled mass that has lower attenuation than the surrounding tissue and thus causes an enhancement artifact below the mass. The smaller mass in the second scan causes a less pronounced artifact and therefore a decrease in echogenicity below the mass compared with the first scan. This can also be seen by comparing Figure 5a and 5b, but it is more obvious in the color display of Figure 5d.

A movie (292 kB) can be displayed showing the difference image of Figure 5d for 47 frames of the scanned volume. Note the shrinkage of the mass in all three dimensions by following the blue rim throughout the movie. Quantitative evaluation of the entire scan using polygons to manually define the border of the lesion in each frame yielded a reduction in lesion volume of approximately 27%.

Reproducibility of Results

More examples must be registered to study case-to-case variations in accuracy and the factors limiting the function of the registration algorithm. So far, two examples of multimode registration, five examples of extended volumes, and five sequential cases have been studied. By visual assessment, the two multimode registrations were of similar quality and four of the sequential cases were of comparable quality. In a fifth case, no registration could be found. Visual inspection showed that either the sonographer had not scanned enough of the same volume in the two sequential scans or the mass had disappeared completely in response to treatment. In the extended-volume studies, four out of five cases were similar to the one displayed here. In the fifth case, the overlap was less than 1 cm and no acceptable registration was found.

[Previous: Materials and Methods] [Next: Discussion]

[Title Page | Abstract | Introduction | Materials and Methods]
[Results | Discussion | References]

Discussion

The examples described are successful and important applications of image registration in 3D US imaging. They demonstrate the feasibility of a new technique for improving US diagnostics and potentially opening a new range of related applications. Routine coregistration and combination of image sets obtained with use of a variety of different US modes or using US and a second imaging modality should be possible with the same or only slightly modified version of the currently used registration software.

In US multimode imaging, coregistration should allow image optimization: replacement of a lower-quality component of one image set with the higher-quality component of a different set, as in the substitution of high-resolution gray-scale data for the lower-resolution gray-scale "background" of color Doppler flow imaging modes. Coregistration should also allow image fusion: the combination of images displaying different physical properties, which increases the diagnostic value of either one of the original images by relating one physical property to another. Note that the reduced quality of the image in color Doppler mode relative to gray-scale mode is due to natural timing constraints in image formation and is therefore likely present to some extent in most or all modern US scanners. The difference is probably more marked here because the matrix array used allows more image improvements in the gray-scale images that cannot be realized in color Doppler modes than is usually possible with one-dimensional arrays.

Possible modes for image fusion can include, but are not restricted to, frequency-shift and power-mode Doppler, harmonic imaging, and new modes being researched and developed, such as imaging with contrast agents or elasticity US imaging (27,28). The quality of the registration depends on the information content of the images; more specifically, the mutual information. Where only gray-scale information was used for the registration, the accuracy did not allow an exact pixel-by-pixel match, but the registration was far better than can be done manually.

In multimodality imaging, coregistration of US scans with MR, CT, and other 3D data sets or with projection images such as mammograms can be envisioned. If a US scan were to be obtained in the same or a similar geometry as a mammogram, coregistration of a projection of the US scan with the mammogram could combine the most inexpensive and commonly used modalities for breast imaging. This would add 3D information to the 2D mammogram and allow more accurate tracking of lesions identified in the mammogram by using 3D US imaging.

Extended volume imaging is a method for overcoming one of the major disadvantages of US imaging compared with most other modalities: the limited FOV and unsystematic coverage of the region of interest. In breast imaging, a wider FOV should be particularly desirable in following up suspicious regions and in detection of preclinical disease. To follow up in 3D the morphology of a large lesion and its effect on surrounding tissue, a larger FOV will be essential. A combination of extended volume imaging and multimode (gray-scale and color Doppler) imaging would even allow tracking of vascular and tissue morphology simultaneously in high-quality images. Screening of women at very high risk for breast cancer is beginning to draw more interest in US imaging, with incidental detection of malignant foci at locations removed from the site of suspicion (29). Accordingly, extended volume imaging is likely to increase the sensitivity of US imaging in breast cancer detection. A wider FOV will also help in covering previously scanned sites and thus determining changes over time in screening of high-risk groups, tracking of suspicious regions, or monitoring response to treatment. Although radiologists and sonographers can reach high skill levels, it is often difficult for some operators to ensure that the same views are obtained in two or more serial studies. Interpretation is also complicated when the interpreter has not personally performed the examination. Both problems could be reduced with extended volume imaging.

The accuracy of coregistration of partly overlapping volumes appears to depend on the size of the overlap. It is possible that the larger the overlap the more common structure is available to align the scans and the less the registration algorithm is potentially affected by noise. The minimum overlap required for acceptable registration accuracy can vary with the information content of the data sets. However, in the examples studied so far, a 1-cm (25%) overlap generally produced acceptable registration, judged by visual inspection.

Coregistration of sequential studies may enhance manual (visual) detection of changes in several ways, and may eventually allow semiautomatic or automatic volume change estimations. First, the registration corrects for slight changes in scan position and view direction, and thus allows direct comparison of the same areas imaged at different times. This may resolve ambiguities in the actual location of the scans and may also help in detecting subtle changes that go unnoticed in unregistered scans. Second, registered sequential scans allow new display techniques that emphasize changes between scans, such as the difference image shown in Figure 5d. Use of this type of difference image may enhance and accelerate the detection of changes, and it may ultimately be possible to segment regions of shrinkage and growth for rapid, semiautomatic volume change estimations. Third, if the registration is predominantly based on a mass and its boundaries, and if nonrigid linear or nonlinear transformations are used, the registration could map the boundaries at one time point to the boundaries at another time point. The transformation matrix itself then contains information about size changes and could also be used for semiautomatic volume change estimations. Note also that the registrations can be obtained semiautomatically and with limited user interaction. Manual registration in 3D by visual comparison of two volumes may be possible, but it is a time-consuming and tedious process and subject to user variability.

For serial studies, the extended volume imaging technique might be combined with coregistration of scans obtained at different times. This would allow the visualization and quantification of changes in large lesions over time. In fact, the acquisition and composition of an extended FOV might prove to be necessary for tracking large, rapidly changing, lesions because, in this case, a small FOV might not contain enough unchanged structure (which is usually found well outside the volume of the mass) for the coregistration to work properly. If routinely used in serial studies of women with high risk of breast cancer, coregistration could help detect early changes not apparent in multiple small-FOV scans, thus increasing the chances of effective treatment.

For validation of quantitative measurements made in coregistered image sets, automated error estimation is desirable. The quality of coregistrations can vary greatly with the available mutual information, which depends on the amount of shadowing, specular reflectors, and local tissue deformation present in the image sets. Manual evaluation, as in the examples presented here, may not be practical to ensure accuracy of quantitative measurements of dimensions over large distances.

A variety of automatic evaluation techniques can be envisioned and will be explored and compared with each other and with

manual evaluation to find the most accurate and practical method.

An accuracy measure similar to the average alignment error obtained manually can be computed by splitting up the two registered volumes into a number of subvolumes and performing an iterated registration on each of the pairs of subvolumes, by using simple rotate-translate or full affine transformations. Since the subvolumes are already approximately aligned, the control points for the second registration can be placed automatically and do not require user interaction. Assuming that the main cause of error in the initial registration is local tissue deformation unaccounted for by the global deformation model applied, an iterated registration on small subvolumes should greatly increase the accuracy of the alignment. If the remaining error after the second registration is assumed to be small relative to the initial error, the registered subvolumes can be used as references representing "true" alignment. The mean translation vector of all subvolumes from their positions after the first registration to their positions after the second registration can be used as an estimate of the average alignment error. Compared with the manually obtained estimate it will have the advantage of covering the entire volume and being almost user independent.

Alternatively, instead of splitting up the volume and performing linear geometric transformations on each subvolume, a reference registration using a global nonlinear transformation can be obtained. The data sets can be registered with a warping transformation defined by an increasing number of control points until the mutual information of the final registration converges. Thus the mean warping distance of the final transformation can be used as another estimate of the alignment error after the initial registration.

Both manual and automatic estimation of average alignment errors can be validated by scanning tissue phantoms with an additional, known distribution of point reflectors. The point reflectors are common landmarks in the registered sets that can be unambiguously identified, thus enabling an accurate manual error estimation that can serve as a standard of reference. For the registration procedure, the point reflectors must be deleted from the digitized data sets (replaced by zero values); otherwise, they would provide additional information that leads to better registration than in the tissue phantom alone. The same data sets (with the point reflectors removed) can be used for both manual and automatic error estimation and compared to the reference standard based on the original data sets.

A problem with phantom studies is the difficulty of accurately simulating breast tissue, including phase aberrations and tissue deformability. Current phantoms known to the authors either do not exhibit the aberrations present in real breast tissue or are much less deformable than breast tissue (30). As a result, the registration obtained in phantoms might be more accurate than in in vivo breast scans and therefore be unsuitable as a reference standard.

The accuracy information also helps determine which kind of mapping transformation is needed to provide clinically useful registrations. In the present study, only global linear (full affine) transformations were used. In cases with strong local tissue deformation, nonlinear warping transformations might be required to keep the registration error small. With warping, the registration algorithm may locally deform the 3D image set in order to map deformed tissues. Initial studies showed that including nonlinear transformations can increase the mapping accuracy significantly (31).

In future studies, the techniques developed here in breast scans could be applied to scans of other organs. Since phase aberrations and tissue deformability, which introduce registration errors, are particularly strong in breast tissue, registrations in liver, kidney, prostate, and other organs are likely to be at least of similar quality as the examples shown here.

[Previous: Results] [Next: References]

[Title Page | Abstract | Introduction | Materials and Methods]
[Results| Discussion | References]

References

1. Pietrzyk U, Herholz K, Heiss WD. Three-dimensional alignment of functional and morphological tomograms. J Comput Assist Tomogr 1990; 14:51-59.

2. Alpert NM, Bradshaw JF, Kennedy D, Correia JA. The principal axes transformation: a method for image registration. J Nucl Med 1990; 31:1717-1722.

3. Faber TL, McColl RW, Opperman RM, Corbett JR, Peshock RM. Spatial and temporal registration of cardiac SPECT and MR images: methods and evaluation. Radiology 1991; 179:857-861.

4. Loats H. CT and SPECT image registration and fusion for spatial localization of metastatic processes using radiolabeled monoclonals. J Nucl Med 1993; 34(suppl):562-566.

5. Hill DL, Hawkes DJ, Gleeson MJ, et al. Accurate frameless registration of MR and CT images of the head: applications in planning surgery and radiation therapy. Radiology 1994; 191:447-454.

6. Ardekani BA, Braun M, Hutton BF, Kanno I, Iida H. A fully automatic multimodality image registration algorithm. J Comput Assist Tomogr 1995; 19:615-623.

7. West J, Fitzpatrick JM, Wang MY, et al. Comparison and evaluation of retrospective intermodality brain image registration techniques. J Comput Assist Tomogr 1997; 21:554-566.

8. van Herk M, Bruce A, Kroes AP, Shouman T, Touw A, Lebesque JV. Quantification of organ motion during conformal radiotherapy of the prostate by three dimensional image registration. Int J Radiat Oncol Biol Phys 1995; 33:1311-1320.

9. Andersson JL. How to obtain high-accuracy image registration: application to movement correction of dynamic positron emission tomography data. Eur J Nucl Med 1998; 25:575-586.

10. Yin FF, Giger ML, Doi K, Vyborny CJ, Schmidt RA. Computerized detection of masses in digital mammograms: automated alignment of breast images and its effect on bilateral-subtraction technique. Med Phys 1994; 21:445-452.

11. Lehmann T, Sovakar A, Schmitt W, Repges R. A comparison of similarity measures for digital subtraction radiography. Comput Biol Med 1997; 27:151-167.

12. Leszczynski KW, Loose S, Boyko S. An image registration scheme applied to verification of radiation therapy. Br J Radiol 1998; 71:413-426.

13. Wilson DL, Carrillo A, Zheng L, Genc A, Duerk JL, Lewin JS. Evaluation of 3D image registration as applied to MR-guided thermal treatment of liver cancer. JMRI 1998; 8:77-84.

14. van den Elsen PA, Pol EJD, Viergever MA. Medical image matching: a review with classification. IEEE Eng Med Biol 1993; 12:26-39.

15. Candiani F. The latest in ultrasound: three-dimensional imaging. I. Eur J Radiol 1998; 27(suppl 2):S179-S182.

16. Campani R, Bottinelli O, Calliada F, Coscia D. The latest in ultrasound: three-dimensional imaging. II.Eur J Radiol 1998; 27(suppl 2):S183-S187.

17. Moskalik A, Carson PL, Meyer CR, Fowlkes JB, Rubin JM, Roubidoux MA. Registration of three-dimensional compound ultrasound scans of the breast for refraction and motion correction. Ultrasound Med Biol 1995; 21:769-778.

18. Meyer CR, LeCarpentier GL, Roubidoux MA, et al. Automated coregistration of three-dimensional ultrasound volumes by mutual information: sequential examples of breast masses. J Ultrasound Med 1998; 17:S1, S87.

19. Meyer CR, Boes JL, Kim B, et al. Semiautomatic registration of volumetric ultrasound scans. Ultrasound Med Biol (in press).

20. Weng L, Tirumalai AP, Lowery CM, et al. US extended-field-of-view imaging technology. Radiology 1997; 203:877-880.

21. Kroger K, Massalha K, Dobonici G, Rudofsky G. SieScape: a new sonographic dimension with fictive images. Ultrasound Med Biol 1998; 24:1125-1129.

22. Sivaramakrishna R, Gordon R. Detection of breast cancer at a smaller size can reduce the likelihood of metastatic spread: a

quantitative analysis. Acad Radiol 1997; 4:8-12.

23. LeCarpentier GL, Tridandapani PB, Fowlkes JB, Moskalik AP, Roubidoux MA, Carson PL. Utility of 3D US imaging in the discrimination and detection of breast cancer. RSNA EJ (in press).

24. Maes F, Collignon A, Vandermeulen D, Marchal G, Suetens P. Multimodality image registration by maximization of mutual information. IEEE Trans Med Imaging 1997; 16:187-198.

25. Kim B, Boes JL, Frey KA, Meyer CR. Mutual information for automated unwarping of rat brain autoradiographs. Neuroimage 1997; 5:31-40.

26. Meyer CR, Boes JL, Kim B, et al. Demonstration of accuracy and clinical versatility of mutual information for automatic multimodality image fusion using affine and thin plate spline warped geometric deformations. Med Image Anal 1997; 1:195-206.

27. Shapo BM, Crowe JR, Erkamp R, Emelianov SY, Eberle MJ, O'Donnell M. Strain imaging of coronary arteries with intraluminal ultrasound: experiments on an inhomogeneous phantom. Ultrason Imaging 1996; 18:173-191.

28. Erkamp RQ, Wiggins P, Skovoroda AR, Emelianov SY, O'Donnell M. Measuring the elastic modulus of small tissue samples. Ultrason Imaging 1998; 20:17-28.

29. Gordon PB, Goldenberg SL. Malignant breast masses detected only by ultrasound: a retrospective review. Cancer 1995; 76:626-630.

30. Madsen EL, Kelly-Fry E, Frank GR. Anthropomorphic phantoms for assessing systems used in ultrasound imaging of the compressed breast. Ultrasound Med Biol 1988; 14(suppl 1):183-201.

31. Krücker JF, Meyer CR, Tuthill TA, LeCarpentier GL, Fowlkes JB, Carson PL. 3-D compounding of B-scan ultrasound images. Acoustical Society of America (in press).

[Previous: Discussion]

[Title Page | Abstract | Introduction | Materials and Methods]
[Results | Discussion | References]

Ultrasound in Med. & Biol., Vol. 23, No. 6, pp. 837–849, 1997
Copyright © 1997 World Federation for Ultrasound in Medicine & Biology
Printed in the USA. All rights reserved
0301-5629/97 $17.00 + .00

ELSEVIER

PII S0301-5629(97)00073-2

●*Original Contribution*

THE 3D AND 2D COLOR FLOW DISPLAY OF BREAST MASSES

PAUL L. CARSON,[†] AARON P. MOSKALIK,[†] ANURAG GOVIL,[†]
MARILYN A. ROUBIDOUX,[†] J. BRIAN FOWLKES,[†] DANIEL NORMOLLE,[‡]
DORIT D. ADLER,[†] JONATHAN M. RUBIN[†] and MARK HELVIE[†]
Departments of [†]Radiology and [‡]Biostatistics, University of Michigan Medical Center, Ann Arbor, MI 48109 USA

(*Received* 19 *December* 1996; *in final form* 8 *April* 1997)

Abstract—A prospective study was performed in 24 women with breast masses on mammography going on to surgical biopsy. 2D and 3D power mode and frequency shift color flow Doppler scanning and display were compared. Vessels were displayed as rotatable color volumes in 3D, superimposed on gray-scale slices. The latter were stepped sequentially through the imaged volume. Radiologists rated the masses in each display (3D, 2D and videotapes) on a scale of 1 to 5 (5 = most suspicious) for each of six conventional gray-scale and six new vascular criteria. Thirteen masses proved to be benign and 11 were malignant. 3D provided a stronger subjective appreciation of vascular morphology and allowed somewhat better ultrasound discrimination of malignant masses than did the 2D images or videotapes (specificities of 85%, 79% and 71%, respectively, at a sensitivity of 90%). Only in 3D did the vascularity measures display a trend towards significance in this small study. © 1997 World Federation for Ultrasound in Medicine & Biology.

Key Words: **Blood, Angiogenesis, Blood volume, Perfusion, Ultrasound, Doppler, Image processing, Three-dimensional imaging, Breast cancer, Diagnostic imaging.**

INTRODUCTION

In order to further standardize breast-lesion vascularity measures, allow better appreciation of the 3D vascular morphology, and evaluate information provided in the new power-mode color-flow images, 3D acquisition and display techniques were developed. A study was performed using 3D ultrasound examinations of women with breast masses scheduled for subsequent breast biopsy. Each examination consisted of 1 or more power-mode 3D scans, a frequency-shift 3D scan of the mass and surrounding tissue, (usually) a video tape record of these scans, and 2D films of interesting gray-scale and vascular features at the time of the examination.

Angiogenesis associated with tumor growth has been claimed to be an indicator of malignancy and possible predictor of metastasis (Folkman and Shing 1992; Weidner et al. 1992; Weidner 1995). Studies suggest that there are fundamental differences between benign and malignant vasculature. As in many other malignancies, rapid, intense and/or extended enhancement with CT, radionuclide and MRI contrast agents are a feature of all or part of most malignant breast lesions (Sakki 1974; Chang et al. 1982; Watt et al. 1986; Wahl et al. 1991; Chenevert et al. 1994).

In recent years, therefore, there has been increased interest in using Doppler ultrasound when examining solid breast lesions to differentiate malignant from benign lesions. Some earlier studies began with the simple criterion of the presence of detectable vasculature near or in the lesion as a positive indicator of malignancy (Dixon et al. 1992; Adler et al. 1990; Cosgrove and Lees 1994; Carson et al. 1992; Lagalla et al. 1994). Other indicators were added, with varied levels of success. The robustness of the simplest criterion, presence of detectable vasculature near or in the lesion, as well as most other vascularity measures, suffers because the threshold is dependent on machine sensitivity. Measures based on color velocity values appear to be more robust than color pixel density (Fein et al. 1995).

Other studies have utilized the velocity information provided by spectral Doppler and color flow Doppler to characterize malignancy by calculating parameters, such as peak flow velocity, resistive index,

Address correspondence to: Paul Carson, Ph.D., Professor of Radiology, Kresge III, Rm. R2315, University of Michigan Medical Center, Ann Arbor, MI 48109-0553 USA. E-mail: pcarson@umich.edu

and pulsatility index (McNicholas et al. 1993; Kuijpers et al. 1994; Madjar et al. 1994; Peters-Engl et al. 1995). The results from these studies have been highly mixed, as might be expected for local measures of complex tumor structures using incomplete search procedures.

Another method to detect malignancy involves observation of the vascular pattern. This can entail counting vessels (Heilenkotter and Jagella 1993; McNicholas et al. 1993; Madjar et al. 1994), counting vessels that penetrate a mass (Bergonzi et al. 1993; Calliada et al. 1994; De Albertis et al. 1995), and evaluating vessel morphology such as tortuosity (Heilenkotter and Jagella 1993; Calliada et al. 1994). The excellent quality and relative simplicity of displaying color-flow image data in 3D was illustrated by Picot et al. (1993). 3D volumetric quantitative measures, such as color pixel density and mean color value, have also been investigated (Pretorius et al. 1992; Carson et al. 1993; Huber et al. 1994; Kedar et al. 1995). Normalization of the signal levels to the level from the largest blood signal at the same depth, and other 3D measures of the power mode signal have been introduced (Carson et al. 1993). Most of these vascularity studies yielded similar results, with a quoted sensitivity of around 90% and a specificity of around 70%, or *vice versa*, depending on how the criteria were chosen. Clearly, there are often differences between malignant and benign vasculature that can be detected by Doppler ultrasound, but the value of Doppler images in addition to pulse echo studies is still debated strongly.

The difficulty in providing accurate differentiation between benign and malignant masses includes more than just finding definitive or dependable measures. The vascularity in some patients may be changed systemically or locally around lesions due to other factors, such as the increased vascularity resulting from needle aspiration (Kedar and Cosgrove 1994). Systemic acoustic differences between patients can be accounted for by comparison to the contralateral breast (Scherzinger et al. 1989; Blohmer et al. 1995). Other factors that can cause ambiguity are differences between machines, machine settings, depth of the lesion, properties of overlying tissues, and Doppler angle. In most studies, many of these factors are ignored, making the results difficult to reproduce.

Diagnosis does not have to rely on vascularity independent of other indicators. Some investigators with careful technique and good equipment have become very skilled at cancer discrimination using pulse-echo gray-scale analysis (Venta et al. 1994; Leucht et al. 1988). When the objective was clearly defined as prevention of unnecessary biopsies and the gray-scale criteria for designating a lesion as benign were very stringently set, Stavros et al. (1995) achieved a false-negative rate of only 0.5% in a population of 750 biopsy-proven cancers. In that study, decisions based on the ultrasound appearance would have eliminated 420 of the 750 scheduled biopsies, with 2 malignant masses being missed. If independent measures such as vascularity were added only to distinguish benign or probably benign from malignant lesions, this extremely small false-negative rate might be achievable in more centers.

A recent large multicenter study with modern color-flow systems (Goldberg et al. 1993) suggested that ultrasound evaluation of breast lesions has been significantly improved in the past few years. Although some of the participating investigators concluded that the additional information from color-flow was marginal, others reported that the improvement in specificity of ultrasound over mammography was statistically significant only if Doppler results were added to the pulse-echo results. The addition of color-flow Doppler to the B-mode improved the diagnostic accuracy by an amount approximately equal to the benefit of adding ultrasound to mammography (Cosgrove and Lees 1994; Cosgrove et al. 1993). Positive predictive value almost doubled over mammography alone and the false-negative rate was only 1.7%.

The possibility of new methods for regional vascularity assessment (Dymling et al. 1991; Carson et al. 1993) helped motivate the development of medical color-flow imaging with display of the Doppler signal power, instead of the estimated Doppler frequency shift (Rubin et al. 1994). The combination of high-resolution power Doppler and frequency-shift color Doppler imaging now provides the opportunity to assess the accuracy of regional vascularity (Rubin et al. 1995) and provide more qualitative studies with available instrumentation, such as the research reported here.

METHODS

Women were selected after identification of a mass based on mammography and/or clinical examination. Masses of very low suspicion (*e.g.*, most fibroadenomas) were not included. All patients in the study were scheduled for surgical biopsy of the mass as part of their clinical management. Informed consent was obtained from all participating women. 3D scans were acquired using the system described and depicted in Moskalik et al. (1995). The system consisted of a conventional ultrasound scanner (Spectra VST, Diasonics, Inc., San Jose, CA, USA), a modified mammography unit that applies mild compression to immo-

bilize the breast, a frame grabber that is used to acquire video images from the ultrasound imager, and a motorized transducer positioner mounted on the mammography unit. A typical scan through an acoustically transparent window produces a 3D volume of ultrasound data of the suspicious region of the breast from a series of approximately coronal 2D images. These are separated typically by approximately $3/f$ (mm), where f is the Doppler imaging frequency in MHz, or, preferably, by half the 6 dB focal slice thickness. These empirical relations are based on our experience with maintaining enough coherence between adjacent slices to allow continuous volume rendering of the vasculature. At the 6-MHz Doppler frequency of our 6–10 MHz linear array, the step size was 0.5 mm. This is accomplished by mounting the imaging array to the positioner. The breast is placed in the mammographic unit, and the array is moved in 0.5-mm steps across the region of interest as the frame grabber acquires the 2D images. Data from the 50–120 images are then transferred to a workstation. With the linear array scanhead employed for this study, the images were typically 38 mm by 40 or 50 mm. Power-mode Doppler ultrasound was performed at a PRF of 700Hz, and an ensemble length of 14, the minimum sample length and the maximum gain not producing frequent color noise. The 2D images utilized for comparison with the 3D included the best free-hand images photographed during a conventional color-flow study, which also served to help identify the mass region for the 3D scan. Also available to the readers when desired for the 2D interpretations were the individual digital images recorded during the slowly stepped slices from the 3D acquisitions. This helped assure that at least as much ultrasound information was potentially available for the 2D as for the 3D readings. The videotapes usually included much of the preliminary searching for the correct region for 3D scanning, and often included the real-time display of the slowly stepped 3D scanning.

Two types of analysis are being performed with the resulting data. The analysis reported in this paper is comparative assessment of visualization using 3D and 2D imaging techniques, with and without vascularity criteria, as described below. The other analysis currently in progress is measurement of the signals produced in the 2 color-flow modes quantitatively to estimate vascularity features in various 3D regions of interest in and around the suspected masses (Carson et al. 1995).

Of 37 attempted studies, 24 were performed satisfactorily and were reviewed by 2 of the 3 reviewers in both the 3D display and 2D images. Eleven masses were pathologically proven to be cancer, five were fibroadenomas, and eight were other benign masses. Videotapes were available or technically acceptable on 14 of 24 cases, allowing videotape analysis on five cancerous, three fibroadenomatous, and six other benign masses. The order of viewing of the 3 display types by an individual reader was rotated randomly. In the conduct of research where humans were the subjects, the investigators adhered to the policies regarding the protection of human subjects as prescribed by 45 CFR 46 and 32 CFR 219 (Protection of Human Subjects).

There are 2 dominant methods of displaying relatively simple 3D objects, such as a few blood vessels, which fill a small fraction of the imaged volume. One method commonly employed in MR angiography is to trace rays in straight lines through the 3D data set and make a projection image like a radiograph with the dominant tissue representing x-ray attenuation as the detected blood flow. Usually, only the pixel with the strongest power-mode signal or highest frequency shift is represented along a given ray. This method is also being employed in several commercial and commercial-prototype packages for 3D ultrasound displays. As employed in our work, the second method requires setting a threshold Doppler power-mode signal level or threshold Doppler frequency shift, depending on the imaging mode. All adjacent pixels at that signal level are connected by 3D surfaces, termed isosurfaces.

With either display method, the selected 3D data can be viewed from any given angle. A rotating 3D display of vasculature that does not fill the volume too densely is effective at revealing the 3D morphology. With substantially more computing power, the 3D display can be rotated and shown in correct positional relationship with selected 2D slices of the full gray-scale/color-flow data. Addition of the gray-scale image or full gray-scale plus color image requires rapid texture rendering, as well as the isosurface rendering. An example of the Doppler isosurface-plus-gray-scale type of display is shown in Fig. 1. Throughout this study, the 3D display was offered as any desired combination of: 1. Stepping through the color flow images in their correct orientations; 2. Continuous 3D rendering of the vasculature, while either (a) stepping through the stack of 2D images, (b) rotating the vascular volume along with 1 chosen gray-scale slice, or (c) rotating the vasculature only.

Recently, we have developed 2 methods of improving the display technique with respect to the time required fully to appreciate the 3D vasculature and its relation to the gray-scale features of the lesion. These have been demonstrated on data from a few of the subjects in this study. The acquired stack of gray-scale slices is viewed sequentially with no vascular isosurface. In one of the new methods, a translucent render-

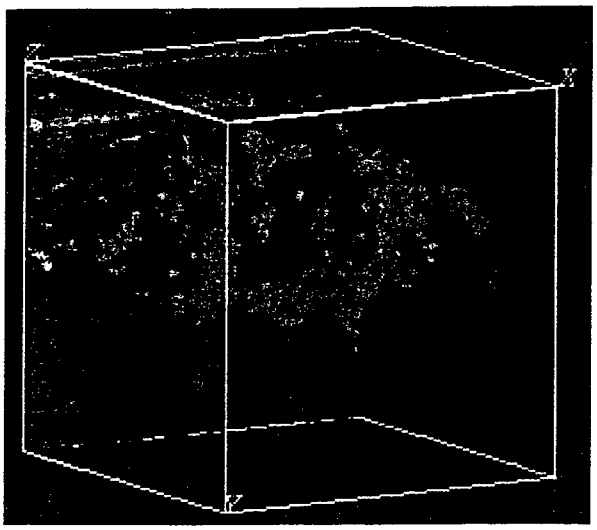

Fig. 1. 3D vascularity display utilizing isosurface rendering of power-mode data taken from a 45-y-old subject with invasive intraductal carcinoma. The gray-scale slice plane is shown in correct spatial relationship to the vessels. The last gray-scale plane is shown here so as not to obscure any of the vasculature. The position of the gray-scale information is usually moved through the volume-rendered vascularity. The entire volume is then rotated further to increase geometrical perception of the vascularity in relation to 1 or more gray-scale slices.

ing of the vasculature is shown superimposed on the gray-scale stack after every 3 to 4 steps. In the other method, the 3D vascular rendering is shown in a second window beside the sequential display of the gray-scale slices. A frame outline or a nearly transparent gray-scale slice is stepped through the 3D vascular rendering to reveal the location in 3D of the gray-scale slices being displayed in the first window. Both methods make it easier to correlate gray-scale information with vasculature, without hiding gray-scale information by the vascular rendering. When very fast display update is desired, a preprocessed stack of images is shown, although this is now becoming less necessary. The rendering of the images into a video or computer-displayed movie is also automated using a command line interface to our 3D rendering and image-processing software (Advanced Visualization System, AVS).

After imaging, the masses of the 24 women were then classified fibroadenoma, other benign or cancer; the first 2 categories were then grouped for analysis as noncancerous. With the videotape display, not all the masses were evaluated. The utility of the gray-scale and vascular criteria in discriminating malignant from benign masses was evaluated. To make this evaluation, assumptions concerning the relative frequency of malignant and benign masses in the population of interest and of the relative costs of misclassification were required. It was assumed that 20% of all masses are malignant, and 80% of all masses are benign, consistent with a typical mix of positive and negative findings at biopsy in a screening situation. There is a tremendous potential flexibility in the ratio of true-positive and true-negative findings in mammography clinics. The fact that typically only 20% of the cases recommended for biopsy prove malignant is a reflection of a broad medical judgment that the cost, in a very general sense of the word, is 5 times higher for a false-negative than for a false-positive. This ratio was assumed for the discriminant analysis.

With these assumptions, the linear discriminator using both the gray-scale and vascularity indices that minimized the expected total generalized cost was estimated. Probabilities of misclassification were estimated using cross-validated resubstitution, that is, each observation in the sample (the training sample) was withdrawn, the discriminating function reestimated, and then the withdrawn observation was classified. This technique produces a relatively conservative estimate of the error rate.

RESULTS

A gray-scale example of the 3D rendering of the vasculature (usually displayed in color) is shown in Fig. 1. This example represents a 3D ultrasound scan of a mass in a 45-y-old woman with microcalcifications in the left breast detected at mammographic screening. A nonpalpable 7-mm intraductal carcinoma (comedo type) with negative margins was diagnosed in a general area of florid fibrocystic change. A more complete illustration of the 3D display can be viewed on the Internet. The Internet images are compressed with some loss of resolution for improved display speed and storage considerations. The address on the World Wide Web is: http://www.med.umich.edu/ultrasound/breast_anim/develop/Case38.html. Instructions are given for viewing this animation with shareware such as Apple's Sparkle. In the Internet example, one of the new display techniques is illustrated. The gray-scale images are stepped through the volume in their relative 3D positions at a fixed rate. Following every 4 ultrasound slices, a view of the 3D Doppler signal isosurfaces is shown in place of the gray-scale for the duration of four image cycles.

The images were obtained in a coronal plane, with the central ultrasound beam at a 3 o'clock angle, but shifted approximately 2.5 cm cephalad to the level of the nipple. The beginning and ending frames, in the front and back of Fig. 1, respectively, are approximately 50 mm and 31 mm from the nipple. The small

Table 1. Six gray-scale criteria were defined with scales from 1 to 5. 5 being those characterized as the most malignant.

	Criterion description	Benign extreme (1)	Malignant extreme (5)
1	Margin of mass/smoothness	Smooth, no lobulations	Microlobulations
2	Shape	Spherical	Highly irregular
3	Sound attenuation of mass	Enhancement	Strong shadowing
4	Echogenicity of mass	Cyst or echogenic mass	Hypoechoic
5	Orientation of mass	Flattened	Taller than wide
6	Visibility of margins	Sharply defined	Diffuse margins

Scaling of Criterion 4, texture of mass, is not a linear scale because it is used to first distinguish between cystic and solid masses. Therefore, a rating of 1 corresponds to anechoic (cystic) and ratings 2–5 are solid masses, with 2 being most echogenic and 5 being hypoechoic.

cluster of microcalcifications seen on the mammogram corresponds to the upper left of slice 40, proximal to its acoustic shadow. This is at the end of a probable earlier surgical scar, apparent from a sharp shadow seen at approximately that location in the preceding few images. Significant vascularity wrapping around the margins of a tissue region is not seen until slices 109 to 133. The tissue partially enclosed by vascularity is slightly hypoechoic, but otherwise unremarkable.

To help standardize assessment of the gray-scale and 3D vascularity measures in breast lesions, the criteria in Tables 1 and 2 were developed for this study. These criteria were taken from the literature and our own experience. The central vascularity of tumors greater than 2 cm diameter was not evaluated, specifically because it was expected that the degree of necrosis would be highly variable and not diagnostic. Central vascularity is being evaluated in a companion quantitative study of these subjects (Carson et al. 1995). Table 3 shows results on several of the vascular criteria that individually were considered good discriminators between benign and malignant masses, because they received higher ratings on the 1 to 5 scale for cancer than for benign masses. For example, mean ratings from the 3D display for criterion 1, vascularity in the outer 1 cm of the mass, was 3.3 for malignant masses and 2.2 for fibroadenomas and other benign masses. With all 3 displays, vascularity from the mass border to 1 cm outside the mass (criterion 2), provided less discrimination between cancer and fibroadenomas than did vascularity in the mass. This is consistent with the diagnostic criterion that fibroadenomas and cancer have extensive external vascularity, but the vessels rarely penetrate the fibroadenoma (Bergonzi et al. 1993; Calliada et al. 1994; De Albertis et al. 1995). The last 2 vascular criteria in Table 2 were positively correlated with malignancy, but were not as discriminative individually. In the analysis below, they did not contribute positively to discrimination using criteria averages and were considered no further.

The radiologists reported a subjective improvement in understanding of the overall morphology and distribution of vessels resulting from the 3D images, as indicated by the relatively good benign/malignant discrimination in 3D by criteria 1–3. There was also an impression by the readers that hand searches in 2D for the correct angles to reveal shunting might be done as well, or better, in some cases, than in 3D. Overall, the morphology and extent of vascularity were believed to be seen much better in power mode than in frequency-shift mode.

In comparison with the 2D displays, there was thought to be little subjective advantage in reading gray-scale criteria with the 3D renderings. What improvement was observed was from seeing the gray-scale slices sequentially in their correct 3D locations.

Table 2. Eight vascular criteria were defined, also scaled from 1 to 5, 5 being the rating of the most malignant character of a criterion.

	Criterion description	Benign extreme (1)	Malignant extreme (5)
1	Vascularity in mass (outer cm)	None	Extensive (> 25% of mass)
2	Vascularity outside mass (to 1 cm away)	None	Extensive (> 25% of area)
3	Visible shunt vessels	None	Very clear or more than 2
4	Vessels wrapping around mass	None	Total involvement > 240°
5	Tortuosity of vessels	Gently curving	Very tortuous
6	Apparently related vessels, beyond 1 cm	None	Unusually large, fast flow
7	Unusual vascularity, no associated mass	None	Multiple, large, fast flow
8	General enlargement of breast vessels	None	Extensive

Table 3. Examples of results from four of the vascular criteria.

	3D	2D	Video
1. Mass vascularity, outer 1 cm			
Benign	2.2	2.0	2.4
Fibroadenoma	2.1	2.0	2.3
Malignant	3.3	2.9	2.9
2. Vascularity outside mass 1 cm			
Benign	2.4	2.2	2.6
Fibroadenoma	3.2	2.7	2.5
Malignant	3.7	2.9	2.8
3. Visible shunt vessels			
Benign	2.1	1.5	1.2
Fibroadenoma	1.6	1.6	2.0
Malignant	2.7	2.4	2.6
4. Vessels wrapping around mass			
Benign	1.9	1.7	1.6
Fibroadenoma	2.8	2.2	2.5
Malignant	3.5	2.6	2.4

The numbers represent the mean ranking for the given criterion over all readings of that mass type: malignant (n = 11), fibroadenomas (n = 5) and other benign masses (n = 8). Noting that a rating of 1 is most benign and a 5 most malignant in appearance, 3D generally received higher rankings because more vascularity was detected. 3D also provided a wider separation between malignant and other masses on all but Criterion 3.

The results of the discriminant analysis described in Methods are given in Table 4 and plotted as the solid lines in Figs. 2–4. Videotape is probably inferior to 2D and 3D, although the small sample size may make the comparison misleading. 3D appears slightly better than 2D, but the discriminator lines are similar.

Relative contributions of gray-scale and vascular indices in the linear discrimination were evaluated for each of the 3 displays. The p-values for significance in the discriminators are given in Table 5. Only in the 3D display did vascularity display a trend towards significance in this small study.

ROC curves for decision rules using gray-scale alone and gray-scale plus vascularity are shown for the 3D display in Fig. 5a. In Fig. 5b, ROC curves for decision rules using gray scale plus vascularity are drawn for the 3 different displays. The accuracies are the areas under these curves (Swets and Pickett 1982), with 3D having the largest accuracy. The discrimination threshold and numbers in Table 4 can be changed from those arrived at by the assumed cost factors. Selecting a 90% ratio of true-positives to all cancers (sensitivity in the group studied), the specificities for 3D, 2D and videotape displays were 85, 79 and 71%, respectively. At that same sensitivity of 90%, the specificities for 3D displays with gray-scale criteria and with gray-scale plus vascularity were 85 and 81%, respectively.

The visual readings as a function of lesion diameter are revealing. Lesion diameters from the largest among the mammography, ultrasound and pathology estimates are given. The diameters in mm as means (and ranges) are: malignant, 16 (6–25); fibroadenoma, 17 (14–23); other benign masses 18, (7–29). A plot of mean 3D gray-scale rating as a function of this maximum diameter shows strong discrimination of the smaller, 6–17 mm diameter, cancers from the benign masses of equivalent sizes. This discrimination is particularly good for cancer and fibroadenomas. 3D vascularity readings separate most of the largest, 15–25 mm, cancers (Fig. 6a). For fibroadenomas, the figure suggests an increase in vascularity with lesion diameter. A combination of the 3D vascularity plus three times the 3D gray-scale reading, all divided by four, reflects the relative weighting (the slope) of the discriminator shown in Fig. 2. This combination variable provides good separation of malignant from nonmalignant masses, as indicated in Fig. 6b. There is some suggestion that addition of lesion size information may aid the discrimination provided by the gray-scale and vascularity criteria shown in Fig. 2.

DISCUSSION AND CONCLUSIONS

New techniques for acquiring, displaying and interpreting 3D Doppler power-mode and frequency-shift color-flow and gray-scale images of the breast were developed and employed in this study. Vascularity, particularly the vascular morphology and extent, were considered subjectively to be revealed better in 3D than in the 2D displays. This was true even though

Table 4. Results using the gray scale and vascularity linear discriminators.

Condition	Benign		Cancer				
Classifeid	Benign TN	Cancer FN	Benign FP	Cancer TP	Specificity TN(TN + FP)	Pos Pr Val TP/(TP + FP)	Neg Pr Val TN/(TN + FN)
Videotape	7	2	2	3	77.8%	60.0%	77.8%
2D	10	3	1	10	76.9%	76.9%	90.9%
3D	10	3	0	11	76.9%	78.6%	100.0%

It was assumed 20% of all masses in the population to be studied are malignant and the financial and personal costs of a false-negative classification are 5 times the cost of a false positive.

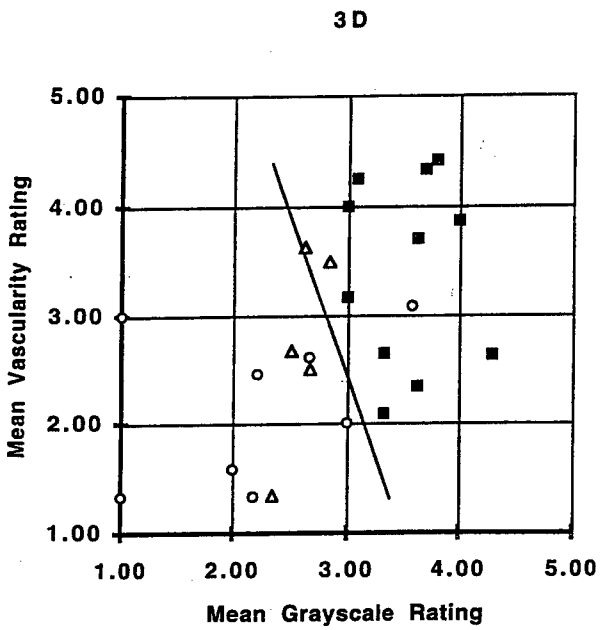

Fig. 2. Scatter plot from the 3D readings of the average ratings of the six vascular criteria versus the average ratings of the six selected gray scale criteria. Benign masses are shown as open symbols, fibroadenomas as (△) and other benign masses as (○). The malignant masses are shown as (■), clustered near the upper right-hand corner, as expected. The linear discriminator is shown as the solid line.

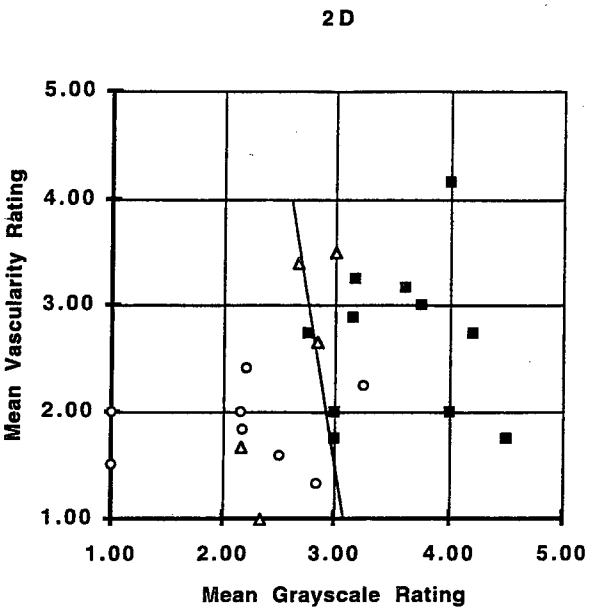

Fig. 3. Mean visual ratings from the 2D images. Vascular and gray scale criteria, the symbols and discriminator line are as in Fig. 2.

all the slices of the 3D image acquisition were available for viewing in the 2D assessment, as desired. The frequency-shift Doppler should emphasize the rapid flow associated with many tumors. Vascular morphology was better seen in power mode than in frequency-shift mode, but the 2 Doppler modes were not compared here. More extensive and angle-independent display of breast vascularity from compounded power and frequency-shift mode color-flow imaging has been illustrated by Moskalik et al. (1995), using reregistration of the different views. However, that technique was not practical for these clinical trials.

For statistical analysis, the incidence assumption that 20% and 80% of the masses are malignant and nonmalignant, respectively, were based on a reasonable mix for the group of patients usually going to biopsy, rather than the group with mammographic or palpable masses in this study. As listed in Tables 3 and 5. as well as Fig. 5b, videotape was probably inferior to 2D and 3D in the discrimination of cancer (lower sensitivity, specificity and negative predictive values). 3D was slightly better than 2D, with a higher sensitivity and negative predictive value.

Only in 3D did vascularity display a trend towards significance. Statistical significance is, of course, a function of sample size. If the distributions had been the same, but with a sample size 3 times larger, vascularity would have been significant at $p = 0.05$. Had it been 4 times larger and with the same results, vascularity would have been significant at $p = 0.01$. With the discriminators determined with vascularity and gray-

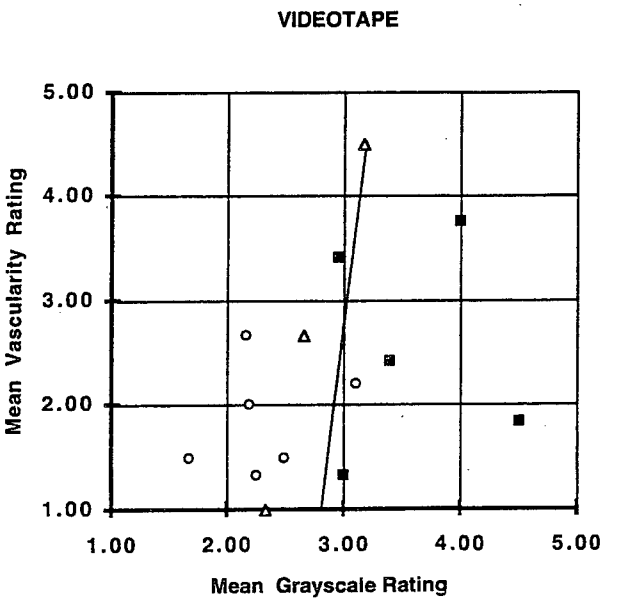

Fig. 4. Mean visual ratings from the videotapes of the actual examinations. Vascular and gray scale criteria: the symbols and discriminator line are as in Fig. 2.

Table 5. The p values for significance in the gray-scale and vascularity discriminators.

	Gray-scale	Vascularity
Videotape	0.0031	0.66
2D	0.0001	0.57
3D	0.0001	0.19

scale measures, the sensitivity, specificity, positive predictive value and negative predictive value of 3D were 100%, 77%, 79% and 100%, respectively. For these numbers to be meaningful for reducing unnecessary biopsies, a modest positive predictive value must be achieved while maintaining a very high negative predictive value in a much larger study, including a mix of all cases going to biopsy, not just those with identifiable masses. This might be feasible in a large study by increasing the assumed relative cost of false-negatives in determining the discrimination line in a new version of Fig. 2. It could then be determined if, with these newer techniques, the results are better than those (sensitivity, specificity, positive predictive value and negative predictive value of 98.4%, 68%, 38%, 99.5%) of the large gray-scale study of Stavros et al. (1995), or the as yet not fully published multicenter study with gray-scale and color-flow imaging (Goldberg et al. 1993, Cosgrove and Lees 1994). It might also prove in the long run that vascularity imaging in the dense breast would reveal some suspected cancers that are not mammographically detected and might otherwise be followed only by periodic exams.

Pulse echo ratings were quite similar for at least the 3D displays and 2D images. This is as expected, because, unlike the vascular display, we have not undertaken the more difficult task of surface rendering of gray-scale structures to show them in 3D much better than in 2D. It was noted subjectively that, even without the 3D vascular rendering, it was helpful to see the gray-scale images in their proper relative locations in space, at least as a substitute for personally performing the gray-scale scanning. Subjective impressions were that the power mode revealed vascular patterns more fully than did the frequency-shift mode of color-flow images. However, that distinction between modes was not the purpose of the study and was not rated systematically.

The videotape was meant to simulate the physicians performing the examinations themselves or, more accurately, observing the real-time examination on a remote monitor. Because videotaped images are of inferior quality and that technique is rarely employed clinically, examinations were not disqualified when there was both no time for separate video recording and the scanner was in a condition such that we were unable simultaneously to record the images digitally and on videotape. The image reviewers rarely found additional information on the videotape records and had a clear preference for the other 2 displays.

Because of the rather large fluctuations in any one vascular or gray-scale criterion in the visual analyses, taking the maximum reading from any 1 vascular and 1 gray-scale criterion did not provide

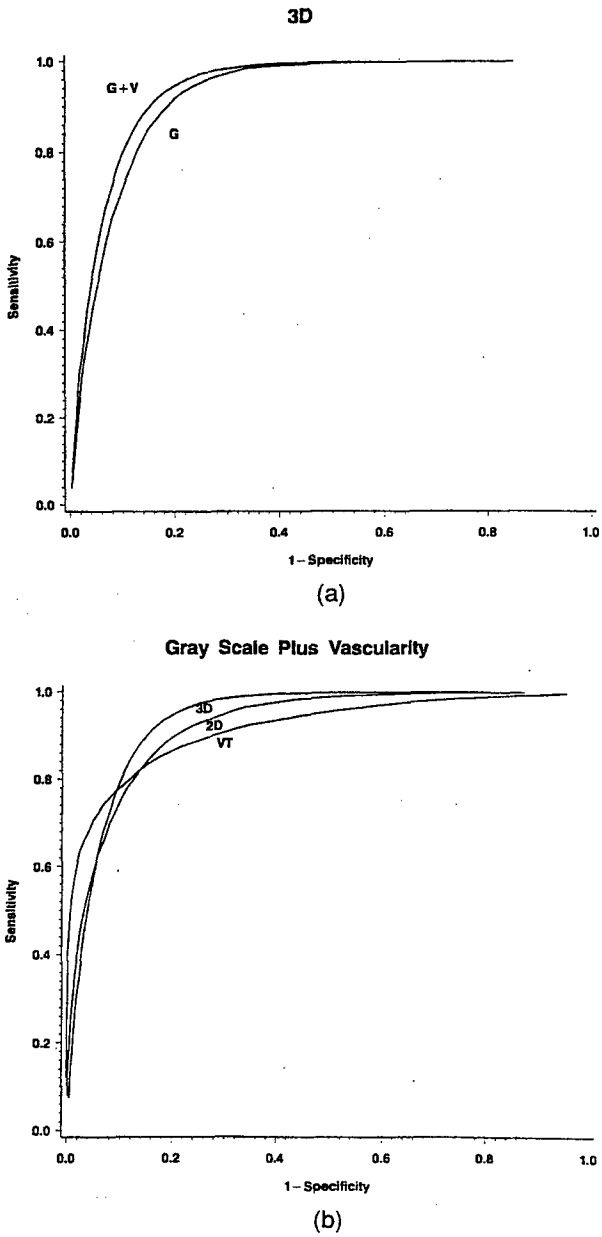

Fig. 5. ROC curves of the data in Figs. 2–4. The curves are for decision rules using: (a) Gray-scale alone and gray-scale plus vascularity for the 3D display, Fig. 2. (b) Gray-scale plus vascularity for the 3 different displays.

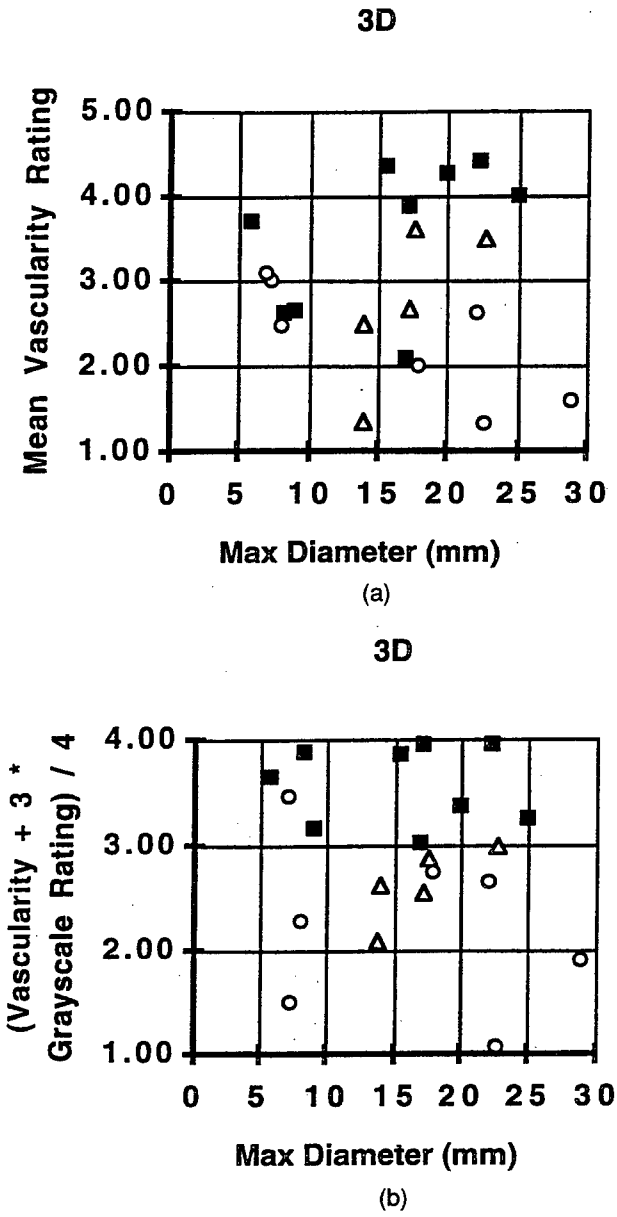

Fig. 6. Visual readings as a function of the largest mass diameter as obtained from 3 different measures of the mass dimensions. Readings of: (a) Mean vascularity. and (b) A combination in which gray-scale readings are weighted by 3 times those of the vascularity readings.

very good discrimination. Other combinations, such as the average reading from the three criteria correlating best with cancer discrimination in the sample, performed only marginally better than any 1 criterion. Only the average readings of the 6 mass-related vascular criteria (excluding criteria 6 and 7 in Table 2) and the 6 gray-scale criteria provided good discrimination. It might be hoped that overall vascularity throughout the 3D volume scanned would be a good discriminator because simple methods might be developed to test that criterion. In this study, however, vascularity throughout the breast was not a particularly good or even average discriminator. Examination time constraints did not allow a consistent assessment of pulsatility or of a high density of small vessel, multidirectional flow in the frequency-shift color-flow images. These might be reassessed, particularly as small-vessel sensitivity of frequency-shift color-flow imaging is increased via the instrumentation or contrast agents.

The apparent increase in vascular penetration of a gray-scale-defined cancer (Fig. 7a, b), compared with a fibroadenoma (Fig. 8a, b) suggests that vascularity in the outer 1-cm radius of the mass, or its ratio to the vascularity immediately outside the mass, should be quite important. However, in this small study, these criteria, 1 and 2, did not stand out over the other mass-related vascular criteria. The observation that the 2 youngest women with breast cancer also had the most vascular lesions is consistent with the fibroadenoma data of Cosgrove et al. (1993).

This research was, in part, an effort to develop more specific hypotheses about visual discrimination of breast cancer with 3D imaging of vascularity and gray-scale features. It would be appropriate to test the conclusions and discriminant values of this study on an independent set of subjects. It is hoped that such study could provide more information on whether or not vascularity is a particularly good discriminator, and possibly detector, of cancer in women less than 40 or 45 y old.

At the initiation of this study, the types of 3D displays employed were cumbersome, using affordable equipment. However, 3D hardware and software are improving rapidly and, indeed, are already at or close to functional speed for these techniques for less than $25000 worth of computer components and software, prior to packaging as a medical product. Now that dedicated chips for 3D display in PCs are beginning to be produced in mass quantities, prices are falling rapidly.

The main issues in evaluating 3D versus 2D techniques with ultrasound are different than those in the other high-resolution tomographic modalities. Conventional 2D ultrasound techniques generally include rapid, intuitive, real-time searches from numerous angles to find any views that best show features of interest through the overlying aberrating tissues. By comparison, any 1 3D scan might not have the best viewing location and angle for most of the region of interest, even when guided by real-time 2D imaging. However, 3D offers systematic scanning and imaging

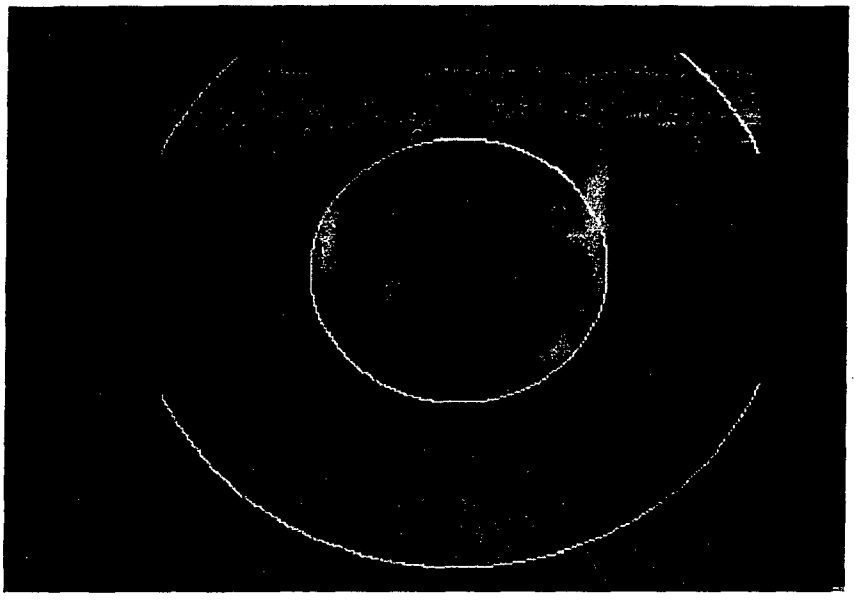

(a)

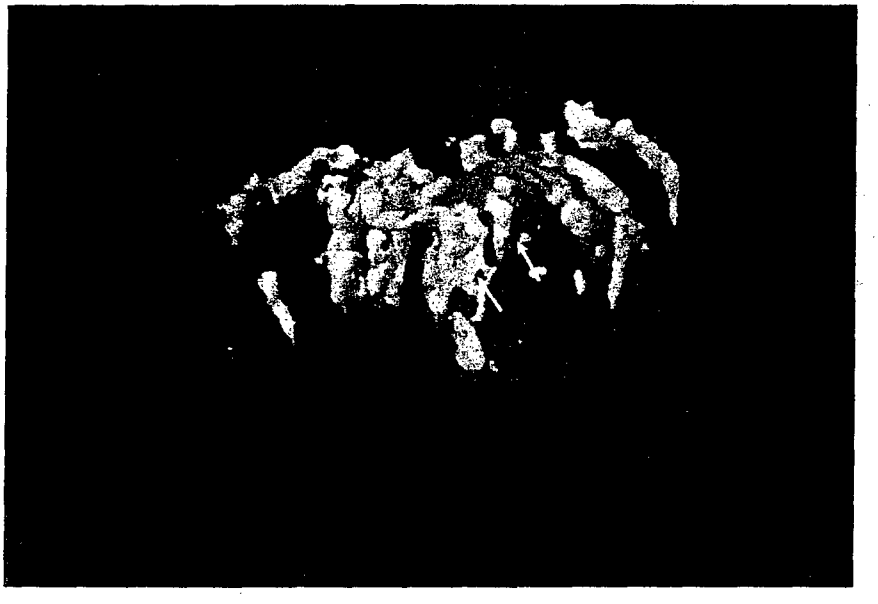

(b)

Fig. 7. Power mode-detected vascularity from a 2.5 × 2 cm malignant nodule in a 33-y-old woman is displayed as bright regions of relatively smooth texture in (a) 2D and (b) 3D. (a) Power-mode color-flow image approximately through the center of the mass, with outlines of the identified mass region and a region 1 cm beyond. (b) Power-mode-detected vascularity displayed as isosurfaces, with a pulse echo slice shown at the edge of the scanned volume on the nipple side. Here, the nodule is outlined at its estimated gray-scale and palpable borders by a translucent ellipsoid at the right posterior edge. Vessels surround and penetrate this ellipsoid. Example penetrating vessels are marked by solid arrows.

of the entire mass region, scanned and sampled at rates optimized for pulse echo or color flow Doppler sensitivity. The 3D display also can be presented at a convenient time with full flexibility. The display offers a high information content per view and reveals correct spatial relationships even in views that cannot be obtained directly in 2D scans. This paper represents a multidisciplinary development and assessment of state-

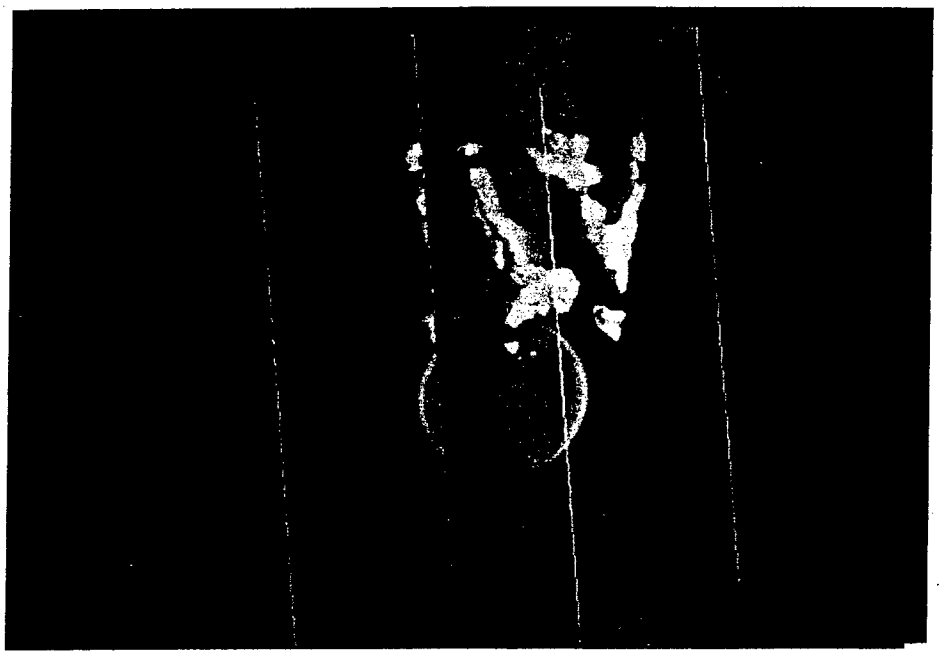

(a)

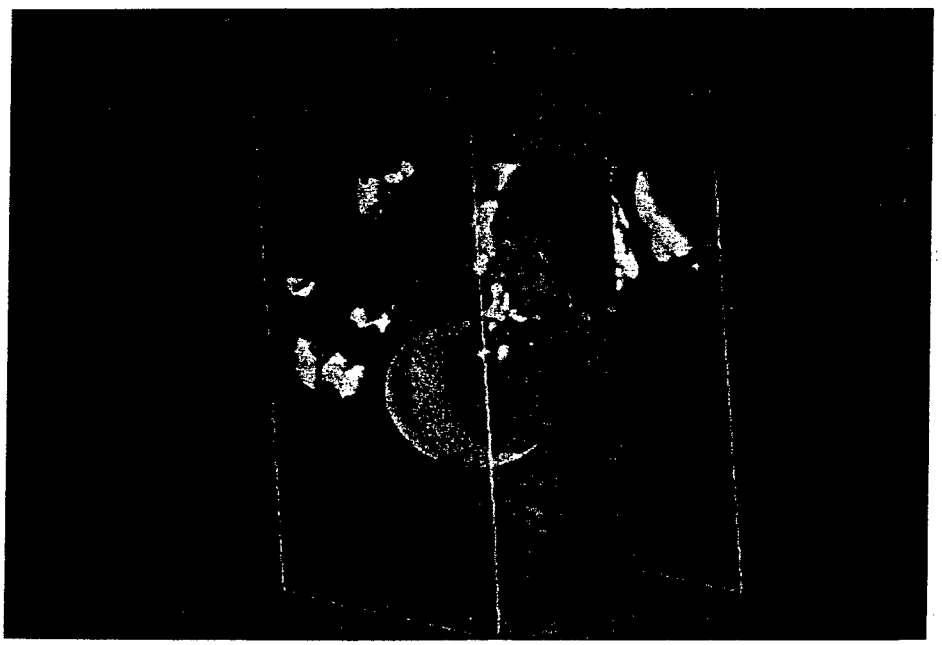

(b)

Fig. 8. 3D displays of power mode-detected vascularity around a relatively vascular, 2.3-cm fibroadenoma in a 45-year-old woman. (a) and (b) A gray-scale plane through the fibroadenoma is shown from each side, along with the ellipsoidal volume selected to follow the gray-scale borders of the mass.

of-the-art 3D ultrasound techniques and offers encouraging, but not yet statistically significant, results as to whether or not 3D imaging and display can offer additional information to that provided by conventional real-time ultrasound techniques in the evaluation of breast lesions.

Acknowledgments—This work was supported in part by USPHS

grant 1RO1CA55076 from the National Cancer Institute and by the U. S. Army Medical Research and Materiel Command under Contract No. DAMD17-96-C-6061. The views, opinions and/or findings contained herein are those of the authors and should not be construed as an official Department of the Army position, policy or decision. Dr. Mihra Taljanovic contributed significantly in performance and interpretation of the earliest subject studies. The authors are indebted to Nancy Thorson for assistance with subject recruitment, records and procedures and to Olga Matlega for assistance with manuscript preparation.

REFERENCES

Adler DD, Carson PL, Rubin JM, Quinn-Reid D. Doppler ultrasound color flow imaging in the diagnosis of breast cancer: Preliminary findings. Ultrasound Med Biol 1990;16:553–559.

Bergonzi M, Calliada F, Corsi G, Passamonti C, Bonfioli C, Motta F, Urani A. Role of echo-color Doppler in the diagnosis of breast diseases: Personal experience. Radiol Med (Torino) 1993;85:120–123.

Blohmer JU, Chaoui R, Schmalisch,G, Bollmann R, Lau HU. Differential breast tumor diagnosis by comparing blood circulation of the tumor with the contralateral breast using color coded, pulsed Doppler ultrasound. Geburtshilfe Frauenheilkd 1995;55:1–6.

Calliada F, Raieli G, Sala G, Conti MP, Bottinelli O, La Fianza A, Corsi G, Bergonzi M, Campani R. Doppler color-echo in the echographic evaluation of solid neoplasms of the breast: 5 years of experience. Radiol Med (Torino) 1994;87:28–35.

Carson PL, Adler DD, Fowlkes JB, Harnist K, Rubin JM. Enhanced color flow imaging of breast cancer vasculature: Continuous wave doppler and 3-D display. J Ultrasound Med 1992;11:377–385.

Carson PL, Li X, Pallister J, Moskalik A, Rubin JM, Fowlkes JB. Approximate quantification of detected fractional blood volume in the breast by 3D color flow and doppler signal amplitude imaging. In: Levy M, McAvoy BR, eds. 1993 Ultrasonics symposium proceedings. Piscataway, NJ: Institute for Electrical and Electronics Engineers, IEEE Cat. No.93CH3301-9, 1993:1023–1026.

Carson PL, Govil A, Moskalik AP, Roubidoux MA, Helvie MA, Adler DD, Fowlkes JB, Rubin JM. 3D Power Mode ROI Analysis for Breast Vacularity Assessment. Abstract booklet. In: Ninth International Congress on the Ultrasonic Examination of the Breast. Sept. 28, Indianapolis. 1995:30–31.

Chang CHJ, Nesbit DE, Fisher DR, Fritz SL, Dwyer SJ III, Templeton AW, Lin F, Jewell WR. Computer tomographic mammography using a conventional body scanner. Am J Roentgenol 1982;138:553–558.

Chenevert TL, Helvie MA, Aisen AM, Francis IR, Adler DD, Roubidoux MA, Londay F. Dynamic 3-D scanning by partial K-space sampling: Initial application for Gad-DTPA contrast enhancement rate characterization of breast lesions. Radiology 1994;196:135–142.

Cosgrove DO, Kedar RP, Bamber JC, Al-Murrani B, Davey JBN, Fisher C, McKinna JA, Alsanjari NA. Breast disease: color Doppler US in differential diagnosis. Radiology 1993;189:99–104.

Cosgrove DO, Lees WR. Abdominal ultrasound workshop. Eurodop: European Doppler Ultrasound Symposium. Oxford, UK: European Ultrasound Society, 1994.

De Albertis P, Oliveri M, Quadri P, Serafini G, Cavallo A, Orlando O, Perona F, Barile A, Gandolfo N. Retrospective analysis of color Doppler ultrasonography and flowmetry findings in solid nodular pathology of the breast. Radiol Med (Torino) 1995; 89:28–35.

Dixon JM, Walsh J, Paterson D, Chetty U. Color Doppler ultrasonography studies of benign and malignant breast lesions. Br J Surg 1992;79:259–60.

Dymling SO, Persson HW, Hertz CH. Measurement of blood perfusion in tissue using Doppler ultrasound. Ultrasound Med Biol 1991;5:433–444.

Fein M, Delorme S, Weisser G, Zuna I, vanKaick, G. Quantification of color Doppler for the evaluation of tissue vascularization. Ultrasound Med Biol 1995;21:1013–1019.

Folkman, J, Shing J. Angiogenesis. J Biol Chem 1992;267:10931–10934.

Goldberg BB, Taylor KJW, Merritt CM, Mendelson E, Madjar H, Bokoban J, Cosgrove D. Multicenter breast mass evaluation using imaging and color Doppler. Imaging: Applications and clinical results (abstract). J Ultrasound Med 1993;60-S2:17.

Heilenkotter U, Jagella P. Color Doppler ultrasound of breast tumors needing excision: Presentation of an examination method. Geburts Frauen 1993;53:247–252.

Huber S, Delorme S, Knopp MV, Junkermann H, Zuna I, von Fournier D, van Kaick G. Breast tumors: computer-assisted quantitative assessment with color Doppler US. Radiology 1994:192: 797–801.

Kedar R, Cosgrove D. Residual breast cyst mimicking a carcinoma on B-mode and color Doppler ultrasonography (letter). J Ultrasound Med 1994;13:119–20.

Kedar RP, Cosgrove DO, Bamber JC, Bell DS. Automated quantification of color doppler signals: a preliminary study in breast tumors. Radiology 1995;197:39–43.

Kuijpers TJ, Obdeijn AI, Kruyt RH, Oudkerk M. Solid breast neoplasms: differential diagnosis with pulsed Doppler ultrasound. Ultrasound Med Biol 1994;20:517–520.

Lagalla R, Caruso G, Marasa L, D'Angelo I, Cardinale AE. Angiogenetic capacity of breast neoplasms and correlation with color Doppler semiology. Radiol Med (Torino) 1994;88:392–5.

Leucht WJ, Rabe DR, Humbert K. Diagnostic value of different interpretative criteria in real-time sonography of the breast. Ultrasound Med Biol 1988;14:59–73.

Madjar H, Prompeler HJ, Sauerbrei W, Wolfarth R, Pfleiderer A. Color Doppler flow criteria of breast lesions. Ultrasound Med Biol 1994;20:849–858.

McNicholas MM, Mercer PM, Miller JC, McDermott EW, O'Higgins NJ, MacErlean DP. Color Doppler sonography in the evaluation of palpable breast masses. Am J Roentgenol 1993;161:765–771.

Moskalik A, Carson PL, Meyer CR, Fowlkes JB, Rubin JB, Roubidoux MA. Registration of 3D compound ultrasound scans of the breast for refraction and motion correction. Ultrasound Med Biol 1995;21:769–778.

Peters-Engl C, Medl M, Leodolter S. The use of colour-coded and spectral Doppler ultrasound in the differentiation of benign and malignant breast lesions. Br J Cancer 1995;71:137–9.

Picot PA, Rickey DW, Mitchell R, Rankin RN, Fenster A. Three-dimensional Doppler imaging. Ultrasound Med Biol 1993; 19:95–104.

Pretorius DH, Nelson,TR, Jaffe JS. 3-dimensional sonographic analysis based on color flow Doppler and gray scale image data: a preliminary report. J Ultrasound Med 1992;11:225–232.

Rubin JM, Adler RA, Fowlkes JB, Spratt S, Pallister JE, Chen JF, Carson PL. Fractional moving blood volume estimation using Doppler power imaging. Radiology 1995;197:183–190.

Rubin JM, Bude RO, Carson PL, Adler RS, Bree RL. Power Doppler: A potentially useful alternative to mean-frequency based color Doppler sonography. Radiology 1994;190:853–856.

Sakki S. Angiography of the female breast. Ann Clin Res 1974;6 (Suppl. 12):1–47.

Scherzinger AL, Belgam RA, Carson PL, Meyer CR, Sutherland JV, Bookstein FL, Silver TM. Assessment of ultrasonic computed tomography in symptomatic breast patients by discriminant analysis. Ultrasound Med Biol 1989;15:21–28.

Stavros AT, Thickman DI, Rapp CL, Dennis MA, Parker SH, Sisney GA. Solid breast nodules: Use of sonography to distinguish between benign and malignant lesions. Radiology 1995;196:123–134.

Swets JA, Pickett RM. Evaluation of diagnostic systems. New York: Academic Press, 1982:29–33.

Venta LA, Dudiak CM, Salamon CG, Flisak ME. Sonographic evaluation of the breast. Radiographics 1994;14:29–50.

Wahl RL, Cody RL, Hutchins GD, Mudgett EE. Primary and metastatic breast carcinoma: Initial clinical evaluation with PET with

the radiolabeled glucose analogue 2-[F-18]-fluoro-2-deoxy-D-glucose. Radiology 1991;179. 765–70.

Watt AC. Ackerman LV. Windham JP. Shetty PC, Burke MW, Flynn MJ, Grodinsky C, Fine G, Wilderman SJ. Breast lesions: differential diagnosis using digital subtraction angiography. Radiology 1986;159:39–42.

Weidner N. Intratumor microvessel density as a prognostic factor in cancer. Am J Pathol 1995;147:9–19.

Weidner N, Folkman J, Pozza F, et al. Tumor angiogensis: a new significant and independent prognostic indicator in early stage breast carcinoma. J Nat Cancer Inst 1992;84:1875–1887.

Back to Contents Send Letter

Utility of Three-dimensional US in the Discrimination and Detection of Breast Cancer

Gerald L. LeCarpentier, PhD, Pamela T. Bhatti, MS, J. Brian Fowlkes, PhD, Marilyn A. Roubidoux, MD, Aaron P. Moskalik, MS, Paul L. Carson, PhD

Department of Radiology
University of Michigan Medical Center
Ann Arbor, Mich, USA

Correspondence:
Gerald L. LeCarpentier, PhD
Department of Radiology
University of Michigan Medical Center
Kresge III Room 3315
200 Zina Pitcher Place
Ann Arbor, MI 48109-0553
Voice: (734) 647-9326
Fax: (734) 764-8541

Acknowledgement: This work was supported in part by PHS grant R01CA53076 from the National Cancer Institute and by the U.S. Army Medical and Material Command under DAMD17-96-C-6061.

Received March 13, 1999; revision requested June 9; revision received September 24; posted October 22.

©RSNA, 1999

Index terms :

- Breast neoplasms, diagnosis, 00.32
- Breast neoplasms, US, 00.12987, 00.12989
- Ultrasound (US), three-dimensional, 00.12989

Back to Contents | To Article | Next Abstract

Send Letter

Utility of Three-dimensional US in the Discrimination and Detection of Breast Cancer

Gerald L. LeCarpentier, Pamela T. Bhatti, J. Brian Fowlkes, Marilyn A. Roubidoux, Aaron P. Moskalik, Paul L. Carson

Abstract

The purpose of this article is to demonstrate evaluation techniques for three-dimensional (3D) ultrasound (US) imaging and their potential application in the discrimination and assessment of breast cancer. Our ongoing studies include women with mammographically observed breast masses scheduled for biopsy. During US imaging of suspicious breast lesions, transducer position is encoded for each power-mode and frequency-shift color Doppler image and for each standard B-mode image, typically 90 images in each mode. Vessels are then displayed as reconstructed color volumes in 3D, superimposed on gray-scale sections. Radiologists identify suspicious masses and rate their appearance for conventional gray-scale assessment and for the new vascular criteria. In an initial patient population, US discrimination of malignant masses in 3D volumes demonstrated superiority over their two-dimensional counterparts. In the related patient group presented here, one particular vascularity measure, speed-weighted pixel density, showed statistically different ($P < .001$) values for benign ($n = 13$) versus malignant ($n = 15$) cases. Given the authors' modest success in discriminating breast cancer in an initial patient pool with use of other vascularity measures, results of this second patient population continue to suggest vascularity as a potential cancer discriminator.

Table of Contents

- Abstract
- Introduction
- Data Acquisition and Processing
  - Image Acquisition
  - Scanning Apparatus
  - Post-Acquisition
  - Regions of Interest
- Examples of Volume Rendering
  - 3D Rendering of Infiltrating Ductal Carcinoma
  - Various 2D Reconstructions
- Clinical Discrimination Results
  - Speed-weighted Pixel Density
  - Comparison With Gray Scale
- Discussion and Conclusions

Utility of 3D US in the Discrimination and Detection of Breast Cancer

Introduction

Subjective assessment of Doppler ultrasound (US) imaging may be enhanced by more-quantitative analyses. Displaying vascularity in three dimensions is relatively simple, since the image segmentation is performed by the color Doppler flow imaging system, and sparse vascular patterns are easily appreciated in three dimensions. A number of investigators (1-4) have done a good job of semiquantitative evaluation of color Doppler flow image characteristics of the breast; however, it may be difficult to objectively sample the sparse breast vasculature throughout the tumor volume in totally free-hand two-dimensional (2D) sampling. Stavros et al have achieved promising results in the evaluation of breast cancer by using a multivariable gray-scale assessment of 2D imaging (5,6). Cosgrove and Lees also indicated that the addition of color Doppler flow imaging to B-mode imaging improved the diagnostic accuracy by an amount approximately equal to the benefit of adding US to mammography. They state that the chance of malignancy after workup must be less than 2% to consistently avoid biopsy (7).

Based on the potential benefits of combining three-dimensional (3D) sampling and quantitative assessments, a preliminary study was performed to evaluate which Doppler signals might provide discrimination of breast cancer from benign masses and to compare 2D and 3D US display modes. The amount of blood flowing as indicated by power-mode color Doppler imaging (p-CDI) (8) and the velocity indicated by mean-frequency color Doppler imaging (f-CDI) both lend themselves to quantitative measurement (9). To evaluate information provided with these measurements and to aid in visual assessment, we undertook a visual and digital analysis of information in a study that included 3D US studies of 20 breast patients scheduled for breast biopsy. We have subsequently analyzed studies of 28 patients, obtained with a different scanner. Three-dimensional breast lesion image volume acquisition techniques and visualization schemes are presented here in general, and a particular vascularity measurement (speed-weighted pixel density) obtained in each of four regions of interest (ROIs) in and around the mass is compared with standard gray-scale criteria for this current patient pool.

[Previous: Abstract] [Next: Data Acquisition and Processing]

[Title Page | Abstract | **Introduction** | Data Acquisition and Processing]
[Examples of Volume Rendering | Clinical Discrimination Results | Discussion and Conclusions | References]

Utility of 3D US in the Discrimination and Detection of Breast Cancer

Data Acquisition and Processing

In an early study, quantitative measures were calculated for 20 different subjects (10). Nine masses were malignant, four were fibroadenomas, and seven were other benign masses. Each examination consisted of one or more p-CDI 3D scans and an f-CDI 3D scan of the mass and surrounding tissue. The 3D scans in these clinical trials were acquired with the system described in a previous study (9). This system consisted of a conventional US scanner (Spectra VST; Diasonics, Milpitas, Calif), a modified mammography unit that applied mild compression to stabilize the breast, and a motorized transducer positioner mounted on the mammography unit. At the 6-MHz Doppler frequency of our 6-10-MHz linear array, signals produced in the two color Doppler flow modes were measured to quantitatively estimate vascularity features in various 3D ROIs in and around the suspicious masses. Click here to link to our Web site and see an early example of a dynamic display technique that we used (11). In an earlier study, independent reviewers gave a higher subjective rating to 3D displays relative to their 2D and videotaped counterparts in their abilility to highlight vascular morphology. In addition, vascular criteria applied to 3D data volumes proved to be slightly more effective in cancer discrimination. For a more detailed description, see Carson et al (11). On the basis of these prior experiences, we continued 3D US scanning with the modifications noted below.

Image Acquisition

The examples shown in subsequent sections were obtained with a new hand-held scanner (12) and a 7.5-MHz linear or 12-MHz array scanhead (Logiq 700; GE Medical Systems, Milwaukee, Wis). Acquisition of 3D US volumes is achieved with a step size between scan planes of typically 0.5 mm for the 50-120 images per scan, covering a volume typically 35 x 45 x 45 mm. P-CDI images are set to maximize sensitivity to small vessel flow, while f-CDI settings are a compromise between slow-flow detectability and aliasing. Because of cyclic flow variations during the cardiac cycle, apparent variation in vessel diameter or flow (or possibly no detectable flow during diastole) may occur with randomly timed image aquisition. To ensure that all of the Doppler images represent flow during similar phases of the cardiac cycle, image acquisition is software-triggered externally by a cardiac-gated computer interface, which also records transducer position and provides operator scan speed feedback.

Scanning Apparatus

The hand-controlled transducer fixture device is designed to provide a guided trajectory for the transducer while the two spatial variables, linear position and rotation angle, are measured, as shown in **Figure 1**. Mounted on the base platform is a miniature linear bearing that allows motion of the transducer along the z axis, normal to the image scan plane. Behind the linear bearing and also mounted on the base plate is a precise linear potentiometer. The translation of the transducer linearly changes the resistance of the potentiometer, ultimately providing an output potential to our computer interface proportional to scanhead position. Resolution of the linear encoder is dictated by analog-to-digital quantization, in this case corresponding to a distance of 18 micrometers. A lightweight rotary optical encoder provides angular measurement by means of a quadurature decoder (designed and built in-house) and software interface, providing an angular resolution of 0.04°. A window in the base plate allows scanhead contact with the patient. The operator is instructed to glide the transducer head steadily during the scan and is also alerted to the beginning and end of the acquisition. Other than a few brief instructions regarding the scanning protocol (ie, direction of scan, relative speed of movement, etc), no special scanning technique is required to make the scan compatible with the subsequent 3D reconstruction.

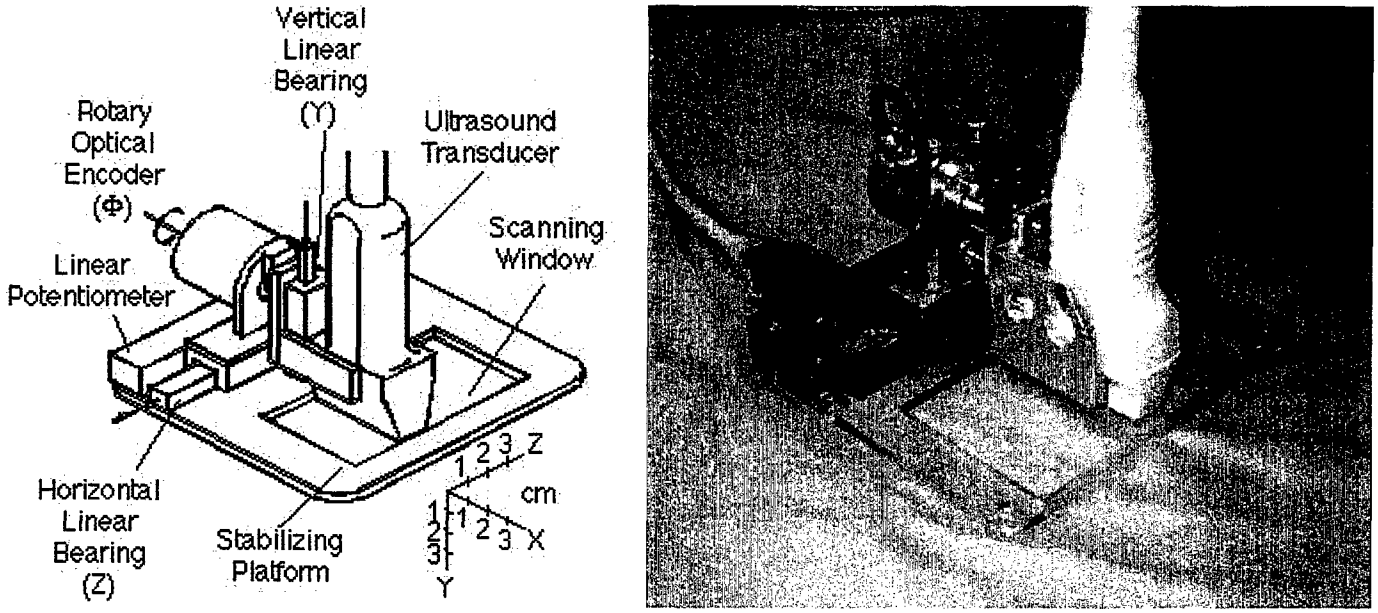

a. b.

Figure 1. (**a**) Schematic of the hand-scan apparatus. (**b**) Photograph of the actual apparatus.

Post-Acquisition

Data are transferred from the scanner to a DEC Alpha workstation (Digital Equipment Corporation, Maynard, Mass), where individual section planes are cropped and "stacked" to form a 3D volume. From the 3D image volume set, vessels are displayed as 3D color volumes, superimposed on gray-scale sections, for the identification of suspicious masses. Our visualization software and related processing modules facilitate 3D viewing. Presently, the clinician is able to position, tilt, scale, and adjust all axes of a "dynamic" ellipsoid whose selection is based on the gray-scale borders of the suspicious mass. This radiologist-defined ellipsoid (RDE) serves as the point of reference for all other ROIs, as described below. Most of the other ROIs are actually defined by the clinician's selection. For the quantitative analysis of vascularity, the methods described in previous studies (9,10) are used. Quantities such as those described previously (9,10) are presented in **Table 1** and are calculated for each of the four ROIs defined in **Table 2**. Also, visual gray-scale features are evaluated on a 5-point scale, averaged, and used for comparison with vascularity.

Table 1
US Vascularity Measures and Their Formulas

Abbr.	Full Name	Formula
PD	Power Weighted Pixel Density	$PD = \sum_{i=1}^{N_b} P_i / N_t$
NMPCP	Normalized Mean Power In Colored Pixels	$NMPCP = \sum_{i=1}^{N_b} \frac{P_i}{P_b} / N_b$
NPD	Normalized Power Weighted Pixel Density	$NPD = \sum_{i=1}^{N_b} \frac{P_i}{P_b} / N_t$
SWD	Speed Weighted Pixel Density	$SWD = \sum_{i=1}^{N_b} V_i / N_t$
$\overline{V}$	Mean Speed in Colored Pixels	$\overline{V} = \sum_{i=1}^{N_b} V_i / N_b$
SNPD	Speed and Power Weighted Normalized Pixel Density	$SNPD = \sum_{i=1}^{N_b} \frac{V_i \cdot P_i}{P_b} / N_t$

Note.--*Nb* = no. of pixels with flow in them, *Nt* = total no. of pixels in the ROI, *Pi* = power Doppler value of the *i* th pixel, *Pb* = estimated power value in 100% blood at the depth of the *i* th pixel, *Vi* = Doppler speed value of the *i* th pixel. *Vi* is calculated from the mean frequency-shift value assuming an isotropic distribution of vessels, because no directional information is obtained.

[illegible]
1. Lesion: normally from the outer gray-scale border up to 1 cm inside
2. Lesion, proximal side only: hemiellipsoidal version of region 1
3. External periphery: mass gray-scale boundary up to 1 mm outside
4. External periphery, proximal side only: hemiellipsoidal version of region 3

[Previous: Introduction] [Next: Examples of Volume Rendering]

[Title Page | Abstract | Introduction | **Data Acquisition and Processing**]
[Examples of Volume Rendering | Clinical Discrimination Results | Discussion and Conclusions | References]

Utility of 3D US in the Discrimination and Detection of Breast Cancer

Examples of Volume Rendering

Figures 2 and **3** are taken from our second, and current, patient population. They serve to demonstate how lesion boundaries can be defined for subsequent quantitative calculations, as well as provide an appreciation of the 3D gray-scale and and vascular renderings. A revealing example of the information available with dynamic 3D can be seen in **Figure 3**. In our chosen coordinate scheme, x represents the lateral direction, y the axial direction, and z the elevational direction. Thus, the scan plane itself can be considered a constant "z" plane, having x-y (lateral-axial) coordinates. Similarly, the plane perpendicular to both the scan plane and the skin surface is considered the constant "x" plane, while the plane at constant depth (C-scan) is the "y" plane. Note in **Figure 3a** and **3b** the excellent section-thickness (elevational) resolution obtained with this matrix array (so-called 1.5 D) transducer.

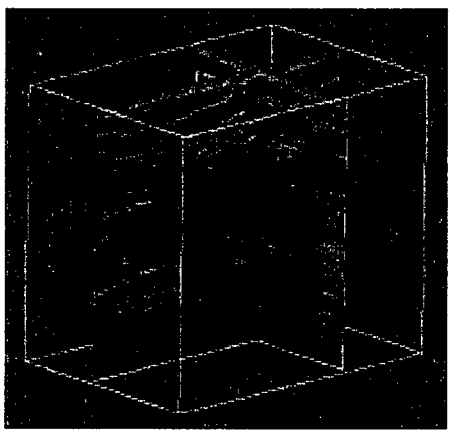

a.

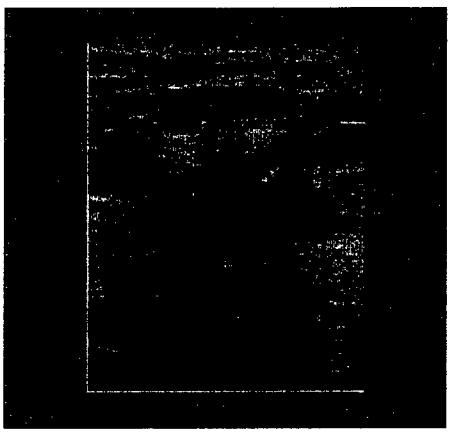

b.

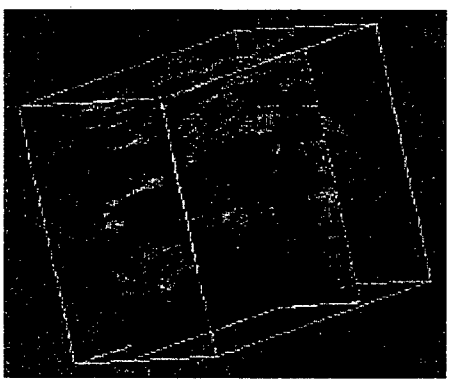

c.

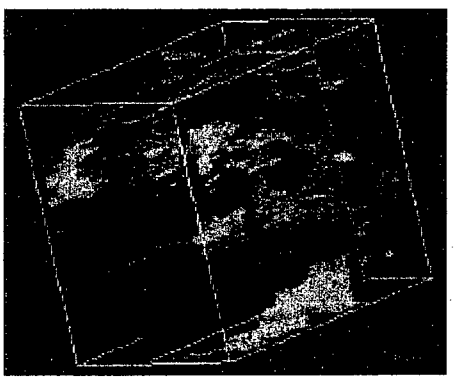

d.

Figure 2. Two-dimensional and 3D power mode display of an elongated infiltrating ductal carcinoma in an 81-year-old woman. **(a)** Three-dimensional view demonstrates two planes, one of which is the original scan plane and the second an orthogonal plane that depicts the extent of the hypoechoic mass. **(b)** Two-dimensional image of the original scan plane demonstrates a vessel penetrating the mass. **(c)** Three-dimensional image with an ellipsoidal ROI defined by the gray-scale borders of the mass, for quantification of vascularity. The ROI is shown as a translucent green ellipsoid, to depict the approximate extent of the lesion, with the penetrating vessel seen as red. **(d)** Three-dimensional display with ROI in green and surface rendering of the vascularity in blue. *(Click any image to view its full-size version [<100 kB each])* .

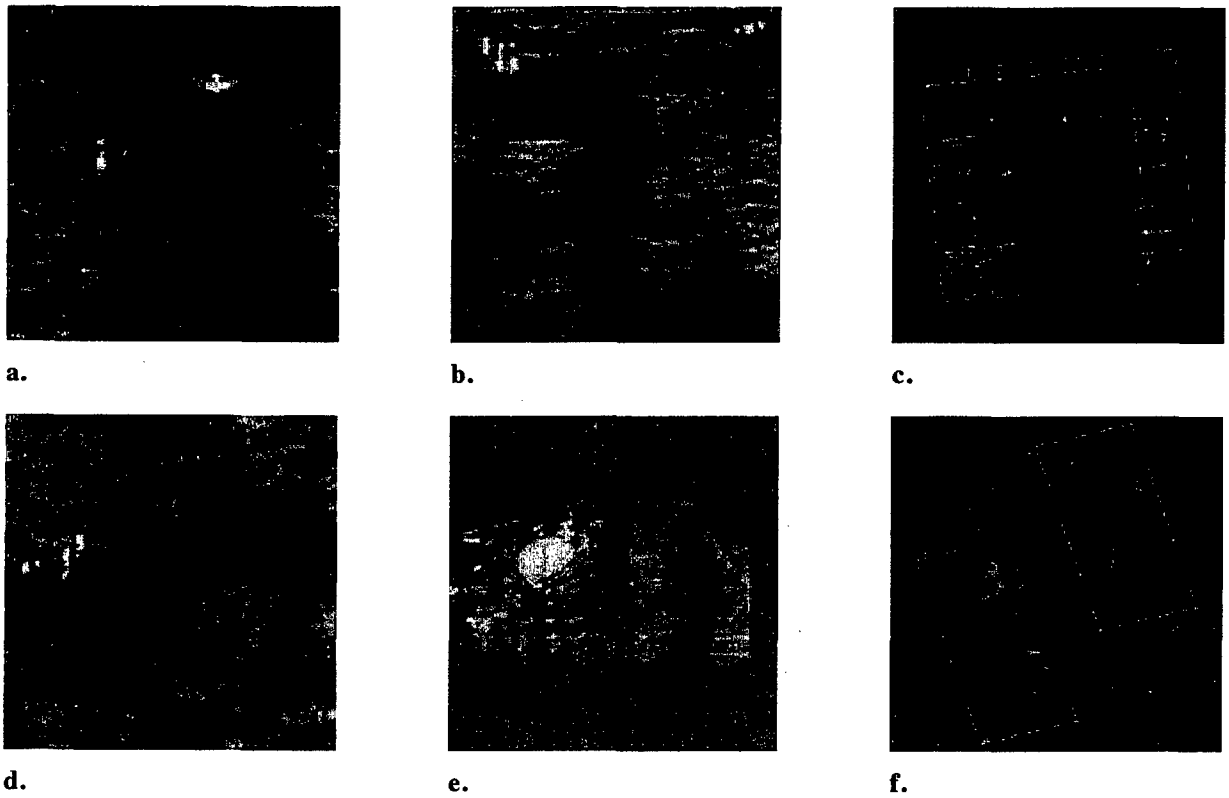

Figure 3. US scans of a 58-year-old woman with a nonpalpable mammographic lesion suspicious for cancer. On the clinical mammogram, the suspect region appeared as a 1.3-cm macrolobular circumscribed mass with no microcalcifications. Final pathologic studies revealed carcinosarcoma (half ductal, half chondrosarcoma). **(a)** Lateral-axial plane (scan plane, or z plane). The smooth ellipsoidal borders (approximately 1.6 x 0.9 cm) of the mass, approximately 0.6 cm from the surface, could cause the reviewer to miss the clearly malignant features in other views. **(b)** Axial-elevational plane (transverse plane, or x plane). The shadowing in this view suggests malignancy, particularly on the right side of the overall mass shown. **(c)** The plane shown here is arbitrarily oriented off either of the axes of the scan plane or transverse plane, and is slightly tilted. The slight outcropping and shadowing on the right side of the mass further suggests a malignant portion to this overall hypoechoic region. **(d)** Lateral-elevational plane (C-scan plane, or y plane). In this constant-depth view, unavailable from the scanner itself, note the malignant multilobular diffuse appearance of the mass. **(e)** The tumor shows ROI definition in 3D and 2D views. **(f)** Three-dimensional view shows irregular margins. *(Click on images* ***a-d*** *to view full-size versions; images* ***e*** *and* ***f*** *link to Quicktime movies [<1 MB each])* .

[Previous: Data Acquisition and Processing] [Next: Clinical Discrimination Results]

[Title Page | Abstract | Introduction | Data Acquisition and Processing]
[**Examples of Volume Rendering** | Clinical Discrimination Results | Discussion and Conclusions | References

Utility of 3D US in the Discrimination and Detection of Breast Cancer

Clinical Trials and Vascularity Measures

Analysis of Clinical Results

Measures of the amount of blood in a region (NPD_{max}) and estimate of perfusion ($[V_m][NPD_{max}]$), mathematically defined in **Table 1** (where *max* refers to the the maximum value calculated in the four regions described in **Table 2**), were plotted versus average gray-scale rating (1 = normal to 5 = highly suspicious) and were evaluated for each subject in the previous study (**10**). Using discriminant analysis to classify cancer versus benign masses and insisting on sensitivities of 100%, we achieved specificities of 82% and 90% for NPD_{max} and ($[V_m][NPD_{max}]$), respectively, when combined with gray-scale ratings. These specificities were higher than for gray scale alone, but the statistical uncertainty in these numbers is large. Our second patient pool is aimed at adding greater statistical significance to these values and exploring other possible quantitative measures. **Figure 4** demonstrates one such measure, speed-weighted pixel density (SWD), as described in **Table 1**. It is mathematically equivalent to pixel density times the average velocity and is thus similar to ($[V_m][NPD_{max}]$) without the power weighting. SWD_{max} refers to the the maximum or peak SWD value calculated in the four regions described in **Table 2**. As shown in **Figure 4**, the mean value of $\log(SWD_{max})$ is significantly different for the benign versus malignant groupings ($P < .001$ that the mean values are equal).

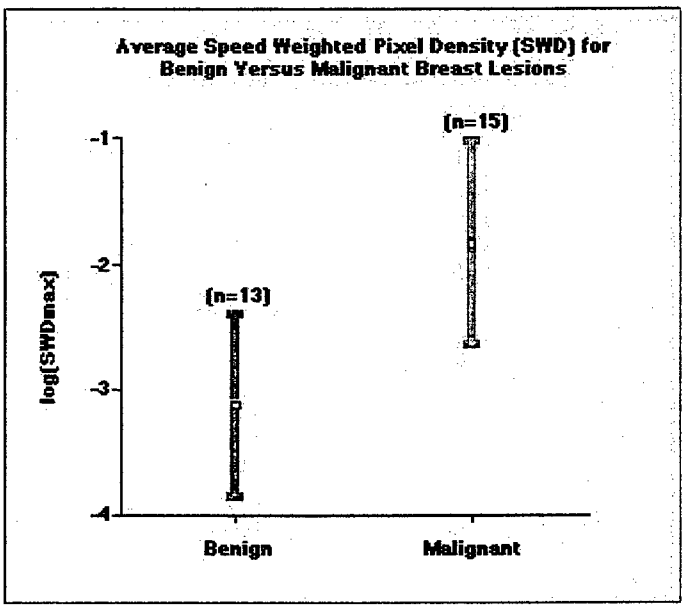

Figure 4. Plot of the $\log(SWD_{max})$ (ie, the maximum SWD value for the four ROIs described in **Table 2**) for benign versus malignant breast lesions. Mean values and their standard deviations are shown for the two poopulations. As demonstrated by *t* test results, the probability that the mean values of these subgroups are different was statistically significant ($P < .001$).

Comparative Results

Receiver operating characteristic (ROC) analysis was performed on the SWD measure and average gray-scale rating using ROCKIT software provided by the University of Chicago's Department of Radiology (from the current version of an ROC software package developed by Charles E. Metz, PhD, and his colleagues). **Figure 5** demonstrates the predictive similarity between the SWD measure and the average gray-scale rating. The graph shows the raw data and maximum likelihood estimates of single binormal ROC curves for both measures, given a subject pool of 28 patients. The Az values calculated for SWD and gray scale were comparable, 0.88 and 0.84, respectively.

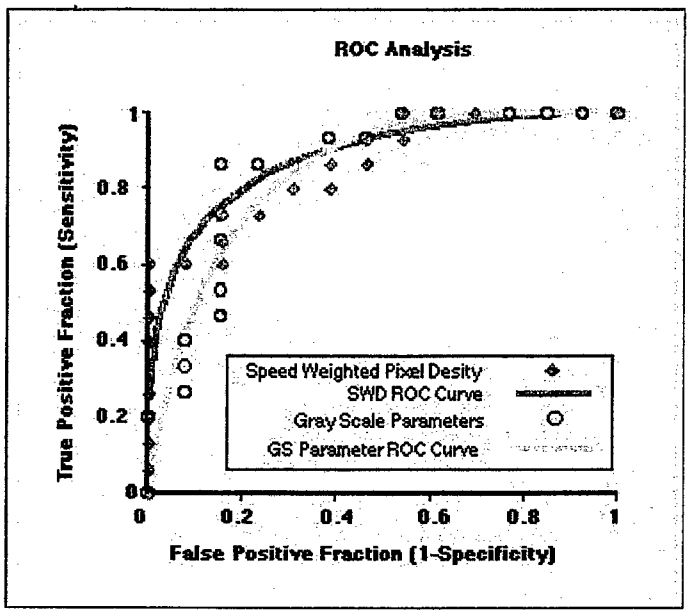

Figure 5. Calculated true-positive fractions versus false-positive fractions of $\log(SWD_{max})$ and average gray-scale ratings for our 28-patient population. Overlaid are smooth calculated ROC curve estimates. Although the area under the curve was slightly greater for SWD performance, the difference in the two areas (Az[SWD] = 0.88 versus Az[GS] = 0.84) was not significant. *GS* = gray scale.

[Previous: Examples of Volume Renderings] [Next: Discussion and Conclusions]

[Title Page | Abstract | Introduction | Data Acquisition and Processing]
[Examples of Volume Renderings | **Clinical Discrimination Results** | Conclusions | References]

Utility of 3D US in the Discrimination and Detection of Breast Cancer

Discussion

Our data transfer, processing, and visualization tools have been developed to the point where full 3D volumes and vascularity surface renderings can be reviewed within an hour of the US examination itself. These developments have facilitated the visualization of vascular morphology and made easier scanning through entire US volume sets from different perspectives. In addition, we have provided the radiologist with a straightforward method for defining reproducible ROI ellipsoids within a given US volume, which facilitates a variety of quantitative measures. As demonstrated by means of ROC analyses, these objective measures of vascularity (most recently SWD) in and of themselves have been shown to be as effective as subjective gray-scale measures for our current patient population.

Given these observations, we believe that vascularity measures should improve the discrimination of benign and malignant solid masses with US and that the results are probably applicable to different scanners. Larger numbers of subjects and improved ease of performance of good vascularity examinations are now needed to allow good judgments of the achievable diagnostic accuracy and cost-effectiveness of adding vascularity to clinical US assessments of breast masses.

Ease of performance is well on its way, with advances occurring rapidly in 3D scanning, image analysis, and image display. If power-mode and color Doppler flow measures (NPD and SWD) each, separately, continue to perform comparably with gray-scale measures and almost as well as the power-mode and color Doppler flow combination required for $\log[(V_m)(NPD_{max})]$ as demonstrated in our earlier report (9), then one of the two color Doppler flow 3D scans can be eliminated to speed up the entire process. Alternatively, the US system manufacturer could supply the power frequency signals simultaneously with sufficient signal dynamic range for accurate assessments of the perfusionlike $\log[(V_m)(NPD_{max})]$ on a pixel-by-pixel basis. For imaging vessel patterns, little would be lost by requiring the same system settings for both frequency-shift and power modes in a single image.

In these studies, gray-scale readings were performed by a radiologist highly experienced in breast imaging and US. If vascularity measures on simple ROIs can perform at least as well as gray-scale assessments for the experienced reader, the potential for use of vascularity measures in improving routine diagnosis is high.

Conclusions

Our modest success in discriminating breast cancer in an initial patient pool with other vascularity measures and the results from this second patient population continue to suggest vascularity as a potential cancer discriminator. Our visualization and quantization tools should continue to facilitate this process.

[Previous: Clinical Discrimination Results] [Next: References]

[Title Page | Abstract | Introduction | Data Acquisition and Processing]
[Examples of Volume Rendering | Clinical Discrimination Results | **Conclusions** | References]

Utility of 3D US in the Discrimination and Detection of Breast Cancer

References

1. Carson PL, Adler DD, Fowlkes JB, Harnist K, Rubin J. Enhanced color flow imaging of breast cancer vasculature: continuous wave Doppler and 3-D display. J Ultrasound Med 1992; 11:377-385.

2. Bamber J, Eckersley R, Cosgrove D, Bell D, Kedar RP. 3-D reconstruction of combined colour Doppler and grey scale images of breast tumours. In: Madjar H, Teubner J, eds. Breast ultrasound update. Basel, Switzerland: Karger, 1993.

3. Cosgrove DO, Kedar RP, Bamber JC, et al. Breast diseases: color Doppler US in differential diagnosis. Radiology 1993; 189:99-104.

4. Cosgrove DO, Bamber JC, Davey JB, McKinna JA, Sinnett HD. Color Doppler signals from breast tumors: work in progress. Radiology 1990; 176:175-180.

5. Stavros AT, Parker SH, Dennis MA, Johnson KK, Thickman DI, Rapp CL. Sonography of solid breast nodules: benign or malignant? (abstr). Radiology 1993; 189(P):406.

6. Stavros AT, Thickman D, Rapp CL, Dennis MA, Parker SH, Sisney GA. Solid breast nodules: use of sonography to distinguish between benign and malignant lesions. Radiology 1995; 196:123-134.

7. Cosgrove DO, Lees WR. Abdominal ultrasound workshop. Eurodop, European Doppler Ultrasound Symposium, Oxford, England, 1994.

8. Rubin JM, Adler RA, Fowlkes JB, et al. Fractional moving blood volume: estimation with power Doppler US. Radiology 1995; 197:183-190.

9. Carson PL, Fowlkes JB, Roubidoux MA, et al. 3D color Doppler image signal quantification of breast masses. Ultrasound Med Biol 1998; 24:945-952.

10. Carson PL, Li X, Pallister J, Moskalik AP, Rubin JM, Fowlkes JB. Approximate quantification of detected fractional blood volume and perfusion from 3D color flow and Doppler power signal imaging. In: Ultrasonics Symposium proceedings. Piscataway, NJ: IEEE, 1993; 1023-1026.

11. Carson PL, Moskalik AP, Govil A, et al. The 3D and 2D color flow display of breast masses. Ultrasound Med Biol 1997; 23:837-849.

12. Fenn RC, Fowlkes JB, Moskalik AP, Zhang Y, Roubidoux MA, Carson PL. A hand-controlled, 3-D ultrasound guide and measurement system. Acoustical Imaging, 1997; 22:237-242.

[Previous: Discussion and Conclusions]

[Title Page | Abstract | Introduction | Data Acquisition and Processing]
[Examples of Volume Rendering | Clinical Discrimination Results | Discussion and Conclusions | **References**]

Discrimination of Sonographic Breast Masses Using Frequency Shift Color Doppler Imaging in Combination with Age and Gray Scale Criteria

Pamela T. Bhatti MSEE, Gerald L. LeCarpentier PhD, Marilyn A. Roubidoux MD, J. Brian Fowlkes PhD, Mark A. Helvie MD, Paul L. Carson PhD

Address correspondence to:

Gerald L LeCarpentier, PhD
University of Michigan, Department of Radiology
200 Zina Pitcher Place Room 3315
Ann Arbor, MI 48109-0553
phone: 734-647-9326
email: gllec@umich.edu

Supported in part by: USPHS grant 1RO1CA55076 from the National Cancer Institute and to a lesser extent by the U.S. Army Medical Research and Material Command under Contract No. DAMD17-96-C-6061.

Submission Type: New Manuscript

Introduction

Although their benefits far outweigh the risk of modest radiation exposure, mammograms do present some shortcomings. Screening mammograms present sensitivities of 68%-85% [1] and 32% specificity [2], resulting in a number of unnecessary benign biopsies. Development of cost-effective, non-invasive adjunctive techniques to mammography for differentiating benign from malignant masses would significantly reduce the number of negative biopsies.

Capitalizing on the high quality of gray scale images produced by current ultrasound (US) equipment, researchers have investigated discrimination techniques based on gray scale measures (GS). Results describing visual gray scale criteria with a negative predictive value as high as 99.5% have been reported [3]. Using the ability to visualize speed and direction of blood flow, a host of studies have examined color flow Doppler imaging as a discrimination technique. Studies based on color flow Doppler compared with those based on gray scale imaging yielded mixed results, leaving the role of color flow Doppler imaging still in debate [4]. Pursuing a multivariable approach, by combining gray scale criteria with color flow and power mode Doppler, Carson et. al [5] reported results of a technique that discriminates breast masses with greater success than gray scale or vascularity alone.

The research described here examines the performance of color flow Doppler signals, quantified as a Speed Weighted pixel Density (SWD), when differentiating benign from malignant breast masses. In addition, a multivariable technique is assessed using vascularity (SWD) combined with each of the following: (1) patient age, (2) gray scale measures, and (3) patient age and gray scale measures.

Materials and Methods

Patient volunteers were recruited from women who presented a sonographically detectable breast mass and were scheduled for biopsy. All patients were informed of the institutionally reviewed and approved experimental procedure and provided written consent prior to the examination. Final diagnoses were obtained by histological analysis of biopsy specimens. A total of 43 patients were scanned. Five patients were excluded from analysis who were either post-lumpectomy, had scans which were not processed successfully, or scans which exhibited severe Doppler artifact due to chest wall motion during breathing.

An ultrasound evaluation for each patient was performed with a GE Logiq 700 scanner (General Electrical Medical Systems, Milwaukee, WI) using an M12 linear matrix array scanhead (6 MHz Doppler, 9 MHz-gray scale). The scanned breast region measured approximately 3 cm in length by 3.8 cm in width by 4 cm deep. The patient's ECG was acquired via a computer interface to a clinical ECG monitor and was used to trigger the footswitch of the GE scanner. Thus, cardiac gating was effectively implemented to effect image capture during systole and maximize the Doppler signal. Using gray scale mode, the sonographer centered the mass in the scan window and verified the limits of the scan. Standard scanner settings are listed in Table 1. Each 3D scan was acquired with a hand-controlled scanning apparatus [6,7]. Interfaced to a PC, where scanhead positions are acquired and stored for each image. 60-90 images per scan were stored in the cine loop, and then were transferred to a workstation. The scan slices were stacked to render a 3D volume. By averaging the slice to slice position data captured by the PC, estimated slice spacing was available for the 3D volume reconstruction. For a more precise morphometric analysis and multiscan registration see Krücker et al. [8].

Each 3D volume was displayed in AVS/Express (Advanced Visualization Systems, Waltham, MA) data visualization software, as a series of three intersecting planes (Figure 1). In-house tools designed with AVS/Express allowed a radiologist to review the slices

and determine the margins of the mass. On each overall reconstructed color flow volume, the radiologist selected a region of interest (ROI), which served to delineate the mass from the surrounding tissue, and approximated the region with a dynamically positioned and shaped ellipsoidal volume in the 3D volume. This ROI, was referred to as the Radiologist's ROI (ROR).

Based on the ROR, four regions were designated from which vascularity was measured (Figure 2). These regions are: (1) the entire ROR, (2) the upper (proximal) half of the ROR, (3) a 3 mm shell in the x, y, and z directions surrounding the ROR, and (4) upper (proximal) half 3 mm shell.

Within each of the four regions, the vascularity information was quantified as the sum of each color pixel weighted by its speed, v_i, with the overall sum normalized by the total number of pixels in the region, N_t, The result is called the Speed Weighted pixel Density (where N_b equals the total number of color pixels).

$$SWD = \sum_{i=1}^{N_b} \frac{v_i}{N_t}$$

Selecting the largest SWD from the four regions yielded the value, SWD_{max}. Software was developed with AVS/Express to compute SWD for all the regions.

Gray scale characteristics of the mass (margin smoothness, margin visibility, shape, height, echogenicity, attenuation, homogeneity, and "overall suspicion") were each ranked on a scale of 1 to 5 (low to high suspicion) and averaged to produce GS_{avg} [9]. These gray scale criteria were similar to those used in previous studies [3,5]. All gray scale images were observed by the same radiologist.

Vascularity, age, and gray scale data were initially assessed with a Bayesian discriminator [10] which was applied to each possible pair of variables to produce the combined indices SWD-Age, SWD-GS, and Age-GS. For all of these calculations, $LogSWD_{max}$ was used (a) to reduce the range of SWD and avoid dominance by a few cases in the determination of discrimination functions and (b) to in some way linearize the

increase in vasularity with (presumably exponential) cell growth in the cases of growing masses. The three variable index SWD-Age-GS was also calculated from a Bayesian discriminator, this time in three dimensions. Including the single variables (SWD, Age, GS), all 7 incdices were compared by Receiver Operator Characteristic (ROC) curves as well as by pair-wise univariate z-score tests [§].

[§] The authors are deeply indebted to Nancy Thorson R.T., for assistance with subject recruitment, records and procedures. Patient data collection was performed with the assistance of Jochen Krücker and Theresa Tuthill Ph.D., who also contributed to statistical data analysis. Aaron Moskalik is acknowledged for his software contribution.

Results

The results are summarized in Figures 3 through 6 and Tables 2 through 5. Of 38 lesions, 18 masses were benign (mean patient age 48±12, ranging from 26 to 70) and 20 were malignant (mean patient age 56±9, ranging from 46 to 72). A summary of patient diagnoses is presented in Table 2, and the distribution of SWD_{max} regions is provided in Table 3.

To assess the various indices in relation to each other, we generated multiple 2D and 3D plots similar to that presented in Figure 3. This particular example shows the relationship between SWD and patient age. Applying Bayesian decision theory [10] and weighing the risk of false negatives the same as false positives, the resulting discrimination line (darker upper line) is shown in the scatter plot of $LogSWD_{max}$ vs. Age. The figure illustrates the grouping of benign and malignant masses. The lower lighter line is drawn to illustrate discrimination at 100% sensitivity. As an alternative representation, a combined $LogSWD_{max}$ and Age (SWD-Age) index for each case was computed using the slope of the discrimination line. Figure 4 illustrates the SWD-Age index for each case as compared to diagnosis. The lines correspond to those in Figure 3, where risks are equally weighted (sensitivity 80% and specificity 89%), and where sensitivity is maximized to yield the lower discriminating line (sensitivity 100%, specificity 72%). Applying an analogous analysis to $LogSWD_{max}$ vs. GS_{avg} yields similar results. When $LogSWD_{max}$, GS_{avg}, and Age are combined, the Bayesian discriminator separates the population with 95% sensitivity and 94% specificity. When requiring a false negative rate of zero, this three variable index demonstrates 94% specificity (true negative fraction) at 100% sensitivity (true positive fraction) as shown in Figure 5. Table 4 summarizes the sensitivities and specificities when optimized for sensitivity.

Figure 6 illustrates the Receiver Operator Characteristic (ROC) curves computed for each index. The curves depict the maximum likelihood estimate of a single binormal curve based on the respective index [10] with the area under each curve representing the diagnostic

accuracy [11]. Performance of the indices is shown in the figure. Disregarding statistical significance for the moment, the indices which performed the best were SWD-Age-GS and SWD-GS, followed by SWD-Age, Age-GS, and finally the single indices GS, SWD, and Age. Pair-wise univariate z-score tests of the difference between the areas under the binormal ROC curves of the all variables are shown in Table 5. Note that Age is a significantly worse diagnostic performer than all multi-variable indices and that SWD-Age-GS performs statistically better than all single variable indices as well as Age-GS. The results also show that GS alone does not perform statistically better than SWD alone, and there is no significant difference between any of the two-variable indices.

Discussion

Earlier studies assessing the performance of color flow Doppler US in cancer discrimination have relied on varied methods for vascularity measurement. Examination of Doppler flow parameters, mean and maximum flow velocities; and spectral analysis, peak systolic and end diastolic Doppler frequency shifts, have been performed [13-17]. Additional investigations include (1) qualitative analysis of Doppler images, observing the amount of reflected signal associated with the mass, and (2) quantitative analysis, calculating the color pixel density, or tabulating a Speed Weighted pixel Density for a region of interest [5,9,14,18-22].

In addition to exploring flow characterization and quantification, studies have also examined the relationship between angiogenesis (suspected to be crucial for tumor growth), metastases, [23,24] and color Doppler signals [25-27]. By studying the correlation between color Doppler and tumor microvessel density, a measure of angiogenesis, researchers have shown that there is little correlation between Doppler flow parameters and microvessel density [25,27] concluding that Doppler US yields information mainly on tumor macrovasculature.

Although these earlier studies assessing color Doppler indicate mixed support for f-CDI in discriminating benign from malignant masses, the data presented by this study indicates that $LogSWD_{max}$ may be useful when applied to ultrasonically discernible masses. Comparison between the areas under the ROC curves, that is, the diagnostic accuracy, indicated SWD performed roughly the same as gray scale, and in combination with age performed better than the Age-GS index. Possibly the success of SWD may be attributed to speed weighting every pixel value. As a result, all flow information is considered when discriminating masses. The weighting of high flow speeds, thought to be illustrative of low resistance to flow often associated with vascular morphology of malignant masses, may enhance vascular quantification. In addition, highly consistent system settings presumably

were critical, as was the selection of a relatively high maximum velocity (6 cm/sec) to balance sensitivity to flow with minimization of aliasing.

It has been reported that patient age may influence vascularity. There is some evidence that vascularity of malignant masses decreases with age [5]. The results presented here suggest that the inclusion of patient age with SWD (Az=0.94) improved discrimination beyond that of SWD alone (Az=0.86). This suggests that future studies including vascularity as a discriminating factor may be strengthened by considering patient age, or possibly just menopausal status.

Based on a criterion that a 2% or less chance of malignancy is required to avoid biopsy [3], the SWD-Age-GS technique described in this study could provide a useful discrimination tool. Based on a group of 38 patients, the findings suggest that by combining vascularity, age and gray scale, the number of benign biopsies could be considerably reduced.

Although vascularity has been presented as a potentially valuable measure in cancer discrimination of sonographic masses, its addition, possibly in combination with age, must provide better discrimination than Age and GS, to merit the addition of color flow to the US exam. A larger group of patients will be required to show with statistical significance that the combined index, SWD-GS-Age, offers consistently improved discrimination over the GS-Age index.

Hypothesizing that there exists a shell thickness limit within which most of the border vascularity information is contained, a 3 mm thickness was selected. Further consideration of this distance is warranted. Future work includes computing vascularity distributions as a function of distance from the mass border to assess the most representative shell thickness for the mass. The ROR and shell were each divided into two halves, proximal and distal, and SWD was computed for the proximal halves as well as the entire volume. Since shadowing by the mass is highly variable, the proximal ROR may be a more accurate representation of vascularity than the entire ROR.

Although our study describes a quantitative, and therefore objective, method for vascularity measurement, there are some limitations. Inherent in the speed computation is the assumption of isotropic blood flow. Specifically, the velocity as measured by the scanner is multiplied by a scaling factor of 2 to account for an isotropic distribution of Doppler angles. In addition the scans are performed with the transducer fixed perpendicular to the breast surface. Therefore, the angle of the transducer cannot be rotated to find the "best" representation of each given blood vessel.

The utility offered by these discrimination techniques relies on the objectivity of the vasularity measures. Identification of a mass and ROR delineation are the least objective steps in the vascularity analysis. The approach requires the radiologist to play a crucial role, but once the ROR is selected, all subsequent processing is done in software, implementable on commercial systems, with no adjustments as long as consistent scanner settings are employed. Ultimately, discrimination is accomplished by combining SWD, a partially objective measure, with patient age and GS, a subjective measure.

Acknowledgments

This work was supported in part by USPHS grant 1RO1CA55076 from the National Cancer Institute and to a lesser extent by the U.S. Army Medical Research and Material Command under Contract No. DAMD17-96-C-6061. The views, opinions and/or findings contained herein are those of the authors and should not be construed as an official Department of the Army position, policy, or decision.

References

1. Rosenberg RD, Hunt WC, Williamson MR, et al: Effects of age, breast density, ethnicity and estrogen replacement therapy on screening mammographic sensitivity and cancer stage at diagnosis. Radiology 209: 511-508, 1999.

2. Sickles EA: Quality assurance. How to audit your own mammography practice. Radiol Clin North Am 30:265-275, 1992.

3. Stavros AT, Thickman D, Rapp CL, et al: Solid breast nodules: use of sonography to distinguish benign from malignant lesion. Radiology 196:123-134, 1995.

4. Wilkens TH, Burke BJ, Cancelada DA, et al: Evaluation of palpable breast masses with color Doppler sonography and gray scale imaging. J Ultrasound Med 17:109-105, 1998.

5. Carson PL, Fowlkes JB, Roubidoux MA, et al: 3-D color Doppler image quantification of breast masses. Ultrasound Med Biol 24:945-952, 1998.

6. Fenn RC, Fowlkes JB, Moskalik A, et al: A hand-controlled 3-D ultrasound guide and measurement system. Acoustical Imaging. Lees S, ed., Plenum Press, N.Y. 23:237-242, 1997.

7. Krücker JF, LeCarpentier GL. Meyer CR, et al: Examples of 3D image registration for multimode, extended field of view, and sequential US imaging. RSNA-EJ, http://ej.rsna.org/ej3/0098-99.fin/titlepage.html, 1999.

8. LeCarpentier GL, Bhatti PT, Fowlkes JB, et al: Utility of 3D Ultrasound in the Discrimination and Detection of Breast Cancer, RSNA-EJ, http://ej.rsna.org/ej3/0103-99.fin/titlepage.html, 1999.

9. Carson PL, Moskalik AP, Govil A, et al: 3D and 2D color flow display of breast masses. Ultrasound Med Biol 23:837-849, 1997.

10. Fukunaga K: Hypothesis testing. In: Introduction to statistical pattern recognition. 2nd. ed. New York: Academic Press, 51-58, 1990.

11. Metz CE: ROC analysis software. From: http://www-radiology.uchicago.edu/krl. Chicago IL: Department of Radiology, University of Chicago, 1997.

12. Swets JA, Pickett RM: Evaluation of diagnostic systems: methods from signal detection theory. New York: Academic Press, 1982.

13. Minasian H, Bamber JC: A preliminary assessment of an ultrasonic Doppler method for the study of blood flow in human breast cancer. Ultrasound Med Biol 8:357-364, 1982.

14. Kedar RP, Cosgrove DO, Bamber JC, et al: Automated quantification of color Doppler signals: a preliminary study in breast tumors. Radiology 197:39-43, 1995.

15. Madjar H, Prompeler HJ, Sauerbrei W, et al: Differential diagnosis of breast lesions by color Doppler. Ultrasound Obstet Gynecol 6:199-204, 1995.

16. Lee WJ, Chu JS, Huang CS, et al: Breast cancer vascularity: color Doppler sonography and histopathology study. Breast Cancer Res Treat 37:291-298, 1996.

17. Sahin-Akyar G, Sumer H: Color Doppler ultrasound and spectral analysis of tumor vessels in the differential diagnosis of solid breast masses. Invest Radiol 31:72-79, 1996.

18. Lee SK, Lee T, Lee KR, et al: Evaluation of breast tumors with color Doppler imaging: a comparison with image-directed Doppler ultrasound. J Clin Ultrasound 23:367-373, 1995.

19. Cosgrove DO, Kedar RD, Bamber JC, et al: Breast diseases: color Doppler US in differential diagnosis. Radiology 189:99-104, 1993.

20. Huber S, Delormes S, Knopp MV, et al: Breast tumors: computer assisted quantitative assessment with color Doppler US. Radiology 192:797-801, 1994.

21. Delorme S, Zuna I, Huber S et al: Colour Doppler sonography in breast tumors: an update. Eur J Radiol 8:189-193, 1998.

22. Bell DS, Bamber JC, Eckersley RJ: Segmentation and analysis of colour Doppler images tumor vasculature. Ultrasound Med Biol 21:635-647, 1995.

23. Folkman J, Merler E, Abernathy C, et al: Isolation of a tumor factor responsible for angiogenesis. J Exp Med 33:275-278, 1971.

24. Weidner N: Intratumor microvessel density as a prognostic factor in cancer. Am J Pathol 147:9-19, 1995.

25. Lee WJ, Chu JS, Houng SJ, et al: Breast cancer angiogenesis: a quantitative morphologic and Doppler imaging study. Ann Surg Oncol 2:246-251, 1995.

26. Buadu LD, Murkami J, Murayama S, et al: Colour Doppler sonography of breast masses: a multiparameter analysis. Clin Radiol 52:917-923, 1997.

27. Peters-Engl C, Medl M, Mirau M, et al: Color-coded and spectral Doppler flow in breast carcinomas: relationship with the tumor microvasculature. Breast Cancer Res Treat 47:83-89, 1998.

Figure Captions

Figure 1. 3D, color Doppler scan volume with region of interest selected. Each slice (right) represents an original image z-plane and approximately 90 of these are stacked to form the overall 3D reconstructed volume. The intersecting color flow planes are shown along with a blue-green 3D surface delineating the volume for calculation of tumor vascularity. Despite the relatively smooth margins of this lesion, all multivariable indices correctly identified this metaplastic carcinoma (with foci of invasive ductal carcinoma) as malignant.

Figure 2. Schematic of Z-plane cross sections of vascularity quantification regions: (a) complete ROR, (b) upper (proximal) half of the ROR, (c) 3 mm shell surrounding the ROR, (d) upper half 3 mm shell.

Figure 3. $LogSWD_{max}$ versus Age for 38 patients studied: 18 benign (open downward pointing triangles) and 20 malignant (filled upward pointing triangles). A linear Bayesian discriminant analysis produces the upper discrimination line shown: 0.22 = log(SWDmax) + 0.478•Age . The lower lighter line shows the data split with a sensitivity of 100%.

Figure 4. Combined SWD-Age Index. The upper threshold line shown represents the discrimination obtained with equally weighted risks, True Positive Fraction (sensitivity) 80% and True Negative Fraction (specificity) 89%. Requiring 100% sensitivity reduces specificity to 72% as depicted by the lower line. Points are spread horizontally for clarity.

Figure 5. Combined SWD-Age-Gray Scale Index. The upper threshold line represents the discrimination obtained with equally weighted risks, sensitivity 95% and specificity 94%. Requiring 100% sensitivity does not alter the specificity in this case.

Figure 6. Receiver operating characteristic curves illustrating diagnostic performance (Az) of SWD, GS, and Age and combinations thereof. Notice that the diagnostic accuracy of the GS-Age combination does not perform as well as the two variable combinations including vascularity, SWD-Age and SWD-GS. When all three variables are combined, SWD-Age-GS, the highest level of cancer discrimination is achieved.

Table 1. Standard scanner settings for patient exam.

Gray Scale	
Number of foci	1
Mean foci depth	2 cm
GS frequency	9 MHz
GS gain	22 dB
Dynamic range	69 dB
f-CDI	
Gain	48 dB
PRF	1000 Hz
Wall filter	75 Hz
Velocity scale	6 cm/sec

Table 2. Summary of patient diagnostics.

Status	N
Benign (Average Equivalent Diameter* = 1.1 cm)	**18**
Resolved prior to biopsy	1
Benign breast tissue	1
Radial Scar	1
Cyst	2
Fibrocystic changes	6
Fibroadenoma	5
Fibroadenoma with fibrocystic changes	2
Malignant (Average Equivalent Diameter* = 1.4 cm)	**20**
Adenocarcinoma	1
Invasive ductal carcinoma	6
Ductal carcinoma in situ (DCIS)	2
Invasive ductal carcinoma with DCIS	7
Invasive lobular carcinoma	1
Invasive lobular carcinoma with LCIS	1
Invasive ductal carcinoma with LCIS	1
Other	1
* Equivalent diameter is the diameter of sphere whose volume is equivalent to the estimated volume of the mass.	

Table 3. Summary regions of interest where maximum SWD occurred.

Region	N
Benign	**18**
Region 1 (entire ROR, Figure 2(a))	9
Region 2 (proximal ROR, Figure 2(b))	0
Region 3 (entire 3 mm shell, Figure 2(c))	2
Region 4 (proximal 3 mm shell, Figure 2(d))	7
Malignant	**20**
Region 1 (entire ROR, Figure 2(a))	2
Region 2 (proximal ROR, Figure 2(b))	7
Region 3 (entire 3 mm shell, Figure 2(c))	1
Region 4 (proximal 3 mm shell, Figure 2(d))	10

Table 4. Performance of multi-variable measures when optimized for sensitivity.

Measure	Sensitivity	Specificity
$LogSWD_{max}$-Age- GS_{avg}	100%	94%
$LogSWD_{max}$-Age	100%	72%
$LogSWD_{max}$- GS_{avg}	100%	89%
Age-GS_{avg}	100%	22%

Table 5. Statistical significance of ROC area (accuracy) comparisons.

Index 1	Index 2	Significance	p-value
SWD-Age-GS	SWD	*	0.013
SWD-Age-GS	Age	***	0.001
SWD-Age-GS	GS	*	0.024
SWD-Age-GS	SWD-Age	~	0.086
SWD-Age-GS	SWD-GS		0.230
SWD-Age-GS	Age-GS	*	0.037
SWD-Age	SWD	~	0.090
SWD-Age	Age	**	0.010
SWD-Age	GS		0.659
SWD-Age	SWD-GS		0.336
SWD-Age	Age-GS		0.871
SWD-GS	SWD	*	0.020
SWD-GS	Age	**	0.004
SWD-GS	GS	*	0.039
SWD-GS	Age-GS		0.171
Age-GS	SWD		0.395
Age-GS	Age	**	0.010
Age-GS	GS		0.193
SWD	Age		0.281
SWD	GS		0.530
Age	GS	~	0.065

***p≤0.001; **p≤0.01; *p≤0.05; ~p≤0.1

Figure Captions

Figure 1. 3D, color Doppler scan volume with region of interest selected. Each slice (a) in the original image z-plane is stacked to form the overall 3D volume reconstructed in (b). In (b) three, intersecting color flow planes are shown along with a blue-green 3D surface delineating the volume for calculation of tumor vascularity. Flow velocity of detected vascularity in the planes shown is depicted in magenta to yellow (c). The scan is directed toward the nipple in the +z direction as shown by the arrows in (b) and (c).

Figure 2. Schematic of Z-plane cross sections of vascularity quantification regions: (a) complete ROR, (b) upper (proximal) half of the ROR, (c) 3 mm shell surrounding the ROR, (d) upper half 3 mm shell.

Figure 3. $LogSWD_{max}$ versus Age for 38 patients studied: 18 benign (open downward pointing triangles) and 20 malignant (filled upward pointing triangles). A linear Bayesian discriminant analysis produces the upper discrimination line shown: 0.22 = log(SWDmax) + 0.478•Age . The lower lighter line shows the data split with a sensitivity of 100%.

Figure 4. Combined SWD-Age Index. The upper threshold line shown represents the discrimination obtained with equally weighted risks, True Positive Fraction (sensitivity) 80% and True Negative Fraction (specificity) 89%. Requiring 100% sensitivity reduces specificity to 72% as depicted by the lower line. Points are spread horizontally for clarity.

Figure 5. Combined SWD-Age-Gray Scale Index. The upper threshold line represents the discrimination obtained with equally weighted risks, sensitivity 95% and specificity 94%. Requiring 100% sensitivity does not alter the specificity in this case.

Figure 6. Receiver operating characteristic curves illustrating diagnostic performance (Az) of SWD, GS, and Age and combinations thereof. Notice that the diagnostic accuracy of the GS-Age combination does not perform as well as the two variable combinations including vascularity, SWD-Age and SWD-GS. When all three variables are combined, SWD-Age-GS, the highest level of cancer discrimination is achieved.

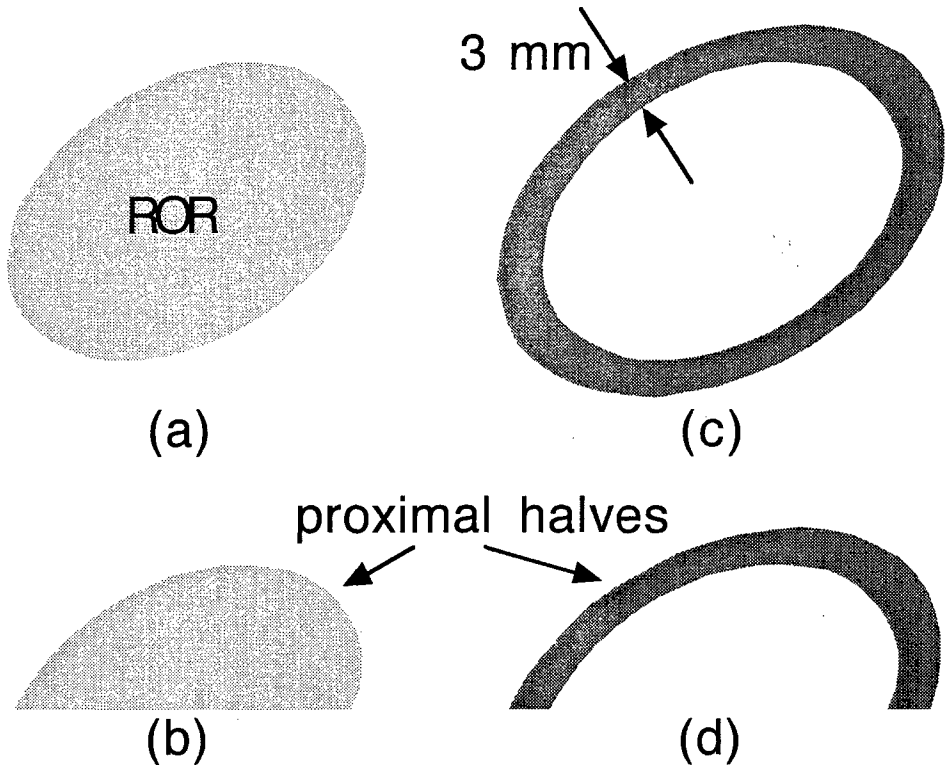

Figure 2. Schematic of Z-plane cross sections of vascularity quantification regions: (a) complete ROR, (b) upper (proximal) half of the ROR, (c) 3 mm shell surrounding the ROR, (d) upper half 3 mm shell.

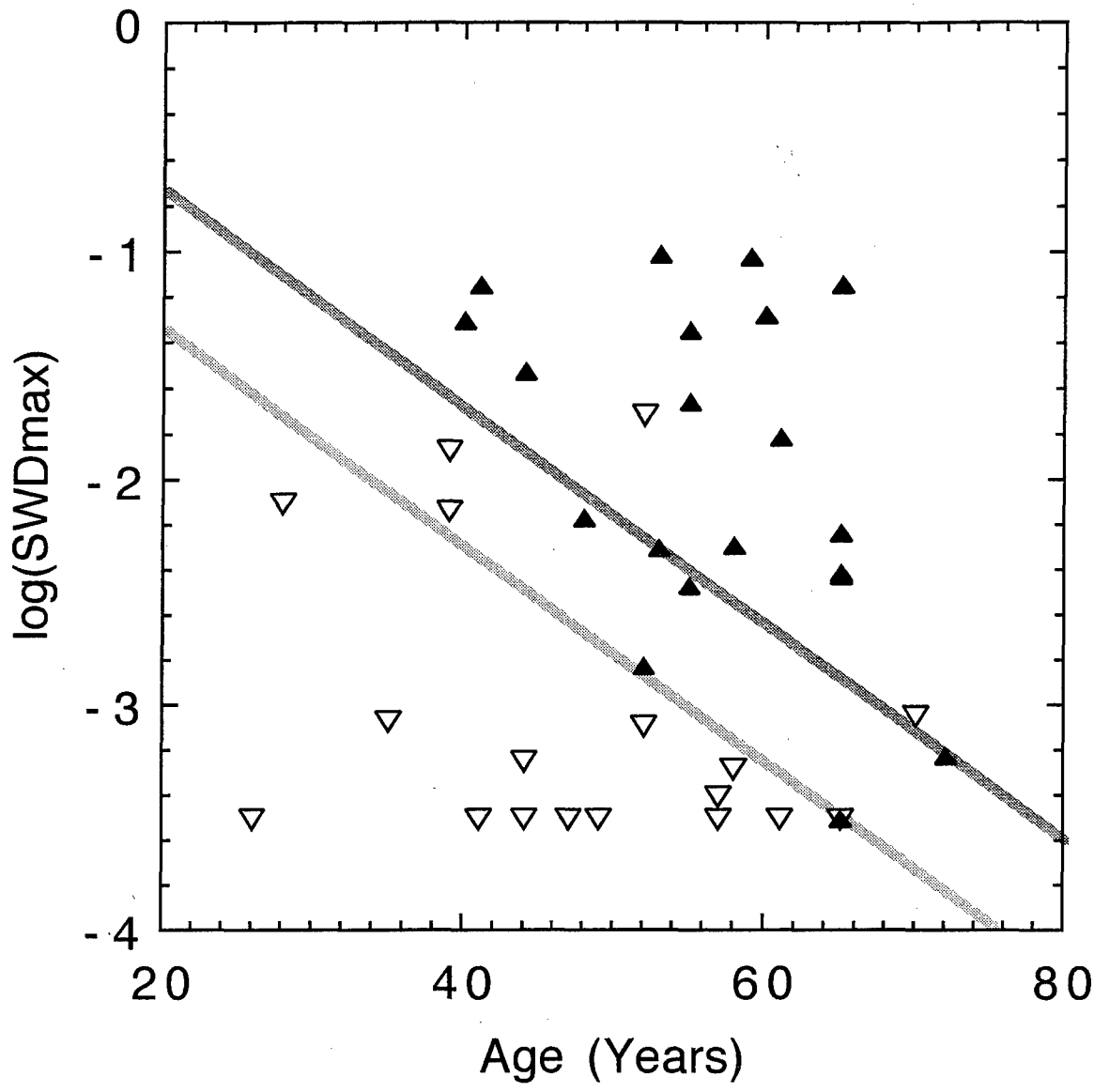

Figure 3. LogSWDmax versus Age for 38 patients studied: 18 benign (open downward pointing triangles) and 20 malignant (filled upward pointing triangles). A linear Bayesian discriminant analysis produces the upper discrimination line shown: 0.22 = log(SWDmax) + 0.478oAge . The lower lighter line shows the data split with a sensitivity of 100%..

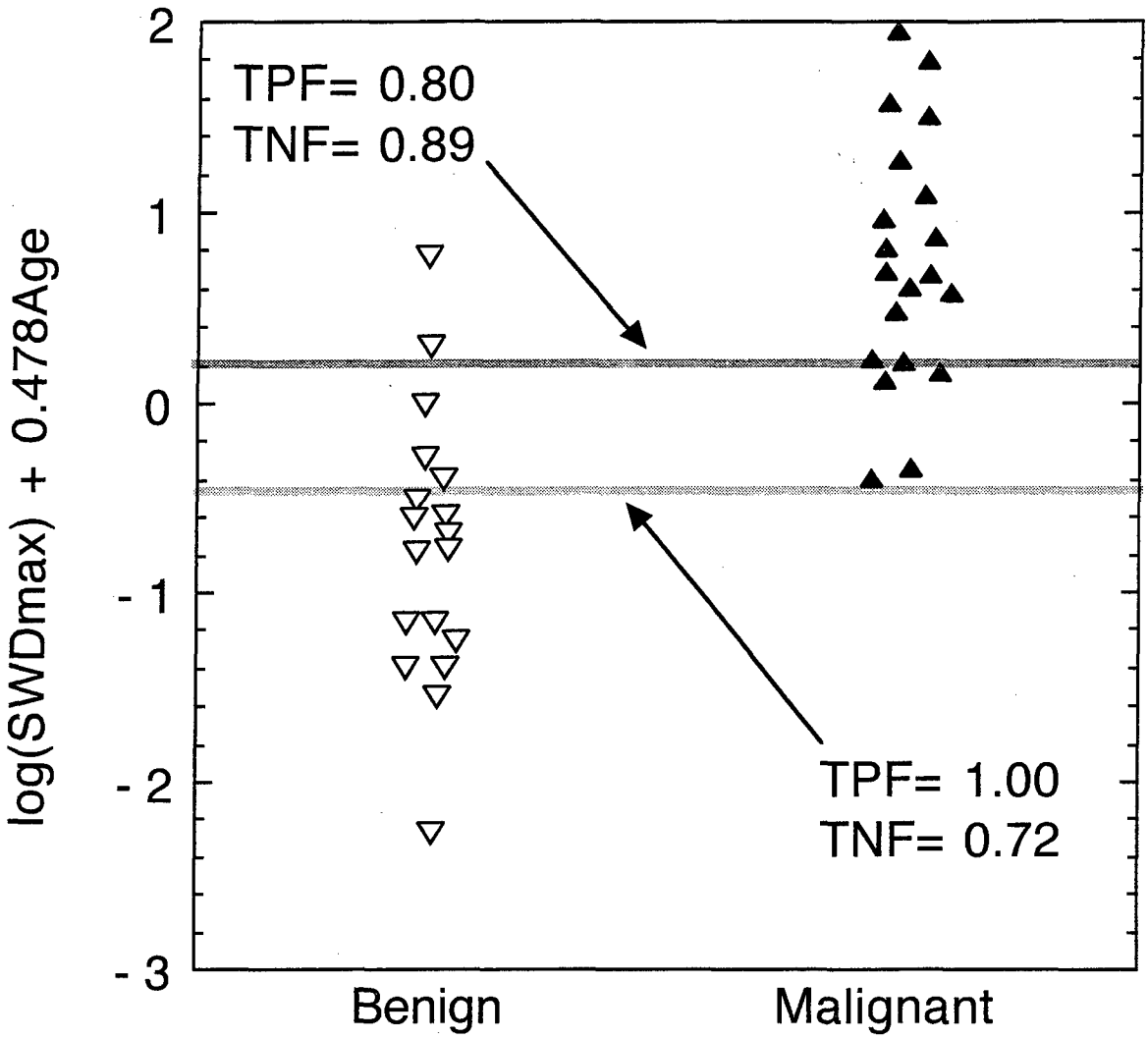

Figure 4. Combined SWD-Age Index. The upper threshold line shown represents the discrimination obtained with equally weighted risks, True Positive Fraction (sensitivity) 80% and True Negative Fraction (specificity) 89%. Requiring 100% sensitivity reduces specificity to 72% as depicted by the lower line. Points are spread horizontally for clarity.

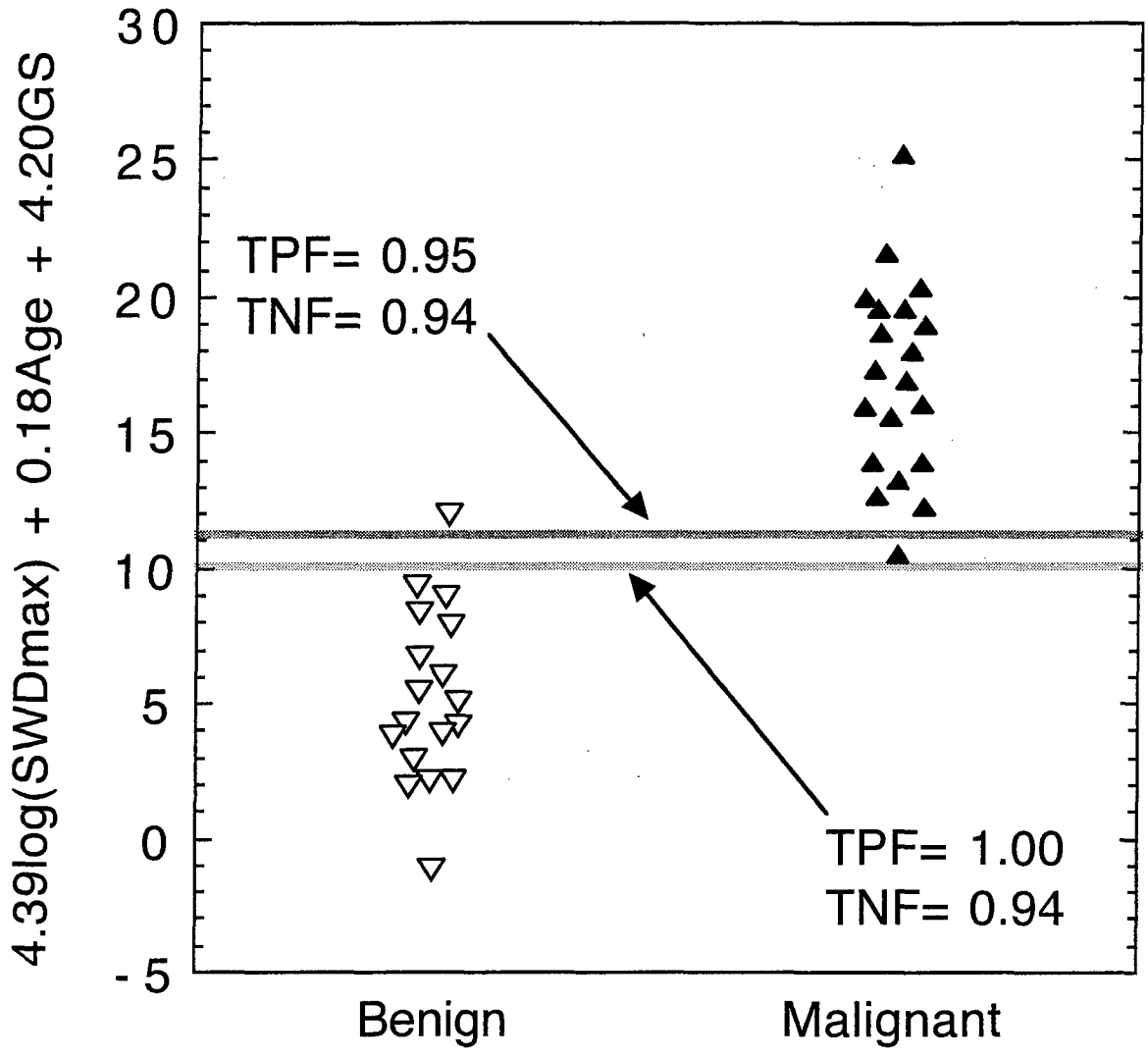

Figure 5. Combined SWD-Age-Gray Scale Index. The upper threshold line represents the discrimination obtained with equally weighted risks, sensitivity 95% and specificity 94%. Requiring 100% sensitivity does not alter the specificity in this case.

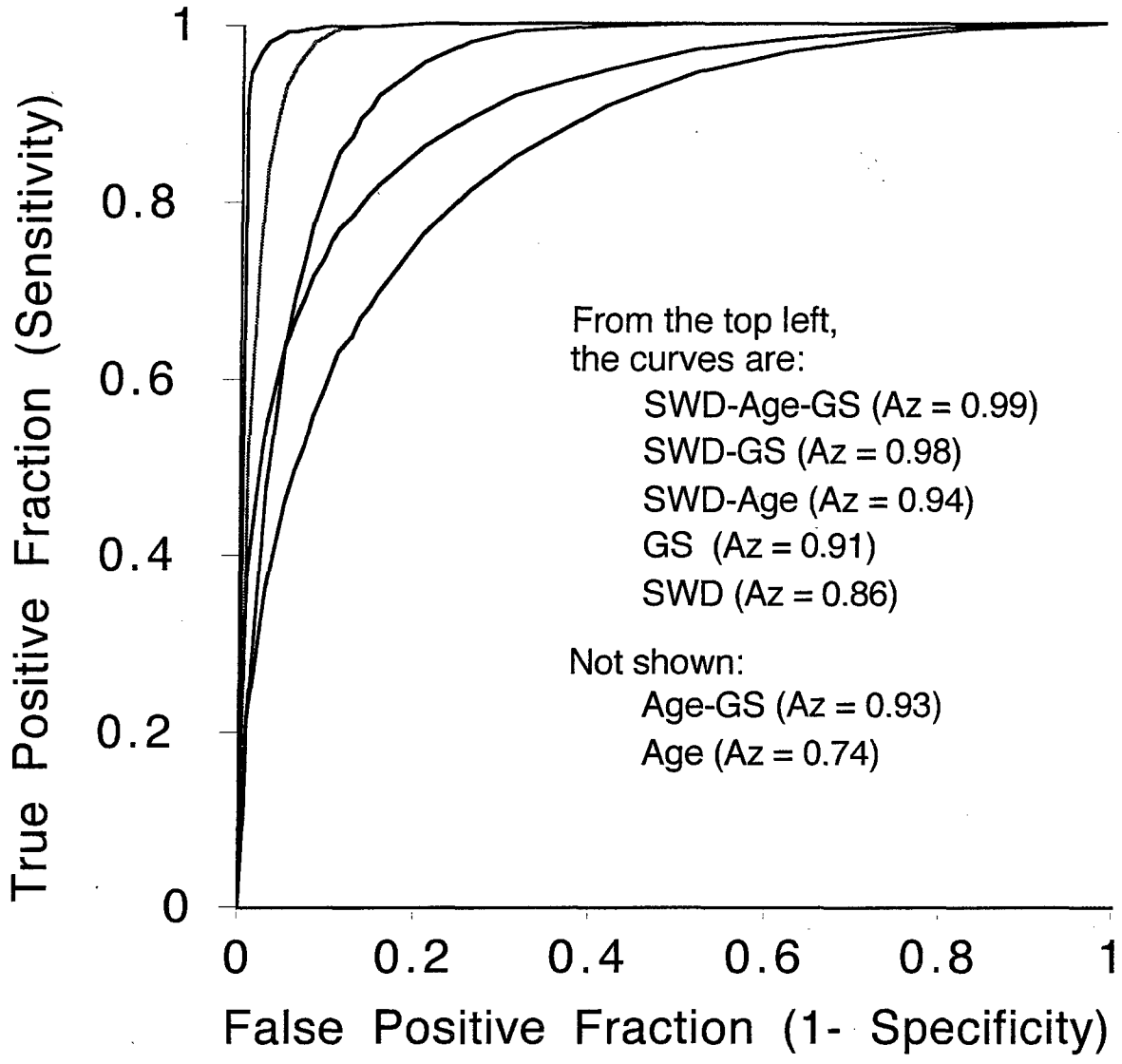

Figure 6. Receiver operating characteristic curves illustrating diagnostic performance (Az) of SWD, GS, and Age and combinations thereof. Notice that the diagnostic accuracy of the GS-Age combination does not perform as well as the two variable combinations including vascularity, SWD-Age and SWD-GS. When all three variables are combined, SWD-Age-GS, the highest level of cancer discrimination is achieved.

Assessment of 3D Doppler Ultrasound Indices in the Classification of Suspicious Breast Lesions Using an Independent Test Population and a 4-Fold Cross Validation Scheme

Gerald L LeCarpentier, Marilyn A Roubidoux, J Brian Fowlkes, Jochen F Krücker, Nancy J Thorson, Karen D Engle, Paul L Carson

The University of Michigan, Ann Arbor, MI

ABSTRACT

OBJECTIVE: To assess various Doppler indices in differentiating benign from malignant breast lesions using initial and validation patient populations. METHODS: Data partially analyzed previously from 38 women in a prior study (group A) as well as all measures from 40 new patients (group B) were used in the current analyses. All patients were scheduled for breast biopsy and displayed an ultrasonically detectable mass. Parallel frequency-shift (fs) and power-mode (pm) color Doppler images (CDI) were acquired with a GE Logiq 700 ultrasound system while translating an M12 transducer and recording its position via a linear encoding apparatus and computer interface. Each reconstructed CDI volume encompassed a suspicious mass, identified by a radiologist defined ellipsoid, where six Doppler vascularity measures (DVMs) were calculated: fs and pm color pixel density (CPD), speed-weighted pixel density (SWD), mean flow velocity (v), normalized power-weighted pixel density (NPD), and the product vNPD. Radiologist defined grayscale ratings (GS) and patient age were also recorded. RESULTS: The areas (Az) under ROC curves in the entire patient pool (46 benign, 32 malignant) confirmed SWD (Az=0.86) as the optimal DVM (previously used in the group A multivariable analysis). Az(fs-CPD) was comparable (0.85), and both demonstrated statistically significant ($p<0.05$) performance differences over NPD (Az=0.75). Other Az values ranged from 0.75 to 0.77. Using group A to optimize the SWD-Age-GS discrimination index (Az=0.99), the same linear combination of these variables was blindly applied to group B (Az=0.97). Az for this three variable discriminator was greater than that for gray scale readings alone (Az=0.82) ($p<0.05$). Similar results were achieved for two-variable combination indices. Further, additional radiologists were recruited for a multi-reader grayscale assesment, and a 4-fold cross validation method was applied to the entire patient population, yielding performance results between those of groups A and B. CONCLUSIONS: Quantitative vascularity measurements, especially fs-CDI indices, considerably improve malignant tissue characterization beyond subjective GS evaluation alone. SWD-Age-GS appears particularly robust, given its consistently high performance, regardless of incidental performance variations in its single variable components.

Table 1. Pathologic distribution of the ultrasonically visible masses. The total distribution represents a prior 38 patient learning set and 40 test set patients.

Status	N
Benign (Average Equivalent Diameter* = 1.0 cm)	**46**
Resolved prior to biopsy	1
Benign breast tissue	2
Radial Scar	2
Cyst	7
Fibrocystic changes	11
Fibroadenoma	15
Fibroadenoma with fibrocystic changes	3
Other	5
Malignant (Average Equivalent Diameter* = 1.5 cm)	**32**
Adenocarcinoma	1
Invasive ductal carcinoma	12
Ductal carcinoma in situ (DCIS)	3
Invasive ductal carcinoma with DCIS	8
Invasive lobular carcinoma	1
Invasive lobular carcinoma with LCIS	2
Invasive ductal carcinoma with LCIS	1
Other	3

* Equivalent diameter is the diameter of a sphere whose volume is equivalent to the estimated volume of the mass.

Table 2. Diagnostic performance of combined measures using the learning set (original 38) to establish discrimination indices, blindly applied to the test population (the New 40).

Discrimination Index	Az (Original 38)	Az (the New 40)
SWD-Age-GS	0.997	0.974
SWD-Age	0.943	0.890
SWD-GS	0.985	0.963
Age-GS	0.933	0.839
SWD	0.864	0.832
Age	0.737	0.618
GS	0.914	0.825

Table 3. Diagnostic performance of various Doppler vascularity measures (DVMs), assessed using the entire patient population. Method 1 versus 2 considers the maximum values from regions 0, 0+2, 1, and 1+3 versus regions 0, 1, 2, 3 as described in the text. There are no statistically significant differences between methods for any given index. The comparable SWD and fs-CPD measures both demonstrated better performance over NPD with statistical significance (p=0.01 and 0.04 respectively).

Doppler Vascularity Measures	Az (Method1)	Az (Method2)
SWD	0.864	0.847
fs-CPD	0.849	0.842
MeanV	0.773	0.786
vNPD	0.771	0.789
NPD	0.749	0.746
pm-CPD	0.749	0.742

Table 4. Statistical difference among grayscale ratings. Three methods to calculate an overall rating were used: (1) the average of all 8 parameters including Gestalt (GSall), (2) the average GS not including Gestalt (GSnoG), and (3) Gestalt (GSG). Three readers and their average ratings (R1, R2, R3, Ravg) provided the comparison groups. Pairwise comparisons (60 combinations) were performed to detect statistically significant differences among grayscale calculation methods and reader ratings in terms of both absolute value and diagnostic performance as described by ROC curves (Az comparisons). The 8 statistically significant ($p<0.05$) comparisons are highlighted below.

Reader(s)	Az(GSall) vs Az(GSnoG)	Az(GSG) vs Az(GSnoG)	Az(GSavg)	Az(GSnoG)	GSavg	GSG
R1	p=0.01					
R2	p=0.04					
Ravg		p=0.05				
R1 vs R3			p=0.04	p=0.02		
R1 vs R2					p=0.04	
R2 vs Ravg					p=0.04	p=0.05

Table 5. Distribution of patients used for 4-fold cross validatition of the multi-variable discrimination indices.

Sub-Group	Number of Benign	Number of Malignant	Total
A	12	8	20
B	12	8	20
C	11	8	19
D	11	8	19

Table 6. Evaluation summary of discrimination indices. The mean Az values highlight the improved performance of SW-GS and particularly SWDAgeGS over grayscale evaluation alone.

Index	MeanAz	abcLearn-DTest	abdLearn-CTest	acdLearn-BTest	bcdLearn-ATest
SWDAgeGS	0.981	1.000	0.963	1.000	0.959
SWDAge	0.907	0.927	0.827	0.959	0.917
SWDGS	0.964	0.960	0.942	1.000	0.954
AgeGS	0.932	0.960	0.898	1.000	0.870
SWD	0.860	0.908	0.768	0.919	0.846
Age	0.683	0.543	0.649	0.774	0.767
GS	0.931	0.955	0.887	1.000	0.880

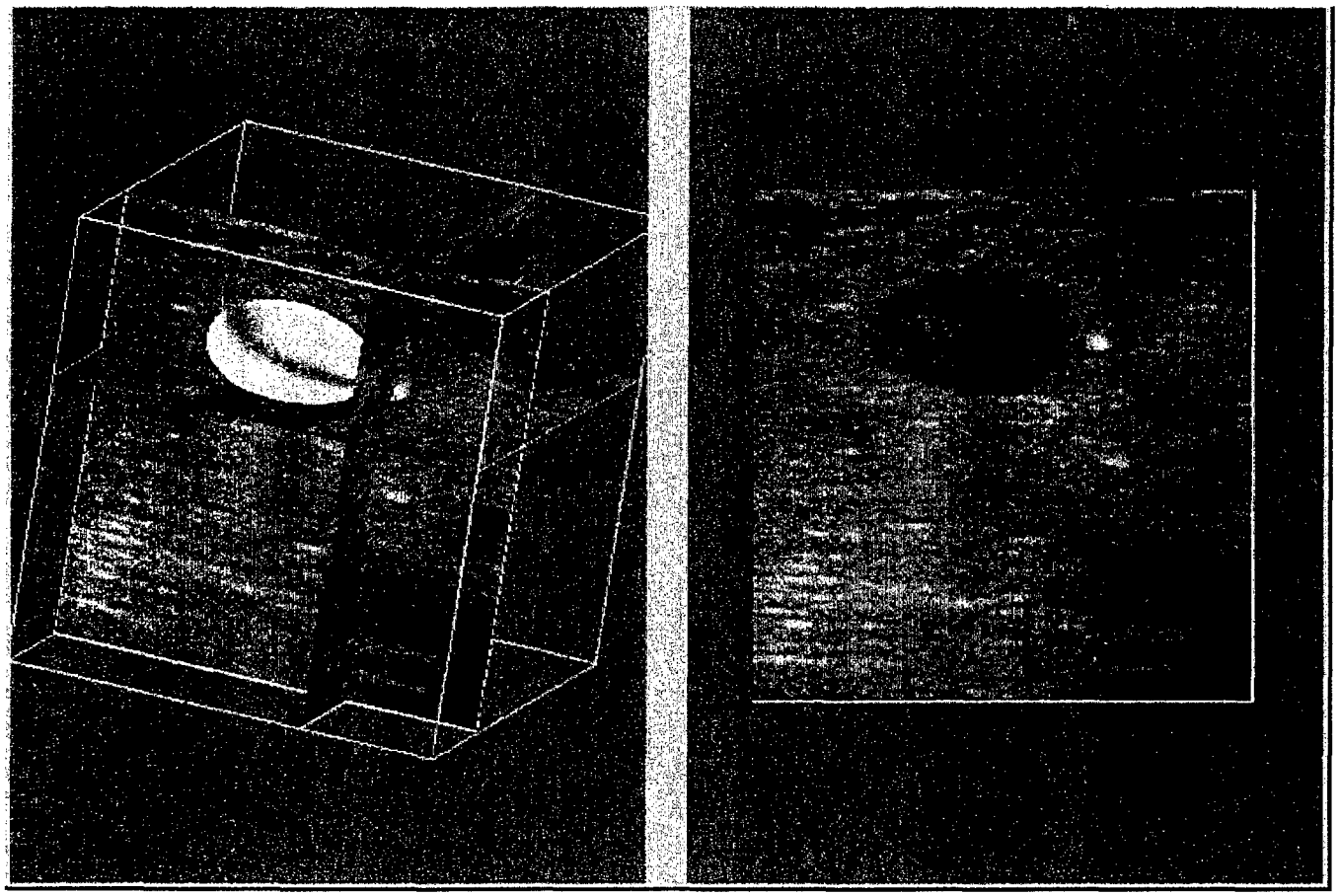

Figure 1. 3D, color Doppler scan volume with region of interest selected. Each slice (right) represents an original image z-plane and approximately 90 of these are stacked to form the overall 3D reconstructed volume. A blue-green 3D surface delineating the volume for calculation of tumor vascularity is shown at left.

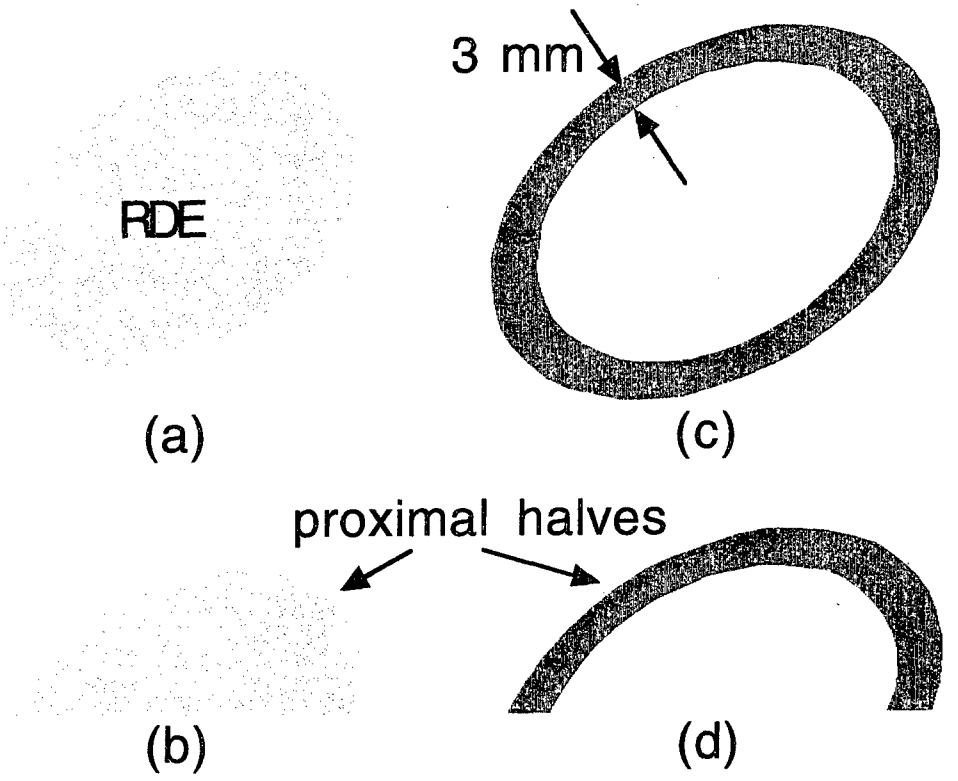

Figure 2. Schematic of Z-plane cross sections of vascularity quantification regions: (a) complete radiologist defined ellipsoid (RDE), (b) upper (proximal) half of the RDE, (c) 3 mm shell surrounding the RDE, (d) upper half 3 mm shell.

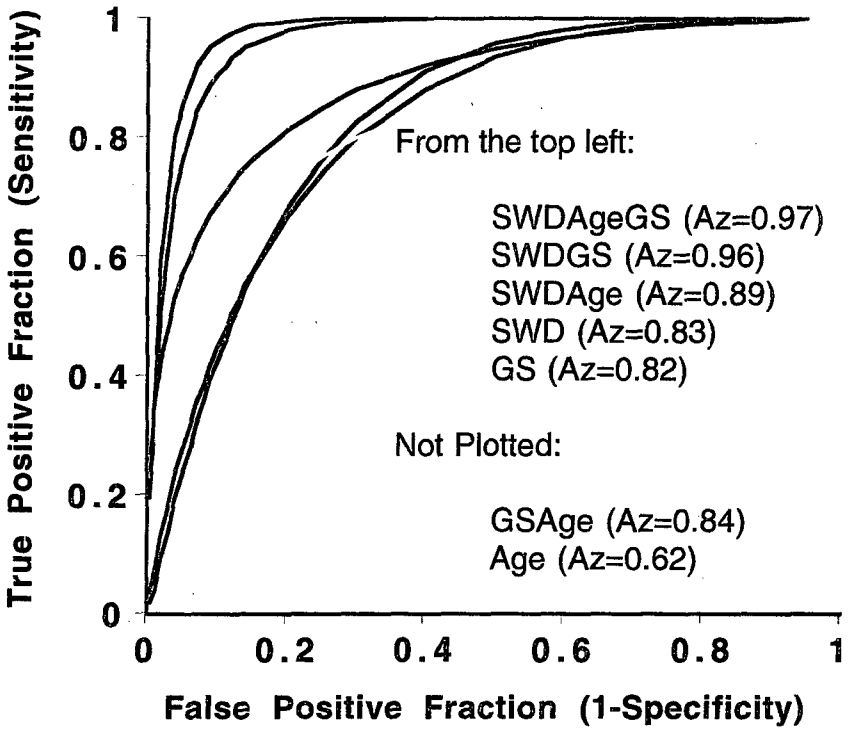

Figure 1. Performance of discrimination indices derived from the second patient population (n=40) as demonstrated by maximum likelihood binormal estimates of ROC curves. Speed-weighted pixel density (SWD), average grayscale rating (GS), and patient age were blindly applied to the multi-variable classifiers derived from the initial patient population (n=38). The high performance (Az=0.97) of the SWDAgeGS exceeded all other indices and demonstrated statistically significant improvement over all single variable indices. as described in the text.

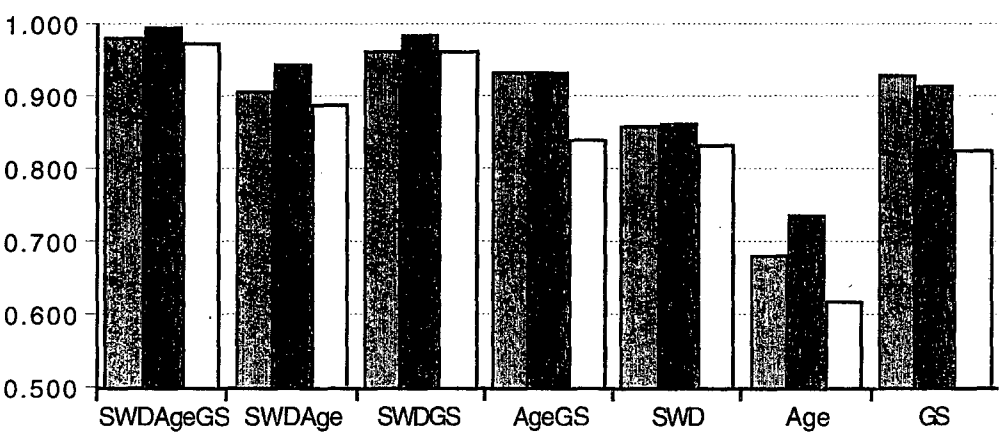

Figure 4. Average performance (as assessed by average Az values) of discrimination indices. The gray bar values were derived using the 4-fold cross validation method described in the text, and the grayscale ratings used represent the average of three independent readers' average grayscale rating for each case. Overall performance of SWDAgeGS (Az=0.981) fell between the test group's self evaluation (black bar, Az=0.997) and the blinded test group performance (white bar, Az=0.974).

RAPID IMAGE REGISTRATION FOR 3D ULTRASOUND COMPOUNDING

Jochen F. Krücker†, Paul L. Carson, Gerald L. LeCarpentier, J. Brian Fowlkes, Charles R. Meyer
University of Michigan, Dept. of Radiology, 200 Zina Pitcher Place, Ann Arbor, MI 48109-0553, USA

Abstract — A Subvolume-based algorithm for Ultrasound REgistration (SURE) has been developed and tested using artificially deformed *in vivo* ultrasound scans. SURE works in two stages, using MIAMI Fuse©[1-2] software to determine a global, affine registration in the first stage before iteratively dividing the volume into subvolumes and computing local rigid registrations in the second stage. Connectivity of the entire volume is ensured by global interpolation using thin-plate splines (TPSs). To simulate sequential scans, a random nonlinear deformation was applied and both correlated and uncorrelated noise was added to 20 image volumes, each reconstructed from 60 to 120 evenly spaced B-scan slices. Registration using SURE reduced the average displacements of 1.5 and 2.0 mm in the artificially deformed volumes to 0.20 and 0.27 mm, respectively. Registration times were below 5 min on a 500 MHz CPU for an average data set size of 13 MB.

I. INTRODUCTION

Tissue deformation and refraction artifacts can limit resolution in three-dimensional (3D) compound imaging. Image registration prior to compounding has been shown to partly correct for these resolution losses [3]. In breast imaging, a non-linear registration transformation with many degrees of freedom is often required for accurate registration of the constituent image volumes. The long computation time commonly required for these registrations has been an obstacle in implementing this technique for more widespread use. Other breast imaging applications of non-rigid registration include screening and sequential scanning to monitor changes in breast masses, where the comparison of registered image volumes potentially allows better assessment of changes and semi-automatic quantification of growth or shrinkage of masses [4]. SURE can provide accurate and fast non-rigid ultrasound registrations that address these needs.

II. MATERIALS AND METHODS

Data Acquisition

A Logiq 700 (GE Medical Systems, Milwaukee, WI) ultrasound scanner with an M12, 1.5D matrix array probe (11 MHz) was used to scan one or multiple breast masses in 10 volunteer patients. For all scans, high-resolution grayscale mode with eight transmit focal zones and a 4 cm field of view were selected. The probe was attached to a linear slider with two degree-of-freedom (elevational translation and elevational tilt) position encoding, and volumes were reconstructed from 60 to 120 B-scan slices with uniform 0.3 mm frame spacing. In each patient, the volume of interest was scanned from five look directions: 0° (reference), +5°, -5°, +10° and -10° relative to the vertical. All of these scans were used to assess the average image distortion in 3D-compounding. For the evaluation of SURE, only the 0° and +5° scan in each patient were used. In addition, five volume scans were obtained in a focal lesion phantom (Computerized Imaging Reference Systems (CIRS), Norfolk, VA) at tilt angles of 0°, 5°, 10°, 15°, and 20°. These data were used to investigate the statistics of the change in speckle pattern when imaged from different look directions.

Artificial Volume Deformation

In order to test the accuracy and robustness of SURE, 20 image volumes were artificially deformed and degraded by additional noise. Subsequent registration of the original with the deformed data sets, and comparison with the known, ideal registrations, allowed quantification of the performance of SURE.

A realistic level of volume deformation in compounding was estimated by comparing affine and nonlinear registrations in 27 of the non-vertical *in vivo* scans in which, by visual assessment, a good registration with the vertical reference scan was achieved by both registrations. All affine registrations were obtained using MIAMI Fuse©. The nonlinear registrations using SURE started with the affine results and ended by using up to 7×7×7 ($x \times y \times z$)

subvolumes. This process is explained in detail below.

The mean deformation D induced by a transformation T was defined as

$$D = \frac{1}{V}\iiint_V |\mathbf{x} - T(\mathbf{x})| d^3\mathbf{x} \qquad (1)$$

where the triple integral extends over the entire image volume V. Note that D potentially includes a linear component in T. For each pair of full affine and nonlinear registration transformations, T_{fa} and T_{nl}, the mean deformation of the difference transform $T_{diff} = T_{nl} - T_{fa}$ was computed. The average value of D for all valid registrations was 1.1 mm (range 0.6 to 1.9 mm). Since even the nonlinear registration does not provide "perfect" registration, these values are believed to be lower bounds for the mean deformations in compound imaging. Therefore, artificially deformed volumes with mean deformations of 1.5 and 2.0 mm were generated as follows. Volume deformations or "warping" from one 3D space ("reference") to another ("homologous") can be introduced using thin-plate splines [5], which are defined by the locations of an arbitrary number (larger than 4) of control points in both the reference and homologous space. The larger the number of control points, the more degrees of freedom in the transformation and the higher the spatial frequencies that can be realized with it. For each of the 20 image volumes used, nonuniformly spaced reference control points were generated by starting with a uniform grid of 5×5×5 points, and then adding a random vector of up to 5 mm length to each point location. Homologous control points were generated by first adding a random shift vector to each reference control point, and then scaling all shift vectors such that the mean deformation of the TPS transform defined by the control points had the desired value.

Two major differences between ultrasound volumes imaged from different look directions are (1) different echo amplitudes from specular reflectors, depending on the angle of incidence of the sound beam, and (2) a change in speckle pattern. Simulating (1) would require segmentation of specular reflectors, which was not attempted here. Instead, random Gaussian noise with amplitudes larger than expected for mere electronic noise was added to introduce additional differences between the volumes. The approximate first and second order statistics of effect (2) were simulated as follows. The four tilted scans obtained in the focal lesion phantom were registered onto the reference scan using MIAMI Fuse©. In a subvolume of fully developed speckle, difference images between the reference scan and the registered tilted scans, as well as the histogram and autocorrelation of the difference images were computed. The histograms displayed an approximately Gaussian distribution, the standard deviation of which increased from 15 to 23 gray-scale (GS) levels (out of 255) when increasing the tilt angle difference between the scans from 0° to 20°. The spatial autocorrelation of the difference images displayed a full width at half-maximum (FWHM) of 0.38 and 0.35 mm in the lateral and axial direction, respectively. These parameters were reproduced in simulated difference images by spatially low-pass filtering a volume of random Gaussian noise and scaling the gray-scale values such that the standard deviation of the histogram had the desired value. Both simulated difference images and uncorrelated noise were added to the deformed image volume. Figure 1 shows an example of one slice of an image volume before and after application of the deformation and noise. The white grid has been superimposed to visualize the *xy*-component of the artificial deformation.

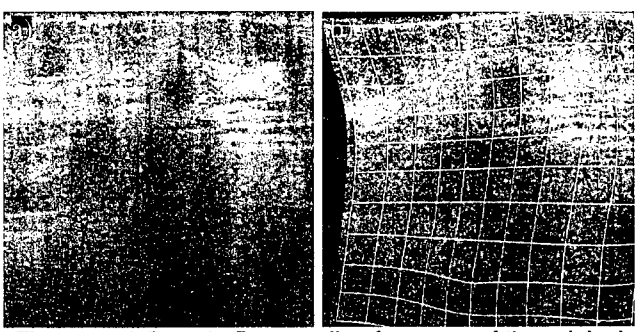

Figure 1: a) Sample B-scan slice from one of the original image volumes. b) Same slice after application of the random deformation and addition of noise. The white grid illustrates the deformation.

Registration using SURE

SURE can work in two stages, using MIAMI Fuse© software to obtain a global affine registration in the first stage before refining the solution using subvolumes in the second stage. The pixel similarity measure used in either stage is mutual information (MI)[1]. If the registration problem is known to have no global affine component or if that component is small, as is the case for the registration of the artificially deformed image volumes used here, the first stage can be omitted. The second stage consists of the following steps (illustrated in figure 2):

1. Downsize homologous image volume as needed

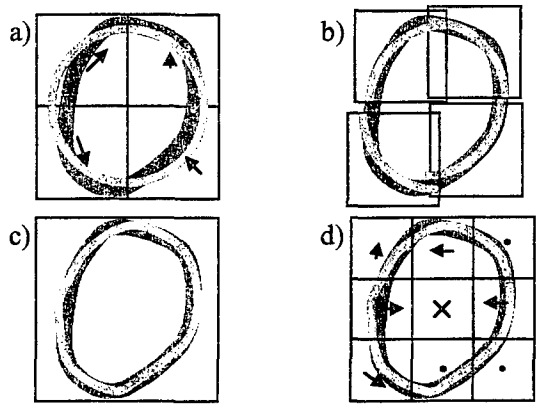

Figure 2: Illustration of the SURE algorithm registering the light gray circle onto the darker shape. a) Divide volume into subvolumes, find local shifts. b) The local shifts lead to better alignment but loss of connectivity. c) Interpolate between subvolumes using TPS with control points at subvolume centroids. d) Iterate with finer subdivision. Note that some subvolumes will be ignored (×), others will remain stationary because they are already aligned (•).

2. Use last registration transform (identity, affine, or TPS) to map reference onto homologous volume
3. Divide reference volume into subvolumes, starting with subdivision of 2×2×2 in first cycle and refining division in subsequent cycles
4. Ignore subvolumes that do not fulfill acceptance criteria (entropy > 5.7, volume overlap > 30%, MI > mean(MI) – 3 · std.dev.(MI))
5. Using method of steepest ascent, shift accepted subvolumes into best local alignment (largest MI)
6. Find new reference control points by applying inverse of last registration transform to centroids of subvolumes. New homologous control points are the shifted centroids of subvolumes. The TPS defined by reference and homologous control points is the new registration transform.
7. Go back to step 1 (fixed number of times, or until average subvolume shift is below threshold).

III. EXPERIMENTS AND RESULTS

In a first experiment, the 20 raw in vivo image volumes were each registered with their corresponding two deformed image volumes having mean deformations of D = 1.5 and 2.0 mm. The noise level in the deformed volumes, measured by the standard deviation σ of the Gaussian random distribution for both the spatially correlated and uncorrelated noise, was 15 GS. The noise level was increased to σ = 20 GS for the volumes registered in the second experiment (D = 1.5 and 2.0 mm). The average correlation coefficient (CC) between the original and deformed volumes was 0.59 and 0.57 for σ = 15 and 20 GS, respectively. For the third experiment, a set with the same parameters (D = 2.0 mm, σ = 15 GS) but higher spatial frequencies in the artificial deformation was generated by using 6×6×6 control points to define the warp. This new set and the previous set of (D = 2.0 mm, σ = 15 GS, 5×5×5 control points) volumes were registered using subdivision into up to a) 4×4×4 and b) 5×5×5 subvolumes. The results of these three experiments in terms of the correlation coefficient and the remaining mean deformation ("registration error") between the registered and the artificially deformed sets are summarized in tables 1 and 2. Figure 3 shows examples of two registrations.

Table 1: Average correlation coefficient (CC) and remaining deformation (D_r) between corresponding registered and artificially deformed volumes, and percent recovery of CC and D_r relative to their theoretical limit (CC: 0.87 to 0.93, based on noise; D_r: 0 mm).

D / σ	1.5 mm	2.0 mm	1.5 mm	2.0 mm
	CC		D_r (mm)	
15 GS	0.89 95%	0.87 94%	0.21 86%	0.27 87%
20 GS	0.82 95%	0.82 94%	0.21 86%	0.28 86%

Table 2: Average remaining deformation (mm) between registered and artificially deformed volumes (D = 2.0 mm, σ = 15 GS) and percent recovery for different numbers of subvolumes (in the registration) and control points (in the artificial warp).

Registration \ Warp	5×5×5 Control Points	6×6×6 Control Points
4×4×4 subvolumes	0.27 87%	0.33 84%
5×5×5 subvolumes	0.17 92%	0.24 88%

Running on a 500 MHz DEC Alpha CPU, the average registration time for the standard registration procedure (4×4×4 subvolumes) was 4.9 min per set (13 MB average size). A faster but less accurate variant of the same registration procedure yielded 20% larger remaining deformations computed in only 1.1 min per set. The more accurate, 5×5×5 subvolume registration took 5.3 min per set.

IV. DISCUSSION AND CONCLUSIONS

The subvolume-based registration algorithm SURE achieved high registration accuracy in non-linear ultrasound to ultrasound registrations. The registration problem was designed to approximate

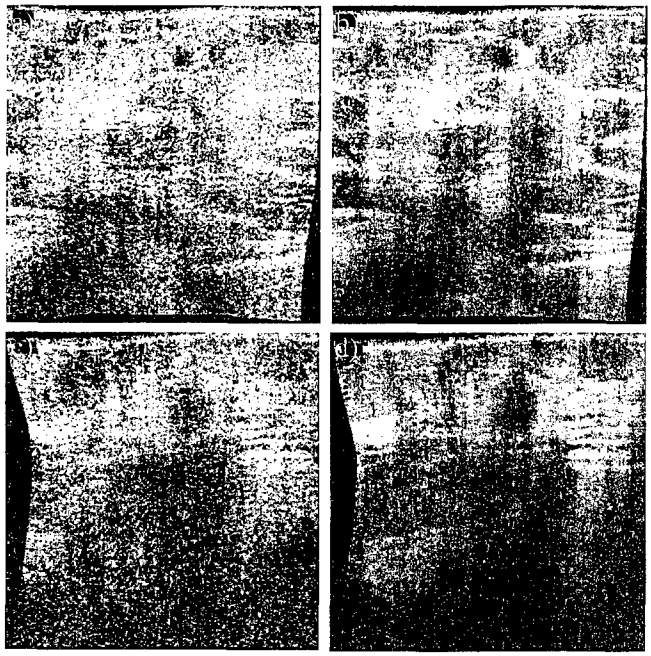

Figure 3: (a, c) Image frames in two cases after artificial deformation and addition of noise. (b, d) the same frames after registration of the corresponding original volumes onto (a, c). The registration error in (a) was in-line with the mean error, whereas the error in (d) was more than two standard deviations above the mean.

conditions found in compound imaging. The change in speckle pattern was simulated by addition of spatially filtered noise, which approximates the first and second order statistics of the actual change. The different appearance of specular reflectors could not be simulated and was replaced by an elevated noise level. The degree to which this resembles a real compound imaging scenario remains uncertain. Nonetheless, the advantage of this method compared with registrations between the actual constituent scans of compound volumes is the existence of a gold standard (the artificial deformation), which allows quantification of the registration error. The procedure was meaningful in that larger spatial frequencies were employed in the artificial warping than in the registration transformation.

The registrations were robust in the sense that irrespective of noise level and mean deformation tested, only one case produced registration errors more than two standard deviations above the mean. This particular case (Figure 3c, d) displayed shadowing and noise, but little or no structural information in the lower half of the scan where the largest registration errors occurred. Image-based registration in areas with little image information is generally difficult or impossible, but is also rarely relevant in practice. It may be concluded that in this case the field of view should have been reduced to the upper half.

SURE's registration speed is highly competitive and compares very well to a different nonlinear registration procedure in which a TPS-transform was optimized globally using the downhill simplex algorithm. Such registrations were carried out for 10 of the 20 image volumes used before and produced registration errors three times larger than those achieved using SURE while increasing the registration time by more than a factor of 10.

V. ACKNOWLEDGEMENTS

This work was supported by U.S. Army contract DAMD17-96-C-6061.

VI. REFERENCES

[1] C. R. Meyer, J. L. Boes, B. Kim, et al. "Demonstration of accuracy and clinical versatility of mutual information for automatic multimodality image fusion using affine and thin-plate spline warped geometric deformations", Med Image Anal, vol. 1, pp. 195-206, 1996/7.

[2] C. R. Meyer, J. L. Boes, B. Kim, et al. "Semi-automatic registration of volumetric ultrasound scans", Ultrasound Med Biol, vol. 25, pp. 339-47, 1999.

[3] J. F. Krücker, C. R. Meyer, G. L. LeCarpentier, J. B. Fowlkes, P. L. Carson, "3D spatial compounding of ultrasound images using image-based nonrigid registration", Ultrasound Med Biol, vol. 26, No. 8 (in press).

[4] J. F. Krücker, G. L. LeCarpentier, C. R. Meyer, et al. "3D image registration for multimode, extended field of view, and sequential ultrasound imaging", RSNA EJ, vol. 3, 1999. http://ej.rsna.org/ej3/0098-99.fin/index.html

[5] F. L. Bookstein, Morphometric Tools for Landmark Data, Cambridge University Press, Cambridge, 1997, ch. 2, pp. 26-34

[6] D. L. Collins, T. M. Peters, and A. C. Evans, "An automated 3D non-linear image deformation procedure for determination of gross morphometric variability in human brain," Visualization in Biomedical Computing (1994), in SPIE, vol. 2359, pp. 180-190.

† Jochen Krücker e-mail: jokr@umich.edu

Appendix 10

ELSEVIER

Ultrasound in Med. & Biol., Vol. 26, No. 8, pp. 0000–0000, 2000
Copyright © 2000 World Federation for Ultrasound in Medicine & Biology
Printed in the USA. All rights reserved
0301-5629/00/$–see front matter

PII S0301-5629(00)00286-6

● *Original Contribution*

3D SPATIAL COMPOUNDING OF ULTRASOUND IMAGES USING IMAGE-BASED NONRIGID REGISTRATION

JOCHEN F. KRÜCKER, CHARLES R. MEYER, GERALD L. LECARPENTIER, J. BRIAN FOWLKES and PAUL L. CARSON

Department of Radiology, University of Michigan, Ann Arbor, Michigan, USA

(*Received* 26 *January* 2000; *in final form* 26 *June* 2000)

Abstract—Medical ultrasound images are often distorted enough significantly to limit resolution during compounding (i.e., summation of images from multiple views). A new, volumetric image registration technique has been used successfully to enable high spatial resolution in three-dimensional (3D) spatial compounding of ultrasound images. Volumetric ultrasound data were acquired by scanning a linear matrix array probe in the elevational direction in a focal lesion phantom and in a breast *in vivo*. To obtain partly uncorrelated views, the volume of interest was scanned at five different transducer tilt angles separated by 4° to 6°. Pairs of separate views were registered by an automatic procedure based on a mutual information metric, using global full affine and thin-plate spline warping transformations. Registration accuracy was analyzed automatically in the phantom data, and manually *in vivo*, yielding average registration errors of 0.31 mm and 0.65 mm, respectively. In the vicinity of the warping control points, registrations obtained with warping transformations were significantly more accurate than full affine registrations. Compounded images displayed the expected reduction in speckle noise and increase in contrast-to-noise ratio (CNR), as well as better delineation of connective tissues and reduced shadowing. Compounding also revealed some apparent low contrast lobulations that were not visible in the single-sweep images. Given expected algorithmic and hardware enhancements, nonrigid, image-based registration shows great promise for reducing tissue motion and refraction artifacts in 3D spatial compounding. © 2000 World Federation for Ultrasound in Medicine & Biology.

Key Words: **Ultrasound imaging, Ultrasonics, Medical imaging, 3D ultrasound, 3D spatial compounding, Automatic registration, Mutual information, Thin plate spline, Refraction Correction.**

INTRODUCTION

Medical image registration is used clinically in a large number of applications such as diagnostics, treatment planning and surgical procedures. It is also a very active topic of research as recent review articles by van den Elsen et al. (1993) and Maintz and Viergever (1998) show.

Spatial compounding, the combination of individual ultrasound images or scans obtained from different look directions, has been investigated since the 1950s (Holmes et al. 1954). Before the advent of gray-scale imaging in the 1970s, compounding by translation and rotation was the method of choice for more complete outlining of organs. In gray-scale imaging, compounding provides additional benefits such as reduction of speckle noise and shadows (Kossoff et al. 1976). Since array probes have become available, 2D compounding by electronic steering of the beam (Berson et al. 1981; Jespersen et al. 1998; Shattuck and von Ramm 1982) has been investigated. One company (ATL Ultrasound, Bothell, WA, USA) now offers a commercial ultrasound scanner with real-time 2D compound imaging ("SonoCT™") using large angle electronic beam steering. A number of theoretical (Burckhardt 1978; O'Donnell and Silverstein 1988; Wagner et al. 1988) and experimental (Trahey et al. 1986) studies investigated the decorrelation of speckle with lateral translation of the transducer to find the optimum displacement for 2D compounding.

Three-dimensional (3D) compounding differs from 2D compounding in that a greater number of independent views can be combined, the compounded field of view is not limited by transducer size, more specular reflectors can be imaged at normal incidence, and it offers the possibility of out-of-plane refraction correction. All of these advantages were exploited in this study. It does not,

Address correspondence to: Dr. Jochen F. Krücker, University of Michigan, Department of Radiology, 200 Zina Pitcher Place, Kresge III, Rm. 3315, Ann Arbor, MI 48109-0553, USA. E-mail: jokr@umich.edu

however, work in real-time, although increased processing power may make the 3D-compounded image available almost immediately following acquisition, as discussed at the end of this paper.

Recently, (Barry et al. 1997) and Leotta (1998) performed 3D compounding by attaching a position encoder to the transducer, scanning the volume-of-interest from several look directions and combining the pixel values using various algorithms. In these studies, external (electronic, mechanical or electromagnetic) position encoding was used to register the positions of images obtained from different look directions. Good results were obtained in phantom scans and in selected *in vivo* applications. However, this approach in general, and methods that require physical motion of the transducer in particular, are limited by tissue motion and refraction artifacts. If tissue is moved or deformed between or during compound scans, it gets registered into different positions relative to the external reference frame. Similarly, refraction due to sound speed inhomogeneities may cause tissue structure to appear in different positions from different look directions. This effect has been used by Robinson et al. (1982) to measure the average sound speed in tissue. If uncorrected, these shifts can cause blurring in the compounded image, and possibly "ghost" artifacts as observed in some single-view imaging situations (Buttery and Davison 1984; Robinson et al. 1981).

Moskalik et al. (1995) were the first successfully to apply image-based registration of separate 3D ultrasound views before compounding to reduce artifacts. They manually defined corresponding points, lines and planes in pairs of volumetric data sets, and employed nonrigid full affine transformations (rotate, translate and shear) to match these features. Rohling et al. (1997, 1998) obtained good results using rigid body transformations for automatic, correlation-based registration prior to compounding.

Meyer et al. (1999a) showed that their mutual information-based software "MIAMI Fuse," developed for multimodality image fusion (Kim et al. 1997, Meyer et al. 1996/7), yields reproducible and accurate full affine and warping transformations in same-modality 3D ultrasound registration. The same algorithm, first introduced by Meyer et al. (1996/7), was used by Krücker et al. (1999) to demonstrate creation of multimode and extended volume ultrasound images, and to track changes of tissue structure and vascularity by registration of serial ultrasound scans obtained months apart. In this study, "MIAMI Fuse" is used to improve 3D compound image quality and reduce artifacts caused by tissue motion and refraction. This is achieved by employing nonrigid transformations for accurate, automatic registration of different views before compounding.

MATERIALS AND METHODS

Data acquisition

All ultrasound data used in this study were acquired using a Logiq 700 (GE Medical Systems, Milwaukee, WI, USA) clinical ultrasound scanner in high resolution, multifocal gray scale mode. The scanhead used was an M12, 1.5D matrix array probe with 38 mm array length and 4.2 mm elevational extent. For all scans, a center frequency of 11 MHz, the maximum number of transmit focal zones (eight), and a 4 cm field of view were used. The scan length ranged from 3 to 4 cm. The probe was clamped to a linear slider mounted on a hand-held frame (Fenn et al. 1997; LeCarpentier et al. 1999) for restriction of the motion to two degrees of freedom. The linear position in the elevational (out-of-plane) direction was encoded with 18 μm accuracy using a potentiometer. The rotational (tilt) motion around the lateral axis was recorded with 0.05° accuracy using an optical encoder. Note that the position is recorded relative to the frame, and thus provides consistent information within individual scans (intrascan registration) only when the frame is not moved relative to the tissue or phantom during a scan. Between individual scans, however, the frame usually was moved for the adjustment of transducer tilt, and the induced tissue deformation differed from scan to scan. Moreover, beam aberrations can cause structure to appear in slightly different locations when imaged from different directions. Therefore the recorded positions could not be used for accurate interscan registration.

Volumetric data were obtained by manually sweeping the probe across the volume of interest and storing the image frames in the internal cine loop buffer of the ultrasound machine. Approximately uniform frame spacing was achieved using position tracking scan software. The software reads the linear position and sends a pulse to the ultrasound machine to trigger acquisition of a new frame each time the position has increased by a user-defined step size. Delays between the trigger and actual acquisition of the new image are accounted for to the extent possible. The acquired image volumes were later saved to disk and transferred to a DEC Alpha workstation for registration and processing.

Images were obtained in a focal lesion phantom (Computerized Imaging Reference Systems (CIRS), Norfolk, VA, USA), and *in vivo*. The phantom is comprised of a densely packed, random distribution of fine particles, which creates speckle in the ultrasound image. In addition, the phantom contains a large number of high contrast (−12 dB), spherical "voids" (3 mm and 5 mm diameter), and two nylon filaments. A 3D view of one of the image volumes acquired in the phantom is displayed in Fig. 1. *In vivo* breast scans were obtained in a volunteer patient who had a circumscribed, benign-appearing F1

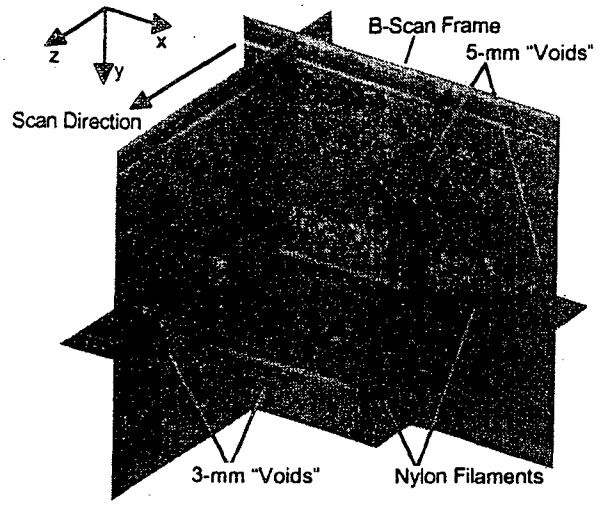

Fig. 1. Three-dimensional view of the reference image volume acquired in the focal lesion phantom.

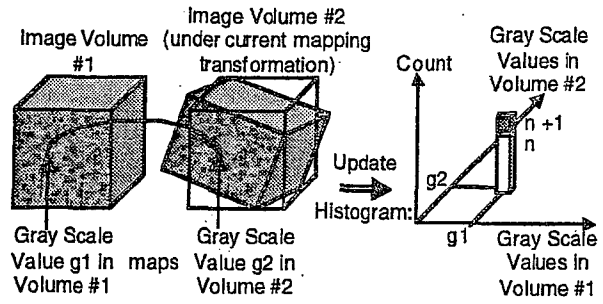

Fig. 2. Construction of the 2D joint histogram needed to compute mutual information. For each mapping evaluated during the optimization, one histogram is computed by raster scanning through the volumes and updating the histogram for each voxel pair.

mass in the lower inner quadrant. One of the *in vivo* volumes is displayed in Fig. 14, together with a ROI and control points explained in the Experiments and Results section.

For each compound study, five to 16 scans of 100 frames were obtained in the volume-of-interest, each scan with a fixed transducer tilt angle between 0° (normal to surface) and about 17°. The encoded position information was used to interpolate each individual image volume into a rectilinear grid, retaining the original pixel resolution of 10 pixel/mm in the *xy*-plane (image plane), and using the user-defined frame spacing along the *z*-axis.

Registration

Alignment between separate scans obtained in the same volume of interest was achieved using semiautomatic Image Volume-Based Registration (IV-BaR) of the gray-scale data sets. The MIAMI Fuse software performing this process has been employed previously for fusion of 3D ultrasound images (Krücker et al. 1999; Meyer et al. 1999a). The theoretical background is presented in detail in Maes et al. (1997) and Viola and Wells III (1997). A summary is given below for convenience.

The registration procedure employs the mutual information I of a pair of data sets to measure their relative alignment. The mutual information is defined as $I(x, y) = H(x) + H(y) - H(x, y)$, where $H(x)$ and H(y) is the entropy of data sets x and y, respectively, and $H(x, y)$ is the joint entropy of the two data sets. $I(x, y)$ can be computed using the probability densities $p(x)$, $p(y)$ and joint probability density $p(x, y)$. The probability densities are approximated by the normalized gray scale histograms. The joint probability density is approximated by the normalized 2D histogram, with the two base axes corresponding to gray scale levels in the two data sets. The histogram value $p(g_1, g_2)$ is equal to the normalized count of pixels with value g_1 in the first data set that match, under the current mapping transformation, a value g_2 at the same location in the second data set. The process of constructing the 2D histogram is illustrated in Fig. 2. F2

The registration optimization works by iteratively maximizing the mutual information I. The only user interaction in the process is the definition of an approximate initial alignment of the two data sets by placing three control points in each set. Even this step can be automated if the relative position and orientation of the data sets is roughly known. The control points define a geometric transformation that is applied to match one data set ("homologous") onto the other ("reference"). The mutual information of the matched pair is calculated, and the Nelder-Maed downhill simplex algorithm is used to modify the position of the control points until I is maximized. The optimization can work in several stages, employing increasing numbers of control points and thus increasingly complex geometrical transformations. For efficient optimization, each stage can use downsized versions of the original data sets and different parameters to confine variation of the control point positions and to determine convergence of each optimization cycle. For this study, two- and three-stage processes were used. The first stage employs three control points (rotate/translate), the second stage four (full affine transformation), and the third stage an arbitrary number of control points greater than four (thin plate spline warping). Each stage comes to a stop and passes its final transformation on to the next stage when the mutual information increment in the last cycle is less than a predefined threshold. Figure 3 shows F3 a flow chart of the registration algorithm.

For nonrigid registrations, Meyer et al. (1999b)

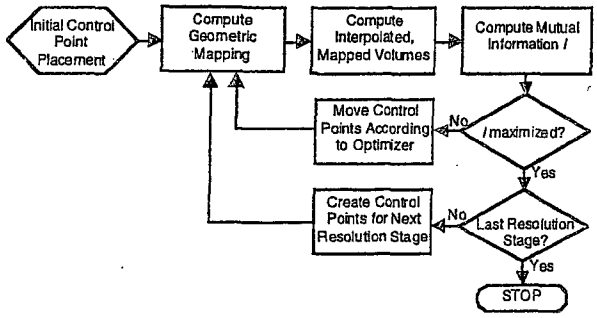

Fig. 3. Flow chart of the registration algorithm.

found an approximately linear increase in iterations with number of control points in brain MRI data sets. This increase went in parallel with an increase in the final mutual information and is expected asymptotically to approach an upper limit that depends on the information content of the image sets to be registered. Combined with the linear increase of computation time per iteration, this yields a quadratic dependency of computation time on the number of control points, up to the upper limit. In the *in vivo* scans reported on in this study, the final mutual information was found to increase only slowly when adding more than 11 control points. This number was subsequently used as a trade-off between registration accuracy and computation time. On a state-of-the-art workstation running at 500 MHz, typical registrations of a 4.5 megabyte data set currently take 5–6 min when using full affine transformations only, and 20–30 min using warping with 11 control points.

Compounding and data analysis

To create a compound image volume from N individual volumes, scans number 2 . . . N are registered and transformed onto the first scan (usually the one obtained at 0° transducer tilt). The image volumes are then converted from gray scale to echo amplitude values, averaged and re-compressed to gray-scale values for display. Different methods of image combination, such as peak or minimum detection for each pixel, were investigated by others (Robinson and Knight 1981). Averaging was chosen for all figures displayed here, because it yields optimal improvement of speckle signal-to-noise ratio (SNR) and only small loss of resolution. The process of obtaining, registering and compounding one pair of scans is illustrated in Fig. 4. F4

Intensity images were created by squaring the decompressed amplitude images (in arbitrary units). Image statistics such as SNR, contrast-to-noise ratio (CNR), and correlation coefficient (ρ) were computed in the intensity images, using the following definitions:

$$\mathrm{SNR} = \langle I \rangle / \sigma \qquad (1)$$

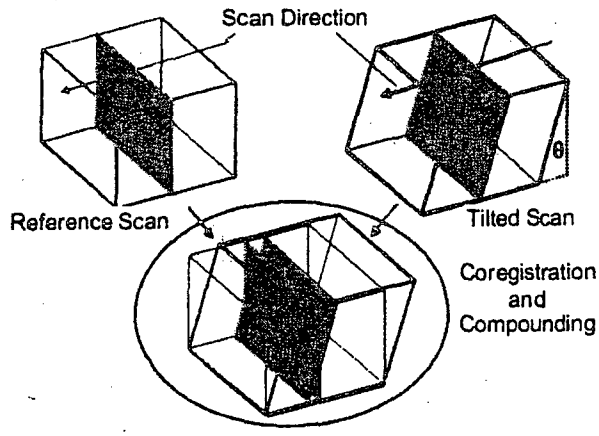

Fig. 4. Illustration of the acquisition, registration and compounding process, exemplified for compounding of only two views. A reference scan is obtained by holding the transducer normal to the skin or phantom surface, and sweeping it slowly in the elevational direction. A second scan is obtained in the same volume, but with the transducer held at an angle θ. The image volumes are then aligned using our automated registration procedure, compounded, and displayed in the original orientation of the reference scan.

where $\langle I \rangle$ and σ are the mean and standard deviation of the intensity, respectively.

$$\mathrm{CNR} = (\langle I_o \rangle - \langle I_b \rangle)/\sigma_b \qquad (2)$$

where $\langle I_o \rangle$ and $\langle I_b \rangle$ are the mean object and background intensity, respectively, and σ_b is the standard deviation of the background.

$$\rho_{ij} = \frac{m_{ij}}{\sigma_i \sigma_j} = \frac{\langle (I_i - \langle I_i \rangle)(I_j - \langle I_j \rangle) \rangle}{(\langle (I_i - \langle I_i \rangle)^2 \rangle \langle (I_j - \langle I_j \rangle)^2 \rangle)^{1/2}} \qquad (3)$$

where m_{ij} is the covariance of images I_i and I_j.

For a compound image averaged from N partly correlated views, the SNR can be written as:

$$\mathrm{SNR}_N = \frac{\sum_{i=1}^{N} \langle I_i \rangle}{\sqrt{\sum_{i=1}^{N} \sigma_i^2 + 2 \sum_{i=1}^{N} \sum_{j=i+1}^{N} \rho_{ij} \sigma_i \sigma_j}} \qquad (4)$$

A similar increase is expected for the CNR if the "background" is located in an area of fully developed speckle and the "objects" in the different scans are perfectly aligned. Equation (4) was obtained using the expression for the variance of an average of N images given by Trahey et al. (1986). Assuming all views have equal means and standard deviations, eqn (4) reduces to:

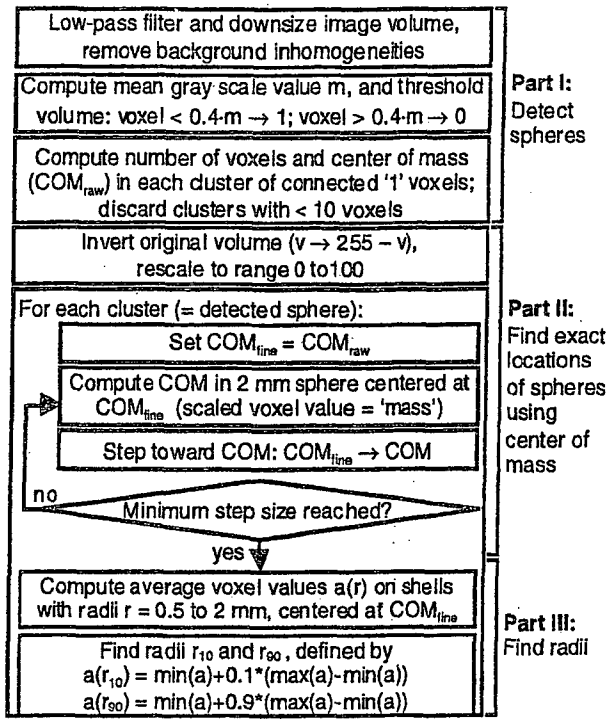

Fig. 5. Flow chart of the algorithm (ALS) used to localize and segment spheres in the phantom scans.

$$SNR_N = SNR_0 \sqrt{N} \frac{1}{\sqrt{1 + \frac{2}{N} \sum_{i=1}^{N} \sum_{j=i+1}^{N} \rho_{ij}}} \quad (5)$$

where SNR_0 is the signal-to-noise ratio of the individual views. This in turn yields the well-known ~~insert equation from msp 12~~ for uncorrelated views. $SNR_N = \sqrt{N} \cdot SNR_0$

An algorithm (ALS) was created for automatic localization and segmentation of hypoechoic spheres in an image volume (flow chart shown in Fig. 5). ALS was used objectively to analyze CNR and registration accuracy in the CIRS phantom. The spheres were first detected using thresholding and then localized by iteratively computing the "center of mass" of the inverted pixel values in the neighborhood of the spheres. Misregistration between pairs of registered data sets was defined as the average displacement between corresponding spheres in the two sets. For each detected sphere, an inner and outer boundary, r_{10} and r_{90}, were defined as in Fig. 5. The difference between r_{90} and r_{10} defines the border width of a sphere and was compared between uncompounded (single sweep) and compounded data sets as a measure of image blur.

EXPERIMENTS AND RESULTS

Angular decorrelation

Earlier studies on 2D compounding found the lateral translation of the aperture for optimal SNR increase to be about $\Delta x_{opt} = 0.4–0.5$ aperture widths, based on the theoretical decorrelation curve derived from a one-dimensional model of the point spread function of a rectangular aperture (Burckhardt 1978; O'Donnell and Silverstein 1988). Trahey et al. (1986) found smaller values for Δx_{opt} (0.2–0.25) using a measured decorrelation curve, but obtained 95% to 97% of the optimized SNR when using $\Delta x = 0.4–0.5$.

In the scanning configuration used for this study, the degree of correlation between pairs of registered data sets is naturally measured as a function of the difference in tilt angle $\Delta\alpha$ at which the scans are obtained. Using the nominal elevational aperture size of the M12 probe (4.2 mm), the result for 2D compounding can be converted into an optimum differential tilt angle. For an average focal distance of 2 cm, and $\Delta x_{opt} = 0.4$ to 0.5, this yields $\Delta\alpha_{opt} = 5°$ to 6°.

To verify that this differential tilt angle is appropriate to use with our particular ultrasound scanner and imaging mode, the angular decorrelation was measured experimentally. In the focal lesion phantom, 16 volume scans containing 100 frames each with frame spacing 0.2 mm were acquired. The scanned region contained about 50 3-mm diameter "voids" on one side, a straight nylon wire along the scan direction in the center, and no visible feature but speckle on the other side. The voids and wire were included to provide sufficient landmarks for the automated registration procedure. Four of the scans were obtained at 0° tilt angle, with the average frame positions in scans 2–4 offset by about 21, 71 and 88 μm, respectively, relative to scan 1. These scans were obtained to evaluate the effect of system noise and random frame positions within the 0.2 mm frame spacing on the degree of correlation achievable following registration. The remaining 12 scans were acquired at tilt angles from 1° to 12° in 1° increments.

All scans were registered to the first 0° scan in a two-stage process employing full affine transformations in the second stage. The decorrelation analysis was performed on a speckle subvolume in a portion of the phantom that was included in all 16 scans. To obtain an estimate of the variation of correlation coefficients and SNRs across the scanned volumes, the subvolume was divided into 75 blocks of 30 × 30 × 9 pixels (x, y, z). Correlation coefficients between the registered scans and the 0° reference were computed for each block. Table 1 shows the average correlation coefficient ρ (and standard deviations) for scans 1–4 registered onto 1. Note that, for the registration of 1 onto itself, ρ is 1.5% below the ideal value of 1.0 due to the precision tolerance of the registration algorithm. For scans 2–4, ρ is 9 to 23% below 1.0, with no significant correlation between the average frame displacement and the final correlation coefficient. In Fig. 6a, the average correlation coefficients are plotted

Table 1. Intensity correlation coefficients in a region of speckle in four scans (1–4) obtained in the focal lesion phantom at 0° transducer tilt and registered onto scan 1 using full affine transformations. $\overline{\Delta z}$ is the average displacement in scan direction of a frame relative to the corresponding frame in scan 1, $\bar{\rho}$ and $\Delta\rho$ are the mean and standard deviation of the correlation coefficient, respectively

Scan No.	$\overline{\Delta z}$ (μm)	$\bar{\rho}$	$\Delta\rho$
1	0	0.985	0.004
2	21	0.913	0.022
3	71	0.765	0.078
4	89	0.888	0.017

as a function of tilt angle for all scans obtained. The value plotted at 0° is the average correlation coefficient of registered scans 2–4.

Each of the registered scans was compounded with the 0° scan. The SNR was computed in the same blocks as the correlation coefficient. In Fig. 6b, the SNR of the compound images is plotted as a function of tilt angle. Again, the value plotted at 0° is the average of scans 2–4 compounded with scan 1. Note that the computed SNR generally increases with decreasing block size. For large blocks, inhomogeneities in the ultrasound image increase the standard deviation and thus reduce SNR. For blocks smaller than or comparable with the speckle size, the intensity variation across an entire speckle cell gets underestimated, which increases SNR unrealistically. The block size chosen was a compromise between the two extremes, with about 40 resolution cells per block.

Compounding in focal lesion phantom

In the focal lesion phantom, a volume containing about 50 3-mm "voids"' was scanned at various tilt angles of the transducer. A reference scan (scan 1) was obtained at 0° , additional scans (scans 2–5) were obtained at 4.0, 8.4, 12.7 and 16.8° . Scans 2–5 were registered with the reference scan in a two-stage process, employing full affine transformations in the final stage. Between 35 and 45 spheres were localized and segmented in each scan using ALS. Figure 7 shows a sample F7
frame from scan 1, with cross-sections of the segmented inner and outer boundaries of the spheres drawn in white. The registration errors for these scans, defined as the average displacement between corresponding spheres, are summarized in Table 2. T2

ALS was applied again to determine positions and radii of spheres in the volumes compounded from of two to five individual scans. The computed border width of the spheres ranged from 0.64 mm to 0.69 mm and did not increase significantly with the number of volumes com-

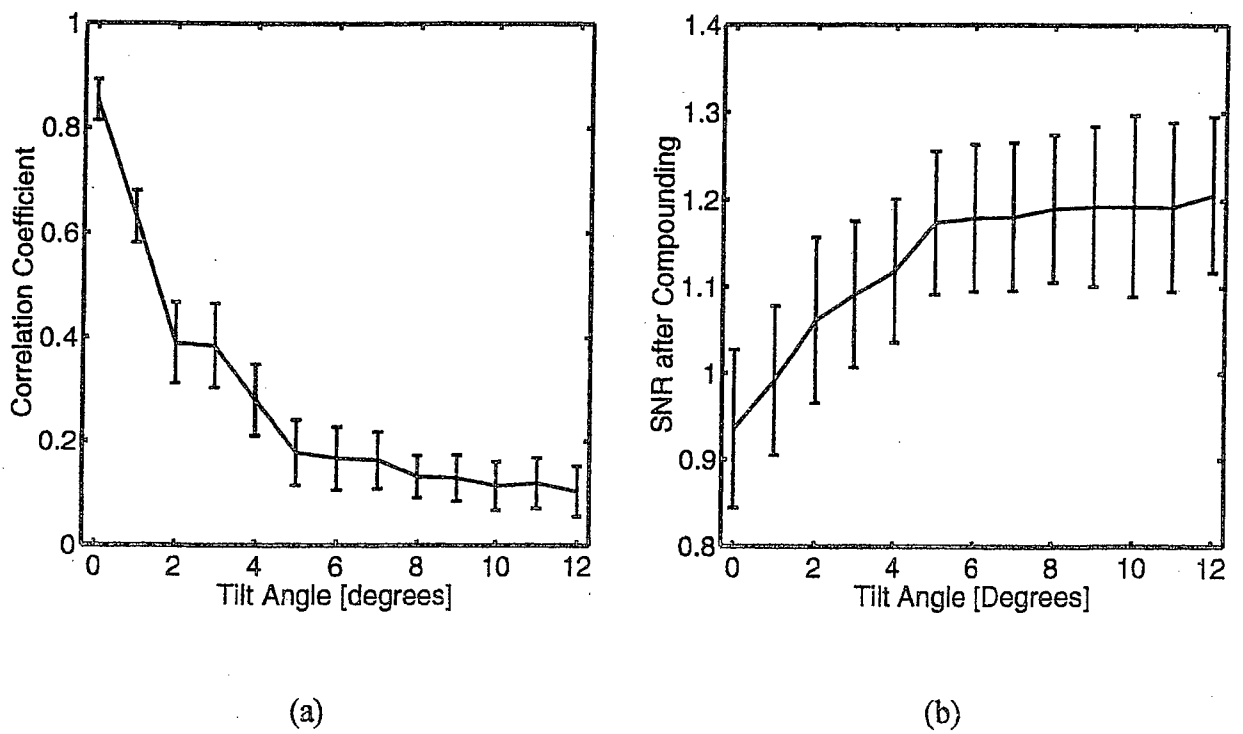

Fig. 6. (a) Correlation coefficients as function of tilt angle. (b) SNR of the speckle region following compounding of two data sets as a function of tilt angle difference. The error bars indicate ± 1 standard deviation.

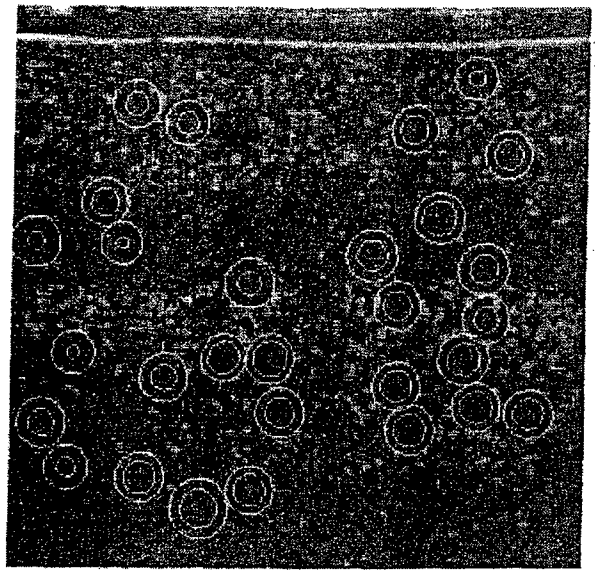

Fig. 7. Sample frame from phantom scan 1 with cross-sections of all segmented spheres drawn in white. The two radii displayed for each circle are r_{10} and r_{90}, the radii of 10% and 90% signal increase from the interior to the exterior of the spheres, as defined in Fig. 5.

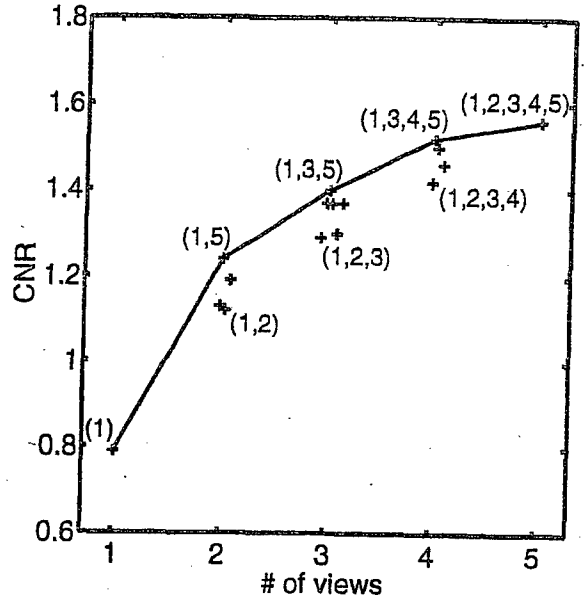

Fig. 8. Contrast-to-noise ratio (CNR) in the focal lesion phantom for a single-sweep volume (one view, reference) and for compound volumes created from two, three, four and five individual views. Each cross corresponds to a compound volume created from a specific subset of the individual scans. For each number of views, the indices in parentheses indicate the subsets of scans that led to the highest and lowest CNR.

pounded. This result differs from an earlier analysis of the 2D border width within the image planes alone. There, the computed average border width was 0.52 mm and showed a significant 17% increase from the uncompounded reference volume to the volume compounded from five scans.

In the same compound volumes, the CNR was computed by choosing a 30 × 280 × 40 pixel volume of speckle as background, and using the interior of all spheres with radius r_{10} as objects. The SNR in the background region alone increased monotonically with the number of compounded scans and reached an improvement of 94% when compounding all five scans, closely matching the value of 90% obtained using eqn

Table 2. Average registration errors of scans obtained in the focal lesion phantom and registered to the 0° reference scan 1 with a global full affine transformation. $\bar{d}$ and d_{max} are the average and maximum displacement, respectively, between the centers of 30–40 spheres identified in the reference and the tilted scans. $\Delta\bar{d}$ is the standard error of $\bar{d}$

Scan No.	Tile angle	$\bar{d}$ (mm)	$\Delta\bar{d}$ (mm)	d_{max} (mm)
2	4.0°	0.26	0.019	0.58
3	8.4°	0.32	0.031	0.72
4	12.7°	0.41	0.038	1.06
5	16.8°	0.25	0.026	0.52
Combined		0.31	0.016	1.06

$\langle I_i \rangle$, σ_i, and ρ_{ij}

(4) with measured parameters ~~insert equation from msp 16.~~ Similarly, the average CNR increased from 0.79 to 1.56, yielding a 97% increase in CNR for the volume compounded from five look directions (Fig. 8). Figures 9 and 10 show examples of axial-lateral and axial-elevational cross-sections, respectively, through (a) the uncompounded volume, and volumes compounded from (b) three and (c) five look directions. Note the better definition and higher contrast of the spheres in the compounded images. Some of the spheres are difficult to identify in Fig. 9a, but are clearly visible and separable in Fig. 9c (white arrows). Also note the reduced shadow below the nylon wire in Fig. 10c. Different CNRs were obtained when using a fixed number, but different subsets of constituent volumes (i.e., different tilt angles). Compounding two scans separated by 16° in look direction (scans 1, 5; Fig. 11a) yielded an 11% larger CNR than two scans separated by 4° (scans 1, 2; Fig. 11b). Compounding three scans separated by 8° (scans 1, 3, 5) yielded a 9% larger CNR than three scans separated by 4° (scans 1, 2, 3).

Figure 12 shows isosurface renderings of a subvolume of the (a) uncompounded and (b) fully compounded scans. In each case, the isosurface level was adjusted for optimal display of the 3-mm spheres. No further processing, such as manual reduction of clutter, was applied.

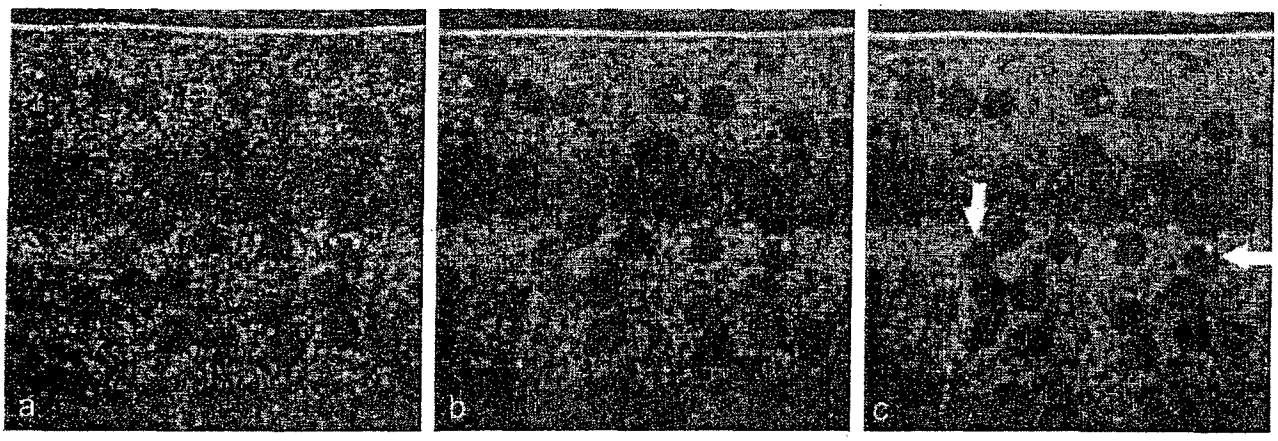

Fig. 9. Axial-lateral (B-mode) cross-section of the image volume obtained in the focal lesion phantom. (a) Uncompounded, (b) compounded from three look directions (θ = 0.0°, 8.4° and 16.8°, (c) compounded from five look directions (θ = 0.0°, 4.0°, 8.4°, 12.7° and 16.8°). Note the overall reduction in granularity and better definition of the circular boundaries in (b) and (c). The white arrows point to spheres clearly visible in (c), but harder to identify in (a). The black arrow points to a border between two spheres well defined in (c), but washed out in (a). The bright band across the center of the images is an artifact produced by the ultrasound scanner.

Compounding in vivo

The lower inner quadrant in the right breast of a 56-year-old female volunteer patient was scanned five times at transducer tilt angles of 0, 6.4, 12.8, −5.1 and −10.2°. The scans consisted of 100 frames each, with an average frame spacing of 0.3 mm. The volume covered a 6.5-mm diameter benign-appearing mass in the second half of the scan. Following interpolation, the volume was cropped to 60 frames of 280 × 280 pixels each to exclude strongly motion-distorted portions of the volume and speed up the registration process.

Scans 2 to 5 (S2 to S5) were registered onto scan 1 (S1) in two processes. First, a two-stage registration with full affine transformations in the final stage was applied,

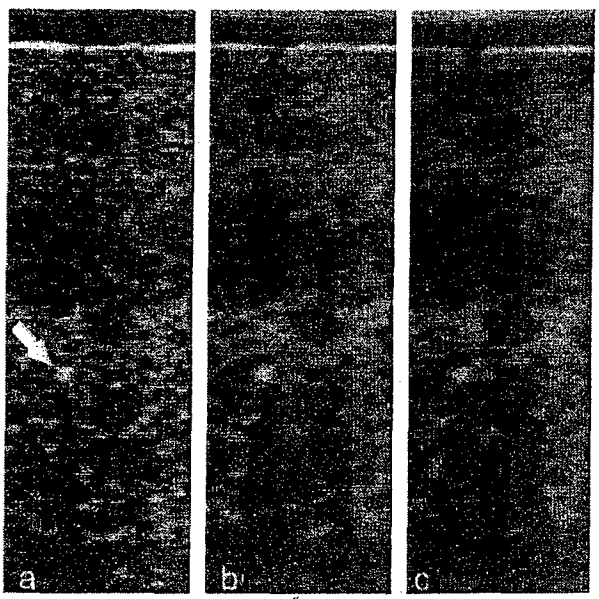

Fig. 10. (a) Axial-elevational cross-section of part of the uncompounded reference volume in the focal lesion phantom. (b) The same cross-section compounded from three and (c) from five look directions. The bright spot (arrow) is the cross-section of a shadow-casting nylon filament. Note the clearer definition of the spheres and the reduced shadow in the compounded views.

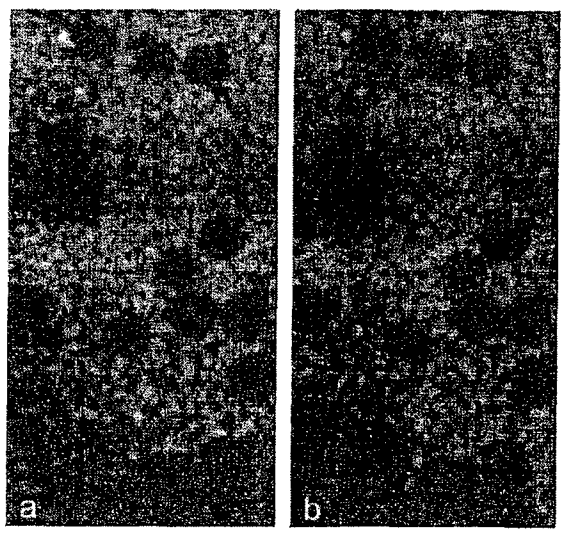

Fig. 11. (a) Cross-section of a subvolume compounded from two look directions separated by 16°. (b) The same cross-section compounded from two views separated by 4°. The images are very similar, but a slightly better reduction of speckle in (a) is noticeable.

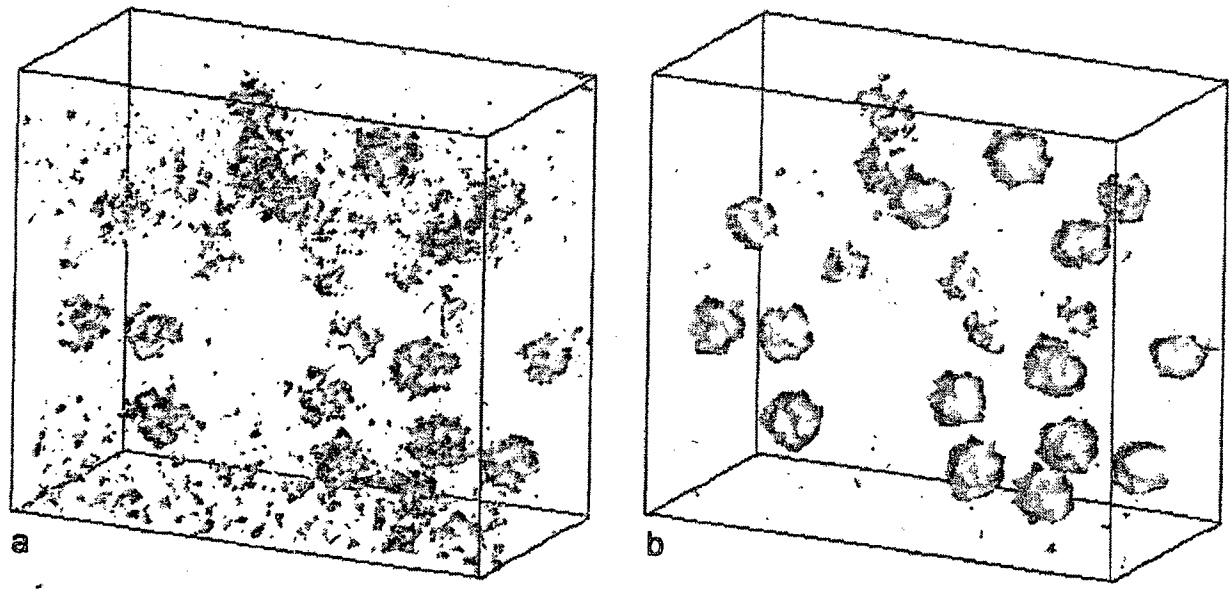

Fig. 12. Isosurface rendering of a 220 × 190 × 35 pixel subvolume. (a) In the uncompounded reference volume and in (b) the volume compounded from five look directions. Note the much more complete display of the surfaces of the 3-mm spheres in (b), as well as the strongly reduced clutter compared to (a).

yielding a first set of registered scans $S2_{fa}$ to $S5_{fa}$. Then, seven control points were added in and around the suspicious mass: one in the center, and one each about 6 mm from the center in the $\pm$ x, y, and z directions. The registration process was repeated using thin-plate spline (TPS) warping with all 11 control points in an additional third stage, yielding a second set of registered scans $S2_{tps}$ to $S5_{tps}$.

Both sets of registered image volumes were compounded. F13 Figure 13 shows examples of uncompounded image frames in the reference (a, d) scan 12 and 9 mm inferior to the mass and the corresponding frames following TPS-warped registration and compounding from (b, e) three and (c, f) five views.

The average registration error was assessed in both sets using manual definition of common landmarks. One B-scan frame each of S1, $S(n)_{fa}$, and $S(n)_{tps}$ were displayed simultaneously. For each $n = 2 \ldots 5$, the operator defined triplets of landmarks by browsing through the frames of each volume separately and placing markers in structurally defined positions visible in all three images. The z-coordinate (frame position) of a marker was determined first by finding the frame (or fraction of frame) in $S(n)_{fa}$ and $S(n)_{tps}$ that best matched a given frame (or fraction thereof) in S1. The x and y coordinates were then determined within these frames, based on landmarks such as intersections of tissue planes, small, point-like reflectors, or centroids of clearly visible structures.

For each $S(n)_{fa}$ and $S(n)_{tps}$, $n = 2 \ldots 5$, 134–156 common landmarks were defined, yielding a total of 566 landmark triplets. Average misregistrations for the full affine and the warping registration were defined as the mean distance between points defined in S1 and $S(n)_{fa}$ or $S(n)_{tps}$, respectively. Table 3 summarizes the resulting T3 registration error estimates. On average, the additional TPS warping reduced the registration error in the entire scans by about 10%. Statistical significance of the difference between the two estimates was calculated using two-sided, paired t-tests on individual volume pairs and on all scans combined. In the combined result, and in the registrations of scan 5 with 1, the error estimate in the TPS-warped registration was found to be significantly smaller than in the affine registration at the $\alpha = 0.05$ significance level. In the remaining tests, the percentile of the t-distribution ranged from 0.859 to 0.972.

A spherical region-of-interest (ROI_0) with radius 6 mm was defined (Fig. 14), centered in the lesion, and F14 thus including the seven warping control points. For each registered scan, an error estimate was calculated based on landmarks in this ROI only, and the results were compared for TPS-warped and full affine registrations. The TPS-warped registrations were significantly more accurate (at $\alpha = 0.05$) for each individual scan, reducing the registration error by 32.9% on average (range 18.5% to 62.3%) compared to the full affine registration.

Concentric, larger ROIs with radii extending 2–10 mm beyond ROI_0 were then defined in the same location, and the analysis was repeated for each ROI. Analyzing each scan individually, the registration error in TPS-warped registrations was significantly smaller (at $\alpha =$

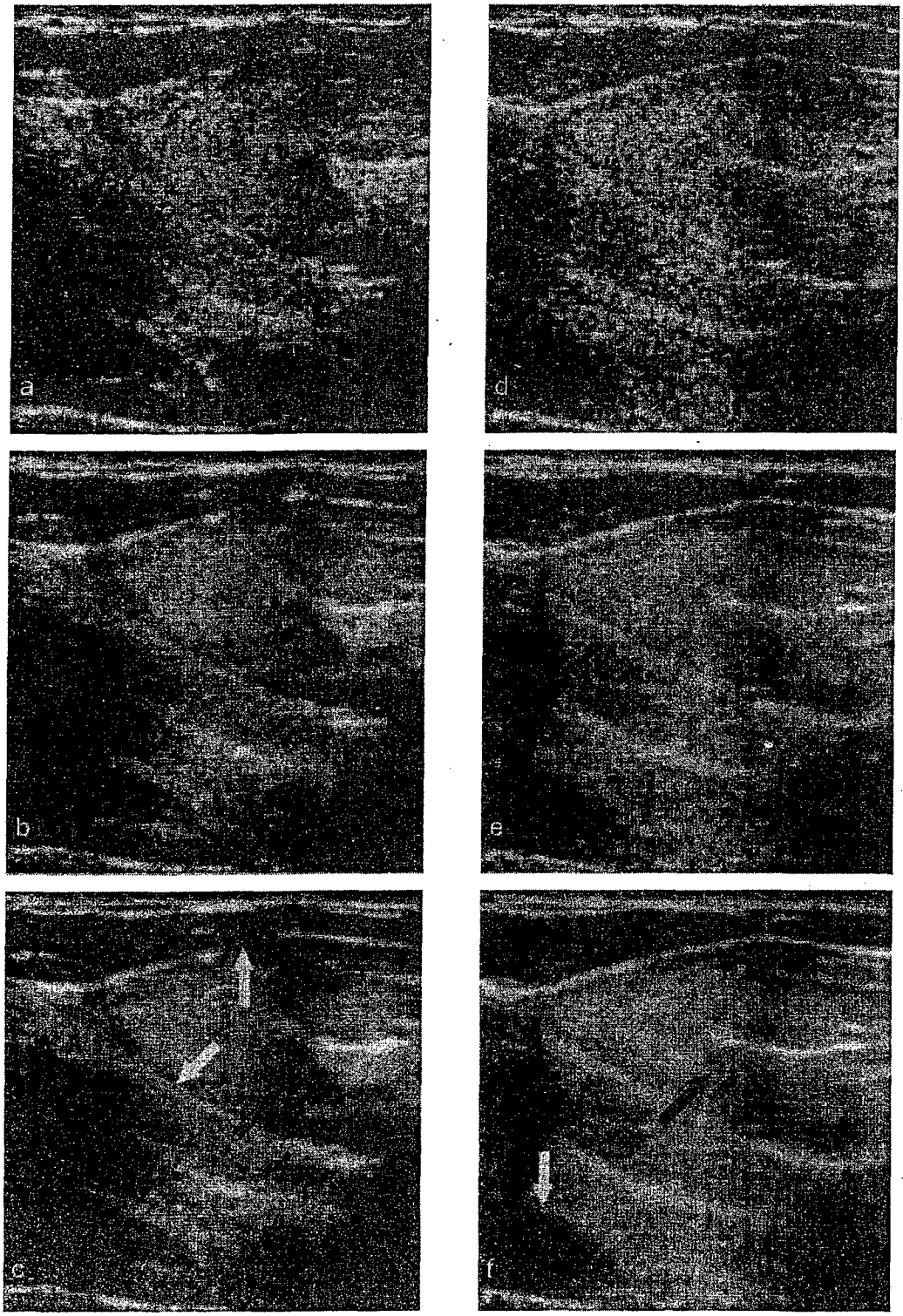

Fig. 13. The two columns of images display two different image frames from the volume scans obtained in a 56-year-old female's breast *in vivo*. From top to bottom, the images are (a, d) uncompounded, (b, e) compounded from three, and (c, f) from five look directions. Image sets registered with TPS warping were averaged to create the compounded views. The black arrows denote one of several slightly hypoechoic, apparently lobulated inhomogeneities which appear above the noise in the compounded views, but not in any of the constituent single views. (c) Note also the improved delineation of connective tissues (white arrows) and of (f) (white arrow) the dark muscle or rib in the lower left of as well as the tissue striations extending to the right of it.

Table 3. Registration errors obtained in four *in vivo* scans following different registrations with reference scan 1. One registration employed global full affine transformations, the other thin-plate spline (TPS) warping. $\bar{d}$ and d_{max} are the average and maximum distance, respectively, between 134 to 156 pairs of landmarks manually defined in each pair of scans (1 and n, n = 2. . .5). $\Delta\bar{d}$ is the standard error of $\bar{d}$

Registration type		Full affine			TPS-warped		
Scan No.	Tile angle	$\bar{d}$ (mm)	$\Delta\bar{d}$ (mm)	d_{max} (mm)	$\bar{d}$ (mm)	$\Delta\bar{d}$ (mm)	d_{max} (mm)
2	6.4°	0.79	0.039	1.95	0.73	0.041	2.54
3	12.8°	0.72	0.053	2.68	0.67	0.046	2.72
4	−5.1°	0.62	0.073	4.92	0.59	0.070	4.80
5	−10.2°	0.58	0.029	2.23	0.48	0.027	2.39
Combined		0.68	0.025	4.92	0.61	0.024	4.80

0.05) than in the full affine registration for ROIs of up to 10 mm radius. For all scans combined, the TPS-warped registration was significantly more accurate for all ROIs tested. The relative difference between the two types of registrations (i.e., the relative improvement achieved by TPS warping) decreased with increasing radius of the ROI. Figure 15a and b show the error estimates and the relative improvement from full affine to TPS-warped registration, respectively, vs. radius of the ROI, for all scans combined.

F15

DISCUSSION

In this study, techniques for creating and evaluating 3D compound images were developed. The feasibility of 3D spatial compounding using automatic, nonrigid registration was demonstrated. In the first experiment, the range of usable differential tilt angles was established. The speckle pattern was found to decorrelate rapidly for small tilt angles ($\alpha \leq 5°$). For larger angles ($5° \leq \alpha \leq 12°$), the correlation decreased significantly more slowly, and remained above the correlation predicted by theory. This effect suggests that the image volume obtained is not "pure" speckle at the high acoustic frequency range employed here. For small tilt angles, the global correlation coefficient is dominated by speckle and thus decreases rapidly. Once the speckle is decorrelated, remaining structure will dominate the correlation coefficient, which then decreases more slowly or remains constant. These results and theory suggest that the ideal differential tilt angle for acquisition of a large number of sufficiently decorrelated views within a given interval of usable tilt angles is about $\Delta\alpha$ = 5° to 6°. Differential angles close to this range were used in subsequent phantom and *in vivo* scans.

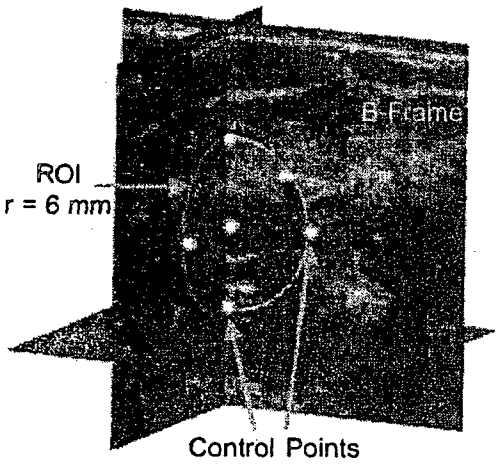

Fig. 14. Three-dimensional display of the *in vivo* image volume showing one of the original B-frames and two orthogonal planes. Five of the control points in the ROI are visible.

In the focal lesion phantom, very accurate registrations with an average registration error of 0.31 mm were obtained. This error includes the finite accuracy of ALS in defining the center of the spheres, and thus constitutes an upper bound for the registration error. The misregistration did not lead to a significant increase of the 3D border width of the spheres segmented in the phantom volumes. However, an earlier analysis based on the 2D border width of cross-sections of the spheres obtained in the axial-lateral image planes had shown a 17% increase of the width in the volume compounded from five views compared to the uncompounded volume. This may be due to the fact that the misregistration is small compared to the elevational resolution of the system, but not compared to the axial and lateral resolution.

The increase in SNR and CNR closely followed the theoretical values for averaged partially correlated images. Using different subsets, but identical numbers, of volumes for compounding only led to a moderate change in CNR, indicating that the image quality does not strongly depend on the differential tilt angle (within a reasonable range). The mean contrast $\langle I_{object}\rangle - \langle I_{background}\rangle$ was not changed significantly between uncompounded and compounded images, resulting in an almost identical increase of CNR and SNR.

The isosurface renderings displayed in Fig. 12 dem-

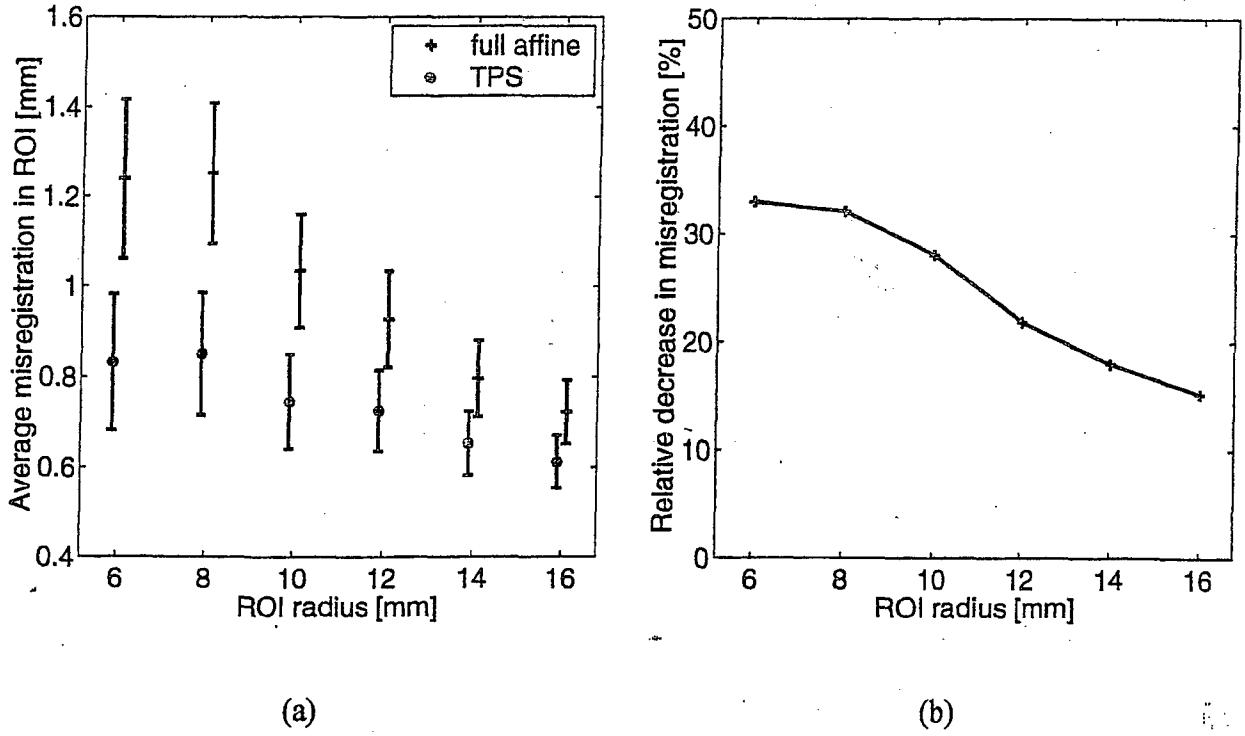

Fig. 15. (a) Registration errors in spherical ROIs centered in a cluster of seven warping control points, for registrations obtained using full affine transformations and TPS warping. The error bars indicate ± 2 standard errors of the mean. (b) The relative improvement from full affine to TPS warped registrations changed monotonically from 33% to 15% for 6 to 16 mm ROI radii.

onstrate the potential value of compounding when using other (nonstandard) display techniques. Clearly, the rendering of the uncompounded volume is unsatisfactory. Most of the spheres have incomplete surfaces, and already clutter is obscuring much of the image. Reducing the clutter by lowering the isosurface level resulted in even sparser display of the spheres' surfaces. A more sophisticated algorithm or manual cropping of clutter would be required to clear up the image. On the other hand, isosurface rendering of the compounded volume gives a reasonable, although not complete, representation of the spheres. Again, additional processing is required to display the complete surfaces of the spheres without clutter, but the images suggest that this can be achieved much easier in compounded than in uncompounded volumes.

A 120% increase in SNR was found in the compounded *in vivo* scans, close to the ideal ~~insert equation from msp 22~~ (corresponding to 124%) for uncorrelated views and larger than the 94% increase in the phantom scans. The larger differential tilt angle ($\Delta\alpha \approx 6°$) is unlikely to account for this result alone. Additional decorrelation between registered views is introduced by increased misregistration, which leads to stronger reduction of speckle in the compound volume.

The examples in Fig. 13 display improvements in several aspects of (c, f) the fully compounded images compared to (a, d) the uncompounded ones. The increase in SNR is evident as a noticeable reduction of speckle, which gives the images (c) and (f) a "smoother" appearance. Note the better delineation of connective tissues (white arrows in (c)) and of the dark muscle or rib (white arrow in (f)) in the compounded images. Most important, note the slightly hypoechoic, lobulated inhomogeneities surrounding the left end of the horizontal hyperechoic structure on the central right (black arrows). Many of these very low contrast structures cannot be seen in the corresponding uncompounded frames. Similar improvements, but less pronounced, are visible in the images compounded from only three look directions (b, e). To some observers, the loss of high-contrast speckle may appear as overall image blur. The sharp delineation of connective tissues in the compounded images, however, shows that this is not the case, and that blurring due to misregistration is small.

Increased misregistration *in vivo* compared to the phantom scans was expected since tissue deformation, specular reflectors, shadows and refraction-causing tissue inhomogeneities make compounding *in vivo* a much more challenging task. The mean error throughout the volume of 0.68 mm (full affine) and 0.61 mm (TPS-

warped) still compares well to the resolution cell size of the transducer (about $0.4 \times 0.8 \times 1.2$ mm^3).[1]

The analysis within the ROI is even more important. Affine registration displayed a significantly larger registration error in the ROI (1.24 mm) than in the remainder of the volume (0.64 mm). Apparently, the lesion and its surrounding tissues are particularly rigid and seem to shift strongly in the softer background tissues that are deformed during the scans. The global full affine registration cannot compensate for these local shifts. By placing additional control points in the ROI and allowing warping transformations, the tissue deformation could be partly corrected, thus decreasing the registration error in the ROI to 0.83 mm.

FUTURE WORK

The registration may be improved by adding more control points in the ROI, or by modifying the initial positions of the control points. Each control point added introduces three additional degrees of freedom and increases the complexity of the registration transformation. More research is needed on how many control points can be supported by a given image set, and how the initial control points can be placed in an optimal way.

To fully exploit the diagnostic value of 3D compounding, compound images may be displayed in parallel with single view images. This would allow simultaneous appreciation of the specific strengths of the two modes (e.g., high CNR in compound images and high spatial resolution in single view images).

So far, compounding using nonrigid image registration has only been applied to breast scans. Compounding other organs that are accessible through a sufficiently large scanning window (e.g., liver, kidneys) should be tested in the future.

Preprocessing of the data sets for improved registration speed, robustness and accuracy, as well as new display techniques, should be explored. Strong shadows in the ultrasound images may set off the registration procedure and should therefore be corrected or excluded from the registration. Low-pass filtering of the speckle noise may accelerate convergence of the optimization algorithm. Registration time is also expected to drop significantly with optimized software, faster computers or dedicated hardware. A ten-fold increase in processor speed can be expected in 5 years at the current rate of change. Upgrades into modest parallel computing, an approach taken by GE Corporate R&D for real-time phase aberration corrections (Rigby et al. 1998), may already bring registration times down to less than 1 min, and thus allow nonrigid registration of one 3D scan while the next one is being acquired. The fundamental limit in compound scan acquisition is the ultrasonic data rate, which in turn determines the frame rate (for conventional 2D acquisition systems) or volume rate (for 3D acquisition systems). Assuming a frame rate of 5–20 Hz for typical high-resolution, multifocal gray scale images, and 100–200 frames per volume, a typical volume can be obtained in 5–40 s. This is on the order of, or below, the estimated processing times above, making the registration procedure the limiting factor in the short- to medium-term future.

The registration procedure may also be applied to improve spatial resolution in 2D compounding. Compared with 3D registration, alignment of 2D images will run at least 50 to 100 times faster due to the reduced amount of data. Two-dimensional registration, however, cannot correct for refraction out of the image plane.

Acknowledgements—This work was supported by U.S. Army contract No. DAMD17-96-C-6061 and, to a lesser extent, USPHS grant 5RO1CA55076. DAMD 17-96-C-6061

REFERENCES

Barry CD, Allott CP, John NW, et al. Three-dimensional freehand ultrasound: Image reconstruction and volume analysis. Ultrasound Med Biol 1997;23:1209–1224.

Berson M, Roncin A, Pourcelot L. Compound scanning with an electrically steered beam. Ultrason Imaging 1981;3:303–308.

Burckhardt CB. Speckle in ultrasound B-mode scans. IEEE Trans Son Ultrason 1978;25:1–6.

Buttery B, Davison G. The ghost artifact. J Ultrasound Med 1984;3: 49–52.

Fenn RC, Fowlkes JB, Moskalik AP, et al. A hand-controlled, 3-D ultrasound guide and measurement system. In: Lees S, ed. Acoustical imaging. New York: Plenum Press, 1997:237–242.

Holmes JH, Howry DH, Posakony GJ, Cushman CR. The ultrasonic visualization of soft tissue structures in the human body. Trans Am Clin Climat Assoc 1954;66:208–225.

Jespersen SK, Wilhjelm JE, Sillesen H. Multi-angle compound imaging. Ultrason Imaging 1998;20:81–102.

Kass M, Witkin A, Terzopoulos D. Snakes: Active contour models. Int J Comp Vis 1987;1:321–331. AQ: 1

Kim B, Boes JL, Frey KA, Meyer CR. Mutual information for automated unwarping of rat brain autoradiographs. NeuroImage 1997; 5:31–40.

Kossoff G, Garrett WJ, Carpenter DA, Jellins J, Dadd MJ. Principles and classification of soft tissues by grey scale echography. Ultrasound Med Biol 1976;2:89–105.

Krücker JF, LeCarpentier GL, Meyer CR, et al. 3D image registration for multimode, extended field of view, and sequential ultrasound imaging. RSNA EJ 1999;3:0098–99. http://ej.rsna.org/ej3/0098–99.fin/titlepage.html.

LeCarpentier GL, Bhatti PT, Fowlkes JB, et al. Utility of three-dimensional US in the discrimination and detection of breast cancer, RSNA EJ 1999;3:0103–99. http://ej.rsna.org/ej3/0103–99.fin/titlepage.html.

Leotta DF. Three-Dimensional Spatial Compounding of Ultrasound Images Acquired by Freehand Scanning. Volume Reconstruction of the Rotator Cuff. Ph.D. thesis, University of Washington, Seattle, 1998.

Maes F, Collingnon A, Vandermeulen D, Marchal G, Suetens P. Multimodal image registration by maximization of mutual information. IEEE Trans Med Imaging 1997;16:187–198.

[1]Axial × lateral × elevational resolution, measured as the full width at half-maximum of the decorrelation curve.

Maintz JBA, Viergever MA. A survey of medical image registration. Med Image Anal 1998;2:1–36.

Meyer CR, Boes JL, Kim B, et al. Demonstration of accuracy and clinical versatility of mutual information for automatic multimodality image fusion using affine and thin-plate spline warped geometric deformations. Med Image Anal 1996/7;1:195–206.

Meyer CR, Boes JL, Kim B, et al. Semiautomatic registration of volumetric ultrasound scans. Ultrasound Med Biol 1999a;25:339–347.

Meyer CR, Boes JL, Kim B, Bland PH. Probabilistic Brain Atlas Construction: Thin-Plate Spline Warping via Maximization of Mutual Information. Proceedings of the Second International Conference on Medical Image Computing and Computer-Assisted Intervention (MICCAI) 1999b:631–637.

Moskalik A, Carson PL, Meyer CR, et al. Registration of three-dimensional compound ultrasound scans of the breast for refraction and motion correction. Ultrasound Med Biol 1995;21:769–778.

O'Donnell M, Silverstein SD. Optimum displacement for compound image generation in medical ultrasound. IEEE Trans Ultrasonics Ferroelec Freq Contr 1988;35:470–476.

Poon CS, Braun M. Image segmentation by a deformable contour model incorporating region analysis. Phys Med Biol 1997;42: 1833–1841.

AQ: 1

Rigby KW, Andarawis EA, Chalek CL, et al. Realtime adaptive imaging. In: Levy M, McAvoy BR, eds. 1998 IEEE ultrason symp procs. Piscataway, NJ: Institute for Electrical and Electronics Engineers, 1998.

Robinson DE, Knight PC. Computer reconstruction techniques in compound scan pulse-echo imaging. Ultrason Imaging 1981;3:217–234.

Robinson DE, Wilson LS, Kossoff G. Shadowing, and enhancement in ultrasonic echograms by reflection, and refraction. J Clin Ultrasound 1981;9:181–188.

Robinson DE, Chen F, Wilson LS. Measurement of velocity of propagation from ultrasonic pulse-echo data. Ultrasound Med Biol 1982;8:413–420.

Rohling R, Gee, A., Berman, L. 3-D spatial compounding of ultrasound images. Inform Proc in Med Imaging 1997;1230:519–524.

Rohling R, Gee, A., Berman, L. Automatic registration of 3-D ultrasound images. Ultrasound Med Biol 1998;24:841–854.

Shankar PM, Newhouse VL. Speckle reduction with improved resolution in ultrasound images. Trans Son Ultrason 1985;32:537–543.

AQ: 1

Shattuck DP, von Ramm OT. Compound scanning with a phased array. Ultrason Imaging 1982;4:93–107.

Trahey GE, Smith SW, von Ramm OT. Speckle pattern correlation with lateral aperture translation: Experimental results and implications for spatial compounding. IEEE Trans Ultrasonics Ferroelec Freq Contr 1986;33:257–264.

van den Elsen PA, Pol E-JD, Viergever MA. Medical image matching—A review with classification. IEEE Eng Med Biol 1993;12: 26–39.

Viola P, Wells III WM. Alignment by maximization of mutual information. Int J Comp Vis 1997;24:137–154.

Wagner RF, Insana MF, Smith SW. Fundamental correlation lengths of coherent speckle in medical ultrasonic images. IEEE Trans Ultrasonics Ferroelec Freq Contr 1988;35:34–44.

Vol. 6, 1–10, January 2000

Advances in Brief

Treatment of Metastatic Cancer with Tetrathiomolybdate, an Anticopper, Antiangiogenic Agent: Phase I Study[1]

George J. Brewer, Robert D. Dick, Damanjit K. Grover, Virginia LeClaire, Michael Tseng, Max Wicha, Kenneth Pienta, Bruce G. Redman, Thierry Jahan, Vernon K. Sondak, Myla Strawderman, Gerald LeCarpentier, and Sofia D. Merajver[2]

Departments of Human Genetics [G. J. B., R. D. D.], Internal Medicine [G. J. B., V. L., M. T., M. W., K. P., B. G. R., S. D. M.], Surgery [K. P., V. K. S.], and Radiology [G. L.], Clinical Research Center [D. K. G.], and Comprehensive Cancer Center [V. L., M. T., M. W., K. P., B. G. R., V. K. S., M. S., S. D. M.], University of Michigan Health System, Ann Arbor, Michigan 48109, and Department of Internal Medicine, University of California at San Francisco, San Francisco, California 94115 [T. J.]

Abstract

Preclinical and *in vitro* studies have determined that copper is an important cofactor for angiogenesis. Tetrathiomolybdate (TM) was developed as an effective anticopper therapy for the initial treatment of Wilson's disease, an autosomal recessive disorder that leads to abnormal copper accumulation. Given the potency and uniqueness of the anticopper action of TM and its lack of toxicity, we hypothesized that TM would be a suitable agent to achieve and maintain mild copper deficiency to impair neovascularization in metastatic solid tumors. Following preclinical work that showed efficacy for this anticopper approach in mouse tumor models, we carried out a Phase I clinical trial in 18 patients with metastatic cancer who were enrolled at three dose levels of oral TM (90, 105, and 120 mg/day) administered in six divided doses with and in-between meals. Serum ceruloplasmin (Cp) was used as a surrogate marker for total body copper. Because anemia is the first clinical sign of copper deficiency, the goal of the study was to reduce Cp to 20% of baseline value without reducing hematocrit below 80% of baseline. Cp is a reliable and sensitive measure of copper status, and TM was nontoxic when Cp was reduced to 15–20% of baseline. The level III dose of TM (120 mg/day) was effective in reaching the target Cp without added toxicity. TM-induced mild copper deficiency achieved stable disease in five of six patients who were copper deficient at the target range for at least 90 days.

Introduction

The concept of antiangiogenic treatment for solid tumors, which was pioneered by Folkman (1–3), has a firm rationale and shows efficacy in animal tumor models (4–12). Compounds that interfere with critical steps in the angiogenesis cascade are reaching the clinic (13). The steps required for successful tumor angiogenesis at the primary and metastatic sites are diverse, and they depend on an imbalance between angiogenesis activators (14–15) such as vascular endothelial growth factor and basic fibroblast growth factor and inhibitors such as thrombospondin 1 (16–20), angiostatin (21–23), and endostatin (10). The relative importance of the different angiogenesis-modulating molecules in different tissues may determine the relative potency of antiangiogenic compounds to elicit a response at both the primary and metastatic sites. Therefore, it would be very desirable to develop an antiangiogenic strategy that would affect multiple activators of angiogenesis in order for it to be generally applicable to human tumors. Because copper is a required cofactor for the function of many key mediators of angiogenesis, such as basic fibroblast growth factor (24–27), vascular endothelial growth factor, and angiogenin (28), we have developed an antiangiogenic strategy for the treatment of cancer based on the modulation of total body copper status. The underlying hypothesis of this work is that a window of copper deficiency exists in which angiogenesis is impaired, but other copper-dependent cellular processes are not affected enough to cause clinical toxicity.

It has been amply demonstrated that copper is required for angiogenesis (29–31), and several years ago, some promising animal tumor model studies were carried out using an anticopper approach (32–33). The chelator penicillamine and a low-copper diet were used to lower copper levels in rats and rabbits with implanted intracerebral tumors. However, although they showed reduced tumor size, the animals treated with the low-copper regimen did not show improved survival over untreated controls.

For the past 20 years, we have developed new anticopper therapies for Wilson's disease, an autosomal recessive disease of copper transport that results in abnormal copper accumulation and toxicity. One of the drugs currently being used, TM,[3] shows unique and desirable properties of fast action, copper specificity, and low toxicity (34–36), as well as a unique mechanism of

Received 7/19/99; revised 11/1/99; accepted 11/9/99.
The costs of publication of this article were defrayed in part by the payment of page charges. This article must therefore be hereby marked *advertisement* in accordance with 18 U.S.C. Section 1734 solely to indicate this fact.
[1] Supported by NIH Grants RO3-CA-77122 (to S. D. M.), P30-CA46592 (to M. W.), and MO1-RR00042 (to the General Clinical Research Center); the Tracy Starr Award from the Cleveland Foundation (to S. D. M.); a grant from the Tempting Tables Organization (to S. D. M.); and donors to the University of Michigan Comprehensive Cancer Center.
[2] To whom requests for reprints should be addressed, at University of Michigan Comprehensive Cancer Center, 7217 CCGC, 1500 East Medical Center Drive, Ann Arbor, MI 48109-0948.

[3] The abbreviations used are: TM, tetrathiomolybdate; Cp, ceruloplasmin; Hct, hematocrit; GI, gastrointestinal; CAT, computer-assisted tomography.

action. TM forms a stable tripartite complex with copper and protein. If given with food, it complexes food copper with food protein and prevents absorption of copper from the GI tract. There is endogenous secretion of copper in saliva and gastric secretions associated with food intake, and this copper is also complexed by TM when it is taken with meals, thereby preventing copper reabsorption. Thus, patients are placed in a negative copper balance immediately when TM is given with food. If TM is given between meals, it is absorbed into the blood stream, where it complexes either free or loosely bound copper with serum albumin. This TM-bound copper fraction is no longer available for cellular uptake, has no known biological activity, and is slowly cleared in bile and urine.

The underlying hypothesis of an anticopper, antiangiogenic approach to cancer therapy is that the level of copper required for angiogenesis is higher than that required for essential copper-dependent cellular functions, such as heme synthesis, cytochrome function, and incorporation of copper into enzymes and other proteins. Because of the unique and favorable characteristics of TM as an anticopper agent compared with other anticopper drugs, we evaluated it in animal tumor models for toxicity and efficacy as an anticopper, antiangiogenic therapy. These studies showed efficacy in impairing the development of *de novo* mammary tumors in Her2-neu transgenic mice (12), and TM showed no clinically overt toxicity as copper levels were decreased to 10% of baseline. Here we report the first human trial of an anticopper approach to antiangiogenesis therapy based on the use of TM in patients with metastatic cancer. This Phase I trial of TM yielded information on dose, dose response, evaluation of copper status in patients, and toxicity (37). Although the study was not designed to definitively answer efficacy questions, we report preliminary observations on efficacy and novel approaches to following disease status in trials of antiangiogenic compounds.

Patients and Methods

Patients. Eighteen adults with metastatic solid tumors exhibiting measurable disease, life expectancy of 3 or more months, and at least 60% Karnofsky performance status were enrolled. We excluded patients with effusions or bone marrow involvement as the only manifestations of disease and those who had severe intercurrent illness requiring intensive management or were transfusion dependent. Patients had to have recovered from previous toxicities and had to meet the following requirements for laboratory parameters: (*a*) WBC $\geq$ 3,000/mm^3; (*b*) absolute neutrophil count $\geq$ 1,200/mm^3; (*c*) Hct $\geq$ 27%; (*d*) hemoglobin $\geq$ 8.0 g/dl; (*e*) platelet count $\geq$ 80,000/mm^3; (*f*) bilirubin $\leq$ 2.0 mg/dl; (*g*) aspartate aminotransferase and alanine aminotransferase $\leq$ 4 times the upper limit of institutional norm; (*h*) serum creatinine $<$ 1.8 mg/dl or calculated creatinine clearance $\geq$ 55 ml/min; (*i*) calcium $<$ 11.0; (*j*) albumin $\geq$ 2.5 g/dl; (*k*) prothrombin time $\leq$ 13 s; and (*l*) partial thromboplastin time $\leq$ 35 s. Other requirements were demonstrable progression of disease in the previous 3 months after standard treatments such as surgery, chemotherapy, radiotherapy, and/or immunotherapy or progressive disease after declining conventional treatment modalities.

Treatment Schema: Doses and Escalation. Three dose regimens were evaluated. All dose levels consisted of 20 mg of TM given three times daily with meals plus an escalating (levels I, II, and III) in-between meals dose given three times daily for a total of six doses/day. Loading dose levels I, II, and III provided TM at 10, 15, and 20 mg, three times daily between meals, respectively, in addition to the three doses of 20 mg each given with meals at all dose levels.

Baseline Cp was taken as the nearest Cp measurement to day 1 of treatment (including day 1) because blood was drawn before TM treatment from all patients. The target Cp reduction was defined as 20% of baseline Cp. Due to Cp assay variability of approximately 2% at this institution, a change of Cp to 22% of baseline was considered as achieving the desired reduction of copper. In addition, if the absolute Cp was less than 5 mg/dl, then the patient was considered as having reached the target Cp. No patient reached the 5 mg/dl target without also being at least 78% reduced from baseline. After reaching the target copper-deficient state, TM doses were individually tailored to maintain Cp within a target window of 70–90% reduction from baseline.

Six patients were to be enrolled at each dose level. After four patients were enrolled at level I, if one patient experienced dose-limiting toxicity (defined as Hct $<$ 80% of baseline), two more patients were enrolled at level I. If no dose-limiting toxicity was observed, patients were enrolled at the next dose level. Treatment was allowed to continue beyond induction of target copper deficiency if the patients experienced a partial or complete clinical response or achieved clinical stable disease by the following definitions. Complete response is the disappearance of all clinical and laboratory signs and symptoms of active disease; partial response is a 50% or greater reduction in the size of measurable lesions defined by the sum of the products of the longest perpendicular diameters of the lesions, with no new lesions or lesions increasing in size. Minor response is a 25–49% reduction in the sum of the products of the longest perpendicular diameters of one or more measurable lesions, no increase in size of any lesions, and no new lesions; stable disease is any change in tumor measurements not represented by the criteria for response or progressive disease; progressive disease is an increase of 25% or more in the sum of the products of the longest perpendicular diameters of any measurable indicator lesions compared with the smallest previous measurement or appearance of a new lesion. Because copper deficiency is not a cytotoxic treatment modality, the patients who provide information about the efficacy of TM for long-term therapy in this population of patients with advanced cancer are primarily those who remained within the target Cp window of 20 $\pm$ 10% of baseline for over 90 days without disease progression.

Monitoring of Copper Status. A method was required to monitor copper status easily and reliably, so that the TM dose could be adjusted appropriately during this trial. With TM administration, serum copper is not a useful measure of total body copper because the TM-copper-albumin complex is not rapidly cleared, and the total serum copper (including the fraction bound to the TM-protein complex) actually increases during TM therapy (34–36). The serum Cp level obtained weekly was used as a surrogate measure of total body copper status. Cp was measured by the oxidase method; the Cp measurements were made by nethelometry (differential light scattering from a

colored or turbid case solution with respect to a control solution) using an automated system and reagents available commercially (Beckman Instruments, Inc., Fullerton, CA). The serum Cp level is controlled by Cp synthesis by the liver, which, in turn, is determined by copper availability to the liver (38). Thus, as total body copper is reduced, the serum Cp level is proportionately reduced. The serum Cp level is in the range of 20–35 and 30–65 mg/dl for normal controls and cancer patients, respectively. Our objective was to reduce Cp to ≤ 20% of baseline and to maintain this level, within a window spanned by 20 ± 10% of baseline Cp, with typical Cp values in the range of 7–12 mg/dl. Because there appears to be no untoward clinical effects from this degree of copper reduction, we have termed this level of copper deficiency "chemical copper deficiency." The first indication of true clinical copper deficiency is a reduction in blood cell counts, primarily anemia, because copper is required for heme synthesis as well as cellular proliferation (36). Thus, the copper deficiency objective of this trial was to reduce the Cp to ≤ 20% of baseline without decreasing the patient's Hct or WBC to below 80% of baseline value at entry.

Toxicity, Follow-Up, and Disease Evaluation. Complete blood counts, liver and renal function tests, urinalyses, and Cp level were performed weekly for 16 weeks and then performed biweekly at the clinical laboratories of the University of Michigan Health System or at other affiliated certified laboratories. Physical examinations and evaluations of toxicity were carried out every 2 weeks for 8 weeks and then performed every 4 weeks for the duration of therapy. Toxicity was evaluated using the National Cancer Institute Common Toxicity Criteria. Extent of disease was evaluated at entry, at the point of achievement of copper deficiency (defined as Cp ≤ 20% of baseline), and every 10–12 weeks thereafter. CAT or magnetic resonance imaging was used as appropriate for conventional measurement of disease at all known sites and for evaluation of any potential new sites of disease. Angiogenesis-sensitive ultrasound with three-dimensional Doppler analyses was used in select cases as an adjunct to conventional imaging to evaluate blood flow to the tumors at different time points.

TM Preparation and Storage. TM was purchased in bulk lots suitable for human administration (Aldrich Chemical Company, Milwaukee, WI). Because TM is slowly degraded when exposed to air (oxygen replaces the sulfur in the molecule, rendering it inactive; Refs. 34–36), it was stored in 100-g lots under argon. At the time a prescription was written, the appropriate dose of TM was placed in gelatin capsules by research pharmacists at the University of Michigan Health System. Previously, we had shown that TM dispensed in such capsules retained at least 90% of its potency for 8 weeks (34). Thus, TM was dispensed to each patient in 8-week installments throughout the trial.

Measurement of Blood Flow. Blood flow was measured by ultrasound in select patients with accessible lesions at the time they became copper deficient and at variable intervals of 8–16 weeks thereafter. Three-dimensional scanning was performed on a GE Logiq 700 ultrasound system, with the 739 L, 7.5 MHz linear array scanhead. The scanning and vascularity quantification techniques were as described previously by the authors (39, 40).

Results

Patient Characteristics

Eighteen eligible patients (10 males and 8 females) with 11 different types of metastatic cancer who had progressed through or (in one case) declined other treatment options were enrolled in the trial in the order in which they were referred. Six, five, and seven patients were enrolled at the 90, 105, and 120 mg/day drug levels, respectively, following the protocol dose escalation schema. One patient originally assigned to the 105 mg/day level was removed early to pursue cytotoxic chemotherapy, due to rapid progression of disease. This same patient was later retreated at the 120 mg/day level for a longer duration; thus, he is counted only at the 120 mg/day level for the analyses. The average age was 59 years; the average baseline Cp was 47.8 mg/dl, which is elevated with respect to the normal level, reflecting the patients' disease status. Table 1 summarizes the patient characteristics for each dose level.

Toxicity

There were no cardiac, pulmonary, GI, renal, hepatic, hematological, infectious, skin, mucosal, or neurological toxicities observed for Cp levels at or above 20% of baseline. Mild (>80% of baseline Hct) reversible anemia was observed in four patients with Cp levels between 10–20% of baseline. Two of these patients had been treated with cytotoxic chemotherapy, and two patients had evidence of extensive bone marrow involvement with their disease at the time of entry into the trial. Although in the latter two cases, the anemia was most likely due to causes other than treatment, TM was temporarily discontinued until Hct was restored to acceptable levels with a transfusion of 2 units of packed RBCs. In one patient, it is very likely that the copper deficiency caused by TM produced the anemia. Stopping administration of the drug allowed the Hct to recover within 5–7 days without the need for transfusion; at the patient's request, TM was restarted at a lower dose, without further complications of anemia. Several patients experienced transient, occasional sulfur-smelling burping, within 30 min of TM ingestion. No additional toxicities of any type were observed with long-term maintenance of mild clinical copper deficiency over 8–15 months. Of note, no evidence of GI or other mucosal bleeding or impaired healing of minor trauma were observed with long-term therapy. One premenopausal patient with extensive metastatic renal cancer experienced normal menstrual periods during TM therapy, including 2.5 months of observation while she was copper deficient with Cp < 20% of baseline.

Cp as a Surrogate Measure of Copper Status

Fig. 1 shows the response of Cp as a function of time on TM therapy, expressed as the ratio of Cp at time t to baseline Cp level for each patient enrolled at the 90, 105, and 120 mg/day dose levels. Increasing the in-between meals dose from 10 mg three times daily to 15 or 20 mg three times daily had no significant effect on the rate of decrease of the Cp level, reaching a level of 50% baseline at a mean of 30 days (median = 28 days). The response of Cp to TM therapy as a function of time exhibited only minor fluctuations; when TM was discontinued, a rapid rise in Cp was observed within 48 h.

Four patients were removed from study due to progression

Table 1 Patient characteristics

	Assigned TM Dose (mg/day)			
	90	105	120	Total
No. of patients	6	5	7	18
Sex (M/F)	3/3	1/4	6/1	10/8
Mean age (SD) (yrs)	64 (12)	60 (12)	53 (17)	59 (14)
Primary Tumor				
Breast	2	2	0	4
Colon	0	1	0	1
Lung	1	0	0	1
Melanoma	0	0	1	1
Pancreas	0	1	0	1
Prostate	2	0	0	2
Angiosarcoma	0	0	2	2
Chondrosarcoma	0	1	0	1
Nasopharyngeal tumor	0	0	1	1
Hemangioendothelioma	0	0	1	1
Renal tumor	1	0	2	3
Baseline				
Baseline Cp mean	52.6	49.3	42.7	47.8
Baseline Cp range	36.6–74.1	38.1–65.0	31.9–52.7	31.9–74.1
Baseline Hct mean	31.9	37.2	41.9	37.3
Baseline Hct range	26.6–35.6	33.8–42.5	35.4–45.7	26.6–45.7

of disease before achieving the target Cp of 20% of baseline, whereas the remaining 14 patients achieved the target Cp level. Because all 14 patients who achieved the target Cp level wished to remain on study, they were allowed to do so, according to the protocol, as long as they did not exhibit disease progression or toxicity. The TM doses were adjusted in these patients to maintain the Cp level between 10–20% of baseline. These patients provide the preliminary evidence of the efficacy and long-term tolerance of this approach.

Dose Adjustments to Maintain Target Cp

TM doses were adjusted to maintain a Cp target level of 20% of baseline and to prevent absolute Cp values < 5 mg/dl. Due to the routine 7-day turn-around for the Cp test at our laboratory, these dose changes were made approximately 7–10 days after the blood for the Cp measurement was taken. After achieving the target Cp, the in-between meals dose was typically decreased by 20 mg. Further decreases of 15–30 mg were necessary during long-term therapy. A patient with metastatic chondrosarcoma secondary to radiation treatment for breast cancer on long-term therapy has stable disease after 12 months of copper deficiency, with stable quality of life. One biopsy-proven metastatic nodule on her third digit is easily measurable and has been stable. Other sites of suspected disease in the chest also remain stable. Interestingly, this patient has required only a minor adjustment to her TM dose from the initial loading dose level to maintain the target Cp throughout this relatively long period. Fig. 2, *A* and *B*, illustrates the Cp response to dose adjustments required for two more representative patients over approximately 100 days of therapy. Thus far, the patient in Fig. 2*A* has required only decreases in dose 60 days apart. Most patients have required both an increase and a decrease in dose during long-term therapy. For example, as shown in Fig. 2*B*, the TM dose was increased after day 100 to respond to an increase in Cp outside the target range. Overall, there was considerable individual variability in the dose adjustments required. In conclusion, the Cp response to TM therapy evaluated weekly is not brittle or subject to wide fluctuations.

Measurement of Response of Metastatic Cancer to TM

Clinical Evaluation. Although the patients received different initial loading doses of TM, the Cp maintenance window of 20 ± 10% of baseline was used in all groups, regardless of the loading dose. Patients who maintained this degree of copper deficiency through tailored adjustments of the TM dose for over 90 days are likely to reflect the antiangiogenic activity of TM against their tumors. The period of 90 days is selected for two main reasons. First, TM is not cytotoxic to either cancer or endothelial cells and mainly impairs endothelial cell function and proangiogenic factor production. This mechanism of action is expected to have a very slow effect on the size of tumor masses. Second, as tumors sequester copper, the microenvironment of the tumor is expected to take a longer time to be rendered copper deficient. Table 2 summarizes the clinical course of the 18 patients.

Fourteen patients achieved the target copper deficiency before disease progression or other disease complications. Of these, eight patients either progressed within 30 days of achieving copper deficiency or have had stable disease for <90 days; it is unlikely that most of these tumors experienced an antiangiogenic environment long enough to evaluate clinical response to this type of therapy. In all patients removed from the protocol due to disease progression or choice and in one patient removed from the protocol due to the need for abdominal surgery to relieve a small bowel obstruction, much more rapid rates of progression of disease were noted clinically after discontinuation of TM therapy.

The remaining six patients experienced stable disease (five of six patients) or progression of disease at one site, with stable disease elsewhere (one of six patients). Two patients who have

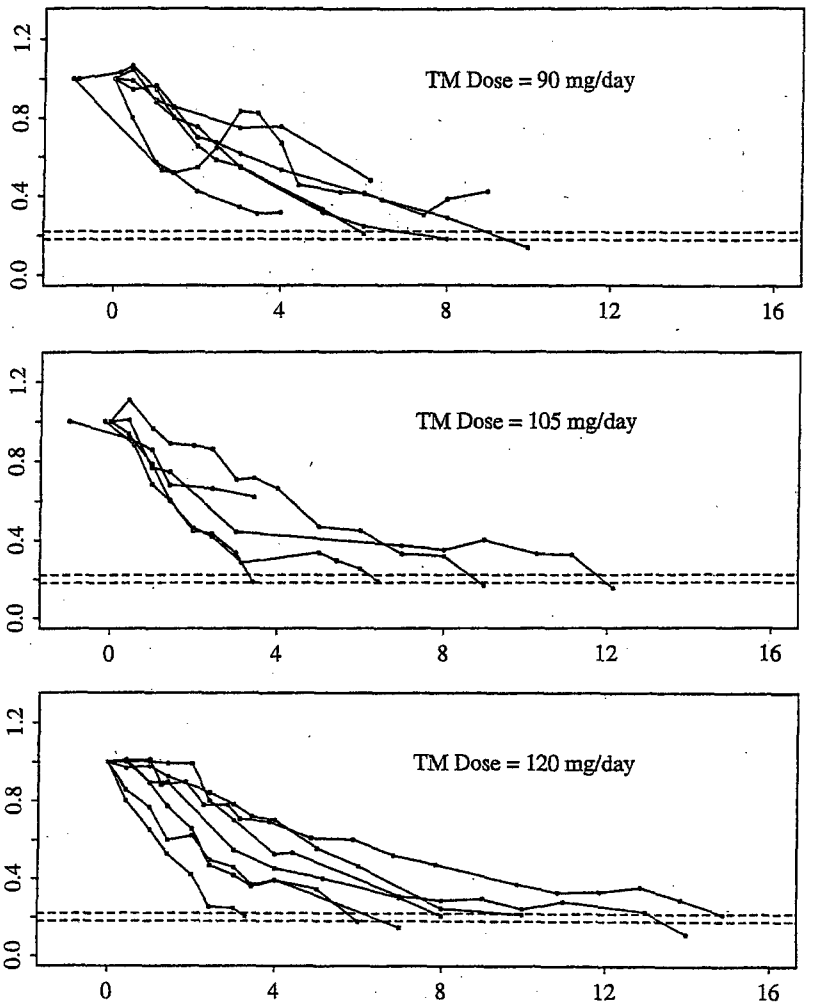

Fig. 1 Cp as a surrogate marker of total body copper status. Rates of decrease of the ratio of Cp at time t to baseline Cp as a function of days on TM therapy are depicted for dose levels I, II, and III. The average time to 50% reduction of Cp is 30 days.

stable disease by standard criteria also experienced complete disappearance of some lung lesions and a decrease in the size of other lung lesions during observation periods at target Cp of 120 and 49 days. The five patients on long-term (>90 days) maintenance therapy with stable disease have been copper deficient for 120–413 days at the time of this analysis.

Radiological Evaluation. Serial evaluations of tumor masses by conventional imaging with CAT scan or magnetic resonance imaging revealed that the radiographic appearance of certain masses changed significantly over time. In particular, areas of presumed central necrosis (corresponding to lower attenuation of the X-ray signal) were observed in a variety of tumor types, most notably renal cell cancer, angiosarcoma, and breast cancer. Seeking to evaluate the blood flow to the tumors as a function of time during copper deficiency on long-term TM therapy, lesions accessible to ultrasound were imaged with color flow three-dimensional ultrasound at the onset of copper deficiency and at 2–4-month intervals thereafter.

A representative example of the comparison between conventional CAT scan images and blood flow-sensitive three-dimensional ultrasound is depicted in Fig. 3. Here, a rib metastasis from renal cell carcinoma is depicted when the patient reached target copper deficiency (Fig. 3, *A* and *C*) and 8 weeks later (Fig. 3, *B* and *D*) by these two complementary imaging modalities. Fig. 3, *A* and *B*, shows stable size of this lesion by CAT scan over time, although a more distinct region of probable central necrosis is observed in Fig. 3*B*. In comparison, the color pixel density shown in Fig. 3, *C* and *D*, is the fraction of image voxels within the margins of the mass filled with color flow signals. There has been a 4.4-fold decrease in blood flow to this mass over a period of approximately 8 weeks. In addition to the mass depicted in Fig. 3, this patient had extensive disease in the chest, pelvis, and femurs.

TM in Combination with Other Treatment Modalities

During the long-term maintenance of copper deficiency, additional treatment modalities were added to TM as deemed appropriate for the optimal management of the patients. A patient with previously untreated metastatic breast cancer is doing well with a good-to-excellent quality of life after 12 months of treatment. She had metastases in the paratracheal, posterior cervical, and retroperitoneal lymph node chains but had declined all cytotoxic therapy. The patient had stable disease for more than 6 months on TM treatment, when, due to a

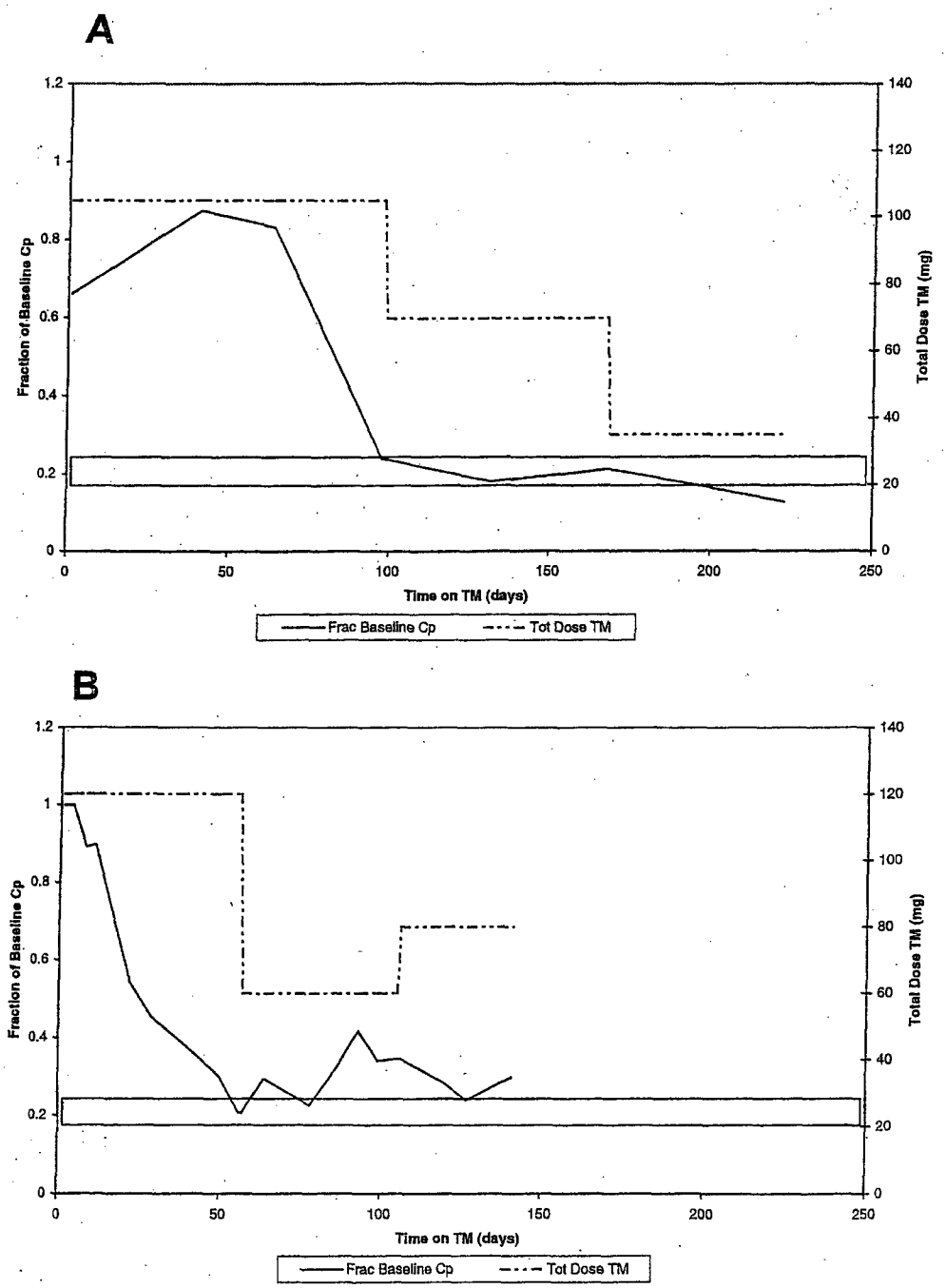

Fig. 2 Management of long-term therapy with TM to maintain a Cp target of 20% of baseline in two patients. *A*, patient required a decrease in dose at two time points that were 60 days apart. To prevent his Cp from falling below 5 mg/dl, this patient will likely require a decrease in TM dose in the future. *B*, TM dose was increased after day 100 to prevent a drifting of the Cp above the target range. Heterogeneity of diet and tumor behavior (such as tumor cell lysis) may account for the individual variability in dose adjustment needs.

slight increase (less than 25% of baseline) in the bidimensional size of the paratracheal and retroperitoneal nodes, she began concurrent trastuzumab (Herceptin; Genentech) therapy after this drug became commercially available. This patient showed a rapid response to trastuzumab at all sites of disease: after one cycle, there was a clinical complete response in the neck; and after three cycles of trastuzumab, there was radiological confirmation of complete response at all previous sites of disease. The patient remains on TM, but the trastuzumab was discontinued after six doses. She continues to maintain her status as a complete responder on TM alone for more than 6 months after discontinuation of trastuzumab therapy. Because the complete response was achieved after the addition of trastuzumab therapy, this patient is classified as having only stable disease on TM on Table 2.

Two patients with extensive angiosarcoma of the face and scalp achieved stable disease on TM. In one patient with severe chronic bleeding from an ocular lesion that threatened the orbit, IFN-α2 was added to TM to attempt to enhance tumor response. Given the suggestion that, based on studies of progressing

Table 2 Summary of type and length of response to TM therapy

	No. of patients (Total = 18)	Duration in days of copper deficiency (average)
Type of response		
Did not achieve target Cp	4	
Achieved target Cp	14	
Target Cp <90 days	8/14	
Disease progression	7	
Stable disease with partial regression of lung lesions	1	49[a]
Target Cp >90 days	6/14	
Stable disease with partial regression of lung lesions	1/6	120[a]
Stable disease	4/6	159[b], 329[a], 351[a], 413[a] (313[a])
Disease progression at one site, stable elsewhere	1/6	120[a]

[a] On therapy.
[b] Patient discontinued therapy.

hemangiomas, the use of low-dose IFN may be efficacious for the treatment of hemangioma (41), IFN-α was administered to both of these patients at a dose of 500,000 units s.c. twice a day. Radiotherapy was also given to these two patients while on TM to attempt to control actively bleeding (but not progressing) lesions. Both patients had disease stabilization for >60 days, with one of these patients remaining with stable disease for over 5 months before discontinuation of therapy due to patient choice. No exacerbation of toxicity was observed by the addition of any of these treatment modalities to TM.

Discussion

This is the first human trial of induction and maintenance of copper deficiency with TM as an antiangiogenic therapy for cancer. In a group of patients with advanced cancer, we have demonstrated that TM is remarkably nontoxic when Cp is lowered to 10–20% of baseline levels for up to 17 months of treatment. The only drug-related toxicity observed was mild anemia, which was easily reversible with adjustment of the TM dose to bring the Cp level to the desired target. Despite the diverse roles that copper plays in essential biological processes including heme synthesis and superoxide dismutase and cytochrome function, no lasting significant adverse effects were observed on reduction of Cp to approximately 20% of baseline or to a range between 5 and 15 mg/dl. From our data, we surmise that this level of copper reduction constitutes the lower limit of chemical copper deficiency and the beginning of mild clinical copper deficiency, the first manifestation of which is mild anemia. Table 3 summarizes the stages of copper deficiency in humans and their clinical characteristics. This information was derived from studies of patients with Wilson's disease, from occasional patients with chemical and clinical copper deficiency, and from copper-deficient small rodents. Note that as Cp is reduced below 5 mg/dl, it becomes an insensitive marker of the degree of copper deficiency. However, based on observations in humans with normal copper metabolism from this trial, we find that Cp is a sensitive and valid marker of copper status for levels above 5 mg/dl. This key finding allows the targeting of the antiangiogenic window of copper deficiency that appears to be required to slow or arrest tumor growth.

The Cp response to TM-induced copper deficiency is monotonic and exhibits little intersubject variability; therefore, there is essentially no risk of sudden changes or unpredictable fluctuations that might make dose management difficult. Following Cp levels once every 1–2 weeks is adequate to monitor copper status early in therapy. As a corollary, overtreatment is easily detectable and correctable. Using the six times/day dose regimen borrowed from our Wilson's disease work and initial TM doses ranging from 90–120 mg/day, the serum Cp was reliably lowered to 50% of baseline in 17 of 18 patients and to 20% of baseline in 14 of 18 patients. Reduction to 50% of baseline was achieved, on average, in 30 days, with further reduction to Cp levels of 5–10 mg/dl taking 20–30 days. Although this rate of decrease in Cp is reasonable for the initial treatment of early malignant lesions or in the adjuvant setting, in widely metastatic advanced cancer, this rate of decrease will not be sufficiently rapid to prevent some disease progression during induction of copper deficiency in a significant number of patients. Because loading dose variations of 90–120 mg/day do not appear to affect the rate of Cp reduction, and given the typical daily intake of copper with food, we conclude that higher doses in-between meals will likely be required to accelerate the rate of induction of copper deficiency. A follow-up trial is under way to test this hypothesis.

As a result of this study, it is apparent that with our present TM dose regimens, there is considerable lag between the initiation of TM therapy and the reduction of copper levels in tumors to a likely antiangiogenic level. Further retarding the ability to reach antiangiogenic levels of copper deficiency is the likelihood that most tumors sequester copper (42–45). Thus, it is reasonable to hypothesize that additional time may be required to deplete the tumor microenvironment to an effectively low level of copper, which is defined as a level low enough to inhibit angiogenesis. It is difficult to estimate this time accurately from our study. Thus, patients with very rapidly progressive large tumors may be relatively poor candidates for this approach to antiangiogenesis therapy as a single modality.

Another level of complexity is added by the fact that in bulky disease, initially effective antiangiogenesis may cause brisk tumor necrosis, as was documented in the mass shown in Fig. 3. Tumor lysis may result in the release of additional copper from the dying cells. In the case of the patient whose mass is shown in Fig. 3, a transient rise in Cp was observed at approx-

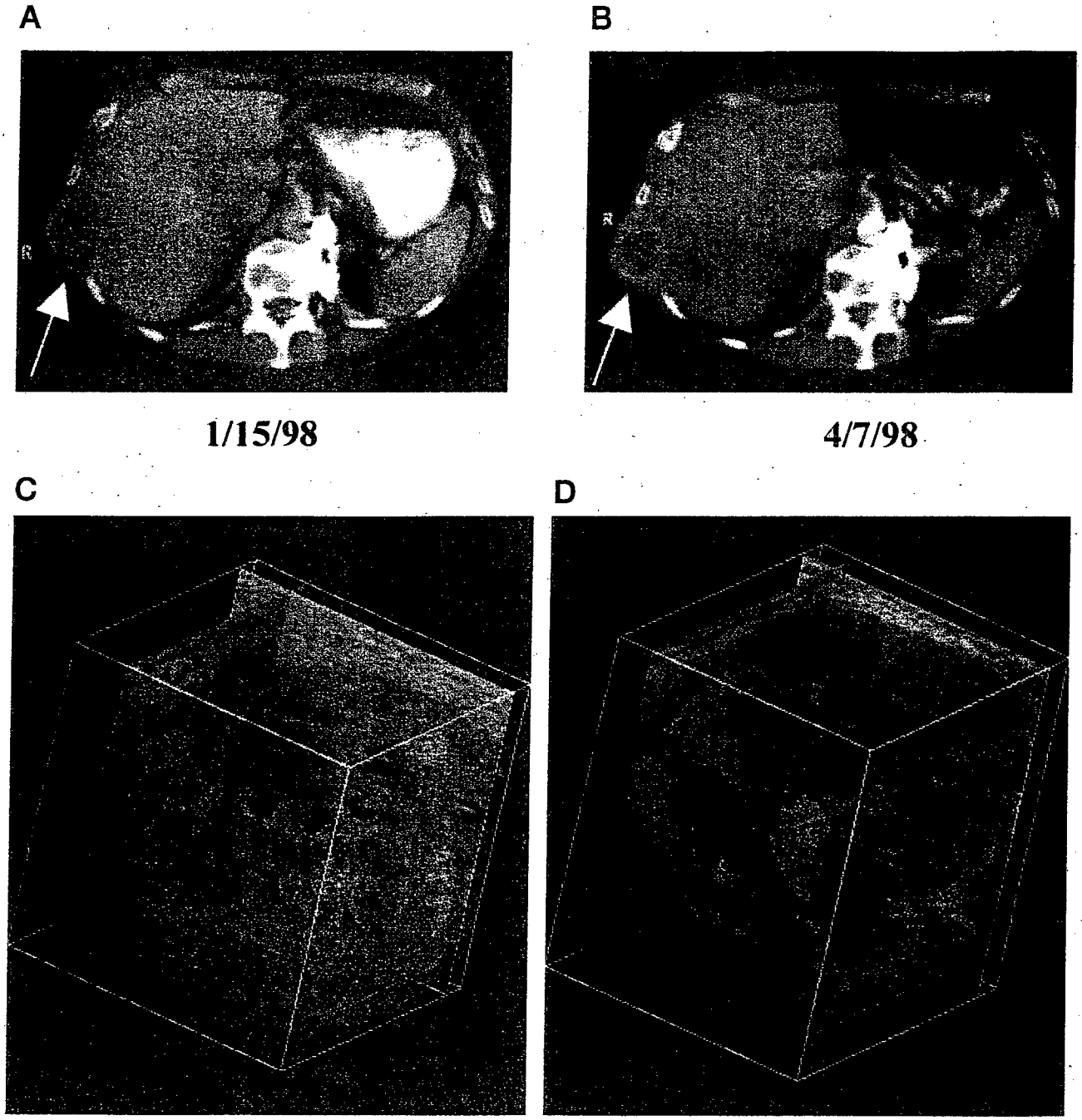

Fig. 3 Evaluation of antiangiogenic response to copper deficiency. CAT scans of the chest of a 59-year-old male with metastatic renal cell carcinoma shortly after achievement of target Cp (*A*) and 8 weeks later (*B*) are shown. Comparable frequency-shift color Doppler image volumes from the superficial renal cell carcinoma rib metastasis were evaluated at the same time points (*C* and *D*). Three-dimensional rendering of the vascularity is shown in *green* superimposed on three orthogonal image planes extracted from the reconstructed grayscale volume. The back plane shown exemplifies one of the frequency-shift color Doppler image planes acquired during the patient scan. Vascularity at initiation of TM therapy (*C*) is markedly greater than that seen 8 weeks later (*D*). Quantitatively, color pixel density is 4.4 times greater in the tumor volume scanned at the first time point; the mean flow velocities are equivalent at both times.

imately the same time as the ultrasound suggested that the large tumor mass might be undergoing central necrosis due to a significant decrease in blood flow. For these reasons, we conclude that a period of 60–90 days of Cp at the target level of 20% of baseline is a reasonable starting point for evaluation of response to anticopper therapy in future trials in patients with measurable disease. In the two patients who exhibited partial regression of lung lesions, tumor control may have begun ear-

Table 3 Stages of copper deficiency and its clinical effects in humans

Type of copper deficiency	Cp level[a]		Clinical manifestations
	% Baseline Cp	Absolute Cp level (mg/dl)	
Chemical	10–30 (target range)	5–15 (target range)	None[b] Probable inhibition of tumor angiogenesis
Clinical			
Mild	<10%	<5	Mild anemia, Hct ~80% of baseline Mild neutropenia
Moderate	<10%	<5	Moderate anemia, leukopenia, possibly symptomatic
Severe	<10%	<5	Severe bone marrow depression, diarrhea, cardiac arrhythmias may occur rarely, peripheral neuropathy[c] In children, inhibition of epiphyseal bone growth

[a] Normal serum Cp levels are 20–35 mg/dl. Cp levels in cancer patients are elevated (20–75 mg/dl).

[b] Bone marrow effects such as anemia and/or leukopenia may occur if the induction of copper deficiency is very rapid, as with high doses of TM, at higher levels of Cp than shown here.

[c] In general, signs and symptoms other than bone marrow depression require severe copper deficiency to have been present for weeks to months.

lier. It is also interesting to note that in both of these patients, the lung parenchymal metastases were the sites of tumor regression. It is possible that mild clinical copper deficiency impairs superoxide dismutase function (46) so that under conditions of high oxidant stress, such as those present in the lung, the metastatic foci are more susceptible to oxidative damage.

Despite individual differences, the use of three-dimensional ultrasound to determine the total blood flow to a given mass demonstrates that maintenance of mild copper reduction to 20% of baseline induced for at least 8 weeks appears sufficient to alter tumor blood flow. Due to the relative insensitivity of CAT to the blood flow or metabolic status of the lesions, parallel imaging modalities, as demonstrated here for three-dimensional ultrasound, will be required to assess functional response in addition to tumor size.

In light of the data presented above, we advance the preliminary conclusion that the size of solid tumors of a variety of types may be stabilized or decreased by TM, given sufficient time in a state of mild clinical copper deficiency represented by a decrease in Cp to or below 20% of baseline, as defined by this study. Among the patients maintained at the target Cp level for more than 90 days, a significant proportion of cases (five of six) were stabilized, with no detriment to their quality of life. However, in this population of patients with advanced disease, only 39% of those treated were able to be maintained at the target Cp for this duration.

The pattern and speed of progression observed in these patients have also provided useful preliminary information. One patient achieved stable disease at all sites but one and has chosen to remain on TM therapy due to disease stabilization at the more life-threatening sites of disease (bowel and paratracheal lymph nodes; the site of progression in this patient with melanoma is a large adrenal metastasis. This and other observations in this trial suggest that whereas copper deficiency may be generally inhibitory of angiogenesis, heterogeneity of tumor type and the specific location of metastases may modulate the response to this therapeutic modality. The small number of patients in this study and the design of this study preclude more detailed conclusions regarding efficacy at specific metastatic sites. Because it appears that lesions progress at a much faster rate on copper repletion than while on TM therapy, future trials may formally incorporate the use of adjunct modalities, either systemically or loco-regionally, to address the specific sites of progression while allowing the patients to remain in a copper-deficient state.

We report preliminary observations of combination therapies of TM with radiotherapy, trastuzumab, and IFN-α without apparent exacerbation of toxicity of the added modality. Taken as a whole, the safety and preliminary efficacy data derived from this trial support the conduct of additional studies designed to test the specific efficacy of TM alone or in combination for the treatment of early metastatic disease, minimal disease, and in adjuvant high-risk clinical settings, including chemoprevention.

References

1. Folkman, J. Anti-angiogenesis: new concept for therapy of solid tumors. Ann. Surg., *175:* 409–416, 1972.

2. Folkman, J. Angiogenesis in cancer, vascular, rheumatoid and other disease. Nat. Med., *1:* 27–31, 1995.

3. Folkman, J. Antiangiogenic therapy. *In:* De Vito, Rosenberg, and Hellman, eds., Cancer: Principles and Practice of Oncology, pp. 3075–3085. Philadelphia, PA: Lippincott-Raven Publishers, 1997.

4. Volpert, O. V., Ward, W. F., Lingen, M. W., Chesler, L., Solt, D. B., Johnson, M. D., Molteni, A., Polverini, P. J., and Bouck, N. P. Captopril inhibits angiogenesis and slows the growth of experimental tumors in rats. J. Clin. Investig., *98:* 671–679, 1996.

5. Millauer, B., Longhi, M. P., Plate, K. H., Shawver, L. K., Risau, W., Ullrich, A., and Strawn, L. M. Dominant-negative inhibition of Flk-1 suppresses the growth of many tumor types *in vivo*. Cancer Res., *56:* 1615–1620, 1996.

6. Warren, R. S., Yuan, H., Malti, M. R., Gillett, N. A., and Ferrara, N. Regulation by vascular endothelial growth factor of human colon cancer tumorigenesis in a mouse model of experimental liver metastasis. J. Clin. Investig., *95:* 1789–1797, 1995.

7. Borgstom, P., Hillan, K. J., Sriramarao, P., and Ferrara, N. Complete inhibition of angiogenesis and growth of microtumors by anti-vascular endothelial growth factor neutralizing antibody: novel concepts of angiostatic therapy for intravital videomicroscopy. Cancer Res., *56:* 4032–4039, 1996.

8. Yuan, F., Chen, Y., Dellian, M., Safabakhsh, N., Ferrara, N., and Jain, R. K. Time-dependent vascular regression and permeability changes in established human tumor xenografts induced by an anti-

vascular endothelial growth factor/vascular permeability factor antibody. Proc. Natl. Acad. Sci. USA, *93:* 14765–14770, 1996.

9. Borgstom, P., Bourdon, M. A., Hillan, K. J., Sriramarao, P., and Ferrara, N. Neutralizing anti-vascular endothelial growth factor antibody completely inhibits angiogenesis and growth of human prostate carcinoma microtumors *in vivo*. Prostate, *35:* 1–10, 1998.

10. O'Reilly, M. S., Boehm, T., Shing, Y., Fukai, N., Vasios, G., Lane, W. S., Flynn, E., Birkhead, J. R., Olsen, B. R., and Folkman, J. Endostatin: an endogenous inhibitor of angiogenesis and tumor growth. Cell, *88:* 277–285, 1997.

11. Benjamin, L. E., Golijanin, D., Itin, A., Pode, D., and Keshet, E. Selective ablation of immature blood vessels in established human tumors follows vascular endothelial growth factor withdrawal. J. Clin. Investig., *103:* 159–165, 1999.

12. Merajver, S. D., Irani, J., van Golen, K., and Brewer, G. Copper depletion as an anti-angiogenic strategy in HER2-neu transgenic mice. Proc. AACR Special Conference on Angiogenesis and Cancer, B11, 1998.

13. Marshall, J. L., Wellstein, A., Rae, J., DeLap, R. J., Phipps, K., Hanfelt, J., Yunmbam, M. K., Sun, J. X., Duchin, K. L., and Hawkins, M. J. Phase I trial of orally administered pentosan polysulfate in patients with advanced cancer. Clin. Cancer Res., *3:* 2347–2354, 1997.

14. Iruela-Arispe, M. L., and Dvorak, H. F. Angiogenesis: a dynamic balance of stimulators and inhibitors. Thromb. Haemostasis, *78:* 672–677, 1997.

15. Hanahan, D., and Folkman, J. Patterns and emerging mechanisms of the angiogenic switch during tumorigenesis. Cell, *86:* 353–364, 1996.

16. Volpert, O. V., Stellmach, V., and Bouck, N. The modulation of thrombospondin and other naturally occurring inhibitors of angiogenesis during tumor progression. Breast Cancer Res. Treat., *36:* 119–126, 1995.

17. Salnikow, K., Wang, S., and Costa, M. Induction of activating transcription factor 1 by nickel and its role as a negative regulator of thrombospondin I gene expression. Cancer Res., *57:* 5060–5066, 1997.

18. Guo, N., Krutzch, H. C., Inman, J. K., and Roberts, D. D. Thrombospondin 1 and type I repeat peptides of thrombospondin 1 specifically induce apoptosis of endothelial cells. Cancer Res., *57:* 1735–1742, 1997.

19. Schapira, D. V., and Schapira, M. Use of ceruloplasmin levels to monitor response to therapy and predict recurrence of breast cancer. Breast Cancer Res. Treat., *3:* 223–224, 1983.

20. Qian, X., Wang, W. N., Rothman, V., Nicosia, R. F., and Tuszynski, G. P. Thrombospondin-1 modulates angiogenesis *in vitro* by up-regulation of matrix metalloproteinase-9 endothelial cells. Exp. Cell Res., *235:* 403–412, 1997.

21. O'Reilly, M. S., Holmgren, L., Shing, Y., Chen, C., Rosenthal, R. A., Moses, M., Lane, W. S., Cao, Y., Sage, E. H., and Folkman, J. Angiostatin: a novel angiogenesis inhibitor that mediates the suppression of metastases by a Lewis lung carcinoma. Cell, *79:* 315–328, 1994.

22. Lannutti, B. J., Gately, S. T., Quevedo, M. E., Soff, G. A., and Paller, A. S. Human angiostatin inhibits murine hemangioendothelioma tumor growth *in vivo*. Cancer Res., *57:* 5277–5280, 1997.

23. Sim, B. K. L., O'Reilly, M. S., Liang, H., Fortier, A. H., He, W., Madsen, J. W., Lapcevich, R., and Nacy, C. A. A recombinant human angiostatin protein inhibits experimental primary and metastatic cancer. Cancer Res., *57:* 1329–1334, 1997.

24. Watanabe, T., Seno, M., Sasada, R., and Igarashi, K. Molecular characterization of recombinant human acidic fibroblast growth factor produced in *E. coli*: comparative studies with human basic fibroblast growth factor. Mol. Endocrinol., *4:* 869–879, 1990.

25. Engleka, K. A., and Maciag, T. Inactivation of human fibroblast growth factor-1 (FGF-1) activity by interaction with copper ions involves FGF-1 dimer formation induced by copper-catalyzed oxidation. J. Biol. Chem., *267:* 11307–11315, 1994.

26. Shing, Y. Heparin-copper biaffinity chromatography of fibroblast growth factors. J. Biol. Chem., *263:* 9059–9062, 1988.

27. Patstone, G., and Maher, P. Copper and calcium binding motifs in the extracellular domains of fibroblast growth factor receptors. J. Biol. Chem., *271:* 3343–3346, 1996.

28. Badet, J., Soncin, F., Guitton, J., Lamare, O., Cartwright, T., and Barritault, D. Specific binding of angiogenin to calf pulmonary artery endothelial cells. Proc. Natl. Acad. Sci. USA, *86:* 8427–8431, 1989.

29. Parke, A., Bhattacherjee, P., Palmer, R. M., and Lazarus, N. R. Characterization and quantification of copper sulfate-induced vascularization of the rabbit cornea. Am. J. Clin. Pathol., *137:* 1121–1142, 1988.

30. Raju, K. S., Alesandrii, G., Zinche, M., and Gullino, P. M. Ceruloplasmin, copper ions, and angiogenesis. J. Natl. Cancer Inst., *69:* 1183–1188, 1982.

31. Ziche, M., Jones, J., and Gullino, P. M. Role of prostaglandin E and copper in angiogenesis. J. Natl. Cancer Inst., *69:* 475–482, 1982.

32. Brem, S. S., Zagzag, D., Tsanaclis, A. M. C., Gatley, S., Elkouby, M. P., and Brien, S. E. Inhibition of angiogenesis and tumor growth in the brain. Suppression of endothelial cell turnover by penicillamine and the depletion of copper, an angiogenic cofactor. Am. J. Pathol., *137:* 1121–1142, 1990.

33. Brem, S., Tsanaclis, A. M., and Zagzag, D. Anticopper treatment inhibits pseudopodial protrusion and invasive spread of 9L gliosarcoma cells in the rat brain. Neurosurgery, *26:* 391–396, 1990.

34. Brewer, G. J., Dick, R. D., Yuzbasiyan-Gurkin, V., Tankanow, R., Young, A. B., and Kluin, K. J. Initial therapy of patients with Wilson's disease with tetrathiomolybdate. Arch. Neurol., *48:* 42–47, 1991.

35. Brewer, G. J., Dick, R. D., Johnson, V., Wang, Y., Yuzbasiyan-Gurkan, V., Kluin, K., Fink, J. K., and Aisen, A. Treatment of Wilson's disease with ammonium tetrathiomolybdate. I. Initial therapy in 17 neurologically affected patients. Arch. Neurol., *51:* 545–554, 1994.

36. Brewer, G. J., Johnson, V., Dick, R. D., Kluin, K. J., Fink, J. K., and Brunberg, J. A. Treatment of Wilson's disease with ammonium tetrathiomolybdate. II. Initial therapy in 33 neurologically affected patients and follow-up with zinc therapy. Arch. Neurol., *53:* 1017–1025, 1996.

37. Brewer, G., and Merajver, S. Treatment of metastatic cancer with the anticopper, antiangiogenic drug, tetrathiomolybdate. J. Investig. Med., *47:* 223A, 1999.

38. Linder, M. C., Houle, P. A., Isaacs, E., Moor, J. R., and Scott, L. E. Copper regulation of ceruloplasmin in copper-deficient rats. Enzyme (Basel), *24:* 23–35, 1979.

39. Carson, P. L., Fowlkes, J. B., Roubidoux, M. A., Moskalik, A. P., Govil, A., Normolle, D., LeCarpentier, G., Nattakom, S., and Helvie, M. R. J. M. 3-D color Doppler image quantification of breast masses. Ultrasound Med. Biol., *24:* 945–952, 1998.

40. LeCarpentier, G. L., Tridandapani, P. B., Fowlkes, J. B., Roubidoux, M. A., Moskalik, A. P., and Carson, P. L. Utility of 3D ultrasound in the discrimination and detection of breast cancer. RSNA EJ, in press, 1999.

41. Takahashi, K., Mulliken, J. B., Kozakewich, H. P., Rogers, R. A., Folkman, J., and Ezekowitz, R. A. Cellular markers that distinguish the phases of hemangioma during infancy and childhood. J. Clin. Investig., *93:* 2357–2364, 1994.

42. Arnold, M., and Sasse, D. Quantitative and histochemical analysis of Cu, Zn, and Fe in spontaneous and induced primary tumors in rats. Cancer Res., *21:* 761–766, 1961.

43. Apelgot, S., Copey, J., Fromentin, A., Guille, E., Poupon, M. F., and Rousel, A. Altered distribution of copper (^{64}Cu) in tumor-bearing mice and rats. Anticancer Res., *6:* 159–164, 1986.

44. Gullino, P. M., Ziche, M., and Alessandri, G. Gangliosides, copper ions and angiogenic capacity of adult tissues. Cancer Metastasis Rev., *9:* 239–251, 1990.

45. Fuchs, M. G., and Sacerdote de Lustig, E. Localization of tissue copper in mouse mammary tumors. Oncology (Basel), *46:* 183–187, 1989.

46. Culotta, V. C., Klomp, L. W. J., Strain, J., Casareno, R. L. B., Krems, B., and Gitlin, J. D. The copper chaperone for superoxide dismutase. J. Biol. Chem., *272:* 23469–23472, 1997.

3-D Compounding of B-Scan Ultrasound Images

Jochen F. Krücker, Charles R. Meyer, Theresa A. Tuthill, Gerald L. LeCarpentier,
J. Brian Fowlkes, Paul L. Carson

University of Michigan, Dept. of Radiology, 200 Zina Pitcher Place *Ann Arbor, MI 48109, USA*

Summary: Two applications of volume registration in 3-D ultrasound imaging, extended volume imaging (EVI) and 3-D Spatial compounding, are demonstrated both in phantom and clinical scans. Extended volumes were composed by obtaining partly overlapping scans, registering the overlapping volumes, and displaying the complete set of volumes in their relative spatial orientations as determined by the registration procedure. 3-D compound images were created by scanning volumes from several elevational look directions, registering, and averaging the different views. In both applications, the volume registration worked accurately and provided significant image improvements.

INTRODUCTION

Image registration, or coregistration, can be used to combine several sets of images obtained with different imaging parameters or modalities, from different look directions, or at different times. In medical imaging, it has mainly been applied to magnetic resonance imaging, X-ray computed tomography, and tomographic nuclear imaging modalities. Recently it has been shown that some image registration techniques can also be used to register 3–D ultrasound data sets [1-3]. In this study, we demonstrate two registration-based examples of image enhancements in 3-D ultrasound: Extended volume imaging (EVI) and 3-D spatial compounding. With EVI, one of the major limitations of high-frequency ultrasound scanners, the small field of view, can be overcome. This application is particularly important in sequential ultrasound exams, e.g. in screening for breast cancer or following cancer therapy, where large fields of view are needed to locate areas of change and to make sure that the same area is covered in sequential scans. Spatial compounding can deliver improved images with reduced speckle noise and increased contrast-to-noise ratio. It also reduces shadowing, and creates more complete images of connective tissues and other specular reflectors.

MATERIALS AND METHODS

Since the registration algorithm we used is fully explained in [4] , we will only briefly describe the relevant features here. The software performs either affine, i.e. linear, geometric transformations to map one image volume onto another, or non-linear thin-plate spline (TPS) warpings. When using full affine transformations, the user places 4 initial control points in each data set. The control points define the approximate mapping transformation from one set (reference) onto another (homologous). By varying the position of the control points, the algorithm refines the transformation until the mutual information (MI) of the reference and the

transformed homologous set is maximized. The MI, defined as the difference between the sum of the individual entropies and the joint entropy of two random variables, thus serves as a cost function in this optimization problem. For warping transformations, the user defines at least one more control point and increases the degrees of freedom of the registration transformation with each additional control point. Note that no pre-processing, like cropping or speckle reduction, has to be applied to the image sets before registration.

A clinical ultrasound scanner (Logiq 700, GE Medical Systems, Milwaukee, Wis) with an 11MHz 1.5-dimensional linear matrix array probe was used for all data acquisition. With electronic elevational (normal to scan plane) focussing, the average axial and elevational resolution cell diameters were 0.31 mm and 0.72 mm, respectively[1]. The transducer was attached to a 2 degree of freedom position encoder that restrained the motion of the probe to linear elevational scanning and elevational tilting. The position information was used to uniformly interpolate and shear the raw B-scan image sets before volume registration. All phantom scans were obtained in a focal lesion phantom (CIRS; Computerized Imaging Reference Systems, Norfolk, Va). All clinical scans were obtained in the female breast.

To create extended volume images, the area of interest was imaged in 3 or 4 approximately parallel, partly overlapping scans (Fig. 1). If 3 scans were used, the central scan (B) served as a reference relative to which the outer scans (A, C) were registered by maximization of the mutual information in the overlaps, AB and BC. In cases where 4 scans were combined (A, B, C, and D), D was first registered relative to C. The combined volume (C&D) and volume A were then registered relative to the global reference B using the overlaps BC and AB.

EVIs were obtained both in phantom scans and clinical breast scans. In phantom scans, the registration accuracy in the extended lateral direction was evaluated by comparing the true position of 50 spheres (3mm diameter) in the phantom to the position found in the extended view. In clinical scans, the registered volumes were visually assessed and the position of common landmarks marked in each set. The average registration error was defined as the mean distance between point pairs defining common landmarks.

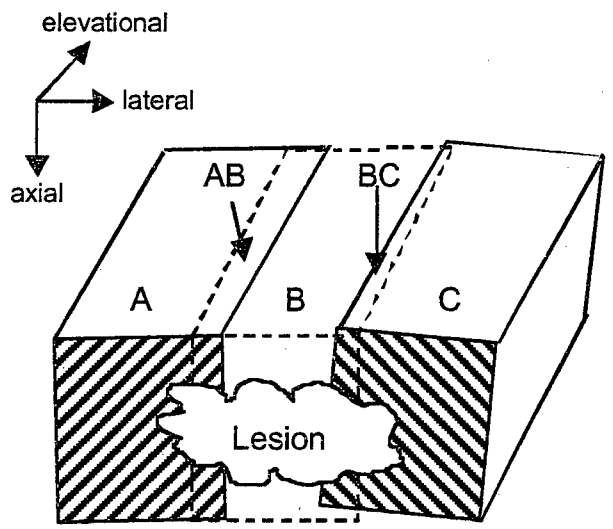

Figure 1: Extended Volume Imaging. Volumes A and C are registered relative to reference volume B.

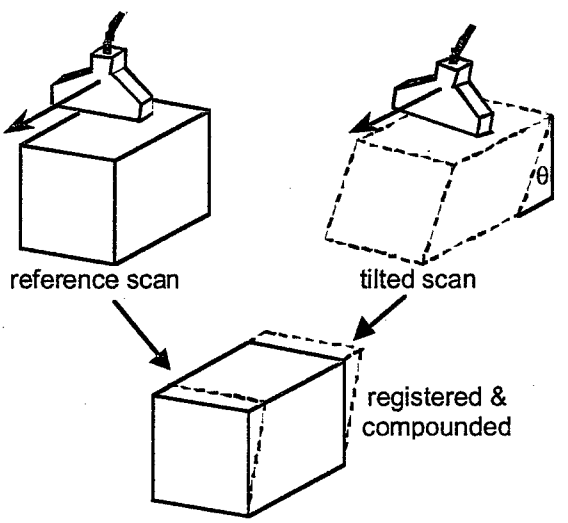

Figure 2: Spatial compounding of volumes obtained at different elevational tilt angles

[1] A phantom was scanned axially and elevationally in an area that produced fully developed speckle. The resolution cell diameters were defined as the standard deviation of the Gaussian fit to the frame-to-frame correlation functions.

For compound imaging, partly uncorrelated views were obtained by changing the tilt angle of the transducer before re-scanning the area of interest (Fig. 2). The interpolated and sheared image sets were registered using either full affine or warping transformations. The registered data sets were then log-decompressed, averaged, and recompressed to the same dynamic range as the original images (69 dB).

The registration accuracy in phantom scans was determined using a semiautomatic edge detection algorithm. Given the approximate center of a spherical hypoechoic area, the algorithm finds the exact center and the two radii on which the average signal increased 10% and 90%, respectively, of the difference between the maximum signal level outside the circle and the minimum inside. The difference between the radii will be referred to as the boundary width of the spheres. The accuracy in clinical compound scans was estimated by the same visual method used for clinical EVI.

RESULTS AND DISCUSSION

Figure 3 displays an example of an axial-lateral cross section through an EVI created from 4 partly (30%, 35%, and 58%) overlapping phantom scans registered with full affine transformations. No averaging or other processing was applied in the areas of overlap. The white arrows indicate the display boundaries between the registered original scans. Note the continuous appearance of specular reflectors across the boundaries and the spherical symmetry of voids placed on boundaries. The total width of the cross section is 10.6 cm. The average lateral deviation of the spheres in the extended volume from their true position is +0.47%.

EVI in clinical scans produced similar alignment quality as long as the breast was stabilized during the scans to keep local tissue deformation at a minimum [5]. The average distance of common landmarks identified in the registered overlaps ranged from 0.8 mm to 1.4 mm (peak: 1.5 to 3.1 mm).

Correlation calculations in phantom scans showed that the change in tilt angle needed to create uncorrelated images is 4 to 6 degrees. In compounding phantom scans obtained at differential scan angles of 4 degrees, the signal-to-speckle noise ratio (SNR) increased 10% to 20% less than the theoretical $\sqrt{N}$ dependence for N compounded, uncorrelated images. The average misregistration in phantom scans using full affine transformations was 0.21±0.02 mm and did not vary significantly with tilt angle. As a result of misregistrations, the average boundary width of the spheres in a phantom image compounded from 5 scans increased 20% compared to the uncompounded image. In the same compound image, the SNR increased 95%.

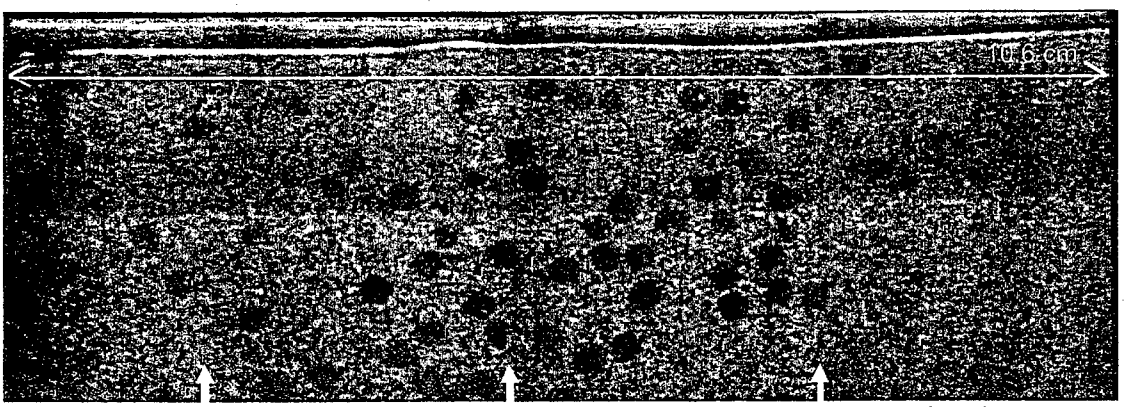

Figure 3: Axial-lateral cross section of an extended volume created from 4 partly overlapping phantom scans.

Figure 4 shows an example of an uncompounded clinical image in breast (a), and the same image compounded from 5 scans at 0°, 6.4°, 12.8°, -5.1°, and –10.2°, using 11 control point warping transformations (b). Statistical analysis showed an almost ideal $\propto\sqrt{N}$ increase in SNR and CNR (contrast-to-noise ratio) for N compounded images. Note the overall reduction in granularity and the better delineation of connective tissues (arrows).

The same data sets were also registered using full affine transformations. Comparing the warped data sets to the linearly transformed sets we found an increase in average estimated misregistration from 0.42±0.10 mm to 0.75±0.12 mm, suggesting that warping can correct for local tissue deformation that is unaccounted for by global linear transformations.

We conclude that image registration is a promising tool in 3-D ultrasound, allowing applications such as accurate extended volume imaging and 3-D compounding. Using image-based registration with non-linear mapping transformations prior to compounding offers the unique potential to correct for tissue motion and refraction artifacts, effects that can greatly distort image quality in other compounding approaches.

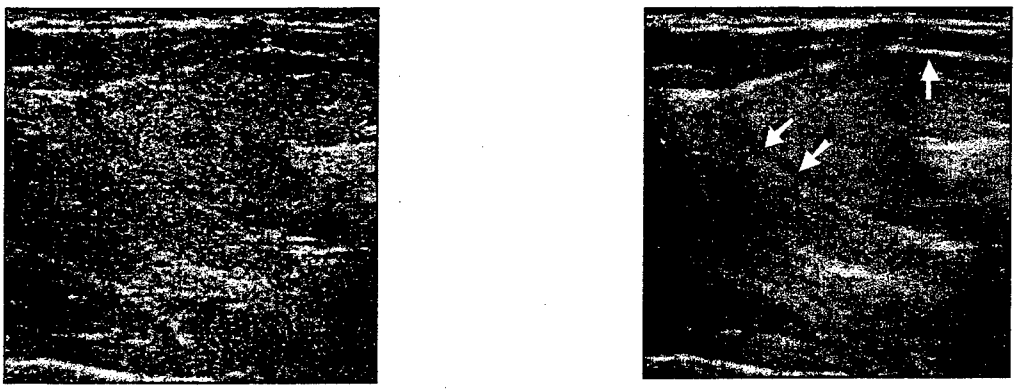

Figure 4: (a) Uncompounded image from reference scan. (b) Same image compounded from 5 scans at 0°, 6.4°, 12.8°, -5.1°, and –10.2°.

ACKNOWLEDGMENTS

This research was partially supported by U.S. Army Contract No. DAMD17-96-C-6061 and, to a lesser extent, USPHS grant 5RO1CA55076

REFERENCES

1. Meyer, C.R., Boes, J.L., Kim, B., et al., *Ultrasound in Med. & Biol.* (in press)
2. Rohling, R.N., Gee, A.H., Berman, L., *Ultrasound in Med. & Biol.* **24**, pp. 841-854 (1998)
3. Moskalik, A., Carson, P.L., Meyer, C.R., Fowlkes, J.B., Rubin, J.M., Roubidoux, M.A., *Ultrasound in Med. & Biol.* **21**, pp. 769-778 (1995)
4. Meyer, C.R., Boes, J.L., Kim, B., et al., *Med. Image Anal.* **1**, pp. 195-206 (1997)
5. Krücker, J.F., LeCarpentier, G.L., Meyer, C.R., Roubidoux, M.A., Fowlkes, J.B., Carson, P.L., submitted to *RSNA Electronic Journal* (1999)

Determination of Scan-Plane Motion Using Speckle Decorrelation: Theoretical Considerations and Initial Test

Jian-Feng Chen,* J. Brian Fowlkes, Paul L. Carson, Jonathan M. Rubin

Department of Radiology, University of Michigan Medical Center, 200 Zina Pitcher Place, Ann Arbor, MI 48109-0553

Received 20 August 1996; revised 26 August 1996

ABSTRACT: The correlation function of the echo signal intensities at a fixed region on a series of B-mode images is directly related to the change of speckle patterns between these images. An indication is given here of how the rate of the change of that correlation function can be used to estimate the scan-plane motion in any direction relative to the imaged tissue or other material. In this first implementation it is assumed that the statistical properties of the echo signals follow those of a complex circular Gaussian, and the case is considered of diffusely scattering tissue with many fine particles per resolution cell and with no phase distortion. The method is applied to data from a one-dimensional linear array and initial results are presented for scanning a tissue-mimicking phantom in the elevational direction of the transducer. Experimental results are in good agreement with the predictions. The current method should provide a good indication of the local rate of scan-head motion in those tissues in which the normalized correlation function of the echo signal intensities behaves, or can be made to behave, as it would for a medium with uniform acoustic properties and containing many, randomly distributed, pointlike scatterers, although application might be made to other situations where a deterministic condition exists for the correlation between images taken at differing locations within a volume. © 1997 John Wiley & Sons, Inc. Int J Imaging Syst Technol, **8**, 38–44, 1997

Key words: ultrasound; 3D; motion estimation; speckle; decorrelation

I. INTRODUCTION

The purpose of this article was to study scan-plane motions through tissue and the estimation of their relative positions by analysis of the correlation of speckle patterns in ultrasonic images. Conventionally, second-order statistics have been used to study the correlation of speckle patterns at different locations within ultrasonic images for tracking the relative motion of blood or other moving tissue [1]. Speckle correlation has also been studied for the purpose of speckle reduction for improving lesion detectability via spatial and frequency compounding [2–5]. These speckle reduction methods involve the averaging of images in which the speckle pattern has been changed. Recently, assessment of blood flow and, potentially, perfusion has been investigated by use of decorrelation of the Doppler signal with time at one location in the image [6]. In this article we use the speckle correlation between corresponding points in a series of scan planes for an alternative purpose: to determine the relative scan-plane positions, orientations, and motions. This may be important for the three-dimensional registration of ultrasonic images, or the detection and correction for tissue motion.

The speckle pattern on conventional B-mode images is caused by the phase-sensitive detection of the scattering from random inhomogeneities in the acoustic properties of biological tissue in the resolution cell of the transducer. When the scan plane is moved slowly, the intensities of time domain echo signals at one distance along one echo line changes, producing a change in the speckle pattern observed at that location on the B-mode images. We analyze the second-order statistical properties of the echo signal intensity from a given depth as a function of time or image frame number, instead of tracking the speckle patterns in subsequent images as a function of position within the images. The second-order statistics are defined as the expectation of the product using pairs of values (intensities) measured at two positions in space, number of frames or times.

In this article, it is assumed that the statistical properties of echo signals follow those of a complex Gaussian. The case considered is of diffusely scattering tissue with many fine particles per resolution cell [2] and with no phase distortion [7]. A method is proposed in which the correlation function of echo signal intensities are used to determine the relative positions of scan planes for motions in the elevational direction. That is the direction, normal to the scan plane, in which the same tissue volume cannot be tracked in the image. The method is applied to data from a modern 1D array imaging system and initial results are presented for 3D scanning of a tissue-mimicking phantom.

II. THEORY

A. The Correlation of Speckle Patterns in 3D B-Mode Images. The speckle pattern in B-mode images is directly related

Correspondence to: J. B. Fowlkes

* *Present address:* Siemens Medical Systems, Inc., P.O. Box 7002, Issaquah, WA 98027-7002

Contract grant sponsor: USPHS; *Contract grant number:* RO1 CA55076

Contract grant sponsor: USAMRDC; *Contract grant number:* DAMD17-94-5-4144

© 1997 John Wiley & Sons, Inc.

CCC 0899–9457/97/010038-07

to spatial variation of the echo signal intensities or their magnitudes. The correlation function of the intensities for a purely random (diffusely scattering) case can be estimated from the correlation function of the complex echo signals. The correlation of the echo signal intensities between two specific positions separated by $\Delta\mathbf{r}$, e.g., $\mathbf{r}$ and $\mathbf{r} + \Delta\mathbf{r}$, is defined as

$$R(\Delta\mathbf{r}) = \langle I(\mathbf{r})I(\mathbf{r} + \Delta\mathbf{r})\rangle \tag{1}$$

where $I(\mathbf{r}) \equiv |U(\mathbf{r})|^2$ and $I(\mathbf{r} + \Delta\mathbf{r}) \equiv |U(\mathbf{r} + \Delta\mathbf{r})|^2$ are the intensities of the echo signals at two specific points, $\mathbf{r}$ and $\mathbf{r} + \Delta\mathbf{r}$. $U(\mathbf{r})$ and $U(\mathbf{r} + \Delta\mathbf{r})$ are the complex echo signals. $\langle \cdots \rangle$ stands for the expectation of a random variable. The Appendix provides a general derivation for the results which is not dependent on the use of intensity data.

Using the moment theorem for the jointly zero mean, Gaussian random variables, and assuming that the real and imaginary parts of the complex echo signal $U(\mathbf{r})$, $U_r(\mathbf{r})$ and $U_i(\mathbf{r})$, are uncorrelated, e.g.,

$$\langle U_r(\mathbf{r})U_i(\mathbf{r} + \Delta\mathbf{r})\rangle = \langle U_r(\mathbf{r} + \Delta\mathbf{r})U_i(\mathbf{r})\rangle = 0,$$

we have [8]

$$R(\Delta\mathbf{r}) = 2\langle U_r^2(\mathbf{r})\rangle\langle U_r^2(\mathbf{r} + \Delta\mathbf{r})\rangle + 4\langle U_r(\mathbf{r})U_r(\mathbf{r} + \Delta\mathbf{r})\rangle^2 + 2\langle U_i^2(\mathbf{r})\rangle\langle U_i^2(\mathbf{r} + \Delta\mathbf{r})\rangle.$$

Using the symmetry of the correlation function of the complex echo signals $U(\mathbf{r})$,

$$\rho(\Delta\mathbf{r}) = \frac{\langle U(\mathbf{r})U^*(\mathbf{r} + \Delta\mathbf{r})\rangle}{\langle I\rangle}, \tag{2}$$

Finally, we have

$$R(\Delta\mathbf{r}) = \langle I\rangle^2(1 + \|\rho(\Delta\mathbf{r})\|^2) \tag{3}$$

or

$$\Gamma(\Delta\mathbf{r}) \equiv \|\rho(\Delta\mathbf{r})\|^2 = \frac{R(\Delta\mathbf{r})}{\langle I\rangle^2} - 1 \tag{3'}$$

where $\langle I\rangle$ is the average echo signal intensity over the region of interest. Here $\|\rho(\Delta\mathbf{r})\|^2$ is called the normalized correlation of the echo signal intensities and is denoted by $\Gamma(\Delta\mathbf{r})$, which has the properties of $\Gamma(0) = 1.0$ and $\Gamma(\infty) = 0$.

Equations (3) and (3′) show that there is a simple relationship between the correlation function of the complex echo signals and the correlation function of the signal intensities, which is directly related to the speckle in B-mode images.

B. Application to Clinical Scanners. The instruments for 3D ultrasonic imaging currently are linear curved, linear, or other array scanners; here, a 1D linear array will be considered. To further simplify our analysis, we confine our measurements to the focal zone or Fraunhofer region of the array transducer. Applying the Huygens–Fresnel principle, the radiating surface of the transducer is considered as a collection of point sources

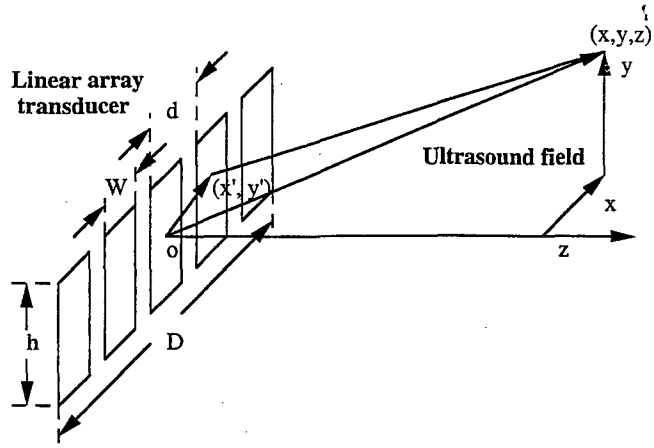

Figure 1. A transducer geometry for describing ultrasound beam patterns for a 1D linear array.

that oscillate sinusoidally. If the sources lie entirely within a simple plane (x', y') as shown in Figure 1, the radiating surface is defined by an aperture distribution function [9]

$$a(x', y') = \frac{1}{Dwhld}\left\{\left[rect\left(\frac{x'}{D}\right)\frac{1}{d}\,comb\left(\frac{x'}{d}\right)\right] \otimes \left[rect\left(\frac{x'}{w}\right)\right]\right\} rect\left(\frac{y'}{h}\right) \tag{4}$$

where (x', y') is a point on the transducer surface, w is the width of array elements, d is the center-to-center distance between array elements, D is the lateral dimension of the radiating aperture, h is the height of array elements in the elevation direction, and functions

$$comb(x) = \sum_{i=-\infty}^{+\infty} \delta(x - i)$$

and

$$rect(x) = \begin{cases} 0 & |x| > \frac{1}{2} \\ 1 & |x| \le \frac{1}{2} \end{cases}.$$

When the scan aperture is used to insonify and receive echoes from a medium containing randomly distributed fine particles, the complex echo signal is given by [9]

$$U(\mathbf{r}) \sim C\,\frac{e^{2ikz}}{z^2}\,h_1^2(x, y) \tag{5}$$

where $k = 2\pi/\lambda_o$ is the ultrasound wave number, λ_o is ultrasound wavelength at its central frequency, z is a distance along the beam axis from the surface of the transducer to the field point, and $h_1(x, y)$ is called the directivity function. $h_1(x, y)$ is specified entirely in the (x, y) plane (within the region of the interest)

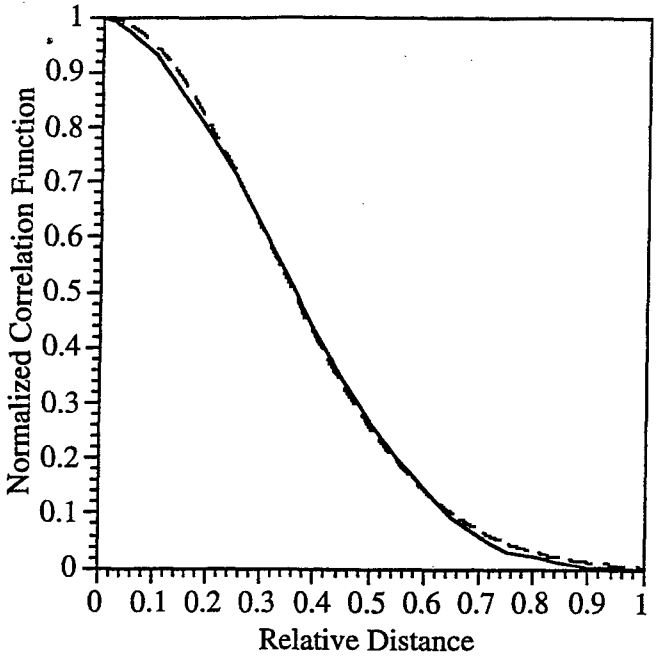

Figure 2. The normalized autocorrelation function of echo signal intensity based on a region of interest in the focal region or in the far-field region. The solid line is the calculation based on Equation (7), while the dash line is the result of a Gaussian fitting curve as shown in Equation (7′).

when the assumption of local plane wave exists. For a 1D array transducer, the directivity function is given by [9]

$$h_1(x, y) \approx \left[\sum_{i=-\infty}^{+\infty} sinc\left(\frac{wx}{\lambda_o z}\right) sinc\left(\frac{Dx}{\lambda_o z} - \frac{iD}{d}\right)\right] sinc\left(\frac{hy}{\lambda_o z}\right). \quad (6)$$

Consider the motion of scan plane in the direction perpendicular to the scan plane (called the elevation direction). In that case, the normalized correlation function of the echo signal intensities [Eq. (3′)] will depend just on the properties of the transducer in that direction and is given by

$$\Gamma(\Delta y_i) \approx (sinc^2 y_o \otimes sinc^2 y_o)^2. \quad (7)$$

$\Delta y_i = i \times \delta y$ is a displacement in the elevational direction, i is the number of steps, and δy is the slice separation (called the step size). $y_o = (h\Delta y_i)/(\lambda_o z)$. Equation (7) shows that the correlation function, $\Gamma(\Delta y_i)$, depends on the parameter y_o and echo signals will be completely decorrelated when $y_o \geq 2$. As shown in Figure 2, the function given by Equation (7) can be well approximated for our purposes by a Gaussian function

$$\Gamma(\Delta y_i) \approx e^{-2a_o(\Delta y_i)^2} \quad (7')$$

where $a_o \approx 2.72h^2/(\lambda_o z)^2$.

III. EXPERIMENTAL PROCEDURES AND RESULTS

Experiments were performed to test the proposed method of determining the relative positions of scan planes by using the speckle decorrelation in B-mode images. In this initial demonstration the motion estimation was restricted to the elevational direction for both simplicity and because this motion constitutes a significant component of the motion which could be used to acquire 3D data sets in clinical practice (a linear translation). However, as will be discussed later, there are a variety of implementations for estimating other motions as well. An ATL Ultra Mark 9 HDI (Advanced Technology Laboratories, Bothell, WA) scanner was employed with their 38-mm-long, 3.5-MHz linear array transducer. The linear array was translated in the elevational direction over a tissue-mimicking phantom (RMI Model 415, Middleton, WI) containing many randomly distributed, point-like particles in a 0.5-dB cm^{-1} MHz^{-1}, 1540 m/s gel. The translation was performed using a system previously developed for mechanically scanning the breast [10]. At each position, a single image was stored using a TARGA frame grabber (Truevision, Indianapolis, IN). A region of interest for future analysis was defined axially as 35 mm $\leq z \leq$ 45 mm and laterally as 12.5 mm $\leq x \leq$ 22.5 mm for the 35-mm-wide images. To determine the correlation function accurately, a uniform step size of $\delta y = 0.20$ mm was used, approximately one sixth of the 6-dB elevational focal beam width of the array at the depth of 35 mm $\leq z \leq$ 45 mm. To estimate the absolute motion in the elevational direction, the reference full width at half maximum (FWHM) of the correlation function and the coefficient in its Gaussian fitting curve were measured over the 35–45-mm depth range using known distance steps and the background scatterers from the same tissue-mimicking phantom described above.

Postprocessing of images was implemented in a modular code under AVS software (Advanced Visual Systems, Inc., Waltham, MA) and run on a Sun Sparc II (Sun Corp., Mountain View, CA). The frame grabbed images from the ultrasound scanner were read into the workstation memory and the red, green, and blue (RGB) images were then processed to select one channel for B-mode. A single 2D plane was displayed to select the region of interest (ROI) (described above) to be processed for determining the slice separation. The normalized correlation function of the echo signal intensities among image ROIs was determined by

$$\Gamma(\Delta y_i) \approx \frac{(m \times n)\sum_{j=1}^{m}\sum_{k=1}^{n} I_{j,k}(\mathbf{r}) I_{j,k}(\mathbf{r} + \Delta y_i \mathbf{e}_y)}{\{\sum_{j=1}^{m}\sum_{k=1}^{n} I_{j,k}(\mathbf{r})\}^2} - 1; \quad (8)$$

here, the average is over the $m \times n$ pixels of the region of interest, and $\mathbf{e}_y$ is a unit vector in the elevational direction.

The processing of ROIs based on Equation (8) was as follows. The $m \times n$ pixels contained in the ROI of each image were simply placed in a 1D vector containing j and k indexed pixels in Equation (8) and the process repeated for each image to create i 1D vectors. Each pixel value was converted to a linear scale by $I(\mathbf{r}) \approx 10^{P(\mathbf{r})/P_o}$, where $P(\mathbf{r})$ is the raw B-mode pixel value in decibels and the constant P_o is used to convert from a 0–255 log scale for intensity to a linear scale. Each of these vectors were then combined in a 2D vector for convenient comparison of each ROI as simply an increment in the i dimension. A group of image

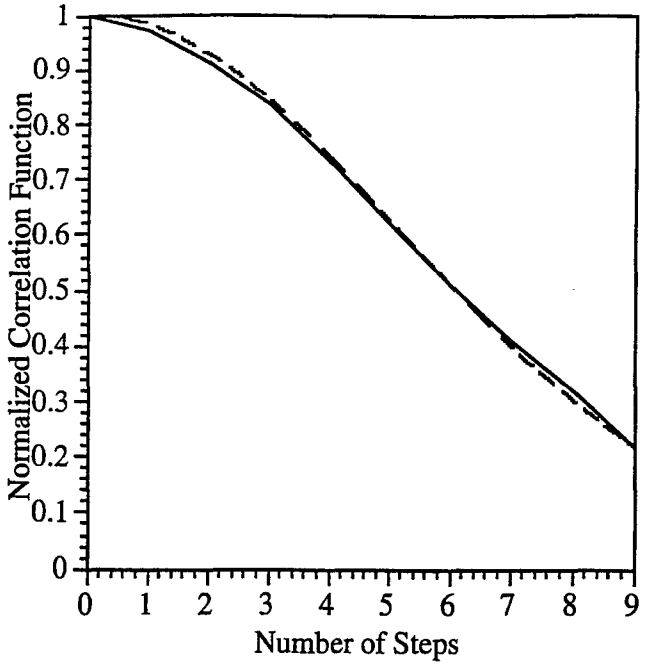

Figure 3. A typical experimental result of the normalized correlation function for the echo signal intensities (shown in a solid line) and its Gaussian fitting curve (shown in a dash line) when a transducer is slowly moved in the elevational direction. The step size is 0.2 mm.

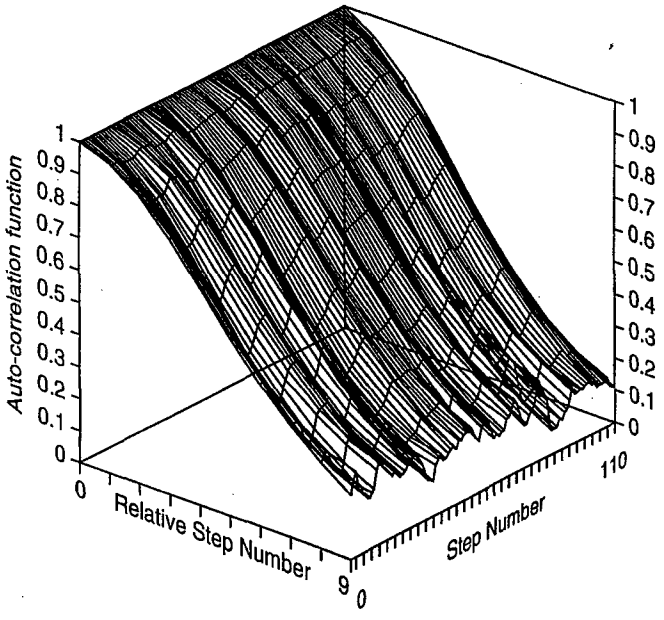

Figure 4. When the scan plane is automatically scanned through a tissue mimicking phantom in the elevational direction with uniform step sizes, the normalized correlation function of echo signal intensities as a function of different number of 0.2-mm steps over a travel distance of 2.0 cm.

ROIs was then analyzed to compute the correlation between successive ROIs, i.e., ROI 1 (i = 1) correlation to ROI 2 (i = 2), ROI 2 to ROI 3, etc. for a series of one-step correlation function values. Then the process was repeated for all possible two, three, $\cdots n$ step correlation function values obtainable from the i images. A correlation curve was created for any step sequence by plotting the zero-step through nine-step correlations. For this test, ROIs from groups of 10 images can be used to determine the slice separation for the center two slices of the 10, e.g., to position image 6 with respect to 5 use information from images 0–9; for image 7 after 6 use image 1–10, etc. This assumes a piecewise smooth motion for the scan head over an approximately 2 mm separation distance but this is a reasonable, first approach to the position estimate. In each case, the correlation function curve was fit to a Gaussian function using a least squares approach as shown in Equation (7′). The coefficients of these Gaussian functions are then used to position the images on an arbitrary grid space and correctly positioned images can then be displayed.

For a mechanical scanning with a uniform known 0.2-mm image slice separation (step size), a typical measurement result of the correlation function of the echo signal intensities as well as its Gaussian fitting curve are shown in Figure 3. Based on the coefficient in this Gaussian fitting curve and the point spread function in the elevational direction, the value of the step size can be estimated at that specific depth. Similarly, a group of the correlation functions are given in Figure 4 with the first curve calculated from the 10 slices starting at slice 1, second curve starting with slice 2, and so on. The step sizes were estimated based on the coefficients of the Gaussian fitting curves; the results are shown in Figure 5. The estimated step size is (0.20 ± 0.01) mm over more than 20 mm travel distance of the scan head. The measurement error is approximately 5%. This error could be caused by the statistical uncertainty of the correlation function estimates, the accuracy of the stepper motor (which is approximately ±5 μm, or ±2.5% based on a 200-μm step size) and friction in the contact between the surface of the test phantom

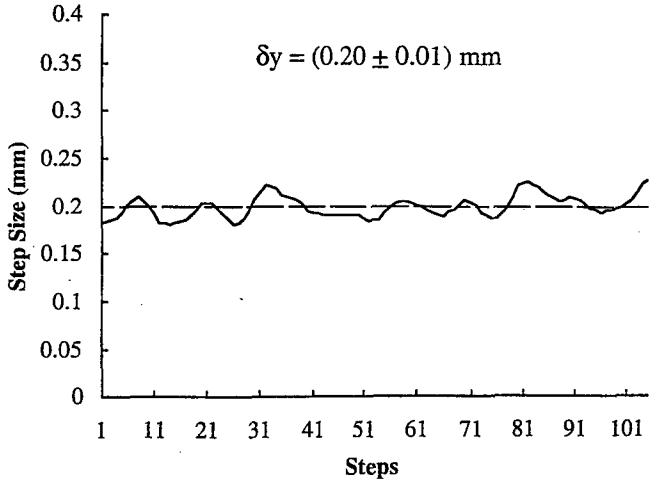

Figure 5. For a mechanical scanning with the uniform known 0.2-mm step sizes (image slice separations), the step sizes estimated by using a series of Gaussian fitting curves to the measured correlation functions as a function of the step number is given by the solid line. The measurement result of the step size is δ = (0.20 ± 0.01) mm.

and the transducer, which might cause nonuniform scan-plane motion.

IV. DISCUSSION AND CONCLUSIONS

As shown in this article, the results of measuring the decorrelation rate between a series of successive images can indicate the distance traveled in the simplest cases of pure elevational motion of the scan plane through an ideal medium. However, this case has not been addressed previously in medical imaging. There are numerous ways in which these concepts could be expanded to use correlation and decorrelation information to monitor scan-plane motion. Many of these can be thought of simply by reversing the concepts used to measure tissue motion, although in current medical imaging cases, fluid and tissue tracking is done within the image plane where each tissue volume remains in the image plane for an extended number of frames. The following are a few example extensions and implementations for monitoring scanner motion using this decorrelation technique alone or in combination with other methods of motion detection.

A. Scan-Head Motion Estimation in Less-than-Ideal Tissues and Other Media. The current theory for the decorrelation of speckle addresses only the case where tissue can be modeled as a medium with acoustically uniform properties and containing many randomly distributed, pointlike scatterers. It may be possible to process the ultrasound data to minimize effects of specular and other scatterers violating the assumptions and to extrapolate detected motion over tissue segments where the decorrelation is anomalous. The best applications will be those in which random cumulative errors in scan position over long distances are not critical or can be corrected. In addition, one may not be restricted to motion estimate based on Gaussian statistics. Other statistical models for tissue may be used and even "training" sets of data for a particular application may prove more accurate for motion estimates.

B. Monitoring Tilt and Rotation of the Transducer. Measuring different motions at different locations within images should indicate transducer motion which is not uniform in the elevational direction. For example, tilting the transducer slightly can be detected by examining the decorrelation rate at different depths in the image using the depth-dependent point spread function. The difference in rate as a function of depth would indicate tilting of the scan head. In addition, transducer rotation might be tracked. For example, several different ROIs on either side of the central axis of the image could be monitored such that differences among these regions provide relative motion information. An important consideration here will be the required size of the ROI selected for the motion. A given ROI must be sufficiently large for a statistical measure of the motion, while the ROI must be small enough that the motion within the ROI can be considered as a single value. This is an area presently being examined.

C. On-the-Fly Processing of Position Information. By restricting the number of scan line locations transmitted and monitored for motion, it should be possible to measure motion rapidly enough to allow real-time scanning. The needed high-speed pulsing might come from power-mode color windows with multiple beamformers. It also should be possible to set motion criteria which will indicate when full images should be taken to provide an automated way of reducing the number of frames acquired in a 3D data set while assuring adequate sampling.

D. Correction for Tissue Motion Such as Respiratory Motion. This speckle decorrelation technique could also allow for the correction of respiratory motion when 3D data set are reconstructed. Elevational as well as in-plane corrections could be applied to keep an ROI stationary in the image. For nonuniform motion and deformation of the tissues, the size of the ROIs might be adaptive to maximize the precision of the correlation estimates, while providing adequate resolution numerous smaller ROIs might be used in conjunction with some spatial smoothing or warping software [11].

E. Use of Technique with Available Coarse Positioning. The currently described technique could also be used for fine positioning in conjunction with other positioning systems. The latter could monitor the long-range motion of the scan head, but might lack the fine spatial resolution required for the best 3D reconstructions. Such encoding devices include optical, mechanical, magnetic, and electric spark systems, all of which have been used in the past for 3D ultrasound imaging.

F. Combination of 2D Speckle Tracking and Decorrelation. One possible implementation would incorporate 2D speckle tracking [1] to monitor motion in the scan plane between adjacent slices and then measure the decorrelation result. The idea is that the 2D speckle tracking would identify the correct vertical and horizontal translation required for placing the adjacent slice with respect to the first. The decorrelation which then remained between the slices would be the result of the translation in the elevational direction and would be an improved estimate over assuming no vertical or horizontal motion. Therefore, one would create a 3D directional vector for the motion at a particular location in the image.

G. Speed or Flexibility of Decorrelation Rate Determination. Use a threshold, rather than a Gaussian fitting function, to increase speed of decorrelation measurement. Alternatively, to maintain noise smoothing with more flexibility, use an adaptive fitting function, rather than a fixed Gaussian. With an adaptive fitting, it may be possible, for example, to correct for periodic motion, such as cardiovascular tissue motion.

In summary, a method is described for determining the scan-plane relative positions in the elevational direction using the decorrelation of speckle signal intensities in B-mode images, which are not due to motion within the scan plane. The method was tested using finely spaced scans in a tissue-mimicking phantom containing randomly distributed, fine, solid particles. The experimental results are in rather good agreement with the known step size, i.e. only 5% rms deviation. Useful implementation will depend on development and testing for more general and challenging conditions, including considerations of various artifacts in speckle tracking such as cumulative error and misinterpreted motion [12]. Experiments are currently being conducted in actual tissue to determine the efficacy of the technique and potential sources of error.

APPENDIX

We consider a complex random process, e.g., the complex echo signal, including both amplitude and phase information. We are interested in the correlation function of the complex echo signals between two subsequent scan plane positions. The complex echo signals are given by [8]

$$U(\mathbf{r}) = U_r(\mathbf{r}) + iU_i(\mathbf{r})$$

and

$$U(\mathbf{r} + \Delta\mathbf{r}) = U_r(\mathbf{r} + \Delta\mathbf{r}) + iU_i(\mathbf{r} + \Delta\mathbf{r})$$

where $\mathbf{r}$ and $\mathbf{r} + \Delta\mathbf{r}$ are the positions within an ROI related to the transducer scan head. The completely random signals are taken to have zero mean and to have the same variances of the real and imaginary parts. Then the autocorrelation function of the resulting signal is given by

$$\rho(\Delta\mathbf{r}) = \langle U(\mathbf{r})U^*(\mathbf{r} + \Delta\mathbf{r})\rangle \tag{A1}$$

where * refers to the complex conjugation, and displacement between points in the two scan planes is given by $\Delta\mathbf{r}$. If this field is simply read out or scanned by an imaging system with a point spread function (psf) $h(\mathbf{r})$, the resulting complex signal $U(\mathbf{r})$ is related to the original field $\alpha(\mathbf{r})$ by

$$U(\mathbf{r}) = h(\mathbf{r}) \otimes \alpha(\mathbf{r}) \tag{A2}$$

where $\otimes$ is a convolution operation and $\alpha(\mathbf{r})$ depends on the properties of the medium. The correlation function of the resulting processing, $\rho(\Delta\mathbf{r})$ is then directly given by [7]

$$\rho(\Delta\mathbf{r}) = h(-\Delta\mathbf{r}) \otimes \rho_\alpha(\Delta\mathbf{r}) \otimes h^*(\Delta\mathbf{r}) \tag{A3}$$

where $\rho_\alpha(\Delta\mathbf{r}) \equiv \langle\alpha(\mathbf{r})\alpha^*(\mathbf{r} + \Delta\mathbf{r})\rangle$. Equation (A3) shows that the correlation function depends on the displacement of the beam related to scatterers in the ROI.

A typical example is the acoustic scattering from a random collection of N scatterers in and extending well beyond a resolution cell or volume. These N scatterers can be divided into L sets, each set containing N_l scatterers ($\Sigma_{l=1}^{L} N_l = N$), and all having the same displacement, $\Delta\mathbf{r}_l$ from the previous set. In that case, we have

$$\alpha(\mathbf{r}) = \sum_{i=1}^{N} |a_i| e^{i\phi_i} \tag{A4}$$

and

$$\alpha(\mathbf{r} + \Delta\mathbf{r}) = \sum_{j=1}^{N} |a_j| e^{i\phi_j} \tag{A5}$$

where a_i is the magnitude of the scattering amplitude of the ith scatterer and there is correlation neither among the scatter phase ϕ_i in the first scattering volume nor among those in the second scattering volume nor between the scattering volumes. Then the correlation function of $\alpha(\mathbf{r})$ is

$$\begin{aligned}\langle\alpha(\mathbf{r})\alpha^*(\mathbf{r} + \Delta\mathbf{r})\rangle &= \sum_{i=1}^{N}\sum_{j=1}^{N} \langle |a_i||a_j| e^{i(\phi_i - \phi_j)}\rangle \\ &= \sum_{l=1}^{L} \{N_l |a_l|^2 \delta(\Delta\mathbf{r}_l)\},\end{aligned} \tag{A6}$$

since all phases average out unless they match up identically. Here, $\delta(\Delta\mathbf{r}_l)$ is the Dirac delta function.

Finally, the correlation function of the readout or scanned process is simplified to

$$\rho(\Delta\mathbf{r}) = \sum_{l=1}^{L} \rho_l(\Delta\mathbf{r}_l) \tag{A7}$$

where $\rho_l(\Delta\mathbf{r}_l)$ is given by

$$\rho_l(\Delta\mathbf{r}_l) = N_l\|a_l\|^2\{h(-\Delta\mathbf{r}_l) \otimes h^*(\Delta\mathbf{r}_l)\}. \tag{A8}$$

In the far field or the focal zone of the transducer, the psf can be approximately separated into the transverse component due to the diffraction limited beam, and the axial component due to the ultrasonic pulse,

$$h(\Delta\mathbf{r}) \approx h_t(r_t)h_r(r_r) \tag{A9}$$

where $h_t(r_t)$ and r_t are the transverse components of the psf and the displacement of the scatterers, and $h_r(r_r)$ and r_r are the axial components of the psf and the displacement of scatterers. As a simple example, when all scatterers are in motion (relative to the scan head) in the lateral direction, the correlation function of the complex echo signal will just depend on the transducer beam properties. When the scatterers are in motion in the axial direction, that function will depend on the ultrasonic pulses.

ACKNOWLEDGMENTS

The authors are grateful to Aaron Moskalik for constructing the mechanical scanning system and developing the algorithms for data acquisition and analysis. This work was supported by in part by USPHS Grant R01 CA55076, and by Grant DAMD17-94-5-4144 from the USAMRDC.

REFERENCES

1. E. J. Chen, W. K. Jenkins, and W. D. O'Brien, Jr. "The impact of various imaging parameters on ultrasonic displacement and velocity estimates," *IEEE Trans. Ultrasonics Ferroelect. Freq. Control* **UFFC-41,** 293–301 (1994).
2. R. F. Wagner, S. W. Smith, J. M. Sandrik, and H. Lopez. "Statistics of speckle in ultrasound B-scans," *IEEE Trans. Sonics Ultrasonics* **SU-30,** 156–163 (1983).
3. S. W. Smith, R. F. Wagner, J. M. Sandrik, and H. Lopez. "Low contrast detectability and contrast/detail analysis in medical ultrasound," *IEEE Trans. Sonics Ultrasonics* **SU-30,** 164–173 (1983).
4. G. E. Trahey, S. W. Smith, and O. T. Von Ramm. "Speckle pattern correlation with lateral aperture translation: experimental results and implications for spatial compounding," *IEEE Trans. Ultrasonics Ferroelect. Freq. Control* **UFFC-33,** 257–264 (1986).
5. M. O'Donnell and S. D. Silverstein. "Optimum displacement for compound image generation in medical ultrasound," *IEEE Trans. Ultrasonic Ferroelect. Freq. Control* **UFFC-35,** 470–476 (1988).

6. R. S. Adler, J. M. Rubin, J. B. Fowlkes, P. L. Carson, and J. E. Pallister. "Ultrasonic estimation of tissue perfusion: a stochastic approach," *Ultrasound Med. Biol.* **21,** 493–500 (1995).
7. L. Nock and G. E. Trahey. "Phase aberration correction in medical ultrasound using speckle brightness as a quality factor," *J. Acoust. Soc. Am.* **85,** 1819–1833 (1989).
8. R. F. Wagner, M. F. Insana, and D. G. Brown. "Statistical properties of radio-frequency and envelope-detected signals with applications to medical ultrasound," *J. Opt. Soc. Am.* **4,** 910–922 (1987).
9. M. F. Insana, T. J. Hall, and L. T. Cook. "Backscatter coefficient estimation using array transducers," *IEEE Trans. Ultrasound Ferroelect. Freq. Control* **UFFC-41,** 714–723 (1994).
10. A. Moskalik, P. L. Carson, C. R. Meyer, J. B. Fowlkes, J. M. Rubin, and M. A. Roubidoux. "Registration of 3D compound ultrasound scans of the breast for refraction and motion correction," *Ultrasound Med. Biol.* **21,** 769–778 (1995).
11. B. Kim, J. L. Boes, K. A. Frey, and C. R. Meyer, "Mutual information for automated multimodal image warping," in *Proceedings of Visualization and Biomedical Computing: Lecture Notes in Computer Science,* Vol. 1131. Springer-Verlag, Hamburg, Germany, 1996, pp. 349–354.
12. F. Kallel, M. Bertrand, and J. Meunier. "Speckle motion artifact under tissue rotation," *IEEE Trans. Ultrasound Ferroelect. Freq. Control* **UFFC-41,** 205–258 (1994).

Theresa A. Tuthill, PhD
Jochen F. Krücker, Dipl Phys
J. Brian Fowlkes, PhD
Paul L.Carson, PhD

Index terms:
Breast, US, 00.12989
Ultrasound (US), experimental
Ultrasound (US), technology
Ultrasound (US), three-dimensional

Radiology 1998; 209:575–582

[1] From the Department of Radiology, University of Michigan Medical Center, 200 Zina Pitcher Pl, Ann Arbor, MI 48109-0553. Received December 23, 1997; revision requested March 23, 1998; revision received April 21; accepted June 9. Supported in part by the U.S. Army Medical Research and Materiel Command under contract no. DAMD17-96-C-6061 and by U.S. Public Health Service grant 1RO1CA55076 from the National Cancer Institute. **Address reprint requests to** P.L.C..

The views, opinions and/or findings contained herein are those of the authors and should not be construed as an official Department of the Army position, policy or decision.

© RSNA, 1998

Author contributions:
Guarantor of integrity of entire study, J.B.F.; study concepts, J.B.F., P.L.C.; study design, J.B.F., T.A.T.; definition of intellectual content, J.B.F., P.L.C.; literature research, T.A.T.; clinical studies, J.B.F., P.L.C.; experimental studies, T.A.T., J.F.K.; data acquisition and analysis, T.A.T., J.F.K.; statistical analysis, T.A.T., J.F.K.; manuscript preparation, T.A.T., J.F.K.; manuscript editing, T.A.T.; manuscript review, J.B.F., P.L.C.

Automated Three-dimensional US Frame Positioning Computed from Elevational Speckle Decorrelation[1]

For ultrasonographic B-scan images collected by means of a handheld transducer moving in the elevational direction, frame spacings are computed with a speckle-decorrelation algorithm, without additional positioning hardware. Fully developed speckle volumes are automatically segmented and spacing computed from the decorrelation curves. Position accuracy is within 10% for phantoms and 15% for breast studies. The algorithm provides image-based registration, which allows accurate three-dimensional volume rendering.

In three-dimensional ultrasonography (US), the position accuracy of each B-scan frame is essential for accurate volume reconstruction. Even for qualitative reconstruction without position measurement, the image spacing must be adequately fine and uniform to avoid streak artifacts. Current position measurement techniques require use of a supplementary mechanical device to record the location of the transducer head during scanning. We propose an alternative scheme that makes use of the residual correlation between frames to estimate the separation distance. Since the observed speckle patterns are wholly determined by the physical properties of the transducer-given scattering dominated by a large number of random scatterers in the insonified volume, the frame separation can be computed from the degree of speckle decorrelation as calibrated for a specific transducer.

In recent years, reconstruction of three-dimensional US scans for potential clinical use has demonstrated moderate success in areas such as breast cancer diagnosis (1), angiography (2), fetal anomalies (3), and prosthesis modeling (4). Traditionally, for accurate three-dimensional rendering (5), the transducer orientation had to be determined with use of an articulated arm, microcontrolled motor-driven translator, or electromagnetic positioner or by means of optical imaging. By computing frame spacing directly from the image series, the hardware necessary for the scanning process is greatly reduced. The ultimate result of techniques that examine image correlation would, then, be image-based registration of B scans obtained with a freely moving, handheld transducer.

In previous work, Chen et al (6,7) introduced the concept of monitoring of scanning plane motion by means of changes in speckle correlation in the elevational direction. Their decorrelation curves were computed from a small set of training images and were valid only within the focal zone. In this study, the transducer was calibrated to determine a depth-dependent beam correlation width to allow analysis over a larger scanning region. An automated adaptive speckle detector was also employed to ensure only true speckle areas were included in the estimate. The current technology (8,9) could then provide three-dimensional reconstruction with use of real-time imaging and freehand scanning.

Materials and Methods

The rate of speckle decorrelation can be derived by means of statistical analysis of speckle formation. A more detailed derivation is given in the Appendix, but the main points and assumptions are presented here. For fully developed speckle, the intensity image should have an exponential distribution and a constant ratio of mean to standard deviation of 1.0. The amount of speckle change from frame to frame is directly related to the second-

order statistics as determined by the frame separation. Note that in this analysis, the normalized autocovariance is referred to as the correlation function.

The algorithm derivation shows that the intensity correlation function is directly related to the amplitude correlation function, which in turn is proportional to the point-spread-function autocorrelation. Assuming a focused transducer, the beam pattern can then be approximated by means of a Gaussian curve that has a depth-dependent width as the beam goes in and out of the focal region. Consequently, the intensity autocorrelation can also be written as a Gaussian function with respect to the frame spacing and will have a SD of $\sigma_v(z)$, the depth-dependent beam correlation width. This correlation width in the focus can be calculated on the basis of the transducer's physical properties, or the correlation width for a longer range can be calibrated by using a speckle phantom. The final result is that by means of Gaussian curve fitting of the correlation function for speckle regions in a set of B-scan frames, the average frame spacing for that set can be back calculated.

In this study, a commercially available US scanner (LOGIQ 700; GE Medical Systems, Milwaukee, Wis) was used, with a 13-MHz, 1.5-dimensional matrix linear array probe. The transducer had a 6-dB lateral beam width of 1.9 mm and an elevational beam width of 2.0 mm at the focus. B-scan images were obtained with both uniformly and nonuniformly spaced elevational sweeps. The scans were digitized to 8 bits and stored as 379 × 380-pixel images, corresponding to 4-cm² regions. The recorded gray-scale images were then log decompressed to obtain an intensity image series.

Since the decorrelation algorithm holds true for only speckle regions, a speckle "detector" based on first-order statistics was developed. The ratio of mean intensity to SD was computed for a region with a moving three-dimensional volume (21 × 21 pixels × 10 frames). A binary mask was formed that displayed regions in which the ratio of mean intensity to SD was between 0.9 and 1.1, and the two-dimensional mask was assigned to the center frame. Pixels in only the mask region were then used to form the average covariance function.

The depth-dependent beam correlation width of the transducer was determined by using a focal lesion phantom (CIRS; Computerized Imaging Reference Systems, Norfolk, Va). The phantom, which has a densely packed, random distribution of fine particles, provided the minimum number of scatterers in the resolution cell necessary to create fully developed speckle. The transducer was affixed to a linear micropositioner, and 120 B-scan images were obtained in an elevational sweep, with a uniform step size of 50.8 μm. With a moving volume of 10 frames, a mask was determined for the central portion of the scans, a region of 300 × 100 pixels. The average autocovariance was computed for each row in the mask, normalized, and then Gaussian curve fitted. The estimated Gaussian standard deviation at each depth was scaled by the step size to determine the depth-dependent beam correlation width, or $\sigma_v(z)$. The depth dependency was then approximated with a polynomial, resulting in a beam correlation width for the given transducer and scanning settings.

The calibration was first verified on other B-scan series in regions of apparently pure speckle in the phantom, with use of uniform frame spacing from 25.4 to 279.4 μm. The same pixel region, range of ratio of mean intensity to SD,

Figure 1. Representative B-scan breast image demonstrates the variety of complex structures present when the position of the scanning head is calculated. Accurate three-dimensional spatial registration would be necessary to determine the size of the fibroadenoma (arrows) in any selected plane.

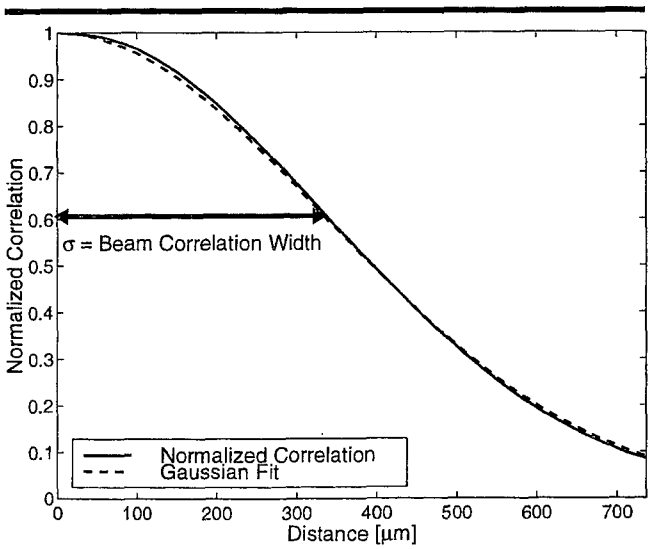

Figure 2. Normalized averaged autocovariance function in the elevational direction for a series of uniformly spaced B scans obtained in a tissue-mimicking phantom. The average was computed over a 30 × 10-mm (300 × 100-pixel) area, and the frame separation was 25.4 μm.

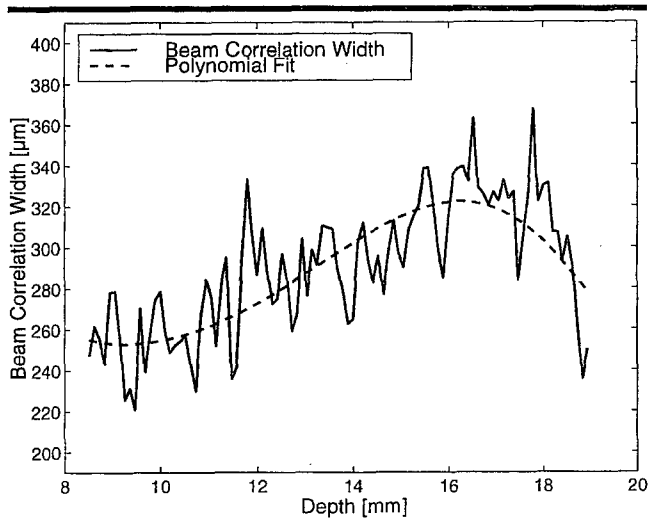

Figure 3. Beam correlation width based on regional covariance curves plotted as a function of depth, for a 13-MHz linear array transducer focused at 1.5 cm.

and number of frames per volume were chosen as were used for the calibration. The speckle-selection and frame-spacing computations were then verified on uniformly spaced scans obtained in a portion of the phantom that contained regions with 3-mm-diameter "voids," spherical regions of weak scatterers.

The algorithm was also tested on a scan series with nonuniform spacing obtained with a freehand scan system (10,11) that allows the user to slide a transducer along a framework at a variable rate. The transducer is affixed perpendicular to the scanning direction to prevent any lateral, range, or rotational movement. Position information to within ±10 μm is stored by means of an encoder connected to a computer. Depending on the frame rate, the transducer must be moved slowly enough to ensure that consecutive frames are not completely decorrelated.

Freehand scans were first obtained in the phantom at "pure" speckle regions and regions containing 3-mm-diameter voids. Finally, clinical images were obtained in a study approved by our institutional review board, with signed informed consent from the subjects. A series of breast scans were obtained in vivo by using the position-encoder apparatus. Figure 1 shows a representative B-scan image obtained with the same settings used for the phantom scans. The frame spacings of these freehand scans were computed by using the calibration data and compared with the spacing given by using the position encoder.

Results

The initial phantom scans were obtained with uniform spacing measured with the micropositioner. Figure 2 shows the average frame-to-frame decorrelation in a pure speckle region, with 25.4-μm spacing, and the Gaussian fit.

For the calibration, a 300 × 100-pixel region (corresponding to 3 × 1-cm² area) was chosen. The resultant depth-dependent beam correlation width of the transducer is shown in Figure 3. Even in regions of apparently "pure" speckle, the distribution of the ratio of mean intensity to SD around its average value of 1.0 broadens as a result of statistical fluctuations when the area in which it is calculated decreases. With a range of ratio of mean intensity to SD of 0.9–1.1 and a window size of 21 × 21 pixels, the area marked as speckle with the speckle selector was roughly 40% of the total region. This low acceptance rate is a trade-off between the high spatial resolution of the mask and the rigorous rejection of nonspeckle regions.

To test the scaling of the calibration set to other frame spacings and to find the maximum image spacing to which accurate separation calculations are possible, the algorithm was applied to subsets of a scan with 25.4-μm frame spacing. A subsample of the frames was obtained to create sets with spacings from 25.4 to 279.4 μm. The result, based on a 300 × 100-pixel region (Fig 4a), shows excellent agreement between calculated and nominal spacings, with less than 3% error up to 125 μm. For larger spacings that approach the correlation half width of the beam, the error increased steadily to −4.9% at 225 μm and −6.1% at 279.4 μm. For smaller regions, the SD of the estimated spacing increased due to the reduced number of pixels. Above 200 μm, the speckle images are fully decorrelated after only two to three frames, which

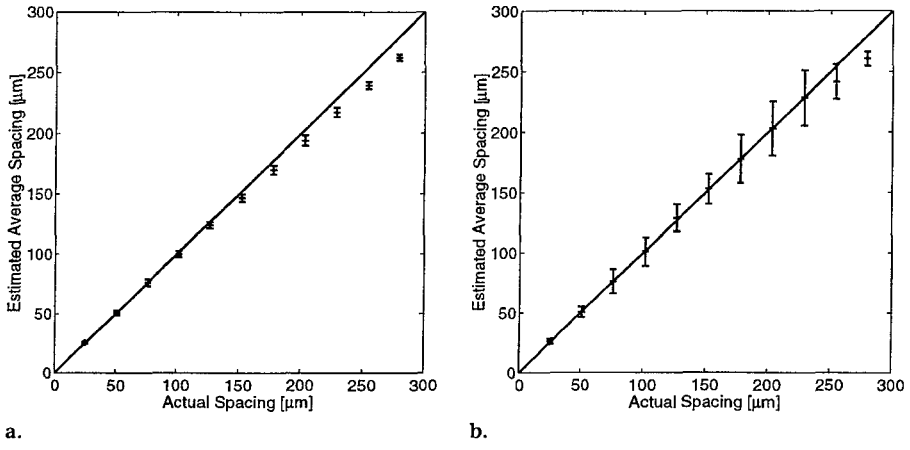

Figure 4. Estimated spacing for a series of uniformly spaced scans, computed over 10 frames, with (a) 300 × 100- and (b) 300 × 10-pixel regions. Error bars indicate ±1 SD of average estimation.

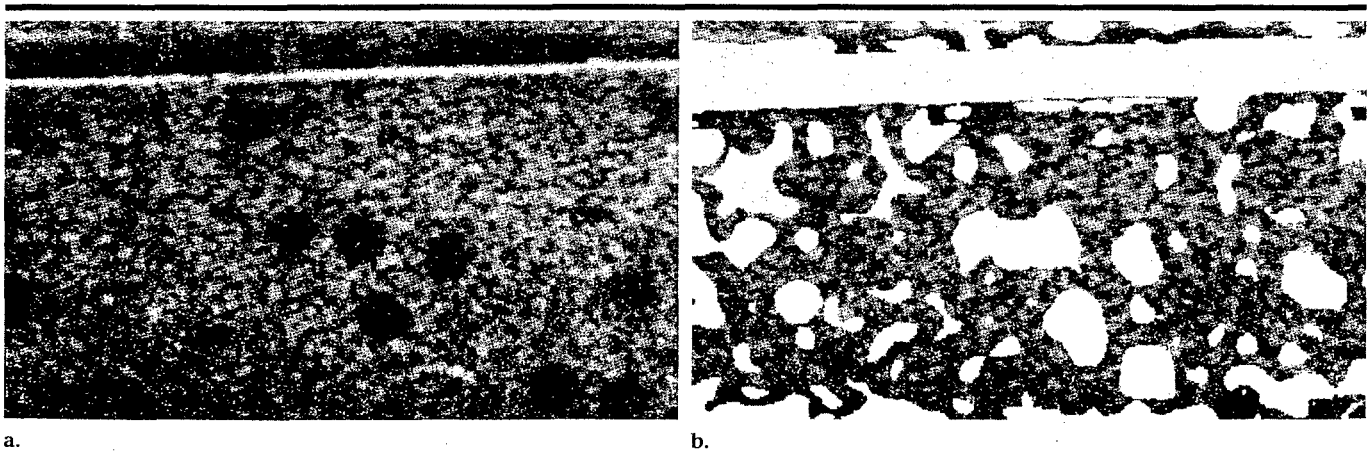

Figure 5. (a) B scan was obtained in a tissue-mimicking phantom that contained 3-mm-diameter voids. (b) Corresponding binary speckle-detector mask was determined on the basis of the ratio of mean intensity to SD for a moving volume (21 × 21 pixels × 10 frames). The white regions denote areas where the ratio of mean intensity to SD decreased to between 0.8 and 1.2.

increases the error considerably in the Gaussian fit. However, the average spacing was reproduced well up to 225 μm for a 300 × 10-pixel region in the center of the focal zone (Fig 4b). The improvement in the mean estimate of the section spacing results from the exclusion of pixels outside the elevational focal zone, which in this case was only approximately 30 pixels deep. The theory (Appendix) assumes the pixels are being taken from the focal zones so some systematic error might be anticipated if pixels from outside this region are included. This argues strongly for the use of multiple elevational electronic focusing.

The efficacy of the speckle detector was demonstrated in regions of the phantom that contain speckle and voids (Fig 5a). The boundaries between the small, weakly scattering voids and the background constitute structure that cannot be used for the section spacing computation. With use of a range for ratio of mean intensity to SD of 0.8–1.2, the selector successfully masked out the voids, leaving the "pure" speckle regions for calculation (Fig 5b).

For the freehand scanning experiments, the frame rate was set to the video rate of 30 Hz. Assuming the largest discernible frame separation is 250 μm, the maximum allowable transducer speed for this frame rate was 7.5 mm/sec. Scan sets of the phantom were recorded as the sonographer attempted to move the transducer at either uniform or variable speeds. Figure 6a displays the estimated and actual frame spacing in roughly uniform scanning, and Figure 6b shows the results in a scan set for which the sonographer increased the transducer speed midway through scanning, over a region of homogenous speckle. The speckle-decorrelation estimator tracked the actual position well, with a mean error of 7% root-mean-square for the frame spacing and of 3% root-mean-square for the total distance traveled. Scanning sweeps performed over the void-filled portion of the phantom showed similar results (Fig 6c, 6d). The total distance traveled in the two-speed scan in Figure 6c is shown in Figure 7a, as is the corresponding percentage of actual pixels used (Fig 7b) as determined with the adaptive mask for ratio of mean intensity to SD. The square of the correlation, R^2, defined as 1 minus the ratio of the variation of the residuals over the variation in position, demonstrates the accuracy of the estimate.

In the clinical study, one image series was obtained from a set of breast scans that depicted a fibroadenoma (Fig 1). The same transducer and scanner settings were used as were used for the phantom scans. Given only one focus, the B-scan image is not ideal and the tumor outline is unclear. However, the speckle correlation estimate for the frame spacing tracked the position data with an accuracy of 87% (Fig 8). The region within and surrounding the tumor deviated from true speckle, and the number of pixels used in the mask for ratio of mean intensity to SD decreased to 1,350. A transverse scan (with the axial and elevational resolution) through the tumor was reconstructed by using the position information (Fig 9a). The resolution of this out-of-plane scan is comparable to that of the original B scan. Finally, Figure 9b shows a reconstructed C-scan section (with the lateral and elevational resolution) obtained midway through the lesion.

In another clinical patient, the sonographer obtained a breast scan while varying the scanning speed. A transverse image was then reconstructed with the assumption of a uniform scanning speed (Fig 10a). The arrow denotes the area where the sonographer slowed down, and the actual frame spacing is decreased. Figure 10b shows the reconstruction obtained with the estimated frame spacing and interpolation. Incorporation of the spacing information subjectively reduced blurring and increased image quality, with better definition of connective tissue structures. For this scan, the maximum position error was 1.49 mm (mean error, 13.9%).

As a final test, a freehand scan that allowed tilting was obtained in the phantom. The transducer was swept smoothly through 30° with the transducer-phantom interface as the axis of rotation. The estimated row spacing was averaged over 250 frames. Whereas exact positioning could not be recorded, the estimated frame spacing increased linearly with depth (Fig

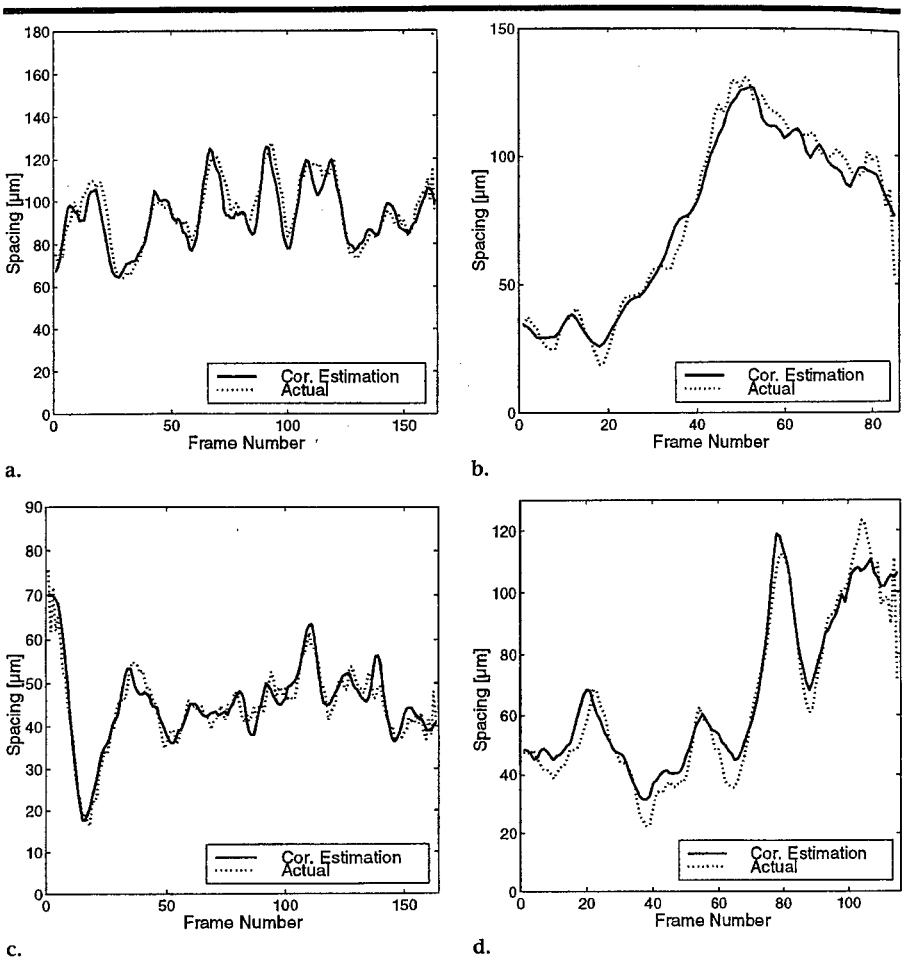

Figure 6. Graphs demonstrate comparison of decorrelation-estimated image separation with spacing computed from position-encoder information for freehand scan sets. **(a)** Scans obtained with approximately uniform speed over the speckle region in the phantom. **(b)** Scans obtained with two speeds over the same region as in **a**. **(c)** Scans obtained with approximately uniform speed over the void region in the phantom. **(d)** Scans obtained with two speeds over the same region as in **c**. In **a–d**, *Cor. Estimation* = correlation estimation.

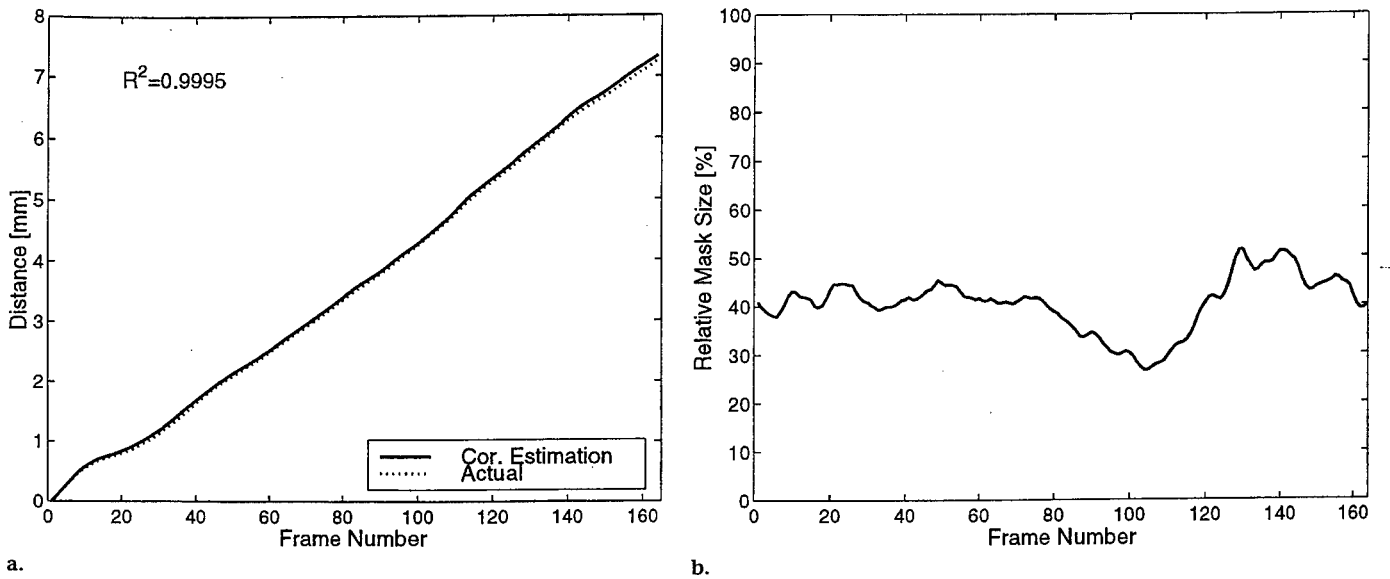

a. b.

Figure 7. (a) Estimated values for the total distance traveled by the transducer, corresponding to the accumulation of the frame spacings shown in Figure 6c. *Cor. Estimation* = correlation estimation. (b) Corresponding percentage of pixels masked by the speckle selector and used in the section spacing estimation.

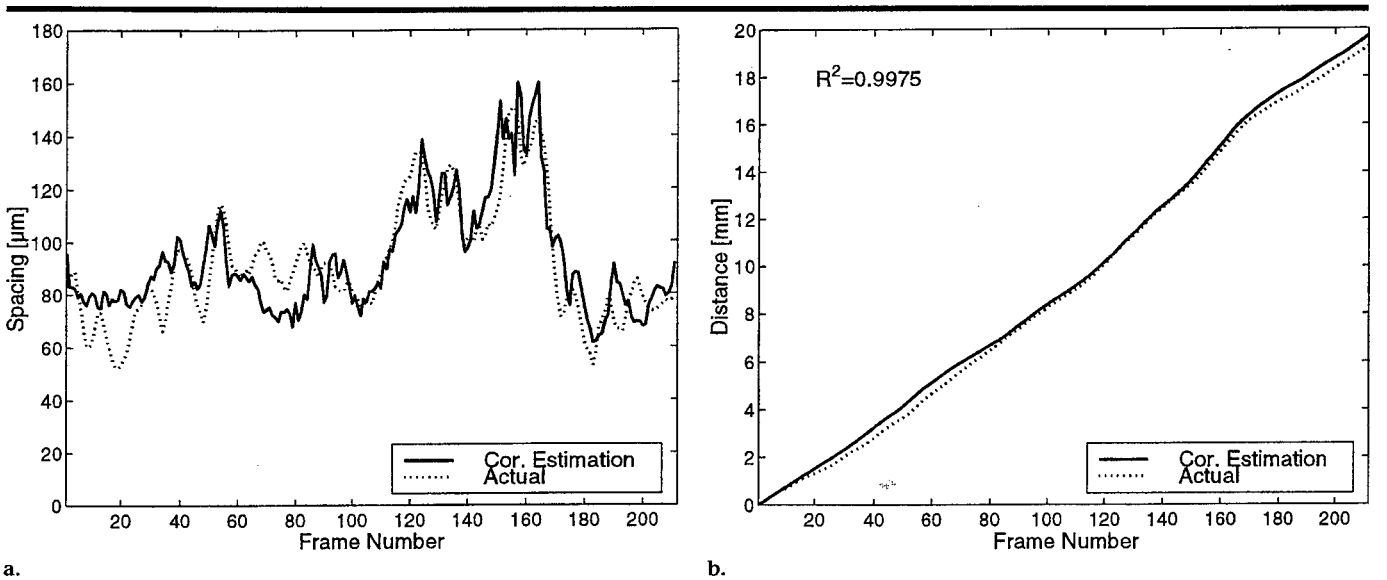

a. b.

Figure 8. (a) Estimated frame spacing for breast images obtained in a freehand scanning study. (b) Corresponding total lateral distance scanned by the transducer. In a and b, *Cor. Estimation* = correlation estimation.

11), indicating the feasibility of tracking transducer tilt and possibly other motions in addition to linear translations.

Discussion

The elevational decorrelation curves matched well with the Gaussian function as predicted by the theory. It should be noted that the error in the autocovariance estimate increased with lag number or the total distance between frames. As the decorrelation curve decreased, the estimate became unreliable, and thus only point values greater than 0.3 were used in the Gaussian curve fit. For large frame spacings, the speckle decorrelated in just a few frames, which reduced the number of points used in the curve fit and thus increased the error for the section spacing approximation.

The beam correlation width for the focused transducer showed interesting results as a function of depth. The curve peaked just above the focal region. Close to the transducer, a fast decorrelation was expected due to the incoherent nature of the beam in the near zone. At large depths, a fast decorrelation rate was also expected due to the dominance of noise in the signal and the incoherence of the beam.

For linear scans, the speckle-decorrelation technique showed excellent results in estimating frame separation and tracking the overall distance traveled. As long as the sonographer did not exceed motion of 200 µm per frame and sufficient areas of speckle were present in the scans, the frame spacing was accurately estimated.

The increased error in the clinical scans

was expected. When the translator framework was placed on the breast, pressure was applied to maintain good contact between the skin and transducer. As the transducer was moved along the surface, there was a slight repositioning of the underlying tissue, which was undetected by the position encoder. Also, breast contains large amounts of phase-aberrating tissue that would degrade the beamforming process and increase the beam correlation width of the transducer. The result is a bias in the estimated frame separation below its actual value. However, it should also be noted that the "actual" separation based on the encoding system may also not be correct due to relative motion between the frame and the tissue. This motion would actually be accounted for by the image-based registration technique, and as such, the result may actually be more accurate than the "actual" result used for comparison. In the same sense, the image-based registration technique would give more accurate spatial measurement in tissues moving rapidly (eg, with respiration) than would measurements based on an external frame of reference. This would be particularly helpful in compounding of pulsed Doppler images (12).

The current setup has some limitations critical to its use in a clinical setting. The scanning speeds for this study were quite slow (maximum velocity, 7.5 mm/sec at 30 Hz). Use of higher frame rates would alleviate this problem, though there is a trade-off with reduced number of focal zones and smaller field of view. In theory, only limited amounts of information, obtainable in real time, would be required, and thus limitations of scanning speed would be reduced.

As previously noted (7), this technique could be implemented in real time since only a portion of the image is needed to determine transducer motion. Similar to or in conjunction with power Doppler estimations, a few pulses at high pulse repetition frequency could be transmitted between acquisition of data from two consecutive images. The correlations could be computed at high speeds with a programmable image processor board as is used with other US imaging technology (13,14).

For the clinical study, the transducer was limited to translational movement. The framework, which also permits rotation around a fixed axis, was designed for scanning of large body parts such as breast, liver, or Achilles tendon. These two encoded motions were chosen as the most useful in circumstances such as scanning up to and under the ribs. Our future work will emphasize regional speckle analysis to calculate motion and thus allow rotation of the transducer. A preliminary frame-to-frame correlation can also be used to account for lateral and axial motion. This would permit scanning with a freely held transducer without use of any position framework.

The speckle-decorrelation algorithm provides image-based registration of US frame sections obtained with a freely moving handheld transducer. Findings in this study have shown that for three-dimensional B-scan sets, the section spacing can be determined effectively on the basis of the speckle decorrelation from frame to frame. By moving a transducer slowly over the region of interest and restricting additional degrees of freedom, the frame spacing is calculated without use of any additional position-encoding hardware. While the errors for the absolute frame distance vary near 10%, the accumulative error, which is critical for tumor or other volume estimation, is much smaller. The efficacy of the technique was further demonstrated (or suggested) in clinical breast scans, and additional work should enhance image-based reconstruction of three-dimensional images.

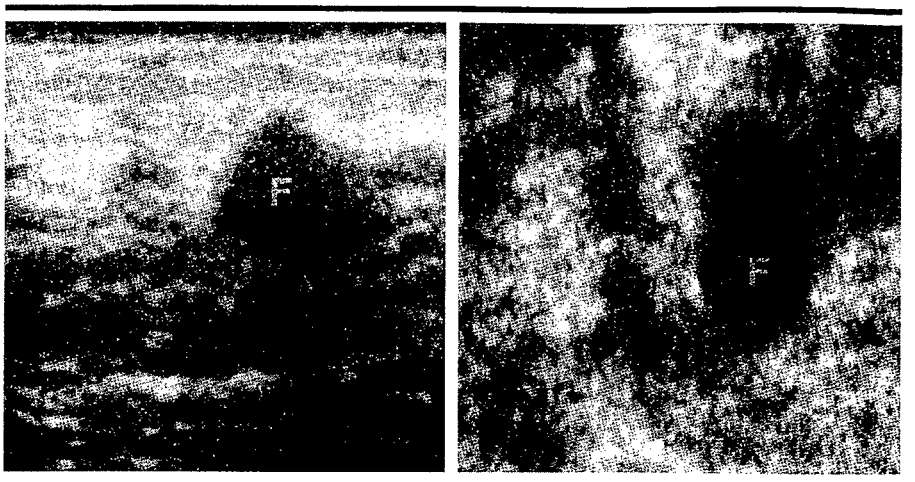

a. b.

Figure 9. (a) Transverse image of a breast fibroadenoma (*F*) formed by selecting a vertical section through a set of B-scan images and correcting for transducer position. (b) C-scan image obtained from the same B-scan set.

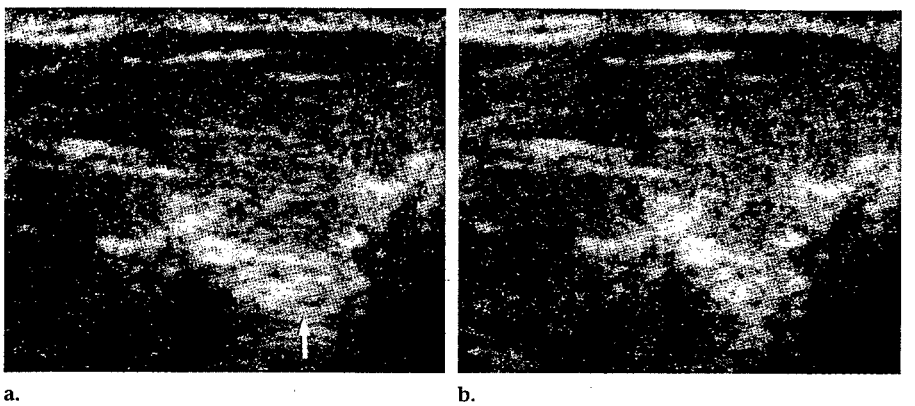

a. b.

Figure 10. Reconstruction images of a transverse image that was obtained from a set of breast scans. (a) Reconstruction image with uniform spacing between frames. Arrow indicates a region where the sonographer slowed down during scanning. (b) Reconstruction image with variable frame spacing determined with the speckle-decorrelation algorithm.

Appendix

Speckle is formed by the coherent scattering from subresolvable particles. The derivation for this algorithm starts with a stochastic analysis of the received amplitude signal (15,16). If the number of

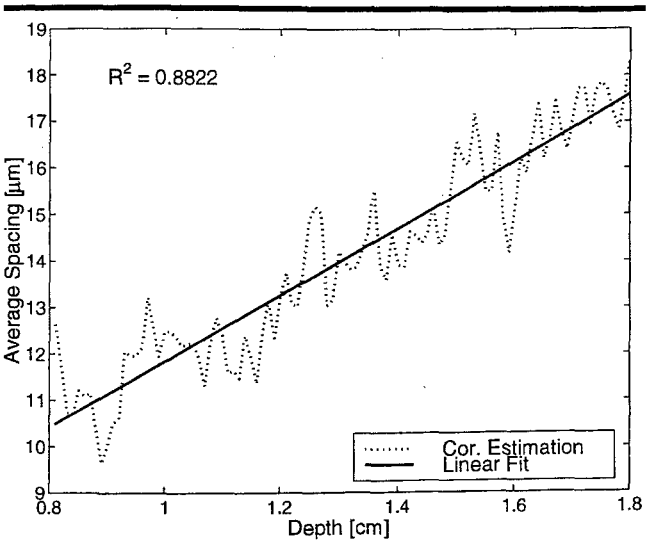

Figure 11. Estimated depth-varying frame spacing for phantom scan series obtained by hand tilting a transducer through an approximately 30° arc, with the face of the scanning head as the axis of rotation. The spacing at each depth was averaged over 250 frames. *Cor. Estimation* = correlation estimation.

independent scatterers in the scanning volume is large, then on the basis of the central limit theorem, the sum of the complex signals will have a Gaussian distribution with mean of zero and variance of σ^2. With use of a transformation of variables, the amplitude, A, is shown to have a Rayleigh distribution, p,

$$p_A(A) = A/\sigma^2 \exp(-A^2/2\sigma^2).$$

Analysis of the first-order statistics provides an interesting result: The ratio of the mean intensity to SD is a constant 1.91.

For this analysis, the statistics for the intensity (I) or squared amplitude are required. By again applying a variable transformation, the intensity is shown to have a negative exponential distribution,

$$p_I(I) = 1/2\sigma^2 \exp(-I/2\sigma^2),$$

which has a mean of $2\sigma^2$ and a variance of $4\sigma^4$. Thus for fully developed speckle, the intensity image should have a constant ratio of mean intensity to SD of 1.0.

Second-Order Statistics

To relate the fluctuations in image intensity from frame to frame, the second-order statistics of the speckle are used (17). The amplitude autocorrelation (R_A) for positions r_1 and r_2 is defined as

$$R_A(r_1, r_2) = \langle A(r_1) A(r_2) \rangle,$$

and the autocovariance (C_A) is

$$C_A(r_1, r_2) = R_A(r_1, r_2) - \langle A(r_1) \rangle \langle A^*(r_2) \rangle,$$

where $\langle\ \rangle$ denotes the expected value. The normalized autocovariance, ρ, is referred to as the correlation function.

The amplitude signal is formed from the convolution of the transducer point-spread function with the insonified scattering train. The autocorrelation function of the amplitude is the convolution of the autocorrelation functions for the point-spread function and the scatterers. For pure speckle, the scatters are independent and the autocorrelation can be approximated as a δ function. Consequently, the amplitude autocorrelation is directly proportional to the point-spread-function autocorrelation.

For a focused transducer, the point-spread function near the focal zone is proportional to the square of the Fourier transform of the transducer aperture (18). With the rectangular linear array, focusing of the electronic beam apodizes side lobes. The beam pattern can then be approximated with a Gaussian curve, and the point-spread-function autocorrelation will also be Gaussian (19),

$$\rho(r_1, r_2) = \exp[-(r_1 - r_2)^2/2\gamma_z^2],$$

where γ_z is related to the beam width.

After a similar derivation (17), the intensity autocorrelation is shown to have the form

$$R_I(r_1, r_2) = \langle I(r_1) I(r_2) \rangle = \langle I_o \rangle^2 [1 + |\rho(r_1, r_2)|^2]$$

and the autocovariance is

$$C_I(r_1, r_2) = \langle I_o \rangle^2 |\rho(r_1, r_2)|^2,$$

where $\langle I_o \rangle$ is the average image intensity. The intensity correlation function is thus directly related to the amplitude correlation function.

This one-dimensional analysis can also be expanded to include temporal correlation properties for relative motion between the transducer and the insonified tissue (20). For a transducer velocity of v_x (in distance per frame) and B-scan frame number n, the normalized intensity elevational covariance for a single pixel location then has a Gaussian shape (19),

$$C(n, z) \propto \exp[-(v_x n)^2/2\sigma_v^2(z)],$$

where $\sigma_v(z)$ is the depth-dependent beam correlation width and is determined by the transducer properties. By fitting the correlation function for a set of N frames to a Gaussian curve, the average frame spacing for that set can be back calculated.

Acknowledgments: The authors are indebted to Gerald LeCarpentier, MD, for his work with the position encoder. Thanks also to GE Medical Systems and Diasonics Vingmed Ultrasound, Santa Clara, Calif, for supplying the US equipment.

References

1. Carson PL, Moskalik A, Govil A, et al. The 3D and 2D color flow display of breast masses. Ultrasound Med Biol 1997; 23: 837–849.
2. Ritchie CJ, Edwards WS, Mack LA, Cyr DR, Kim Y. Three-dimensional ultrasonic angiography using power-mode Doppler. Ultrasound Med Biol 1996; 22:277–286.
3. Nelson TR, Pretorius DH, Sklansky M, Hagen-Ansert S. Three-dimensional echocardiographic evaluation of fetal heart anatomy and function: acquisition, analysis, and display. J Ultrasound Med 1996; 15:1–9.
4. He P, Xue K, Murka P. 3-D imaging of residual limbs using ultrasound. J Rehabil Res Dev 1997; 34:269–278.
5. Fenster A, Downey DB. 3-D ultrasound imaging: a review. IEEE Eng Med Biol 1996; 15:41–51.
6. Chen JF, Fowlkes JB, Carson PL, Moskalik A. Determination of scan-head motion using decorrelation of speckle (abstr). Med Phys 1995; 22:974.
7. Chen JF, Fowlkes JB, Carson PL, Rubin JM. Determination of scan-plane motion using speckle decorrelation: theoretical considerations and initial test. Int J Imaging Syst Technol 1997; 8:38–44.
8. Fowlkes JB, Carson PL, Moskalik A, Chen JF, Rubin JM. Method and apparatus for composition and display of three-dimensional image from two-dimensional ultrasound. International patent pending PCT/US96/10189. 1996.
9. Li M. System and method for 3-D medical imaging using 2-D scan data. US patent 5,582,173. Dec 10, 1996.
10. Fenn RC, Fowlkes JB, Roubidoux MA, Moskalik A, Carson PL. A miniature position-encoding system for flexible, hand-controlled, 3D ultrasound (abstr). J Ultrasound Med 1997; 16(suppl):11.

11. Fenn RC, Fowlkes JB, Moskalik A, et al. A hand-controlled, 3-D ultrasound guide and measurement system. In: Lees S, Ferrari LA, eds. Acoustical imaging. New York, NY: Plenum, 1997; 237–242.
12. Moskalik A, Carson PL, Meyer CR, Fowlkes JB, Rubin JM, Roubidoux M. Registration of three-dimensional compound ultrasound scans of the breast for refraction and motion correction. Ultrasound Med Biol 1995; 21:769–778.
13. Basoglu C, Reeve J, Kim Y, Marquis S. UWGSP8: a programmable ultrasound subsystem for native image processing. SPIE Med Imaging 1996; 2707:378–388.
14. Weng L, Tirumalai AP, Lowery CM, et al. US extended field-of-view imaging technology. Radiology 1997; 203:877–880.
15. Abbot JG, Thurstone FL. Acoustic speckle: theory and experimental analysis. Ultrason Imaging 1979; 1:303–324.
16. Tuthill TA, Sperry RH, Parker KJ. Deviations from Rayleigh statistics in ultrasonic speckle. Ultrason Imaging 1988; 10:81–89.
17. Wagner RF, Smith SW, Sandrik JM, Lopez H. Statistics of speckle in ultrasound B-scans. IEEE Trans Sonics Ultrason 1983; SU-30:156–163.
18. Macovski A. Medical imaging systems. Engle Cliffs, NJ: Prentice Hall, 1983; chap 9.
19. Wear KA, Popp RL. Methods for estimation of statistical properties of envelopes of ultrasonic echoes from myocardium. IEEE Trans Med Imaging 1987; MI-6:281–291.
20. Adler RS, Rubin JM, Fowlkes JB, Carson PL, Pallister JE. Ultrasonic estimation of tissue perfusion: a stochastic approach. Ultrasound Med Biol 1995; 21:493–500.

Frederick W. Kremkau, PhD ▮ Christopher R. B. Merritt, MD ▮ Paul L. Carson, PhD ▮ Laurence Needleman, MD
Thomas R. Nelson, PhD ▮ Dolores H. Pretorius, MD ▮ Jonathan M. Rubin, MD, PhD

The American Institute of Ultrasound in Medicine and the Society of Radiologists in Ultrasound

Future Directions in Diagnostic US[1]

From modest beginnings about 50 years ago, ultrasonography (US) has become the most rapidly growing diagnostic imaging method in worldwide use today. Its versatility, portability, low cost, and efficacy have made US an indispensable tool in patient care. Recently, the value of US has been enhanced by improvements in both imaging and Doppler technology and the development of echo-enhancing agents.

Diagnostic US is based on the scattering of sound by tissue. Current methods of detecting and displaying amplitude and frequency contents of the backscattered ultrasound echoes have achieved high sensitivity and resolution, permitting excellent imaging of soft tissues and detection and characterization of tissue motion and blood flow in real time. Benefiting from dramatic improvements in computer power, basic US functions of gray-scale imaging and Doppler are expected to become even more powerful in the future. Even more exciting possibilities arise from the exploration of the complex interaction of sound with tissues to develop opportunities for novel methods of imaging that are not possible with other methods. Opportunities for further progress in diagnostic US are the following: (*a*) improved signal detection: echo-enhancing agents (contrast agents), harmonic imaging; (*b*) improved image display: three-dimensional US; (*c*) novel methods: anisotropic imaging, perfusion imaging, co-registration, elastography; (*d*) instrumentation: microimaging, endoimaging, telesonography; (*e*) therapy and intervention: high-intensity focused ultrasound therapy, guidance, gene therapy; (*f*) applications: intraoperative and endoscopic.

New developments that will affect the future of US are currently in progress and will constitute the focus of this overview. They include contrast agents, intraoperative and endoscopic applications, and three-dimensional imaging. Several other areas of development included in this discussion have not yet substantially penetrated clinical US but show promise for altering and improving the practice of US.

Index terms:
Radiology and radiologists, research
Subspecialty society messages
Ultrasound (US)

Radiology 1998; 209:305–311

[1]From the Center for Medical Ultrasound, Wake Forest University School of Medicine, Medical Center Blvd, Winston-Salem, NC 27157-1039 (F.W.K.); the Division of Diagnostic Ultrasound, Thomas Jefferson University Hospital, Philadelphia, Pa (C.R.B.M., L.N.); the Department of Radiology, University of Michigan, Ann Arbor (P.L.C., J.M.R.); and the Department of Radiology, University of California, San Diego (T.R.N., D.H.P.). Received March 17, 1998; accepted May 16, 1998. **Address reprint requests to F.W.K.**

© RSNA, 1998

See also the article by Leopold (pp 312–313) in this issue.

Contrast Agents

Contrast agents (1–8) improve US by increasing the echo strength from within the body rather than by altering the US equipment. US contrast agents address several fundamental acoustic difficulties in imaging patients when there may be insufficient US contrast between diseased tissues and normal regions because the acoustic properties are not substantially different. Also, Doppler is less reliable in slow-flow velocities and in low-volume flow rates such as in high-grade stenoses, in which there are few moving erythrocytes to produce an adequate signal. Doppler signals also may be inadequate due to attenuation in such situations as deep vessels or when overlying plaque or bone diminishes the echo strength returning to the transducer.

The pharmaceutical industry is now creating a variety of US contrast agents. Agents being investigated include intravenous blood-pool agents that increase Doppler and gray-scale US signals systemically, and enteral agents that improve visualization of the bowel and the abdominal organs beneath the bowel. Companies have begun to market contrast agents overseas for radiologic and cardiac applications and in the United States for echocardiography.

Intravenous contrast agents rely on microbubbles of gas to strengthen the echoes by increasing backscatter. Manufacturing techniques ensure that there is uniformity of a small bubble size that permits the bubbles to cross the pulmonary circulation and capillary beds. Various designs have been used to keep bubbles intact so that the duration of enhancement can be extended to minutes. These designs include the use of fluorocarbons or other gases to resist dissolution and the use of a coating or shell over the bubbles to make them more resistant to destruction. The quantity of gas used is quite small, and the materials used with the gas are chosen to be as inert as possible, leading to safety profiles that have been quite good in clinical trials.

Clinical trials of contrast agents have shown that both spectral and color Doppler signals are increased after intravenous administration. Contrast material has been administered to a variety of sites, with the largest experience in the renal and liver circulations. Studies of both the main renal arteries (Fig 1) and intrarenal waveforms have shown improved imaging performance and faster examinations because of intravenous administration of

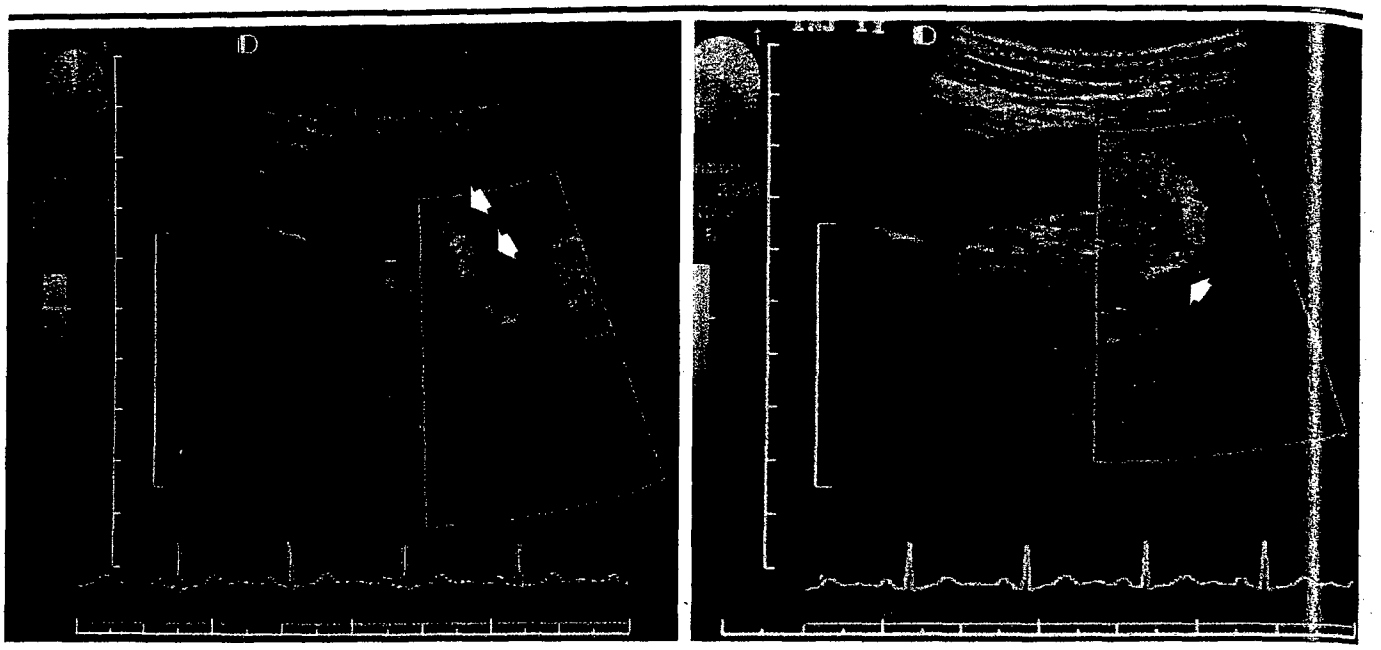

a. b.

Figure 1. Normal renal artery (angiographically proved) initially misinterpreted at US as renal artery stenosis. **(a)** Baseline Doppler image shows a portion of the renal artery (arrows). Spectral Doppler image initially showed increased velocity since the vessel was assumed to be straight and an incorrect spectral Doppler angle was assigned (not shown). **(b)** Contrast material–enhanced Doppler image shows a longer length of the renal artery and shows that the vessel actually has a tortuous course (arrow). The Doppler angle was then correctly assigned, and no elevated velocity was found.

contrast material. US examination in difficult liver cases such as slow flow in portal veins in patients with cirrhosis and in complete interrogation of transjugular intrahepatic portosystemic shunts has also been shown to be more accurate after administration of contrast material. More complete transcranial Doppler signals can be obtained after administration of contrast material. Contrast material cannot make a signal appear where the area of interest is completely obscured by bowel gas, but it can improve a partial signal that may be present. If contrast material can improve confidence in a negative examination or prove there is a pseudoocclusion, confirmatory, often more expensive testing can be eliminated. Gray-scale enhancement also is possible with some agents (Fig 2).

US studies with use of contrast agents initially will be used in selected cases in which US information is incomplete or difficult to obtain. This may be applied to individual patients or to all who will undergo a technically demanding study, such as renal artery or transcranial Doppler studies. Absence of nephrotoxicity may help make it an attractive alternative to iodinated contrast material in certain other patients. Wider adoption of US contrast agents will depend on whether they can improve accuracy or efficiency in more routine cases. Studies of accuracy, patient outcomes, and costs, with larger numbers of patients, will further clarify the role of these contrast agents.

For contrast agents to be widely adopted in radiologic practice, several obstacles must be overcome. US is perceived to be completely noninvasive. This changes with an intravenous injection, but the invasiveness may be acceptable if the test is more accurate, the cost is modest, and the administration is not burdensome. Even with an added cost, contrast agents may be effective if they can eliminate the negative consequences of inadequate or inaccurate US or obviate the use of alternative, more expensive, and sometimes riskier tests.

Further uses of microbubble US agents are actively being investigated. Agents with specialized applications, such as organ- or disease-seeking materials, are being evaluated. Some agents are removed by the reticuloendothelial system and can enhance normal liver but not tumors, which lack these cells. It is hoped that this will improve the sensitivity of hepatic US. Agents that attach to pathologic tissues are also being developed. For instance, some agents have been shown to attach to thrombi. This approach may have therapeutic implications. Microbubbles of a disease-seeking agent can contain gas and a chemotherapeutic agent. After the bubble attaches to the abnormality, a higher energy ultrasound beam can break the bubble and release the medicine locally for a potentially greater response than with traditional administration. US equipment also is being changed to use contrast material more effectively. One promising approach is harmonic imaging. Since bubbles resonate nonlinearly, they emit harmonic frequencies, in which case the instrument receives echoes at a different frequency than is transmitted. Contrast effects may be seen better or for a longer time with use of harmonic rather than fundamental frequencies. Other properties of bubbles are being investigated to exploit their unique properties. Bubbles behave differently at different pressures, which may allow noninvasive determination of blood pressure. It can thus be seen that microbubble agents have a vast potential role in improving US imaging.

Intraoperative and Endoscopic Applications

US has been keeping pace with the radical changes in surgery and continued growth of endoscopic procedures. Intraoperative US is an established accurate tool for surgical decision making. US imaging using specially designed laparoscopic US probes is another effective tool for providing important information. Laparoscopy

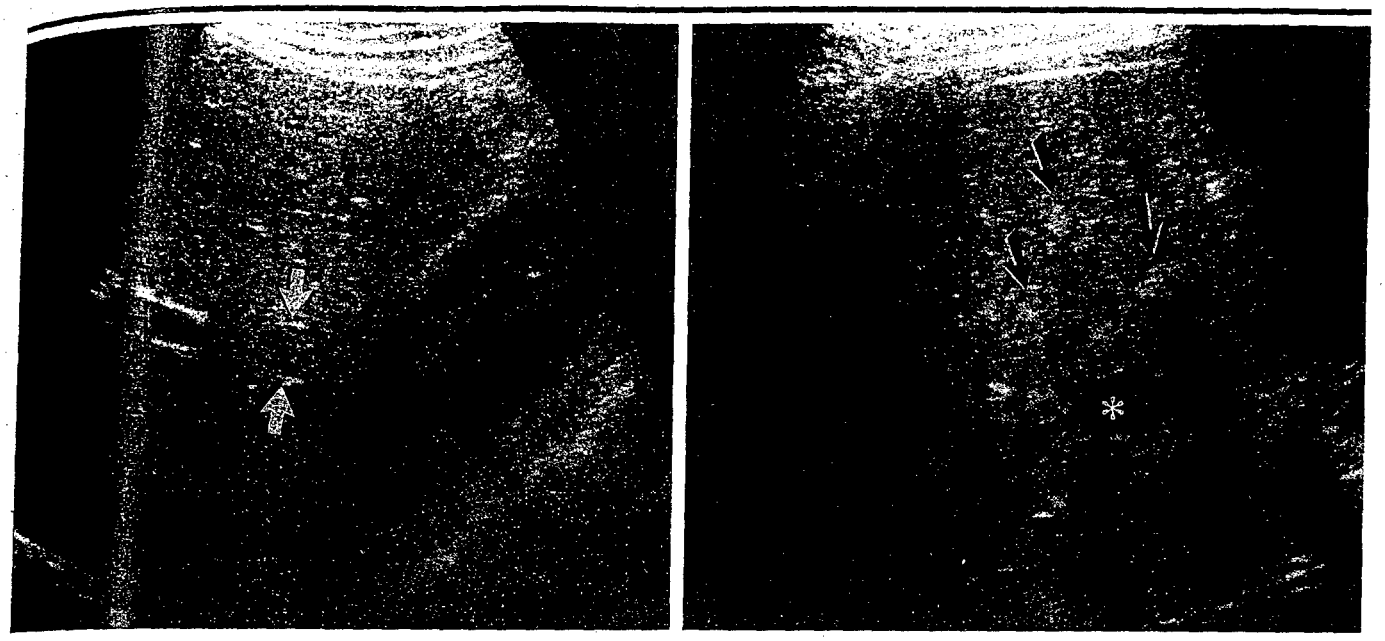

a. b.

Figure 2. Liver metastasis. (a) Baseline US image shows a nearly isoechoic liver lesion (arrows) that is difficult to distinguish from adjacent normal liver. (b) After intravenous administration of contrast material, there is gray-scale enhancement of the liver, and the lesion stands out as hypoechoic (*) against the more echogenic liver. The blood has markedly increased echogenicity, and the portal veins are markedly echogenic (arrows). Some portal veins shadow from the amount of contrast agent within them.

can eliminate needless surgery and can decrease the need for hospitalization. Cryoablation can now be performed laparoscopically in some patients. Endoscopic US is another growing technique that can help to stage gastrointestinal tumors and guide biopsies and other interventions. Smaller laparoscopic and more flexible endoscopic designs will allow these procedures to become even easier and more routine. The role of miniature transducers, initially designed for intravascular US, is being expanded to image many structures such as the ureter, esophagus, and anal canal. Design changes will allow better imaging through these tiny probes as well. The surgeon and endoscopist need an imaging test to show them what is below the surface and to guide therapy. Radiologists should be prepared to be part of the team providing diagnostic US during these procedures or be left behind as this revolution sweeps across medicine.

Three-dimensional US

Three-dimensional US is a new, exciting technology that allows physicians to use US to view anatomy and pathologic conditions as a volume, thereby enhancing comprehension of patient anatomy (9–11). Ongoing developments in computers and technology now permit acquisition, analysis, and display of volume data in seconds, facilitating many opportunities for rapid diagnosis and interventional techniques. Both commercial and academic interest in three-dimensional US is mounting, and continued advancements and understanding are expected in the near future.

Thus far, three-dimensional US has demonstrated several advantages compared with two-dimensional US. First, volume data can be viewed by using a standard anatomic orientation with planar images to obtain simultaneous display of coronal, sagittal, and axial planes in addition to orientations that are difficult or impossible to obtain with conventional two-dimensional US due to anatomic constraints (eg, coronal plane of the uterus). Second, rendering of the entire volume allows the continuity of curved structures such as liver vessels, the fetal spine, or fetal face to be viewed in a single image. Additionally, by rotating the volume interactively, it is possible to view the structure from multiple orientations or perspectives that enhance understanding of patient anatomy. Third, more accurate measurement of organ volume and irregularly shaped objects may be readily obtained (12). Fourth, volume data may be used to guide interventional procedures providing accurate identification of needle or catheter placement. Fifth, volume data may be archived and subsequently reviewed for further critical review or teaching purposes on site or via the Internet after the patient has left the clinic.

Ongoing clinical research is evaluating clinical applications likely to have the greatest effect on diagnosis and patient care. To date, fetal (13,14), cardiac (15–17), and gynecologic (18) areas have received the most attention with other clinical areas receiving increasing interest, including imaging of vascular anatomy, prostate volume measurement and assessment of seed placement, guidance of interventional needles and catheters, neonatal head evaluation, and evaluation of breast mass vascularity (19). In the fetus, improved visualization of fetal features, including the face (Fig 3), spine, and limbs, has improved identification of anomalies and has been immediately appealing for clearly sharing developmental information with the family and colleagues. Cardiac applications have provided a "surgeon's-eye view" with use of transesophageal and transthoracic techniques to assess valve geometry and motion and plan operative procedures.

Gynecologic applications include evaluating congenital anomalies of the uterus, endometrial cancer, adnexal masses, intrauterine device position, and follicular cysts. Applications in other specialties

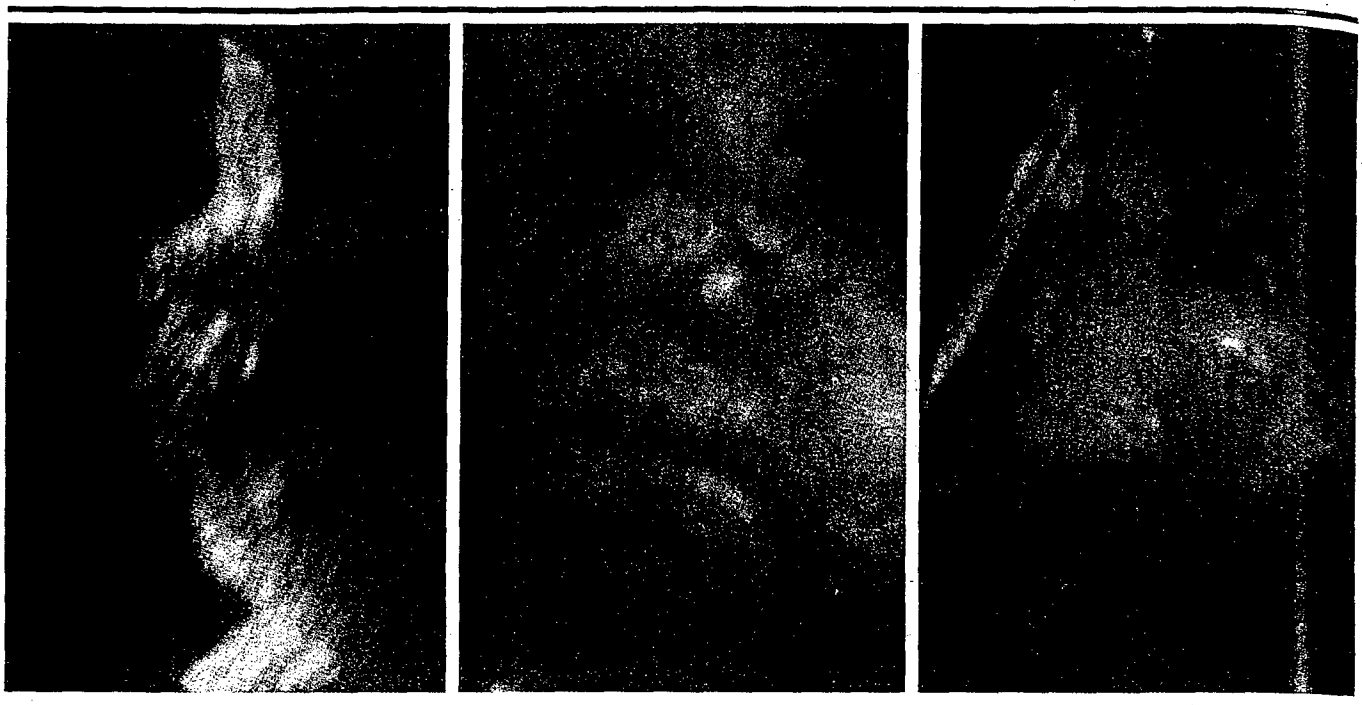

a. b. c.

Figure 3. (**a**) Sagittal section through a three-dimensional US volume data set of a 35-week-old fetus is similar to a conventional two-dimensional US image of the facial profile. (**b**) Rendered view of the face from the same volume provides a more recognizable picture of the face. (**c**) Rendered view of another 35-week-old fetus with cleft lip/palate and hypotelorism. The rendered images clearly demonstrate both normal and abnormal anatomy in a readily comprehended fashion.

such as urology, gastroenterology, dermatology, and ophthalmology are expanding the range of applications for three-dimensional US methods.

Coming soon will be further developments that will broaden the adoption of three-dimensional US imaging worldwide, including (*a*) improved overall scanning system performance and smaller scanners and transducers, (*b*) improved user interfaces making it easier to evaluate volume data and understand patient anatomy, (*c*) physiologic gating with both the cardiac and respiratory cycles eliminating motion artifacts and opening a window to dynamic processes, (*d*) combination of volume imaging and US contrast agents to enhance visualization of vascular anatomy (Fig 4), (*e*) faster volume acquisition, analysis, and interactive displays, ultimately leading to (*f*) real-time volume imaging in the near future.

Ultimately, three-dimensional US technology will provide a central integrating focus in US imaging. Three-dimensional US equipment will provide more conventional two-dimensional US imaging capability but seamlessly expand imaging to include volume acquisition and display as necessary to obtain the diagnosis. Focused application of three-dimensional US methods will expand the areas in which US is the predominant imaging modality beyond those areas in which US currently is the method of choice. Through rapid transmission of volume data to specialists at distant locations, patient care will benefit from improved diagnosis and treatment.

Aisotropic Imaging

Anisotropy, directional dependency, of the amplitude of a backscattered wave is a well-known property of US (20–24). Tissues in which backscatter anisotropy has been recognized include the renal cortex, myocardium, cerebral periventricular areas, and, most prominently, muscles and tendons. Anisotropy has mostly been a curiosity whose clinical importance rested only in recognizing its existence and accounting for its effects on images. It has never seriously been employed as a method of diagnosis or enhancement of echo contrast. Yet, the effects of anisotropy on backscatter can be huge, with angle-dependent backscattered differences having been measured that can vary by orders of magnitude (25,26). One could employ these very large dynamic ranges in differentiating normal anisotropic tissue from isotropic abnormalities such as tendon tears or in measuring surface-roughening effects of diseases as in osteoarthritis. Preliminary studies have shown remarkable angle-dependent sensitivities for backscattered ultrasound. Roughnesses as small as 5 μm (root-mean squared), easily small enough to detect the earliest structural changes in osteoarthritis, can be detected even with the use of standard diagnostic frequency (5-MHz) transducers (26,27). Even though cartilage surface may be difficult to visualize in vivo, it and other areas of demonstrable anisotropy such as myocardium, renal cortex, and tendons are waiting to be exploited.

Perfusion Imaging

An ultimate goal of vascular imaging is blood flow perfusion. In US, perfusion-like estimates (pixel counting) using spectral or color Doppler abound in the literature, but actual estimates of true perfusion are rare. Perfusion represents the volume of blood per mass of tissue (fractional blood volume) divided by the mean transit time of the blood through the tissue. Recent developments in blood flow quantitation appear to make such true perfusion estimates tractable. New techniques for estimating mean transit time include Doppler-based techniques (28), speckle

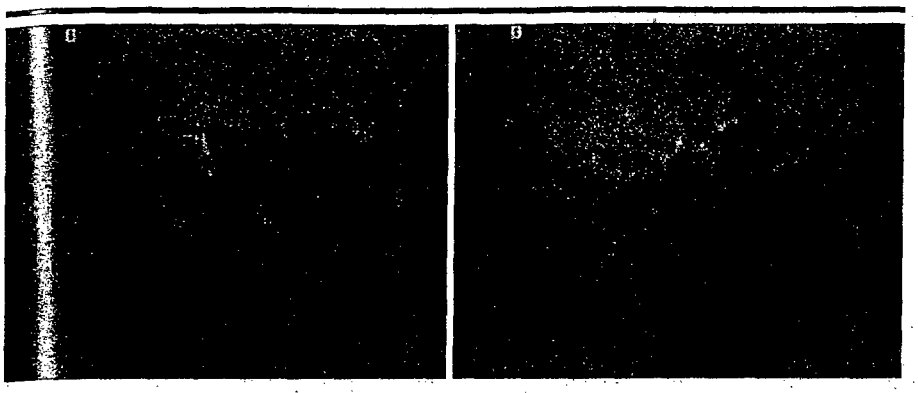

a.

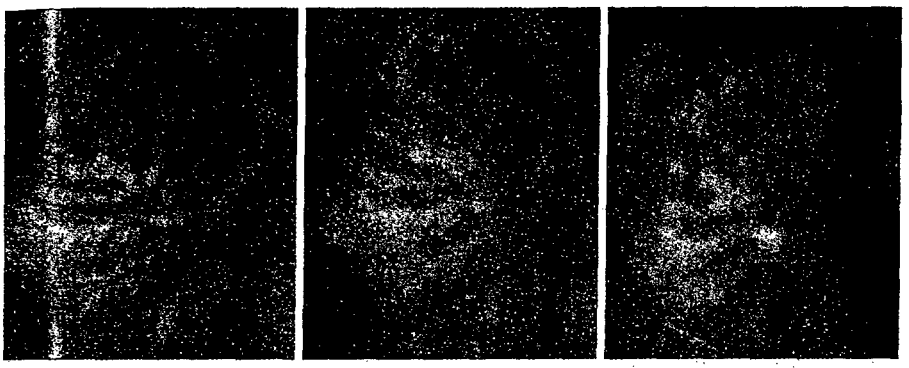

b.

Figure 4. Three-dimensional US study of a canine kidney after administration of a contrast agent (Imagent; Alliance Pharmaceutical, San Diego, Calif) and wide-band harmonic imaging (Siemens, Erlangen, Germany). (a) Two-dimensional US images of the kidney obtained during data acquisition. (b) Three volume-rendered images of the kidney from different projections. The continuity of the renal vasculature is clearly visible. Three-dimensional US combined with harmonic imaging and contrast agents provides superior spatial and temporal resolution compared with those of conventional Doppler imaging methods for the evaluation of vascular anatomy.

decorrelation techniques (29), both of which can be done with or without contrast agents, and methods requiring US contrast agents (30–32). US bubble contrast agents have particular advantages in this regard since they are totally intravascular, can exploit harmonic imaging to remove soft-tissue flash artifact (33), and can be manipulated externally by the ultrasound beam to actually alter the bubble distribution in vivo (30–32). In fact, extremely short boluses have been generated by using strongly focused exogenous ultrasound sources without injection of contrast material (34). Such manipulations can potentially remove the previously confounding effects of separating bolus shape from the tissue response making mean transit time estimates tractable. Finally, fractional blood volume estimates can now be made either with use of power Doppler with or without contrast agents or gray-scale imaging with contrast agents (35,36). Early imaging with these techniques has produced perfusion images in vivo that portend a whole new class of US-based diagnostic capabilities.

Co-registration of Sequential Images

Co-registration of US data sets from examinations at different times offers the exciting possibility of much more consistent and sensitive detection of changes in tissues between studies and better image quality. This could open new possibilities for screening and assessment of growth of suspicious regions or of masses during treatment. The three-dimensional image registration software, MiamiFuse (University of Michigan, Ann Arbor), was originally developed for fusion of data sets from multiple modalities (37). Its initial application to US images (38) has required very little preprocessing or specific image features, as the software is based on a statistical maximization of a measure aptly referred to as mutual information. The technique appears to work even in the presence of substantial tissue shear, warping, and limited overlap of scan regions.

There are other reasons why US examinations might benefit from registration of several image sets or examinations. For example, images from different transducer positions are partially uncorrelated, and summing them, in compound scanning, can improve the contrast-to-(speckle) noise ratio (39). Also, multiple viewing directions may depict and better represent flow than can a single view. This technique of co-registration by mutual information might be combined with beam reformation (40,41) for aberration correction to realize the high detail resolution of large apertures. Co-registration of images might also be combined with image-based location of images (42) in a freehand, three-dimensional scan to provide improved image quality and spatial fidelity. This is particularly appealing in the presence of respiratory motion during slow scanning required for sensitive three-dimensional imaging of vascularity.

Limitations on Image Improvement by Safety Considerations

In 1992, the U.S. Food and Drug Administration increased the limiting-guideline spatial-peak, time–average intensity levels for all applications to the levels previously allowed only for peripheral vascular studies (43). For general and obstetric examinations, these intensities were allowed to increase by a factor of almost 8. Since that time, the clear improvement in frame rate and quality of color flow images and of multiple-focal-zone gray-scale images has been made possible largely, and at little increased system cost, by the change in allowed output. The U.S. Food and Drug Administration acted (*a*) because professional organizations cooperated with industry to provide users with an indication of the relative output in the most biophysically relevant terms available—the thermal index, TI, and the mechanical index, MI (44); and (*b*) on the assumption that users would pay attention to those convenient indicators on the displays of systems capable of exceeding the former allowable output levels.

These indices are the best, usually conservative, estimates currently available in real time of the possible peak temperature rise (TI) and $p/f^{1/2}$ (the peak negative pressure divided by the square root of the frequency, or MI). When users increase their awareness of these indicators and employ them in mental risk-benefit analyses whenever the levels are high, it will be less likely that serious damage will occur. It would also be possible then that the limiting guidelines would be raised or

of Radiologists in Ultrasound have a great opportunity to contribute to the success of translating the research of today into effective clinical practice of tomorrow.

References

1. Liu JB, Goldberg BB. Endoluminal ultrasound: vascular and nonvascular applications. London, England: Dunitz, 1998.
2. Feld R, Liu JB, Nazarian LN, et al. Laparoscopic liver sonography: preliminary experience in liver metastases compared with CT portography. J Ultrasound Med 1996; 15:289–295.
3. Needleman L, Forsberg F. Contrast agents in ultrasound. Ultrasound Q 1996; 13:121–138.
4. Cosgrove D. Ultrasound contrast enhancement of tumours. Clin Radiol 1996; 51(suppl):44–49.
5. Otis S, Rush M, Boyajian R. Contrast-enhanced transcranial imaging: results of an American phase-two study. Stroke 1995; 26:203–209.
6. Tachibana K, Tachibana S. Albumin microbubble echo-contrast material as an enhancer for ultrasound accelerated thrombolysis. Circulation 1995; 92:1148–1150.
7. Fritzsch T, Schlief R. Future prospects for echo-enhancing agents. Clin Radiol 1996; 51(suppl):56–58.
8. Melany ML, Grant EG, Duerinckx AJ, Watts TM, Levine BS. Ability of a phase shift US contrast agent to improve imaging of the main renal arteries. Radiology 1997; 205:147–152.
9. Fenster A, Downey DB. Three-dimensional ultrasound imaging: a review. IEEE Eng Med Biol Mag 1996; 15:41–51.
10. Nelson TR, Pretorius DH. Interactive acquisition, analysis, and visualization of sonographic volume data. Int J Imaging Sys Technol 1997; 8:26–37.
11. Pretorius DH, Nelson TR. Three-dimensional ultrasound. Ultrasound Obstet Gynecol 1995; 5:219–221.
12. Riccabona M, Nelson TR, Pretorius DH, Davidson TE. Three-dimensional sonographic measurement of bladder volume. J Ultrasound Med 1996; 15:627–632.
13. Merz E, Weber G, Bahlmann F, et al. Application of transvaginal and abdominal three-dimensional ultrasound for the detection or exclusion of malformations of the fetal face. Ultrasound Obstet Gynecol 1997; 9:237–243.
14. Pretorius DH, Nelson TR. Fetal face visualization using three-dimensional ultrasonography. J Ultrasound Med 1995; 14: 349–356.
15. Greenleaf JF, Belohlavek M, Gerber TC, Foley DA, Seward JB. Multidimensional visualization in echocardiography: an introduction. Mayo Clin Proc 1993; 68:213–219.
16. Belohlavek M, Foley DA, Gerber TC, et al. Three- and four-dimensional cardiovascular ultrasound imaging: a new era for echocardiography. Mayo Clin Proc 1993; 68:221–240.
17. Nelson TR, Pretorius DH, Sklansky M, Hagen-Ansert S. Three-dimensional echocardiographic evaluation of fetal heart anatomy and function: acquisition, analysis, and display. J Ultrasound Med 1996; 15:1–9.
18. Jurkovic D, Geipel A, Gruboeck K, et al. Three-dimensional ultrasound for the assessment of uterine anatomy and detection of congenital anomalies: a comparison with hysterosalpingography and two-dimensional sonography. Ultrasound Obstet Gynecol 1995; 5:233–237.
19. Carson PL, Moskalik AP, Govil A, et al. The 3D and 2D color flow display of breast masses. Ultrasound Med Biol 1997; 23:837–849.
20. Insana MF, Hall TJ, Fishback JL. Identifying acoustic scattering sources in normal renal parenchyma from the anisotropy in acoustic properties. Ultrasound Med Biol 1991; 17:613–626.
21. Insana MF. Modeling acoustic backscatter from kidney microstructure using an anisotropic correlation function. J Acoust Soc Am 1995; 97:649–655.
22. Miller JG, Perez JE, Mottley JC, et al. Myocardial tissue characterization: an approach based on quantitative backscatter and attenuation. Proc IEEE Ultrason Symp 1983; 1947:782–793.
23. Bowerman RA, DiPietro MA. Erroneous sonographic identification of lateral ventricles: relationship to the echogenic periventricular "blush." Am J Neuroradiol 1987; 8:661–667.
24. Rubin JM, Carson PL, Meyer CR. Anisotropic ultrasonic backscatter from the renal cortex. Ultrasound Med Biol 1988; 14:507–511.
25. Hoffmeister BK, Wong AK, Verdonk ED, Wickline SA, Miller JG. Comparison of the anisotropy of apparent integrated ultrasonic backscatter from fixed human tendon and fixed human myocardium. J Acoust Soc Am 1995; 97:1307–1313.
26. Chiang EH, Laing TJ, Meyer CR, Boes JL, Rubin JM, Adler RS. Ultrasonic characterization of in vitro osteoarthritis articular cartilage with validation by confocal microscopy. Ultrasound Med Biol 1997; 23: 205–213.
27. Adler RS, Dedrick DK, Laing TJ, et al. Quantitative assessment of cartilage surface roughness in osteoarthritis using high-frequency ultrasound. Ultrasound Med Biol 1992; 18:51–58.
28. Dymling SO, Persson HW, Hertz CH. Measurement of blood perfusion in tissue using Doppler ultrasound. Ultrasound Med Biol 1991; 17:433–444.
29. Adler RS, Rubin JM, Fowlkes JB, Carson PL, Pallister JE. Ultrasonic estimation of tissue perfusion: a stochastic approach. Ultrasound Med Biol 1995; 21:493–500.
30. Fowlkes JB, Sirkin DW, Rhee R, Rubin JM, Carson PL. In vivo interruption of contrast agents for temporally short arterial bolus production. J Ultrasound Med 1997; 16:S36.
31. Matsumura T, Moriyasu F, Nada T, et al. Efficacy of continuous infusion and flash echo mode on contrast-enhanced power Doppler imaging of the liver (abstr). Radiology 1997; 205(P):279.
32. Kamiyama N, Mine Y, Kono Y, Goto Y, Shiki E, Moriyasu F. Dual window method of harmonic imaging and flash echo imaging associated with an US contrast agent (abstr). Radiology 1997; 205(P):279.
33. Burns PN, Powers JE, Hope-Simpson D, Uhlendorf V, Fritzsch T. Power Doppler imaging combined with contrast-enhancing harmonic Doppler: new method for small-vessel imaging (abstr). Radiology 1994; 193(P):366.
34. Ivey JA, Gardner EA, Fowlkes JB, Rubin JM, Carson PL. Acoustic generation of intra-arterial contrast boluses. Ultrasound Med Biol 1995; 1:757–767.
35. Rubin JM, Adler RS, Fowlkes JB, et al. Fractional moving blood volume: estimation with power Doppler US. Radiology 1995; 197:183–190.
36. Rubin JM, Bude RO, Fowlkes JB, Spratt RS, Carson PL, Adler RS. Normalizing fractional moving blood volume estimates with power Doppler US: defining a stable intravascular point with the cumulative power distribution function. Radiology 1997; 20:757–765.
37. Meyer CR, Boes JL, Kim B, Bland PH, et al. Demonstration of accuracy and clinical versatility of mutual information for automatic multimodality image fusion using affine and thin plate spline warped geometric deformations. Med Image Anal 1997; 1:195–206.
38. LeCarpentier GL, Moskalik AP, Meyer CR, et al. Breast and prostate 3D color flow ultrasound quantification and image fusion (abstr). Radiology 1997; 205(P):740.
39. Moskalik A, Carson PL, Meyer CR, et al. Registration of three-dimensional compound ultrasound scans of the breast for refraction and motion correction. Ultrasound Med Biol 1995; 21:769–778.
40. Mast TD, Nachman AI, Waag, RC. Focusing and imaging using eigenfunctions of the scattering operator. J Acoust Soc Am 1997; 102:715–725.
41. rishnan S, Li PC, O'Donnell M. Adaptive compensation of phase and magnitude aberrations. IEEE Trans Ultrasonics Fer Freq Control 1996; 43:44–55.
42. Chen JF, Fowlkes JB, Carson PL, Rubin JM. Determination of scan-plane motion using speckle decorrelation: theoretical consideration and initial test. Int J Imaging Sys Technol 1997; 8:38–44.
43. Food and Drug Administration. 510(k) guide for measuring and reporting output of diagnostic ultrasound medical devices. Rockville, Md: Center for Devices and Radiological Health, 1992.
44. American Institute of Ultrasound in Medicine and National Electrical Manufacturer's Association. Standard for real-time display of thermal and mechanical acoustic output indices on diagnostic ultrasound equipment (revision 1). Laurel, Md: American Institute of Ultrasound in Medicine and National Electrical Manufacturer's Association, 1998.
45. Edwards MJ. Hyperthermia as a teratogen: a review of experimental studies and their clinical significance. Teratog Carcinog Mutagen 1986; 6:563–582.
46. Dalecki D, Child SZ, Raeman CH, et al. Age dependence of ultrasonically induced lung hemorrhage in mice. Ultrasound Med Biol 1997; 23:767–776.
47. Brayman AA, Strickler PL, Luan H, et al. Hemolysis of 40% hematocrit, Albunex®-supplemented human erythrocytes by pulsed ultrasound: frequency, acoustic pressure and pulse length dependence. Ultrasound Med Biol 1997; 23:1237–1250.
48. Ophir J, Cespedes I, Garra B, et al. Elastography: ultrasonic imaging of tissue strain and elastic modulus in vivo. Eur J Ultrasound 1996; 3:49–70.

DEPARTMENT OF THE ARMY
US ARMY MEDICAL RESEARCH AND MATERIEL COMMAND AND FORT DETRICK
810 SCHRIEDER STREET, SUITE 218
FORT DETRICK, MARYLAND 21702-5000

Received
10/29/2001

REPLY TO
ATTENTION OF:

MCMR-RMI-S (70-1y) 17 Oct 01

MEMORANDUM FOR Administrator, Defense Technical Information Center (DTIC-OCA), 8725 John J. Kingman Road, Fort Belvoir, VA 22060-6218

SUBJECT: Request Change in Distribution Statement

1. The U.S. Army Medical Research and Materiel Command has reexamined the need for the limitation assigned to technical reports written for grants. Request the limited distribution statements for the Accession Document Numbers listed at enclosure be changed to "Approved for public release; distribution unlimited." These reports should be released to the National Technical Information Service.

2. Point of contact for this request is Ms. Judy Pawlus at DSN 343-7322 or by e-mail at judy.pawlus@det.amedd.army.mil.

FOR THE COMMANDER:

PHYLIS M. RINEHART
Deputy Chief of Staff for
Information Management

Enclosure